Master of Philosophy in Mechanical Engineering

Final Thesis

Industrial Robotics for Advanced Machining

Kieran McMullen

Date: 31/07/2022

Dr. Erdem Ozturk

Dr. Charles Lord

MPhil Thesis submitted to the Department of Mechanical Engineering, University of Sheffield

1 Preface

Acknowledgements

I would like to thank Dr Erdem Ozturk and Dr Charles Lord who provided invaluable supervision and advice throughout the course of this project.

I would also like to thank Austin Cook, David Dawson, Stephen Penny and Jon Carberry, who provided industrial support. Special thanks should also go to Huseyin Celikag and Chao Sun, who aided greatly in providing specific knowledge required throughout my research and whose work within AMRC is referenced often throughout this thesis, as well as Rob Ward who served as my student mentor for much of my time at the IDC.

EPSRC and BAE Systems must also receive thanks for their respective contributions of funding of the project.

I am also very grateful to everyone working or studying at the IDC, University of Sheffield or AMRC who has given assistance in any form over the past 3 years, including technicians, the administrative team and university lecturers, as well as fellow students.

I must also thank my family and friends, as their support enabled this research to continue despite the disruption of the pandemic.

Statement of Inclusion of Research of Huseyin Celikag

The work of Huseyin Celikag has been made use of at various times in the course of this project, and the contributions are listed here:

- Experimental frequency response function files captured from modal testing of the ABB IRB 6640 industrial robot.
- Images, Kinematic and joint stiffness parameters, examples of cartesian stiffness of the ABB IRB 6640 industrial robot.
- Segments of Matlab Code which performs inverse kinematics on end effector target locations to calculate constituent joint angles to achieve those targets.
- Experimental methodology for Mini-Project 2.
- Workpiece material for Mini-Project 2.

Other citations of literature by Huseyin Celikag are properly referenced in this thesis and can be found listed as references alongside other citations, including the names of other authors where applicable.

List of Figures

List of Tables

Explanation of the EngD Programme

At the outset, the goal of this project was to submit a thesis intended to satisfy the standard for a Doctor of Philosophy (PhD) degree. The project was undertaken within the Industrial Doctorate Centre (IDC), one of several centres for the pursuit and awarding of doctorates within the University of Sheffield, with the IDC specialising in Engineering Doctorates (EngD), to be partially funded and informed by industrial partnerships, with the remainder of the project funded by the University.

An EngD is defined by the UKRI as an alternative to a PhD with the expectation of an industrial career to follow.

The structure of this program was originally projected over 4 years, with year 1 to consist of educational and training activities, as well as correspondence with an industrial sponsor to align the research with a real-world problem. Years 2-4 were to consist of PhD research activities.

The confirmation review process was carried out at the end of Quarter 3 of Year 2, and then again at the end of Quarter 2 of Year 3. The review process indicated that a PhD thesis of sufficient quality was not expected if given another 1.5 years of research. It was therefore decided that it would be more appropriate to submit the existing body of work for the awarding of a Master of Philosophy (MPhil) degree at the conclusion of Year 3.

Contents

2 Introduction

Industrial robots are commonplace in manufacturing for transporting goods and for the manipulation of tools for tasks such as spraying and welding. They are preferred due to their high load carrying capacity and large working volumes compared with a relatively small footprint and a high degree of flexibility and adaptability in their range of applications.

According to Armarego and Brown, machining is defined as a type of material shaping manufacturing operation, alongside other shaping methods such as casting and plastic deformation [1]. It is often claimed to be the most important operation due to involvement in the production of any given manufactured item, sometimes indirectly through production of dies or fixtures [1].

Metal cutting has been studied by many investigators to produce analytical models of given operations to indicate how operations may be improved, and there are often multiple models for a given operation [1]. As an example, Orthogonal cutting (with only two dimensions to consider) is often examined for its simplicity and may be modelled using the thin plane model for high speeds and thick zone model at lower speeds [1]. This contrasts with oblique cutting, where the cutting edge is inclined (not normal) to the workpiece, and chip flow is in three dimensions [1]. Orthogonal cutting is utilised within idealised cutting experiments, while nearly all practical cutting operations use an inclined edge of some kind [1].

Automated machining operations are often carried out using computer numerical control (CNC) machine tools. These machines are designed specifically with properties which complement machining mechanics, as high accuracy in machining requires stiffness between the workpiece and tool to ensure cutting forces do not result in high deformation or displacement of the tool from the desired path. Doing so ensures form errors on the finished part are prevented. Reduction or prevention of machining chatter is also important, as it leaves parts with rougher surfaces. High tool-workpiece dynamic stiffness can prevent chatter by reducing the maximum dynamic displacements of the tool. Dynamic tool displacements result in dynamic chip thickness, and thus greater dynamic forces, which in turn cause greater dynamic displacements. Due to a difference in phase between displacement and cutting force, a positive feedback cycle is induced, which is known as the regenerative effect. Aside from the regenerative effect, any mode coupling between the cutting process and the modes of the machine will contribute to vibrations and should also be minimised. CNC machines also differ greatly from industrial robots in their working volumes, which are much smaller and limited to parts that are small enough to enter and leave the machine. This working volume is usually small compared with the space the machine itself occupies. Conversely, robots often have large dextrous working volumes compared with a small base size.

The goal of much robotic machining research is to work toward machining systems which can achieve both the high machining standards of multi-axis CNC machines and the dextrous working volume, small footprint, and task flexibility of serial robots. There are several methods of modifying the physical or control aspects of serial manipulator robotic machining cells to achieve higher effective tool/workpiece stiffness as a means of achieving this goal.

The industrial case study taken as an example for this project is that of robotic drilling of holes in restricted access spaces for aerospace manufacturing. The solution considered in this thesis relies on the stiffness and inertia modelling of the serial manipulator and characterisation of the drilling process. Dynamic modelling is carried out to determine the frequency response of the robot at various configurations, so that commands to the robot controller can be optimised to improve the process outcome.

2.1 Aims and Objectives

While issues surrounding tool-workpiece stiffness of robotic milling has been well explored in literature, the subject of robotic drilling, which considers a similar dynamic system, has received a more limited amount of research. This will form the aims and objectives of this thesis.

The aim of this research is to produce a model and automated program for determining the dynamic stability of a given robotic drilling process whilst the robot is in a given configuration. This is with the goal of mitigating compliance induced errors through optimisation of controllable machining system variables. The final output of the research is intended to be applied to robotic drilling with the aim of reducing the necessity for prefabricated guide fixtures in the process of robotic drilling in restricted access spaces. A given industrial case study (reported in Section 2.2) will be taken as an intended testing scenario.

The expected research output of this project includes a theoretical basis, usable Matlab scripts for conducting the optimisation process, and comparison of the simulation with analysed data.

These actions will be achieved by addressing the following objectives:

- Investigate current literature and available technologies for compliance compensation in robotic machining and current understanding of static and dynamic drilling forces (presented in Section 2).
- Produce a dynamic model of the robot (stiffness, inertia and damping) to determine end effector response to dynamic forces (model is described in Section 4.1).
- Characterise the static and dynamic mechanical properties of the drilling process (model described in Section 4.3).
- Produce frequency domain stability lobes for a range of spindle speeds and a range of configurations (theory discussed in Section 4.3.2, implementation discussed in Section 5.4).
- Carry out comparison of predicted stability lobes with existing prediction outputs of 2-dimensional drilling stability lobe generation methods to determine reliability (results discussed throughout Section 5.4).

2.2 Industrial Case Study

The following case study was compiled from informal discussions with BAE Systems engineers and shared documentation about their operations. After reviewing this section, no concerns have been raised or omissions requested by their representative.

The manufacturing of some complex aerospace structure components requires the drilling of up to 100,000 holes to allow for part assembly [2]. Due to the restricted access of some of the drilling sites, the process has yet to be fully automated, with approximately 50% of holes in fighter aircraft drilled manually using corner drills, pistol drills and advanced drilling units depending on the level of restrictions in effect for a given drilling site.

There is a need for collaborative robots (co-bots) in this working environment. BAE Systems uses a Kuka KMP200 mobile platform, fitted with a Kuka LBR Iiwa 14 R820 Co-bot (see Figure 1) to perform the process, however this robot currently requires a drill rail/fixture to provide the proper positional accuracy and directional stiffness for the ADU to drill at the required quality,

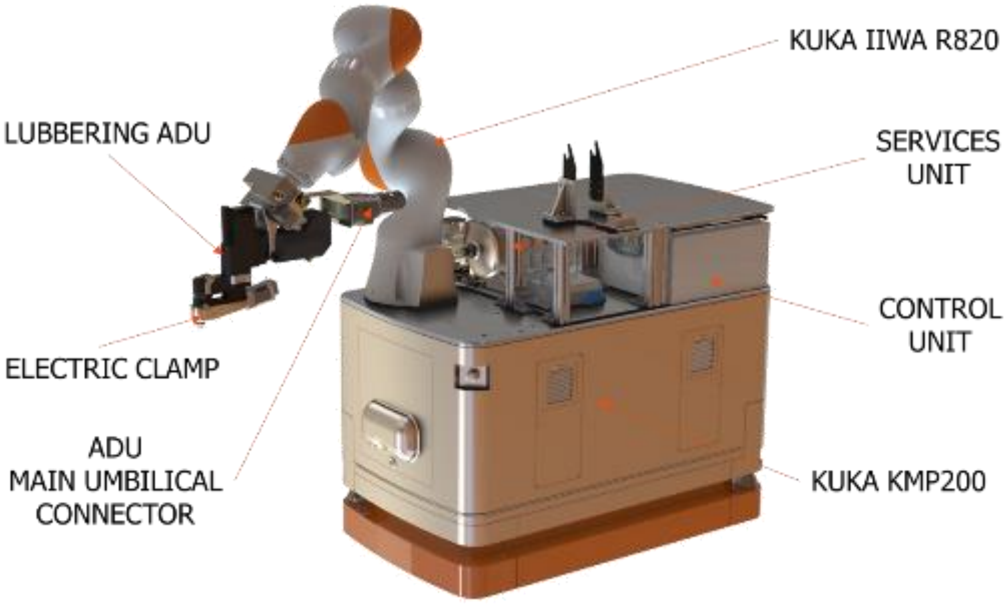

Figure 1: Mobile Multifunction Platform Diagram [2].

Traditional taper locks or concentric collets are considered too bulky for this purpose, however jigs which utilise hardened steel drill bushes are currently used, but this necessitates the design, manufacture and fitting of these jigs in order to drill holes. A 7th axis of motion is included for axial translation of the spindle for applications such as this, meaning the robot is not necessarily required to follow a toolpath during the drilling process, beyond the positioning of the ADU.

According to Seghedin and Chitariu, bushes are applied in drilling operations "for guidance of drills, in order to ensure a certain position of the tool regarding the certain reference elements of the workpiece, or to increase the stiffness of drills, when the tool diameter is reduced, or when the surface of the machined workpiece is inclined [3]."

Figure 2 shows a computer model of the drilling jigs, where the dark grey parts depict the locator holes for the end effector, and the orange holes represent the bushes used to guide the drilling process. The top right orange hole without two adjacent locator holes is a “pilot hole” used to locate and secure the fixture in place. Around 10% of holes are pilot holes for fixturing of the jig and are machined into the components before assembly. Drilling positions are usually located within 200mm of pilot holes.

The required tolerances for hole drilling at this stage of manufacturing as reported by BAE Systems are as follows:

- Positional accuracy ±0.25mm
- Perpendicularity/vector ±0.5°
- Target hole tolerance H11, but potentially intending to reach H8.

The relevant hole tolerance descriptions can be found in ISO 286 [4]. H11 is defined by this standard as a maximum deviation of +0.000mm/+0.060mm for holes of a nominal size up to and including 3mm, with larger hole tolerances of 3-6mm: +0.000mm/+0.075mm, 6-10mm: +0.000mm/+0.090mm) [5]. H8 is described as 3mm: +0.000mm/+0.014mm, 3-6mm: +0.000mm/+0.018mm, 6-10mm: +0.000mm/+0.022mm [5]. The maximum hole size required was stated to be “6mm or ¼-inch (6.35mm).”

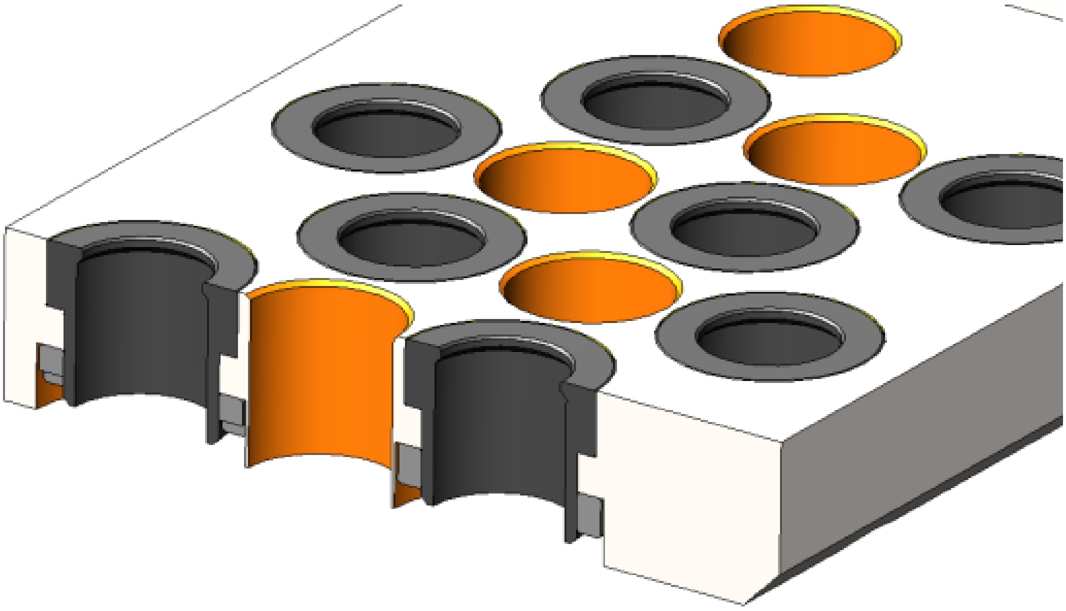

Figure 2: Images of drill rails used for guidance of the drilling process [6].

A new end effector was later designed by Electro Impact so that one bush is required per drilled hole, as the locating structure was placed around the drilling hole, rather than adjacent to it. This reduced the number of holes on the jig to the number of holes to be drilled, with some additional holes for fastening. This is not known to affect the stiffness or accuracy of the robotic drilling cell.

Discussions took place with several individuals familiar with the Kuka Iiwa/ADU drilling cell for information about the drilling process. They were unanimous in their assessment that the robotic arm was the most compliant element.

The rated positioning accuracy of the Kuka Iiwa robot arm is ±0.1mm [7], which is less than the ±0.25mm tolerance required for hole positioning, indicating that the compliance, not the kinematic precision is the cause of low drilling accuracy.

Modelling of the drilling process is the first step toward modelling the robotic drilling cell as a whole, as this will provide the nominal machining forces the arm will be subjected to.

3 Literature Review: Industrial Robotics for Advanced Machining

3.1 Introduction

This review will mostly be concerned with material removal processes through milling and drilling by industrial, anthropomorphic (shoulder-elbow-wrist arrangement) robotic manipulators with 6 degrees of freedom. It will examine the current state of this practice, advantages of the technology, issues which inhibit the proliferation of robotic machining and a range of methods of mitigating those issues.

3.2 Current Status of Robotic Machining

Robotic machining was first proposed by Appleton and Williams in 1987, as a means of replacing human operators on shop floors [8](Cited by W. Ji and L. Wang [9]).

Existing examples of robotic machining processes include robotic grinding, deburring, drilling, milling and polishing [10] which require tools to accurately follow trajectories whilst also applying and maintaining forces on parts [11]. These processes may be categorised on the basis of material removal rate (MRR) [9]. Low-MRR processes would otherwise tend to be performed by human operators (examples include grinding, chamfering, polishing, deburring) therefore robots would be expected to replicate human motions, with compliance between the tool and workpiece [9]. This means the challenges to robotic Low-MRR processes lie with programming that can match human operator speed, not with the physical properties of the robot [9].

High-MRR processes are usually the preserve of CNC machines (examples include milling and drilling), requiring the robotic analogues to exhibit high stiffness alongside quick and accurate motions [9]. This review will be concerned with high-MRR processes, where cutting forces are higher and stiffness is more critical to the process.

CNC machine tools remain the preferred choice for performing the majority of these machining operations, due to higher accuracy and dynamic stability [12]. In a review of recent progress in robotic machining, Kim et al. stated that robotic machining is generally applied to processes with small machining loads, which remove small volumes and exert little abrasive force, or on materials that are soft and light [13]. They also concluded that robots achieved higher quality polishing operations than 3 axis machine tools [13].

Due to much higher average stiffness, machining compliance is not as common or significant in industry standard CNC milling machines operating on hard materials because those machines exhibit much greater stiffness between the tool and the workpiece being machined, with an estimated stiffness of 50N/µm compared with a robot's stiffness estimated at less than 1N/µm [10], therefore the significant cutting forces generated during milling do not cause large dynamic or static deflections which would then affect the cutting operation [14].

Robotic machining is already carried out in industrial environments, an example being their implementation for the pre-machining of parts, a task which requires lower tolerances [15]. Compatible materials include wood, wax, foam and resin, which makes them an appealing tool for rapid prototyping [10]. It is estimated by the International Federation of Robotics (IFR) that 294,000 industrial robots were sold in 2016, increasing by 30% in 2017 [16]. 1.4% of industrial robots were reportedly intended for machining (defined as grinding deburring, milling, polishing), according to the IFR [16]. This indicates that robots are not currently preferred as a machining solution.

Robotic machining is also carried out using mobile robots, which in many cases consist of an arm, or parallel kinematic machine on a mobile platform, in order to increase the working volume of the machining cell, though this can sometimes be replaced with a simpler rail system to extend the cell's working volume in a pre-defined direction [17].

A conference paper produced in 2017 by Grau et al. predicts that the enhanced communication networks promised by the fourth industrial revolution will bring greater innovation to industrial robotics, increasing flexibility and dexterity, as well as improved learning and collaboration both amongst robots and between robots and humans [18]. This may suggest that emerging data science and more powerful decision-making software for understanding and predicting systems with a large number of variables could be investigated for application to the characterisation, optimisation and implementation of compliance error reduction in robotic machining.

Grau et al. [18] also observe a gap between smart robotic applications developed in academia and industry requirements, concluding that collaboration between industry and academia may be useful in closing this gap, which supports the undertaking of this project.

3.3 Advantages of Robotic Machining

There have been observations of potential or realised advantages of robotic machining over competing technologies, which will be explained in this section.

According to a robotic machining white paper published in 2008 on the website of the Robotic Industries Association: “The inherent 5+ axis machining capability combined with flexibility, large work envelope, and multiple station capability is a flexible solution that allows end-users to expand the range of machining applications at a price point which can compete with a traditional CNC machine [19]”. A standard serial manipulator has 6 degrees of freedom within its dextrous working volume, leaving one degree of redundancy for 5 axis machining tasks, which may be optimised for increased stiffness during milling in some cases [20].

A larger work envelope is particularly useful for aerospace applications, where work-piece dimensions far exceed the normal working volume of CNC machines, but the accurate machining of complex shapes is still required [17].

Industrial robots are described by Ji and Wang as “multi-function and low-cost machines,” and therefore potential replacements for CNC machines, which they go on to describe as “able to deliver higher machining accuracy with high stability” [9]. This trend is consistent with other observations of the limitations preventing industrial robots from use in industrial machining.

3.4 Barriers to the Proliferation of Robotic Machining

Application of robots to machining processes remains low despite observations of potential advantages over CNC machining. This lack of interest may be explained by the significant obstacles which emerge when attempting to combine robotics with the machining of harder materials such as metals and composites [10]. Indeed, an overview of robotic machining in 2015 stated: “In terms of accuracy, the industrial robot is worse than any conventional machine tool but better or comparable to a rapid prototyping machine type STL or SLS. [10]". These obstacles include significant deviations from the desired toolpath, which can then result in form errors in the produced parts, as well as decreased surface quality due to machining chatter [11].

Effective machining robots must be able to accurately follow trajectories and must also be reliable and durable to be competitive in industrial settings [18]. Other desirables are configurability, ease of programming, versatility, and sensory input [18]. In a review of industrial robotic machining, Ji and Wang comment that low material removal rate operations require prohibitively large amounts of programming to manage the flexibility of the robot [9]. Managing this is a major obstacle to competing with human operators [9]. This suggests that high MRR processes are a preferable research area to explore.

Part quality standards are evaluated according to path straightness (ISO 12780), surface flatness (ISO 12781), and circularity (ISO 12181) [21]. Klimchik et al. observed from experimentation with five models of KUKA robot arm that circularity and hence accuracy has an "almost linear" relationship with cutting force magnitude [21]. That study considered circularity to be an acceptable performance measure for accuracy, as it indirectly took path straightness and surface flatness into account [21]. This further suggests that robotic machining cannot currently compete with machine tools for milling processes with high process forces.

Kim et al. describe two major sources of positioning errors: geometrical and non-geometrical, and further characterise them in Figure 3 [13]. They state that geometrical errors can be mitigated by kinematic calibration, however low stiffness is a non-geometrical error which requires compliance error compensation. Low stiffness and kinematic parameters are respectively corrected by error compensation and kinematic calibration [13].

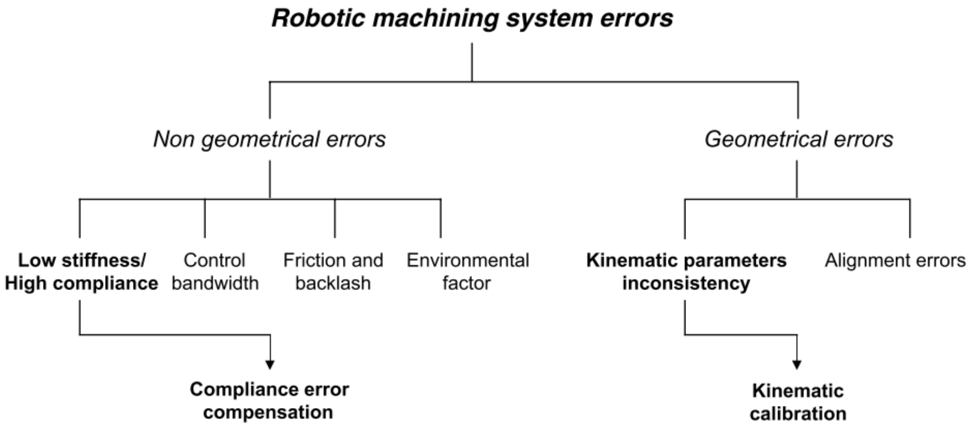

Figure 3: Categories of robotic machining system errors (Kim et al.) [13].

According to Hooke's Law, a known resistance to deformation under a known force can be derived into the physical parameter of stiffness or the inverse, compliance. Compliance tends to be high in serial robots. This lack of stiffness can partially be ascribed to the serial manipulator robot's physical similarity to a cantilever [15], with a solid structure fixed at one end and the other freely moving at the length of the arm. When subject to forces perpendicular to the arm span, deformation of the structure from the desired position occurs. This effect increases with the distance of the end effector from the base.

Compliance also results from the use of flexible joints with rotational actuators [22], which cannot be removed from the design as they also enable the greater range of kinematic configurations the serial manipulator exhibits, making the substitution of CNC milling machines with machining robots a significant exchange of attributes [11]. The stiffness of a robotic manipulator varies depending on the configuration of the robot, and previous research has addressed machining robot parameterisation (the derivation of a system's physical parameters) to enable users to predict robot behaviour for given configurations and optimise configuration accordingly [16 - 17].

Serial axis models are often used along with component stiffness values to study robot configuration. Figure 4 shows one example of a visualisation of a kinematic model that might describe a 6-DOF manipulator, with the cylinders showing the axial alignment of rotational joints, and "L" values describing link lengths between joints. Coordinate systems are also visualised in terms of x and z, where z_0 represents the connection to the rigid base, while z_6 represents the mobile end effector axis, and the intervening series of joints and links is visualised.

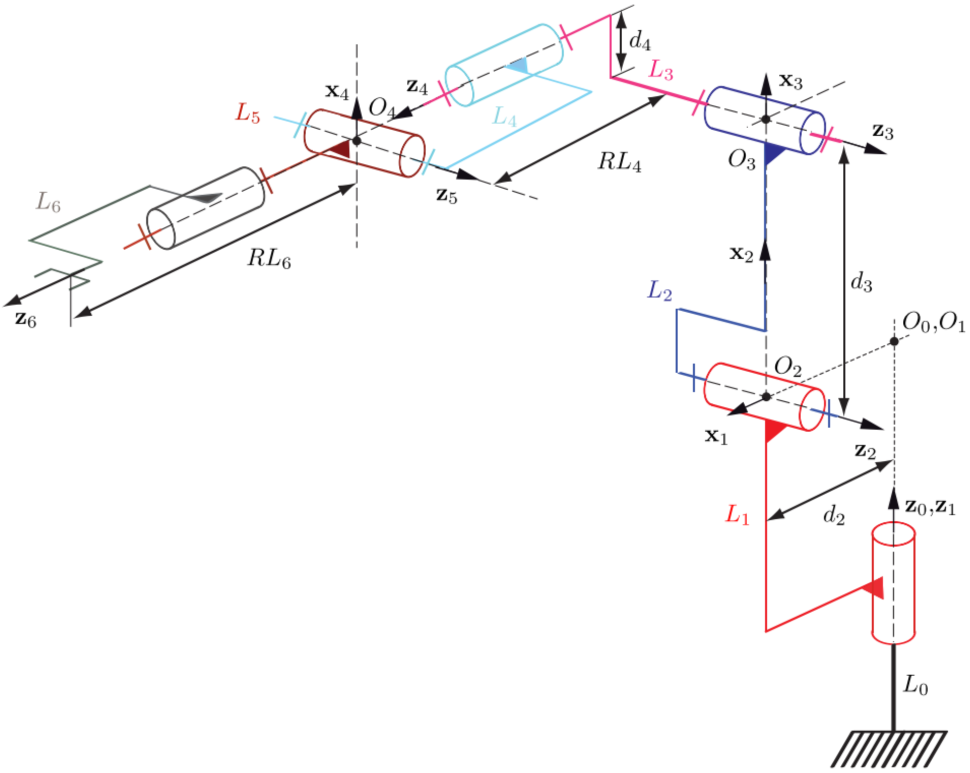

Figure 4: Visual depiction of the kinematic parameter model of a 6-DOF manipulator (Dumas et al.) [23]

Machining vibrations (dynamic effects) are also of importance. Altintas et al. describe two forms of milling chatter [24]:

- Chatter resulting from the regenerative effect (wherein chip thickness modulates as a work surface undergoes repeated cutting) [24]. In milling, this is caused by a significant phase difference in chip thickness between rotations, resulting in rapidly varying cutting forces where the phase difference is significantly large [12].
- Chatter resulting from the self-excited mode coupling effect (wherein natural modes are closely matched in principle directions) [24].

They go on to conclude that under high-speed milling, it was possible to predict chatter frequencies and stability limits, with some errors attributed to changes in cutting force coefficients or spindle dynamics, as well as stating that "no self-excited mode coupling chatter was observed at high spindle speeds" [24]. At lower speeds, the robot's low frequency structural modes caused chatter [24]. They state that any stability analysis would require consideration of the high pose dependency of structural modes, either through measuring FRF at different configurations or by accurately modelling the arm to predict the FRF at different points [24]. This understanding should be considered a starting point for methods with the specific aim of reducing dynamic effects in robotic machining.

However, Celikag et al. investigated milling mode coupling chatter stability boundaries using zeroth order and multi-frequency approximations, finding that simulations did not accurately describe the observed spindle speed dependent process stability [25]. They concluded that the regenerative chatter mechanism described observed stability more effectively, and that mode coupling chatter did not occur in milling due to the tool cutting the chip surface left by the previous tool pass period [25]. They specify that mode coupling occurs under free vibration, while mode coupling chatter is "a special type of instability that could only occur in special type of operations and machine tool systems" as a result of mode coupling [25].

3.5 Existing Methods of Improving Robotic Machining

There are several methods of improving the quality of robotic machining already in use, examples of these methods will be explored in this section of the review.

3.5.1 Optimisation of the Existing Robotic Machining Cell

The first approach this review will explore is the modification of the software involved in controlling the robot. According to Klimchik et al., trajectory improvement can be accomplished through two actions [26]:

- Correction of compliance errors through increasing the accuracy of the manipulator model used by the robot control program, which is based on parameters reached through measurement and testing of the manipulator [26].
- Correction of compliance errors through inputting modified trajectories which account for and cancel out errors, resulting in an outcome closer to the

intended trajectory [26]. This action can be performed using either online or offline methods, as depicted in Figure 5.

(a) Off-line: modification of the target trajectory

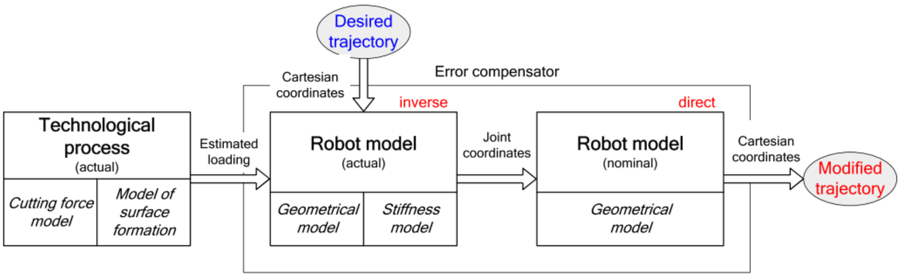

(b) On-line: machining using revised trajectory

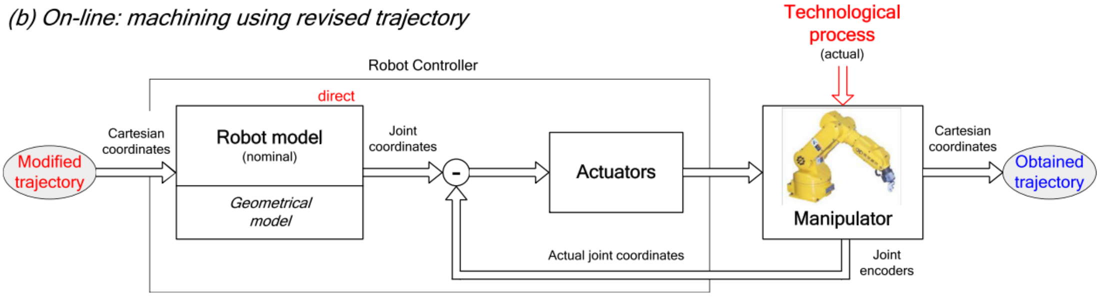

Figure 5: Flow Diagrams representing on-line and off-line methods of optimisation for compliance compensation (Klimchik et al.) [21]

3.5.2 Manipulator Model Modification

Gautier et al. have proposed a method which combines the direct and inverse dynamic identification models (DIDIM) for the identification of dynamic and friction parameters of robots given their actual control laws and torque data which may be of a low sample rate, however this approach was only validated using a 2 DOF robot, with validation on a 6 DOF planned for future work [27]. This type of model could theoretically be implemented in a robot controller for greater accuracy, as the controller could correct for the errors which may occur as a result of the robot's friction parameters.

Huynh et al. presented a novel method for updating elastic of multibody models to generate digital twins for manufacturing processes [28]. This method uses a combination of genetic and deterministic algorithms to apply curve fitting to experimental FRFs taken at different locations on the structure [28]. The locations and orientations of spring-damper pairs are deduced and used along with CAD derived inertial properties to determine kinematics of the model [28]. The curve fitting is then performed, with the algorithms used to provide optimal elastic parameters [28]. This method was then validated on a manipulator, with results described as "exact." [28] They caution that it is impossible to find a linear stiffness value that matches all resonances in all positions, and state that application in different postures may yield the nonlinear stiffness and damping laws [28]. This method is reliant on genetic algorithms to determine joint values [28], while the use case examined in this thesis does not require derivation of joint stiffnesses, as existing values are taken as accurate.

Huynh et al. have produced a 12 module C++ library called "Dystamill" for the purpose of "2D ½" milling simulations for cutting force prediction and milling stability assessment from cutting parameters [29]. This model is based on one physical model and two mechanistic models [29]. Tool dynamics are represented by experimentally derived tooltip structural modes [29]. Workpiece surface is represented by coordinate points, which are updated and used predict cutting forces [29]. They also state that the optimal operating conditions for stability can be given [29].

3.5.3 Robot Command Modification

According to Burn et al. "most industrial robots have position control loops that are not easily modified" in the respect of applying force control, as would be useful in the case of resisting the applied static machining forces, particularly when those forces may be predictable [30]. For this reason, indirect methods are preferred, such as changing commanded trajectories to compensate for trajectory errors [30]. This implies stiffness identification is still required even in cases where cutting forces can be accurately predicted, as the robot cannot simply be commanded to oppose known forces.

Chen et al. proposed a stiffness performance index for optimisation of robotic posture and feed orientation during milling [31]. Experiments were performed which validate the feasibility of the model for improving planar machining accuracy, making it possible to optimise feed orientation and decrease machining errors [31]. The performance index could be highly applicable to stiffness compensation if it were applied to multiple solutions as a measure of success.

Research by Furtado et al. has shown it is possible to reduce machining waviness by around 22% when machinining repeated, specific geometries under constant conditions by producing a waviness profile and then introducing a mirrored version of that profile to the trajectory through the robot control software [32]. This method may be applicable to other cases for similar effects on path-following accuracy but are not presumed to be applicable to right-first-time manufacturing processes, without the use of accurate waviness prediction.

Mousavi et al. used offline simulated dynamic behaviour of a robotic drilling cell to optimise configuration with changing position during robotic milling, finding their model accurately predicted whether chatter would or would not occur for the same trajectory with different configurations [33].

Tunc and Shaw reported on the effects of using a hexapod robot for mobile milling [34]. They describe asymmetrical flexibility, with stability dependent on position and feed direction [34]. They also describe the cross-transfer function being a significant factor for stability predictions in cases where depth of cut is less than 50% of tool diameter [34]. They demonstrated that adjusting spindle speed according to stability diagrams could improve stable cut depth by up to 25% [34]. Tunc and Shaw also investigated the dynamic response of a hexapod robotic platform machining system [35]. They found that the hexapod is flexible and may be as flexible as the cutting tools. FRF may become position dependent and asymmetrical [35]. They determined feed rate direction and vibrations which are aligned to spindle axis to be important factors to stability [35]. Cross transfer dynamics for robot and tool modes may become significant with the distance of the robot from the nominal position [35].

3.5.4 Augmentation of the Robotic Machining Cell

Rather than optimisation of existing hardware, some solutions augment the standard robotic machining cell with additional controlled actuators. Schneider et al. applied the COMET approach to robotic machining, concluding that: “Calibration of robot kinematics and the calibration of the work cell can improve positioning accuracy and result in better precision in machining [36].” However, they also state that “the intrinsic oscillation of a serial robotic system can only be eliminated by external devices [36].”

A different solution proposed by Lai et al. is the use of two robots which are attached to the same spindle [37]. The first robot has the usual fixed base and end effector while the second is connected to the same end effector, but with a gripper at the opposing end (see Figures 6 and 7), allowing the second "base" to be repositioned so as to connect the tool to any of a number of pre-placed gripper points, creating a higher-stiffness parallel manipulator in the most suitable position for machining at particular sites [37]. An issue with this design is that the gripping points would need to be pre-placed, possibly to complement the geometry of the part being machined, which makes the feasibility of this concept dependent on batch size or required end quality of the part.

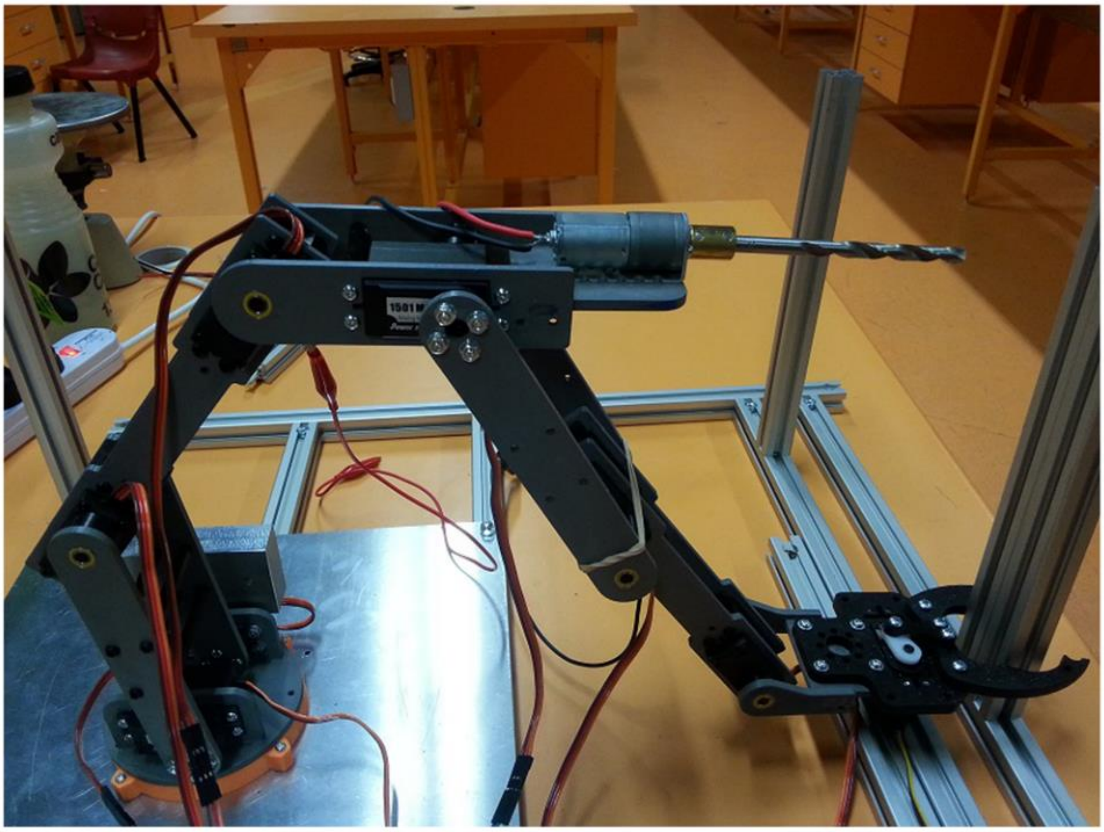

Figure 6: Parallel-serial manipulator prototype for experimentation [37].

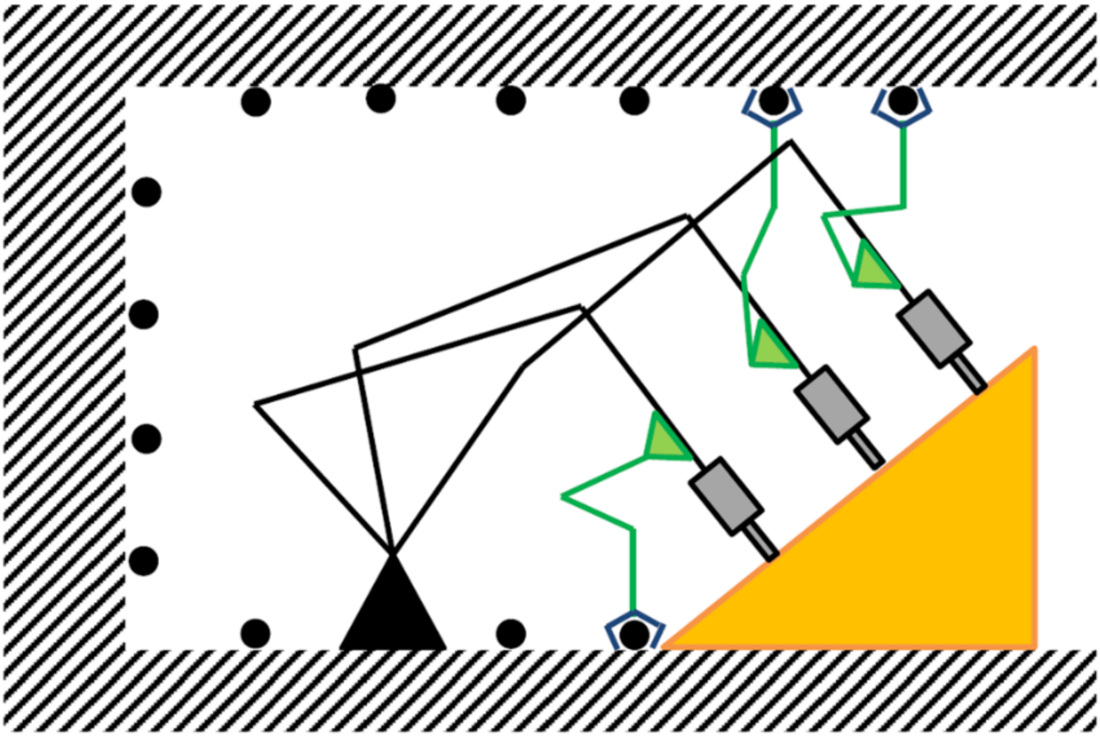

Figure 7: Concept sketch for parallel serial manipulator, showing a manipulator in different configurations for drilling at different locations [37].

Research has been carried out into the use of semi-active vibration control methods to improve the quality of robotic machining products [38]. One such method involves the use of computer-controlled magneto-rheological elastomers to absorb vibrations and suppress chatter, resulting in chatter absorption described as “successful” and reduced chatter marks [38]. Surface roughness improvement of between 30-50% was reported [38]. This level of chatter reduction may imply stability lobe volume is increased, making the robot able to conduct higher quality machining at greater distances from the base or in less stable configurations.

Guo et al. examined the mechanism of vibration in robotic boring [39]. They state that the robot itself vibrates, rather than the boring bar, and that this vibration is forced vibration with displacement feedback, with the final contour of the hole being related to rotational frequency of the tool [39]. A pressure foot vibration suppression method was proposed and found to be effective in experimental results [39].

Her and Kazerooni examined robotic deburring of 2D planar parts with unknown geometry [40]. They state that for stable robotic deburring force control is required tangent to the part, and trajectory control is required normal to the part [40]. They addressed this by using a roller bearing below the cutter, which feeds back into a tracking controller to guarantee stable deburring [40].

3.6 Discussion

The various methods of improving compliance-related quality issues in robotic machining which have been discussed in this review can be separated into two categories of optimisation and augmentation, which are further broken down and related in Figure 8.

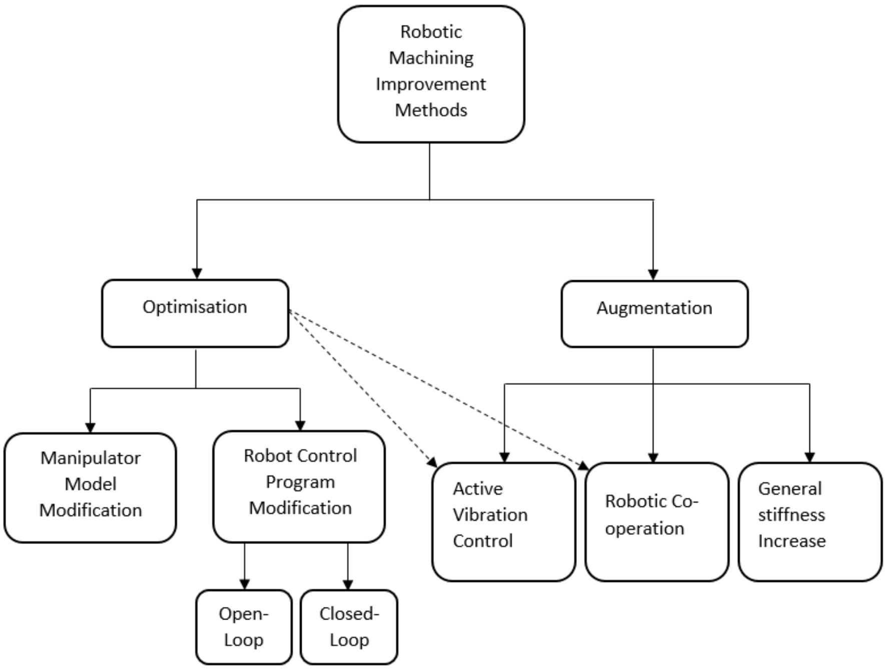

Figure 8: Tree of Mitigation Methods for Compliance Issues in Robotic Machining

3.6.1 Optimisation

Robot control input optimisation can be divided into open-loop methods and closed loop methods, which are not mutually exclusive.

- Open loop compensation requires experimentation and lead time to produce an optimised cutting trajectory solution which results in higher accuracy.
- Closed loop compensation usually requires additional sensors added to the machining cell and complex programming to react to errors as they occur.

3.6.2 Augmentation

Augmentation can also be further categorised into the following types.

- Simply upgrading to a manipulator with a higher stiffness rating, thereby improving the coverage of stability lobes in the operating space.
- Methods which aim to improve the robot's resistance to dynamic effects during machining, such as active vibration control. These methods do not necessarily improve static compliance effects and require signal processing [41] according to either measured vibrations or predictive modelling.
- The addition of physical augmentations to the machining cell. A simple example is the use of a non-active pressure foot for drilling operations to connect the workpiece and tool. Actuators can sometimes be used where passive methods are insufficient, as with actuated pressure foot systems. More complicated examples exist, up to and including the use of other robots to support or otherwise assist the machining. These methods often require their own optimisation processes before implementation, creating an overlap with robotic behaviour optimisation.

3.6.3 Comparison of Optimisation and Augmentation Methods

It may be concluded from the information compiled in this review that optimisation has a more defined scope than augmentation, meaning less freedom of choice for research topics and a more limited range of options for where novelty may be found. As optimisation utilises the existing cell, this leaves a more clearly defined goal and measure for success. Optimisation research tends to involve advancing the computer modelling of physical systems or more refined decision-making processes. Limiting factors are computing power, lead time for experimental data collection and measurability of serial manipulator parameters. Optimisation can often be expected to deliver incremental progress which is then generally applicable to a diverse range of use cases. If novel approaches to the processes of modelling or controlling are available and a versatile solution is desired, optimisation is likely preferable.

In contrast, for augmentation methods there exists a greater range of possibilities, as the researcher can add new elements to the robotic machining cell, up to and including other robots. Each arrangement could be expected to have its own theoretical optimum state which would not necessarily translate over to other arrangements. Measures of success are less defined and results more difficult to compare with prior research, with limited applicability beyond their own specific use cases. Adding technology to a machining cell can therefore have more uncertainty but offers potential advantages over optimisation for specific use cases. For example, if dynamic effects are to be specifically targeted and static behaviour is of a lower priority, then active vibration control or similar methods may be able to increase the range of stable working volume of the robot in the face of compliance-enabled chatter. If there are novel additions in hardware which may be applied and a specific use case is the basis of the problem, then augmentation may be preferable.

Augmentation and optimisation may be seen as complementary, as optimisation has the goal of seeking the optimum behaviours possible with the existing robotic machining cell, while augmentation seeks to increase the system capability and thus create greater optima. There is some overlap in the research carried out to achieve the two approaches as any added actuators require control, and therefore may be optimised, but this optimisation does not usually have the same degree of novelty as pure optimisation methods, for example the use of signal processing in active vibration control, or force control for actuated pressure foot methods.

The decision depends on several factors relating to the nature of the problem preventing the robotic machining cell from accomplishing a desired task, which must be understood before generating mitigation methods. For this project, a case study in robotic drilling of holes in aerospace materials is taken as the intended application. A brief review of robotic drilling developments and drilling modelling is presented in the following section.

3.7 Machining Operations

Altintas and Engin produced a method for mathematical modelling of the mechanics and dynamics of milling tools of a variety of types (Cylindrical, tapered, ball, bullnose etc.) with arbitrary geometries [42]. When used in combination with an orthogonal cutting database, this method allows the chip thickness at each point of the cutting edge to be calculated, enabling the prediction of cutting forces, vibrations, surface finish and chatter stability lobes to be predicted for an arbitrary end mill [42].

Examples of predictions by the method are provided for ball, helical tapered ball and bull nosed end mills are provided as validation [42].

Altintas, Yang and Kilic have also shown that axis tracking errors in multi-axis machining are proportional to amplitudes of average and tooth passing harmonics of cutting forces, which are proportional to feed rate, or maximum chip thickness, thus making the errors predictable before they occur [43]. They then exploited this relationship with an algorithm embedded into the virtual machining system to automatically adjust feed rate in order to accommodate part geometry, constraining path tracking and contour errors to the desired tolerance [43].

3.8 Drilling Operations

In response to the case study explored in Section 2.2, a further review of literature has been carried out surrounding specifically drilling and robotic drilling rather than generalised robot machining.

Armarego and Brown describe drilling in the following terms: "Drilling is a metal removal process for producing holes in components [1]. The process involves feeding a revolving cutting tool along its axis of rotation into a stationary workpiece [1]. A circular hole is therefore generated in the workpiece [1]. Feed velocity or (feed rate) is usually small compared to the peripheral tool velocity [1]."

The twist drill is described to have straight cutting edges and a chisel edge [1]. They go on to state that a web thickness is needed between the straight cutting edges to stiffen the drill and protect the drill point, and also that no cutting is performed by the drill periphery beyond the outer corner, cutting only occurs at the lips and chisel edge [1]. Chips travel along the flutes and the chip-flow direction is affected by the point angle [1].

In contrast to conventional drilling, orbital drilling is also used, wherein a drill of smaller radius is moved eccentrically around a hole axis to create a hole which is of greater diameter [44]. Feed is both axial and radial. Orbital drilling is also used in some cases of hole drilling in metallic aircraft components [44]. SAE investigations state that more complex geometry is possible than conventional methods, however some holes drilled during experimentation were rejected due to cutter breakage [44].

3.8.1 Modelling of Drilling

A review of some recent developments in the modelling of drilling processes and relevant studies has been carried out.

Voronov et al. have proposed a model of torsional-axial oscillations of vibratory drilling, which considers continuous and discontinuous cutting as well as the influence of new surface formation equations [45]. They describe this model as more effective and accurate and report that for a 2-DOF system, the torsional vibrations do not significantly change the stability lobes of continuous cutting but can change the character of system vibrations and the shape of the chips in the instability region considerably [45]. This model could be applied to characterise the robotic drilling process.

Polini and Corrando have proposed a generalised kinematic approach for error modelling of drilled hole locations, which relates locator error with workpiece form deviation and volumetric error of the machine tool [46]. They state this model allows for the error sources affecting a drilling operation to be explicitly identified and mapped to the pose accuracy of the drilling process [46]. They also state dynamic behaviour of the machine tool is not considered [46]. This may be useful for predicting static machining errors.

The semi-discretization method was applied to drill motion equations by Jiménez et al. for the prediction of whirling vibrations (low frequency lateral vibrations) [47]. They state that the model can predict the appearance of whirling vibrations, as well as the frequencies at which they will be excited, based on the drill geometry, rotation speed and feed [47]. They reported good agreement between predictions and experimental results [47]. This model could possibly be applied as part of a simulation to predict the dynamic behaviour of a robotic drilling process.

Hohl et al., in a paper on an analytical criterion for identifying self-excited modes in drilling systems, state that mode coupling between axial and torsional vibrations are shown by several studies to be the root cause of stick/slip, the most common form of torsional vibration, and denoted self-excitation of the first torsional mode of the whole drilling system [48].

Bayly et al. used a quasi-static model of drilling, including cutting, rubbing and bending forces [49]. They concluded that adding rubbing forces to the model causes instability of backward whirling modes [49]. They found that including the chisel point results in least stable modes of 3 cycles per revolution, while removing it results in dominant modes of 7 cycles per revolution [49]. They found experimental results to be consistent with basic predictions of their quasi-static analysis, and thus stated discrete-time quasi-static model is a promising approach to drilling vibration and lobed holes [49].

Ahmadi et al. presented a four DOF drilling model with lateral, axial and torsional deflections of the drill with process damping, as well as whirling vibrations [50]. They report that they could predict the borders of stable radial depth of cut with varying spindle speeds [50]. They were able to show the stability for all three common modes of vibration (lateral, torsional-axial and whirling) [50]. They found that with a sharp drill (low process damping), torsional-axial chatter is the dominant mode of vibration, while for a worn drill (high process damping), lateral vibration is the dominant unstable mode [50]. They conclude by stating lateral vibration is more important for the roundness and dimensional accuracy of holes, while torsional-axial chatter results in damage to the drill [50].

Ema et al. studied whirling vibration and determined that it is a regenerative chatter vibration resulting from the regenerative effect at the major cutting edge and the frictional forces where the flank of that edge interferes with the workpiece surface [51]. The distinctive whirling vibration waveforms are due to the amplitude and vibration speed of the drill being restricted by vertical friction force [51].

Wan et al. examined the mechanics and dynamics of multifunctional (drilling, boring and chamfering) tools to predict stable cutting conditions, with cutting force coefficients estimated using the orthogonal to oblique cutting transformation [52]. They conclude that a semi-discrete time domain stability solution which considers varying directional factors, process damping and multiple time delays for multifunctional tools has benefits over frequency domain solutions [52]. They also propose to address a generalised solution for turning, drilling, boring and milling [52].

By considering the identical chip removal mechanics for all metal cutting operations, Kilic and Altintas produced a mathematical model of mechanics and dynamics for many cutting operations with arbitrary tool geometries [53]. Cutting forces can be predicted from shear angle, shear stress and average friction between rake face and chip (the latter from a database of orthogonal cutting properties) [53].

3.8.2 Recent Developments for Increasing Machining Plane Stiffness in Robotic Drilling

Bi and Liang produced a robotic drilling system in 2011 which was able to achieve an accuracy of 0.3mm and repeatability of 0.2mm within the robot's working volume for the given process [54]. They stated that they also achieved a H9 hole tolerance for Ti and Al alloy metals [54]. This was achieved by using a pressure foot fixed to the end effector to improve drilling stiffness, and real time thrust force feedback to control the clamping force [54]. The use of a pressure foot may be considered a simple way of improving stiffness in the machining plane by making use of the force exerted normal to the machining plane.

Zhang et al. conducted research on stiffness properties analysis and enhancement in robotic drilling [55]. They concluded that a unidirectional drilling thrust force will cause three-dimensional deformation of the end effector, diminishing diameter accuracy and drilling quality [55]. They further conclude that pre-load pressing force (applied through a pressure foot mounted to the end effector) can strengthen stiffness in the machining plane [55]. They give a model of stiffness under a given pre-load pressing force, with results presented using a stiffness promotion coefficient [55]. A matching criterion between thrust force and robot drilling posture was used to ensure stability [55]. The researchers reported "effective" improvement of machining plane stiffness and that drilling stability and hole diameter precision could be enhanced and state their proposed method can provide guidance for pressing force and process parameter selection in robotic drilling [55]. The methodology behind their predictions of end effector deformation due to thrust force may be useful in characterising the robotic drilling process, but the use of a pressure foot is not ideal for restricted access drilling due to the size of the pressure foot, which would prohibit drilling in tight corners of the workpiece.

Shen et al. propose a method for optimising operating stiffness of robotic drilling systems, as well as evaluating absolute positioning error in drilling of sheet metal [56]. They concluded that installation angle of the spindle has a “great impact” on operating stiffness [56]. In their example case, stiffness performance was improved by five times between best and worst installation angle [56]. They also propose a compensation method which takes deformation and positioning error of the end effector into account [56]. The change in positioning errors they observed is visualised in Figure 9. They also report that deformation resulting from their compensation method resulted in lower stiffness in the Y direction than the X direction [56]. A compensation method of this sort may improve the accuracy of the robotic drilling process under the predictable drilling forces.

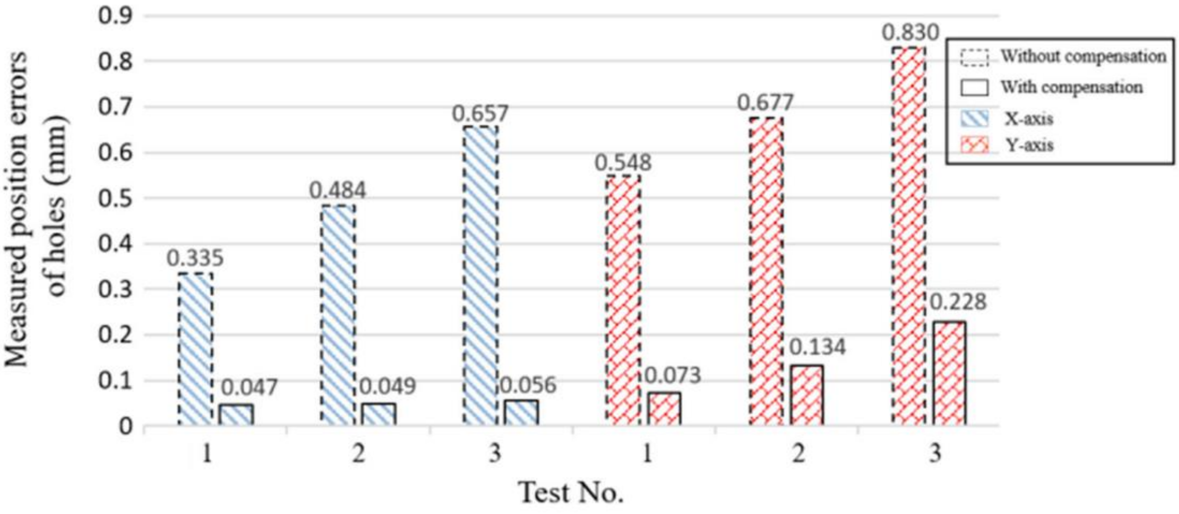

Figure 9: Distribution of hole position errors before and after the use of compliance compensation [56].

Busson et al. conducted configuration optimisation of a Kuka LBR Iiwa robot using the identified joint stiffness model to identify theoretically high stiffness configurations [57]. They reported that for a given position, the Cartesian stiffness ranged from less than 100N/mm to greater than 300N/mm (see Figure 10). This represents an approximate stiffness range that would be available for drilling without the use of drill guide rails, depending on the relative positions of the robot base and the drilling site [57]. There may be some issues with relying entirely on kinematic redundancy for compliance reduction, as the restrictive workpiece geometry may prevent the manipulator adopting certain configurations.

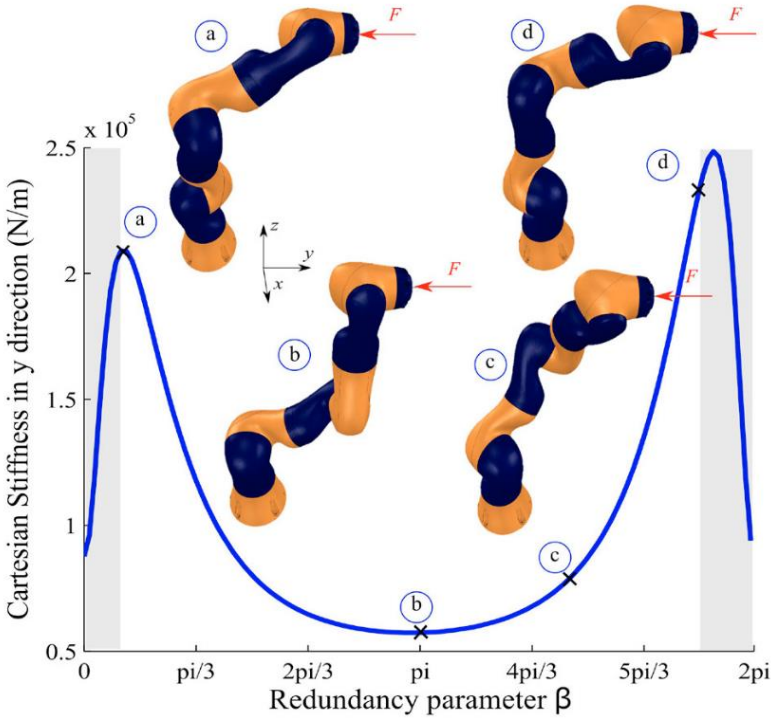

Figure 10: Theoretical Cartesian stiffness along pure y translational direction over a range of kinematic redundancy [57].

3.9 Conclusions from Literature Review

In conclusion, there is no evidence found that the discussion of methods of compliance induced error mitigation for generalised robotic machining (typically milling) could not also be applied to robotic drilling.

It should be noted that robotic drilling does differ from milling in the applicability of passive and active pressure feet, made possible due to the lack of tool lateral motion relative to non-machined surfaces of the workpiece. This lack of significant lateral motion allows for the simulation of dynamic behaviour over a range of spindle speeds instead of a range of tool positions, which may enable greater optimisation for the drilling point than was possible for the milling trajectory.

Both optimisation and augmentation methods can be applied to robotic machining (including drilling) to improve or compensate for low stiffness in the serial manipulator depending on the use case and degree of compliance error mitigation required.

This project will therefore explore the stability of the drilling process through dynamic simulations with the goal of optimising the drilling process through configuration and spindle speed control.

Drilling process forces can be characterised into predictable terms by the drilling parameters (spindle speed, feed rate), drill geometry (flute no, tool diameter, tip angle), and a set of cutting force coefficients (CFCs) which apply to one specific combination of material and tool. These cutting force coefficients are usually derived from experimentation with the process they describe, as described in Appendix A and B.

4 Dynamic Modelling

4.1 Methods of Modelling of Robot Dynamics

There are three methods of modelling the mechanical (stiffness and inertia) properties of serial robots such as the ABB IRB 6640 and Kuka Iiwa [58]:

- Finite Element Analysis (FEA), where the robot structure is reduced to flexible links connected through flexible joints, which are further reduced to a finite number of elements of a number that is practical with the available time and computing power [59]. The behaviours of the elements are accumulated to determine the dynamic behaviour of the robot. This method closely approximates the actual robot geometry and therefore the simulated behaviours are closest to the actual dynamics of the robot, but the computer memory required is often much higher than alternative methods [60].
- Virtual Joint Method (VJM), or Jacobian matrix method [61] where the robot is modelled as a set of rigid links connected by flexible joints which are equivalent to rotational springs. The Jacobian matrix is generated, relating joint motion/stiffness to end effector motion/stiffness. The required computing power is low compared with alternative methods, as is the accuracy [58].
- Matrix Structural Analysis (MSA), where the robot is modelled as a multibody [61] series of flexible joints and flexible links (as with FEA) however, the links are reduced to Euler beam elements of known material properties, length, cross-section and second moment of area for the length of the beam [62]. This allows the flexibility to be simplified into a series of stiffness matrices which can be used to model the collective stiffness of the end effector. This method is more complex and more accurate than VJM, but less so than FEA, and may be understood as the simplest form of FEA with flexible links.

As the higher modal frequencies of the robot (relevant to machining frequencies) require that the link flexibility be considered in the dynamic model, VJM is not recommended for the dynamic modelling this project involves. The use of the FEA method has also been rejected, as the need to simulate dynamics under varied configurations would make the simulation process impractically long. This leaves MSA as the chosen method of dynamic modelling of the robot arm.

4.2 Dynamic Modelling of Robotic Drilling

The robot dynamic model allows for the simulation of dynamic behaviour and derivation of frequency response functions under different input values, allowing results to be varied and outputs to be logged.

4.2.1 Kinematics and Configuration Variation Stage

It is known that there is one axis of redundancy present when using six axis robots for machining processes such as drilling [33], [63]. By setting the end effector (TCP) at a range of orientations about the tool axis, the redundancy can be exploited to give a range of configurations for a single drilling target point/axis. As infinite cases cannot be simulated with limited computing power, the range of the redundant axis should be divided up into a practical number of increments.

The first step in varying configuration is to create a variable kinematic model of the robot.

The Denavit-Hartenberg convention (pictured in Figure 11) is used to easily compose multiple links into a single transformation using four known geometric measurements, as in Table 1 and Table 2.

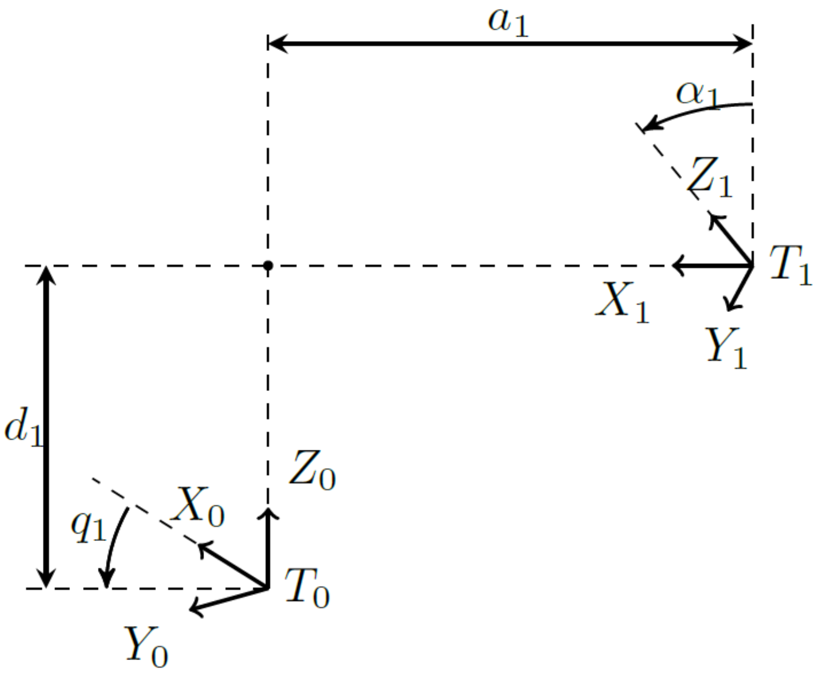

Figure 11: Diagram of Coordinate transformation based on standard Denavit-Hartenberg notation [64].

The robot tool parameters must be calculated for a given end effector assembly (tool, tool holder and spindle and attachment) (see Table 1), Terms definitions are: translational offset along previous Z-axis (d_n), angular offset about previous Z-axis (here also robot joint angle) (θ_n or q_n), translational offset along modified X-axis (a_n), angular offset about modified X-axis (α_n).

d_7 **(Offset, m, previous z)**	θ_7 **(Angle, degree, previous x)**	a_7 **(Offset, (metres) along new X axis)**	α_7 **(Angle, degree) common normal)**
0.5599 m	45°	0.1989 m	0°

Table 1: End effector kinematic parameters [64].

d_n **(Offset (metres) along current Z axis)**	θ_n **(Angle (radians) from previous x axis)**	a_n **(Offset, (metres) along new X axis)**	α_n **(Angle, (radians))**
0.7682	0	0.3242	-pi/2
0	0	1.2844	0
0	0	0.1784	-pi/2
1.1454	0	0	-pi/2
0	0	0	pi/2
0.1996	0	0	0

Table 2: ABB IRB 6640 Denavit-Hartenberg parameters [64].

The following Denavit-Hartenberg formula is used to convert these link geometries into homogenous 4x4 transformation matrices (T_n, where n represents the number of the link). which can be manipulated by matrix multiplication rules. Angle of joint n (θ_n) is set by the rotation of the numbered link's joint (n).

$$^{n-1}T_n = \begin{bmatrix} \cos(\theta_n) & -\sin(\theta_n)\cos(\alpha_n) & \sin(\theta_n)\sin(\alpha_n) & a_n * \cos(\theta_n) \\ \sin(\theta_n) & \cos(\theta_n)\cos(\alpha_n) & -\cos(\theta_n)\sin(\alpha_n) & a_n * \sin(\theta_n) \\ 0 & \sin(\alpha_n) & \cos(\alpha_n) & d_n \\ 0 & 0 & 0 & 1 \end{bmatrix}$$

$$= \begin{bmatrix} & Rot. & & Transl. \\ 0 & 0 & 0 & 1 \end{bmatrix} \qquad [1]$$

Where "Rot." is the 3x3 rotation matrix, and "Transl." is the 3x1 translation vector of a link.

From each valid Tool Centre Point target, there is a homogenous transformation matrix ($^0T_7$), Given the dimensions of the 7th link ($^6T_7$) (end effector and tool) it is possible to produce a unique target vector for the robot's 6th joint via the Denavit-Hartenberg convention (see Equation 2). This convention is commonly used to understand robot kinematics [65] (cited by [66]). A rigid connection between links 6 and 7 is described by keeping the joint angle fixed for all cases but varying the orientation of the end effector through modifying the rotation matrix of $^0T_7$.

$$^0T_6 = {}^0T_1\ {}^1T_2\ {}^2T_3\ {}^3T_4\ {}^4T_5\ {}^5T_6 = TCP * \left[\ {}^6T_7\ \right]^{-1} \qquad [2]$$

Where vector ${}^{0}T_{6}$ completely describes the end effector position and orientation relative to the robot base and therefore can be used to determine the positions/orientations of the rest of the serial link, and TCP is the DH matrix formed by the desired rotation and translation of the tool.

Using a Matlab program for inverse kinematics developed as part of previous research by Celikag et al with the ABB IRB 6640 [64], sets of joint angles can be generated which completely describe the robot configuration which achieves ${}^{0}T_{6}$. Figure 12 shows the translations of these matrices, and may be compared with the alternative visualisation of Figure 13, and the photograph of the IRB 6640 in this configuration in Figure 23 (b).

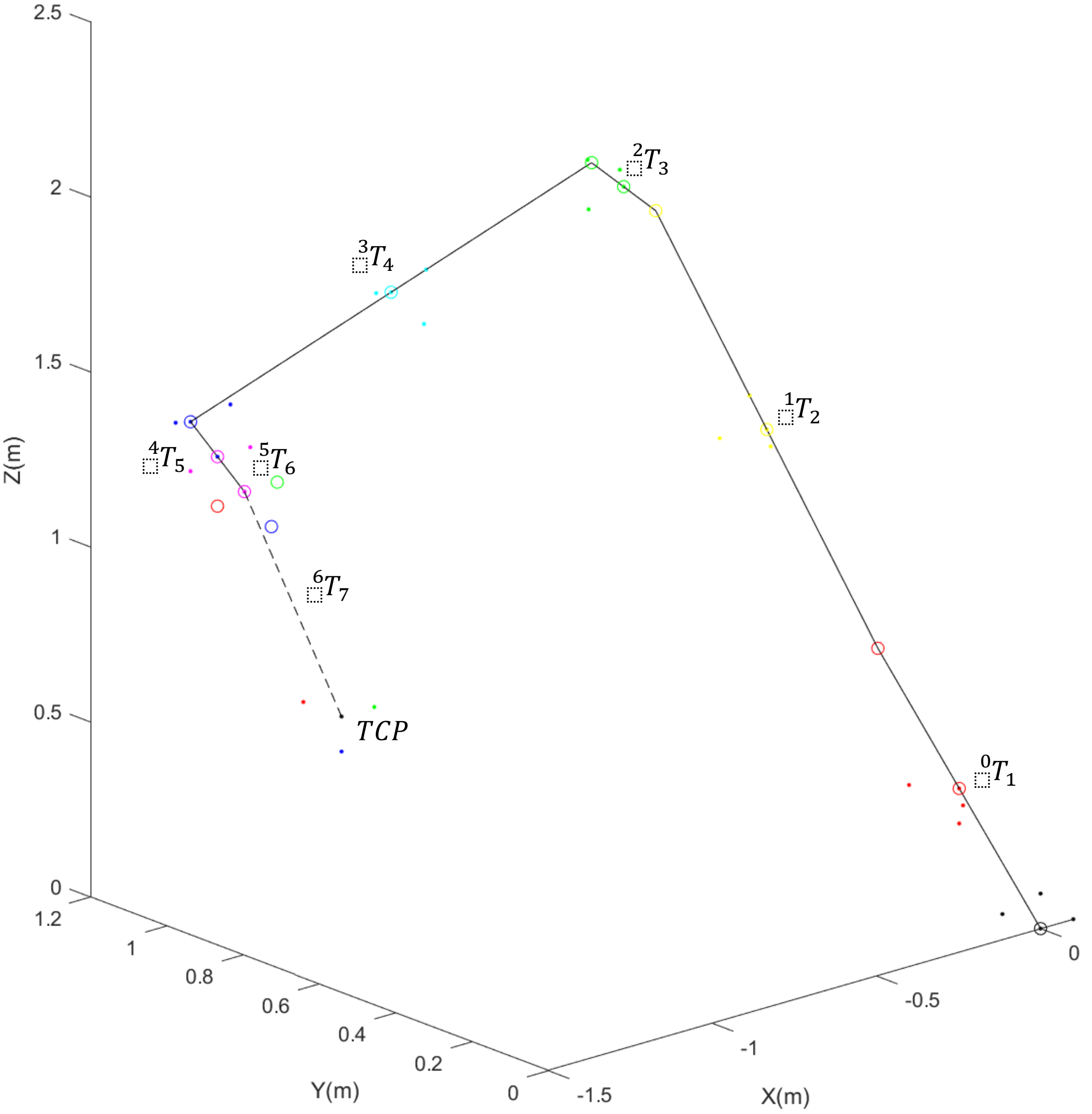

Figure 12: Kinematic visualisation of Robot, with TCP (lower left), Robot Base (lower right), joint and estimated centres of mass locations.

The joint angles and kinematic parameters can then be input into a function of Peter Corke's robotics toolbox [67] to visualise the robot in 3 dimensions, as pictured in Figure 13.

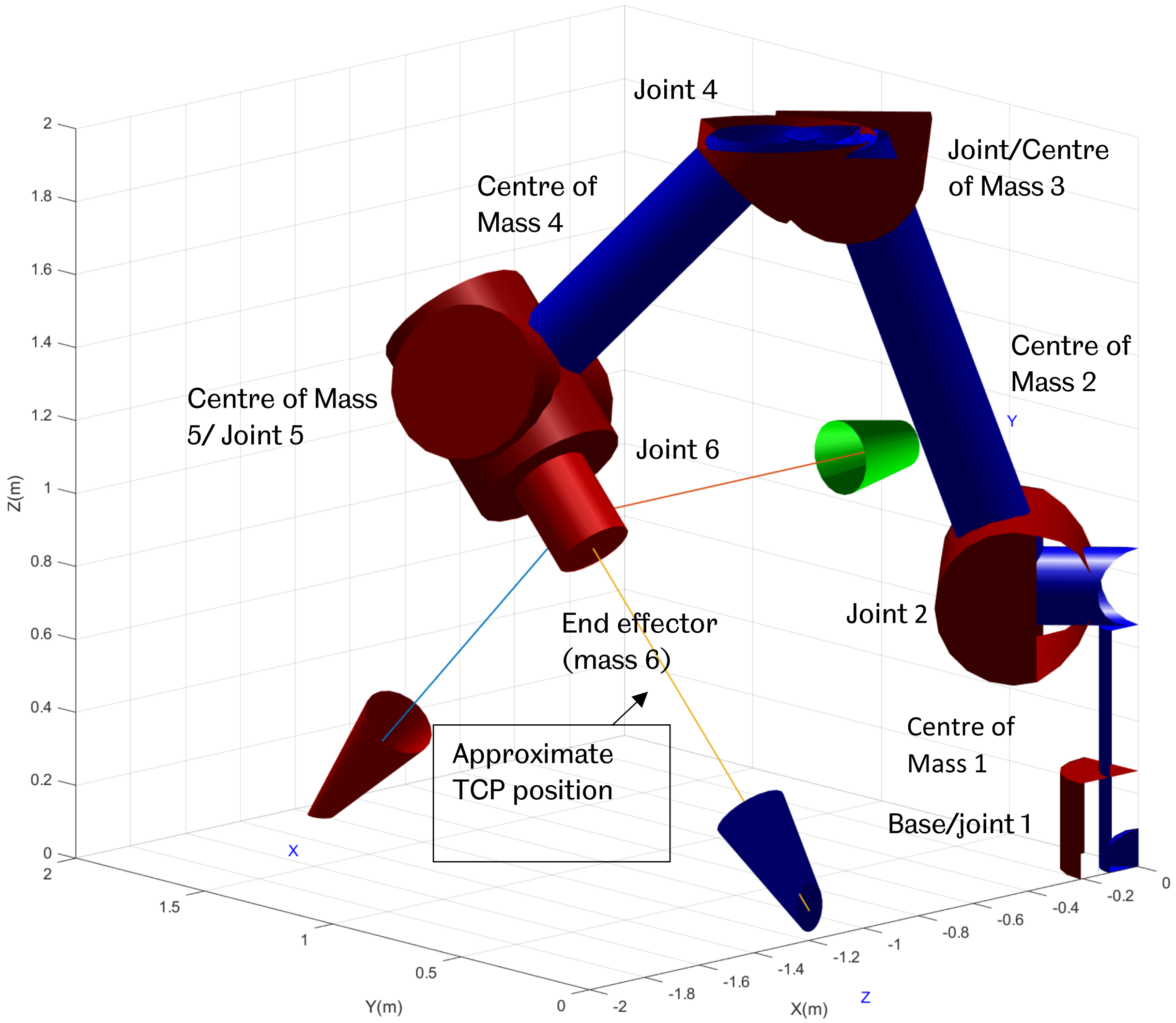

Figure 13: Robot position visualised using pre-rendering toolbox.

This is useful when confirming that the robot is placed to achieve accurate end effector position, however it is also useful to visualise the TCP and the 6th joint flange position to confirm that tool position is fixed, while end effector angle of approach is changing.

4.2.2 Robot Inertia Identification

Identification of the robot's individual link inertia matrices was carried out by examination of STEP files acquired from ABB [68], with Siemens NX. The "body measurement" feature was used. For the purposes of this simulation, constant density throughout the body is assumed for inertia calculations, and additional components not featured in the STEP files are ignored. The midpoint between joint axes of each link model is assumed to be of negligible distance from the centre of mass. The inertia matrix is here considered to consist of the total estimated mass (M_{link}) of the link resistance to motion in XYZ (as the resistance to force is expected to be the same in all three axes of translation), and the corresponding moment of inertia ($J_{link,x}, J_{link,y}, J_{link,z}$) (resistance to torque for each individual axis of rotation, given the part's orientation). As the links are modelled as beam elements, they are presumed to be symmetrical in all 3 axes about centre of mass, so the product of inertia terms are modelled as zero. The inertia matrix (M_C) of the robot structure will therefore be formatted as:

$$M_C = \begin{bmatrix} M_1 & 0 & 0 & 0 & 0 & 0 \\ 0 & M_2 & 0 & 0 & 0 & 0 \\ 0 & 0 & M_3 & 0 & 0 & 0 \\ 0\ 0\ 0 & & & M_4 & 0 & 0 \\ 0\ 0\ 0 & & & 0 & M_5 & 0 \\ 0\ 0\ 0 & & & 0 & 0 & M_6 \end{bmatrix}_{36x36}$$

Where M_n refers to 6x6 inertia matrix of link each numbered link:

$$M_n = \begin{bmatrix} M_{link} & 0 & 0 & 0\ 0\ 0 & & \\ 0 & M_{link} & 0 & 0\ 0\ 0 & & \\ 0 & 0 & M_{link} & 0\ 0\ 0 & & \\ 0\ 0\ 0 & & & J_{link,x} & 0 & 0 \\ 0\ 0\ 0 & & & 0 & J_{link,y} & 0 \\ 0\ 0\ 0 & & & 0 & 0 & J_{link,z} \end{bmatrix}_{6x6} \qquad [3]$$

As the orientation of each link will deviate from the orientation of the CAD model when inertia measurements were taken $[J_{CAD}]$ (a 3x3 diagonal matrix), a solution has been devised in which each link is visualised as Link 1 of the system (so as to accumulate the correct rotations from DH parameter manipulations), connected to the base by initial joint $[J_{Link\ 1}]$, and from observation, a rotation matrix ($[R_{CAD}]_{3x3}$) is used to rotate the inertia terms first joint axis of the link to the orientation seen in the CAD file. By multiplying the captured moments of inertia by the inverse of this matrix ($[R_{CAD}]_{3x3}{}^{-1}$), they can each be moved to their “Link 1” orientation $[J_{link\ 1}]$, and then by multiplying by the DH rotation of the link for the current configuration ($\left[R_{DH,inst}\right]_{3x3}$), the moment of inertia matrix should accurately describes the body for any configuration $[J_{inst}]$.

$$J_{inst} = R_{DH_{inst}} J_{link\ 1} \qquad [4]$$

Where: $J_{link\ 1} = (R_{CAD})^{-1} J_{CAD}$

- R_{CAD} refers to the orientation of the link in the CAD model.
- $[J_{inst}]$ is a 3x3 matrix that replaces columns 4-6 of rows 4-6 of M_n. Examples of the inertia matrix may be found in Appendix J.

4.2.3 Robot Kinetic Model

The joint compliances of the ABB IRB 6640 robot have been captured during the course of experimental work by Celikag (see Table 3).

Joint Compliance Parameters	ABB IRB 6640 205/2.75
$C_{\theta,1}\ (rad/Nm)\ \times 10^{-6}$	0.66
$C_{\theta,2}\ (rad/Nm)\ \times 10^{-6}$	0.51
$C_{\theta,3}\ (rad/Nm)\ \times 10^{-6}$	0.48
$C_{\theta,4}\ (rad/Nm)\ \times 10^{-5}$	0.18
$C_{\theta,5}\ (rad/Nm)\ \times 10^{-5}$	0.42
$C_{\theta,6}\ (rad/Nm)\ \times 10^{-5}$	0.20

Table 3: Joint Compliance values derived by Celikag et al [64].

Stiffnesses are easily calculated from these values by $K_n = \frac{1}{C_n}$, yielding the following in Table 4.

Joint Stiffness Parameters	ABB IRB 6640 205/2.75
$K_{\theta,1}$	$1.52\ (\mathrm{Nm/rad})\ \times\ 10^6$
$K_{\theta,2}$	$1.96\ (\mathrm{Nm/rad})\ \times 10^6$
$K_{\theta,3}$	$2.08\ (\mathrm{Nm/rad})\ \times 10^6$
$K_{\theta,4}$	$0.56\ (\mathrm{Nm/rad}) \times 10^6$
$K_{\theta,5}$	$0.24\ (\mathrm{Nm/rad}) \times 10^6$
$K_{\theta,6}$	$0.50\ (\mathrm{Nm/rad}) \times 10^6$

Table 4: Celikag et al. compliance parameters presented as stiffness values

The stiffness matrix of the robot has been constructed based on the method outlined by Klimchik et al. [62], which uses screw theory to describe the end to end stiffness of a link-joint-link series (where each link has two points of dynamic movement at each end and the joint has an angular stiffness) by simplifying the stiffness of the joint and links into a six dimensional Cartesian stiffness matrix between the two ends of the system (see Figure 14).

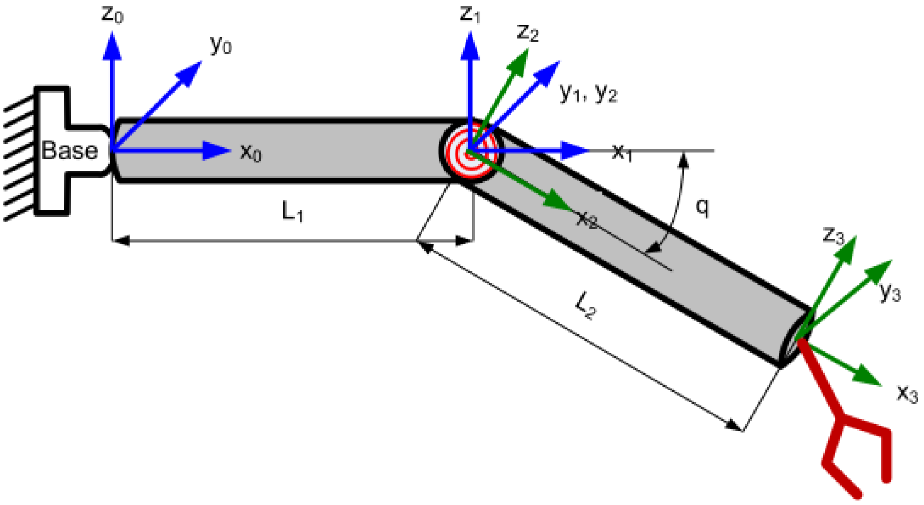

Figure 14: Serial Link Element Model (Klimchik et al [62])

Figure 15 visualises the elastic joint stiffness system connecting a mass and a fixed point. The robot model is constructed from breaking the 7-link system down.

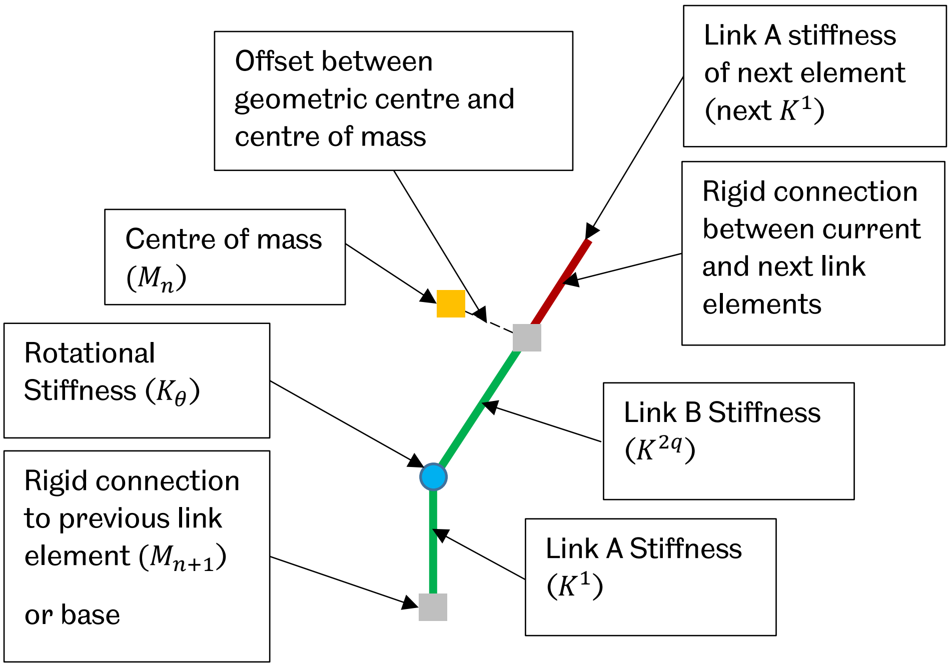

Figure 15: Elementary Dynamic Model Component

The joint stiffnesses (K_θ) used are those given for the ABB IRB 6640 in Table 4. The link stiffnesses are estimated by assuming robot links are uniform and beam-like, and applying the beam element stiffness formulae given by Klimchik (Equation 5) [62]:

$$K_{11} = \begin{bmatrix} \frac{E*S}{L} & 0 & 0 & 0 & 0 & 0 \\ 0 & \frac{12*E*I_z}{L^3} & 0 & 0 & 0 & \frac{-6*E*I_z}{L^2} \\ 0 & 0 & \frac{12*E*I_y}{L^3} & 0 & \frac{6*E*I_y}{L^2} & 0 \\ 0 & 0 & 0 & \frac{G*J}{L} & 0 & 0 \\ 0 & 0 & \frac{6*E*I_y}{L^2} & 0 & \frac{4*E*I_y}{L} & 0 \\ 0 & \frac{-6*E*I_z}{L^2} & 0 & 0 & 0 & \frac{4*E*I_z}{L} \end{bmatrix}$$

$$K_{12} = \begin{bmatrix} \frac{-E*S}{L} & 0 & 0 & 0 & 0 & 0 \\ 0 & \frac{-12*E*I_z}{L^3} & 0 & 0 & 0 & \frac{6*E*I_z}{L^2} \\ 0 & 0 & \frac{-12*E*I_y}{L^3} & 0 & \frac{-6*E*I_y}{L^2} & 0 \\ 0 & 0 & 0 & \frac{-G*J}{L} & 0 & 0 \\ 0 & 0 & \frac{6*E*I_y}{L^2} & 0 & \frac{2*E*I_y}{L} & 0 \\ 0 & \frac{-6*E*I_z}{L^2} & 0 & 0 & 0 & \frac{2*E*I_z}{L} \end{bmatrix}$$

$$K_{21} = K_{12}^T$$

$$K_{22} = \begin{bmatrix} \frac{E*S}{L} & 0 & 0 & 0 & 0 & 0 \\ 0 & \frac{12*E*I_z}{L^3} & 0 & 0 & 0 & \frac{-6*E*I_z}{L^2} \\ 0 & 0 & \frac{12*E*I_y}{L^3} & 0 & \frac{6*E*I_y}{L^2} & 0 \\ 0 & 0 & 0 & \frac{G*J}{L} & 0 & 0 \\ 0 & 0 & \frac{6*E*I_y}{L^2} & 0 & \frac{4*E*I_y}{L} & 0 \\ 0 & \frac{-6*E*I_z}{L^2} & 0 & 0 & 0 & \frac{4*E*I_z}{L} \end{bmatrix} \qquad [5]$$

Where terms are beam length (L), beam cross section area (S), second moments of inertia (I_y, I_z), polar moment (J), Young's modulus (E) and Coulomb's modulus (G).

These terms must be determined for each of the 12 beam elements of the robot structure and are derived. Estimated from the geometry and materials of the links.

Lengths can be easily calculated from examining DH parameters. assuming the centre of mass of each link is at the geometric midpoint, then by inspecting about each joint, the length of each Link A is half of the previous link length and the Link B length is half of the next link length. The exact material of the robot structure and the irregular shape of the links is not considered, Young's and Coulomb's moduli of the links are taken as 250 GPa (25% larger than the usual range for steels).

The fully derived Cartesian stiffness matrix for a 2-link system with an elastic joint, when one end is fixed and the other undergoes a wrench (W_3) and an extension (Δt), is given by Klimchik et al. [62] as:

$$\begin{bmatrix} 0_{5x1} \\ 0_{1x1} \\ 0_{6x1} \\ W_3 \end{bmatrix}_{18*1} = \begin{bmatrix} \Lambda_*^r & -\Lambda_*^r & 0_{5x6} \\ K_\theta * \Lambda_*^e & \Lambda_*^e * K_{11}^{2q} - K_\theta * \Lambda_*^e & \Lambda_*^e * K_{12}^{2q} \\ K_{22}^1 & K_{11}^{2q} & K_{12}^{2q} \\ 0_{6x6} & K_{21}^{2q} & K_{22}^{2q} \end{bmatrix}_{18*18} * \begin{bmatrix} \Delta t_1 \\ \Delta \mathrm{t}_2 \\ \Delta t_3 \end{bmatrix}_{18*1} \qquad [6]$$

- Where the Λ terms are 1x6 vectors of true-false (1-0) for which dimension is elastic. Λ^e has one true value, Λ^r is the reverse, with one false value (both are diagonalised to 6x6, and all rows of zeros removed, expected to leave Λ_*^e as 1x6 Λ_*^r as 5x6).
- K^1 is the first element stiffness matrix in the pre- joint orientation, while K^{2q} denotes the second element rotated into the post-joint orientation.
- $K_{11}, K_{12}, K_{21}, K_{22}$ terms are defined previously in this section (Equation 5).
- K_θ is the rotational joint stiffness of the joint of interest.

Once these component matrices have been determined or estimated, the above matrix formula can be processed into the simpler form:

$$W_3 = K_n * \Delta t_3 \qquad [7]$$

- Where K_n is the 6x6 Cartesian stiffness (in the rotated coordinate system) of a link-joint-link system.
- W_3 is the wrench applied between ends of the element system.

- Δt_3 represents the relative displacements of the two ends of the system from equilibrium.

Using the simplified stiffness system described previously, it should be possible to construct a dynamic model of the whole robot as a multi-degree of freedom mass-spring system (see Figures 14-16). Figure 16 shows graphic interpretation of the complete model kinematic model, where the dotted lines individually represent K_n, while collectively they represent K_C. Examples of K_C are found in Appendix J.

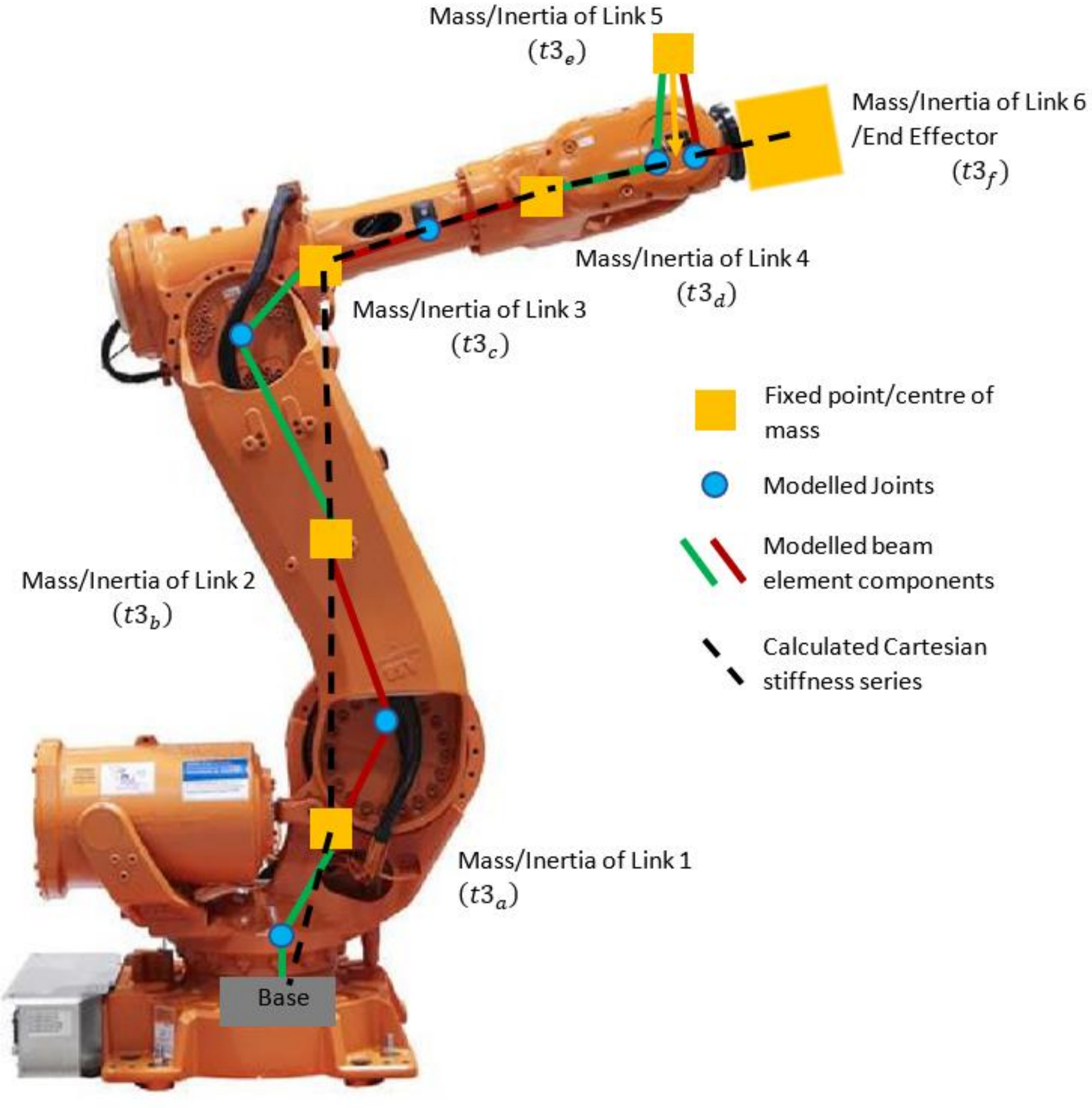

Figure 16: Visualisation of ABB IRB 6640 robot model with visible elements (with exaggeration between links 4 and 6 due to smaller scale). Original image sourced from ABB [69].

Joints are considered to be massless and are represented as elastic joints between link masses. Stiffness values are applied between the centres of mass of the adjacent links. This creates a serial system of six stiffness vectors and six inertia vectors, with the first stiffness applied between the base (link 0) and the centre of mass of link 1, and the final stiffness between the centre of mass of link 5 and the end effector centre of mass (Link 6). Individual stiffness matrices can be converted into a single 36x36 matrix.

In order to apply the screw theory formulae to the geometry described by DH parameters, the 6 stiffness elements must undergo rotation so that for each system of Link A-Joint-Link B, the orientation of Link A matches the base coordinate system, while Link B orientation has been rotated through the joint rotation (a 6x6 matrix where two identical 3x3 rotations are positioned diagonally) (R_n). This rotation is calculated from the kinematics determined from:

- The translations of the aggregated DH homogenous transforms (Equation 2) (where those translations are converted to angular spherical coordinates, and those angles are converted to a rotation matrix). These give the rotations of the links about the Z and Y axis.
- The rotation matrices of the aggregated DH (Equation 2) under the given configurations (where the homogeneous transformation matrix are modified such that Y is always the joint rotation axis, and Z is the link span). These rotations give the missing 3rd rotation about X required to completely describe the link orientations in space.

The following conversion is used once the rotations are known:

$$K_{global} = transpose(R_n) * K_{local} * R_n \qquad [8]$$

where

$$R_n = \left[\ R_{agg\ n}\right]^T\ *\ [R_{agg\ n-1}]$$

- Where R_n is the relative rotation through a joint between two adjacent links.
- Where $R_{agg\ n}$ is the aggregated rotations of a link, from multiplying the rotation matrices from preceding DH matrices from the base coordinate system to the given link.
- Where $R_{agg\ n+1}$ is the likewise aggregated rotations of the next link.

These link elements with their given rotations have been calculated and visualised in Matlab (see Figure 17). The element representing the base to link 1 is presented in black, the element represented in magenta is the robot end effector, other colours show the sequential elements (ascending in order) in the serial link model from base to end effector.

- “◊” Markers represent the link masses.
- “X” markers represent local X axes.
- "∇" markers represent local Y axes.
- "*" markers represent local Z axes.
- "⊙” markers represent joints.

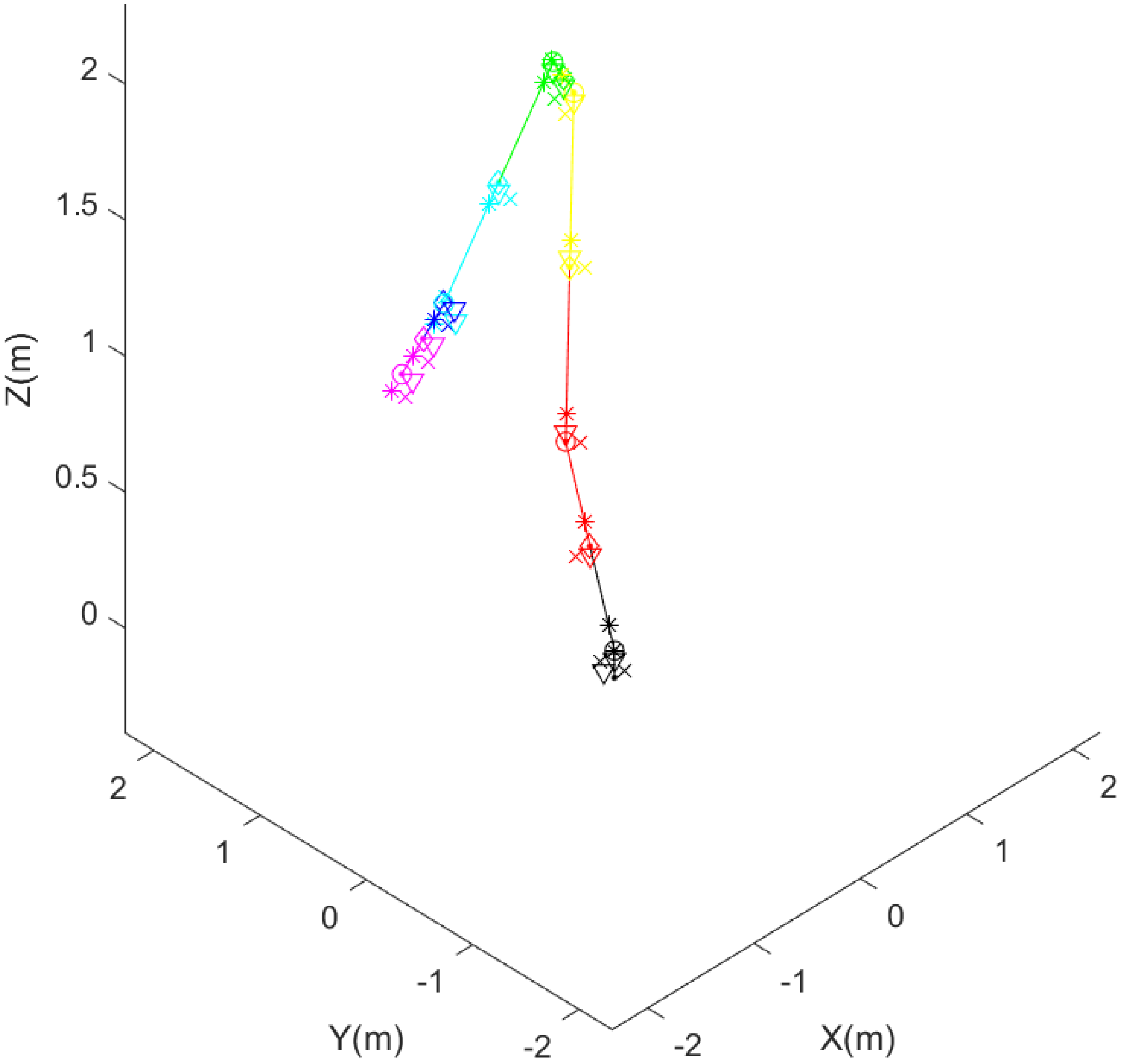

Figure 17: Visualisation of stiffness elements composited into full robot structure.

Each elementary stiffness is calculated as a 6x6 stiffness matrix, however the cells of the matrix which represent XYZ directional stiffnesses (rows 1,2,3, columns 1,2,3) are diagonal. This means they may be converted into a vector and rotated to yield the approximate stiffness for each element in the world coordinate system by the following formula:

$$[K_{n\,global}]_{3x1} = \left[R_{agg\,n}\right]^{-1}{}_{3x3} * [K_{n\,local}]_{3x1} \qquad [9]$$

The stiffness force (F_K) on the numbered link masses of this mass-spring system has been derived as:

$$F_K = \begin{bmatrix} F_1 \\ F_2 \\ F_3 \\ F_4 \\ F_5 \\ F_6 \end{bmatrix}_{36x1} =$$

$$\begin{bmatrix} (K_2+K_1) & (-K_2) & 0 & 0 & 0 & 0 \\ (-K_2) & (K_3+K_2) & (-K_3) & 0 & 0 & 0 \\ 0 & (-K_3) & (K_4+K_3) & (-K_4) & 0 & 0 \\ 0 & 0 & (-K_4) & (K_5+K_4) & (-K_5) & 0 \\ 0 & 0 & 0 & (-K_5) & (K_6+K_5) & (-K_6) \\ 0 & 0 & 0 & 0 & (-K_6) & (K_6) \end{bmatrix}_{36x36} \begin{bmatrix} s_1 \\ s_2 \\ s_3 \\ s_4 \\ s_5 \\ s_6 \end{bmatrix}_{36x1}$$

[10]

- K_n describes the elementary stiffness matrices.
- F_n describes the resultant force applied on each link mass by those stiffnesses.
- s_n describes the displacement of each link mass.

Drilling forces would be applied to the end effector mass when drilling occurs. Mousavi et al. have defined a multibody, flexible joint and body approach which uses the MSA method to approximate robot dynamic behaviour [70]. Mousavi et al. describe beam elements which are modelled without a shearing effect, which is assumed to be negligible [33], (meaning torsional deflection between beam elements is neglected). To retain simplicity of methodology, here they are not omitted, as they are included in the MSA formulae presented by Klimchik et al [62], though their impact on dynamic behaviour and drilling stability is presumed to be negligible.

The natural frequencies (ω_{ri}) and mode shapes of the robot (p_i) can be estimated from stiffness and inertia matrices by the eigenvalue problem [70]:

$$(K_C - \omega_{ri}^2 M_C)p_i = 0 \qquad [11]$$

Where K_c is a (6m) x (6m) stiffness matrix describing stiffness in 6 dimensions and M_c is a (6m) x (6m) inertia matrix with J as inertia about an axis, with “m” referring to the number of bodies [62] as defined in Section 4.2.3. Both matrices are presented in the in the global coordinate system, as in Equation 12 [62]:

$$K_C = \begin{bmatrix} (K_2 + K_1) & (-K_2) & 0 & 0 & 0 & 0 \\ (-K_2) & (K_3 + k_2) & (-K_3) & 0 & 0 & 0 \\ 0 & (-K_3) & (K_4 + K_3) & (-K_4) & 0 & 0 \\ 0 & 0 & (-K_4) & (K_5 + K_4) & (-K_5) & 0 \\ 0 & 0 & 0 & (-K_5) & (K_6 + K_5) & (-K_6) \\ 0 & 0 & 0 & 0 & (-K_6) & (K_6) \end{bmatrix}_{36x36} \qquad [12]$$

- Where K_C is the stiffness matrix describing the whole robot structure.

Solving this Eigenvalue problem using the Matlab "eig" function gives the natural frequencies and mode shapes of the system [70]. The FRF of a proportionally damped system for a given frequency can be expressed as:

$$H_{jk}(\omega) = \sum_{r=1}^{N} \frac{\tilde{\varphi}_j^{(r)} \tilde{\varphi}_k^{(r)}}{\omega_r^2 - \omega^2 + 2\omega\omega_r\zeta_r i} \qquad [13]$$

The normal modes of the system $(\tilde{\varphi}_j^{(r)}, \tilde{\varphi}_k^{(r)})$ are easily acquired through solving for eigenvectors in Matlab, and orthonormal modes $(\varphi_j^{(r)} \varphi_k^{(r)})$ can be gathered from the following formula where M_{rr} represents the mode adjusted mass:

$$H_{jk}(\omega) = \sum_{r=1}^{N} \frac{\tilde{\varphi}_j^{(r)} \tilde{\varphi}_k^{(r)}}{\omega_r^2 - \omega^2} = \sum_{r=1}^{N} \frac{\varphi_j^{(r)} \varphi_k^{(r)}}{M_{rr}(\omega_r^2 - \omega^2)} \qquad [14]$$

- Where $M_{rr} = \{\varphi^{(r)}\}^T [M] \{\varphi^{(r)}\}$

Taking this relation and applying it to the orthonormal modes in Equation 13 gives the following expression of receptance (displacement/force) FRF function in terms of normal modes.

$$H_{jk}(\omega) = \sum_{r=1}^{N} \frac{\varphi_j^{(r)} \varphi_k^{(r)}}{M_{rr}(\omega_r^2 - \omega^2 + 2\omega\omega_r\zeta_r i)} \qquad [15]$$

Where:

- ω_r respresents the natural frequency of the corresponding mode r.
- ω represents a given input frequency.

- ζ_r is the damping ratio (amplitude of response at resonance ($\omega = \omega_r$).
- ($\varphi_j^{(r)}, \varphi_k^{(r)}$) are modes for a given input and output degree of freedom, while r represents a given mode.

This formula results in the following examples of the output profile (also found in Appendix J) (Figure 18, 19) for the X direction, with two modes visible (at approximately 67.5Hz, 130.3Hz):

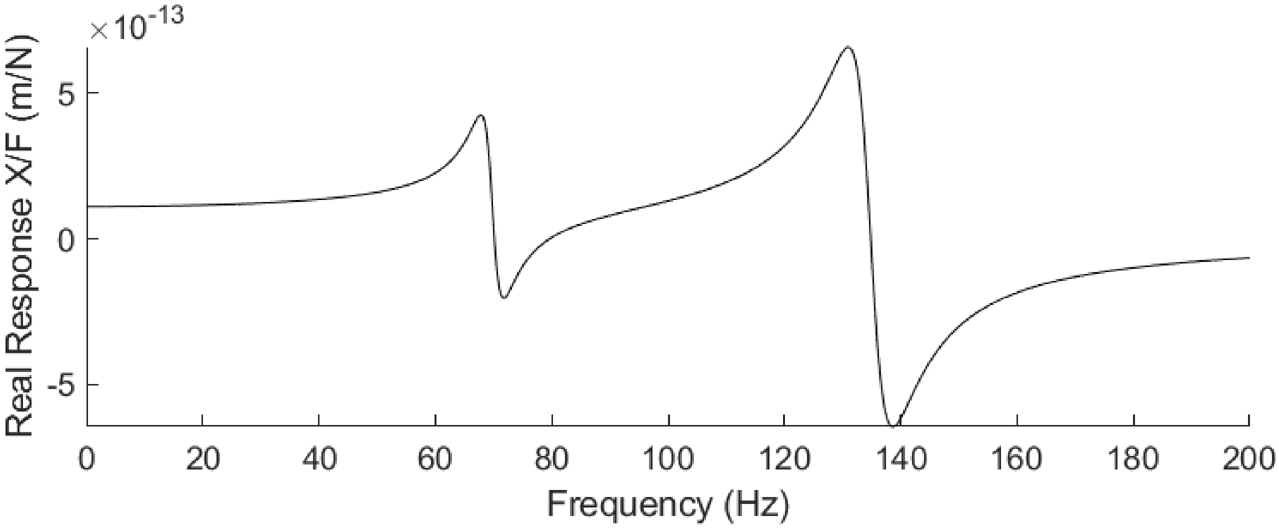

Figure 18: Simulated FRF in the Y direction, real component.

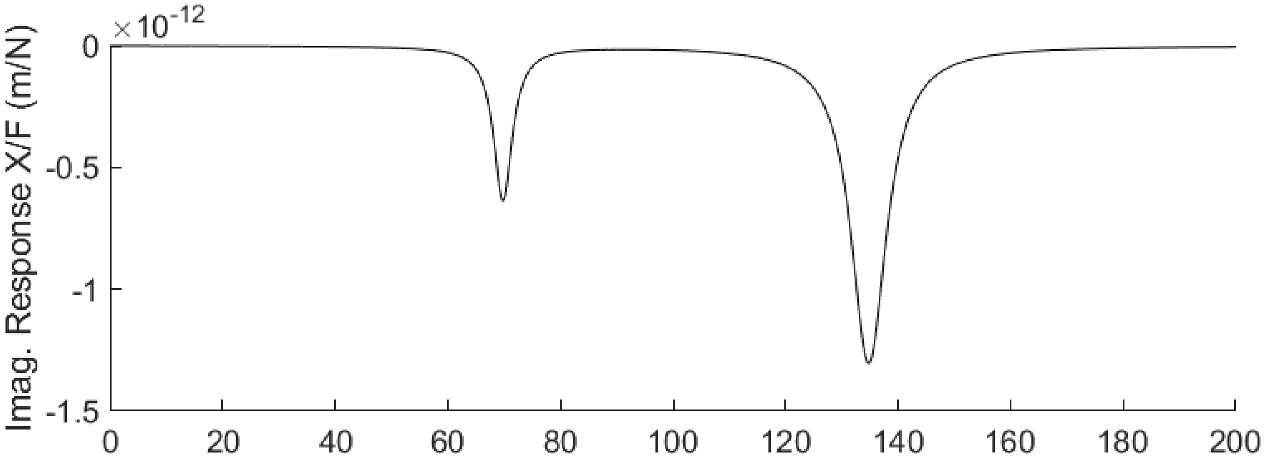

Figure 19: Simulated FRF in the Y direction, imaginary component

The stiffness diagram for the Kuka iiwa shows a static stiffness of 100,000 N/m, compared with a 10,000,000 N/m zero-frequency response for the ABB IRB 6640. The first robot is much smaller (human arm size) while the robot being simulated in

Figures 18 and 19 is much larger in terms of mass and volume, it is entirely possible the motors and drivetrain exert 100x greater resistance to deformation.

4.3 Drilling Mechanics and Dynamics

To facilitate the modelling of dynamic drilling forces, a theory of mathematical prediction of drilling stability in the frequency domain presented by Altintas [12] has been selected and will be summarised in this section. This, along with the workpiece material, cutting parameters and tool geometry, will form the basis of the characterisation of the drilling operation, which will later be combined with the characterisation of the serial manipulator FRFs.

As Figures 20 and 21 show, the forces on the cutting lips of the drilling tool are dependent on the instantaneous uncut chip area, which is dependent on the pilot hole radius and the lateral deflection of the tool relative to the pilot hole [12]. As the force on the cutting lip can cause lateral deflections, there is a regenerative cycle which results in significant chatter in cases where the cutting lip positions are not sufficiently stable [12], which results from a lack of stiffness of the tool relative to the workpiece.

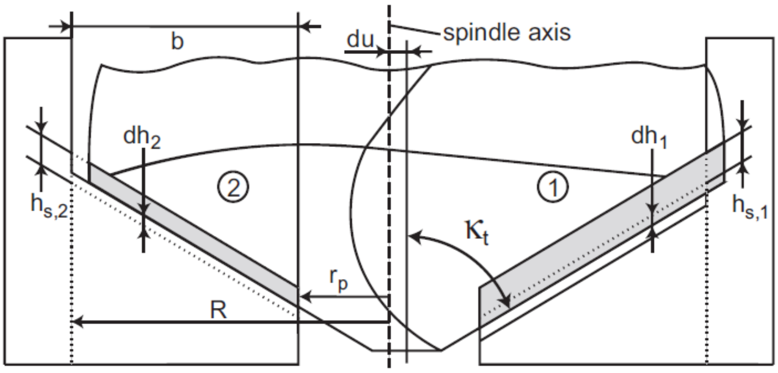

Figure 20: Visualisation of cutting lip contact area with deflected tool end [12].

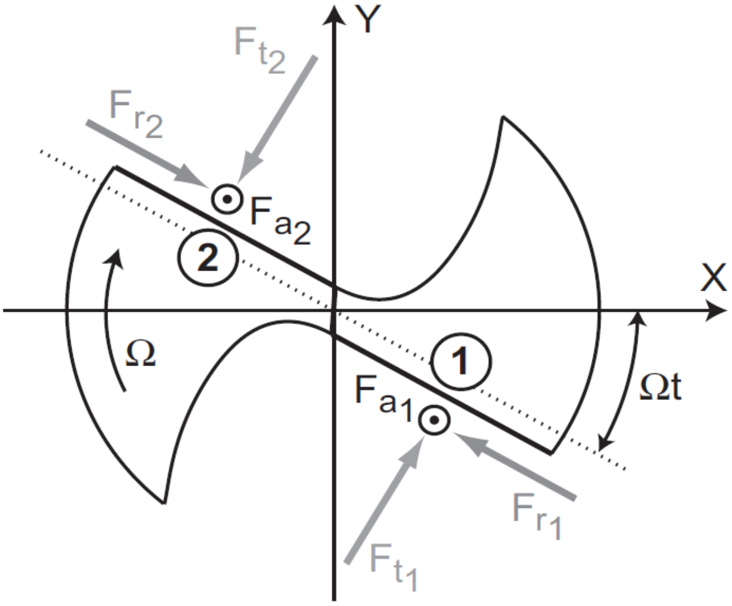

Figure 21: Visualisation of forces on drill cutting lips [12].

4.3.1 Time Domain Solution

The time domain solution must first be formulated to identify the average directional parameters of the drilling process. The frequency domain solution can then be determined. The regenerative chatter forces on the tool depend on the regenerative displacements, with Altintas giving the following relationship for a drilling tool with two flutes.

$$\{F(t)\} = -2k_{tc}b[B_0]\{r\Delta\} \qquad [16]$$

Where:

$$\{F(t)\} = \begin{Bmatrix} F_x \\ F_y \\ F_z \\ T_c \end{Bmatrix} \ , \ \{r\Delta\} = \begin{Bmatrix} dx \\ dy \\ dz \\ d\theta \end{Bmatrix} \ ,$$

$$[B_0] = \begin{bmatrix} \frac{+k_{rc}}{2tan\kappa_t} & \frac{+1}{2tan\kappa_t} & 0 & 0 \\ \frac{-1}{2tan\kappa_t} & \frac{k_{rc}}{2tan\kappa_t} & 0 & 0 \\ 0 & 0 & k_{ac} & \frac{f_r}{2\pi}k_{ac} \\ 0 & 0 & (1-k_{rc})R_t & \frac{f_r}{2\pi}(1-k_{rc})R_t \end{bmatrix}$$

Other term definitions:

- b represents the radial depth of cut.
- (k_{tc}, k_{rc}, k_{ac}) represent average cutting force coefficients (tangential, radial, axial) of the process.
- R_t represents the tool diameter.
- f_r represents axial feed per revolution.

It should be noted that because the directional factor $[B_0]$ matrix shown has several zero values in off-diagonal terms, the lateral dynamic cutting forces (F_x, F_y) and axial cutting forces (F_z, T_c) are decoupled from each other, and from the corresponding vibrations connected to those decoupled forces lateral (dx, dy) and axial/torsional $(dz, d\theta)$.

4.3.2 Frequency Domain Solution Stage

Roukema and Altintas proposed a novel method to calculate chatter stability lobes for drilling, considering lateral torsional and axial vibrations [71]. They state that experiments show that torsional-axial chatter is dominant in drilling, while lateral chatter is not dominant, but may become important in drills with larger length to diameter ratios [71]. Torsional axial chatter has a steady state torque and thrust in drilling, which contributes strongly to chatter [71]. They comment that models would greatly improve if process damping and drill-hole contact stiffness are accurately modelled [71].

The frequency domain solution has also been defined by Altintas and Roukema and will be summarised here [71]. Whirling vibrations, along with force visualisation and resulting hole finish, are not considered by the frequency domain Roukema-Altintas model [71]. This requires the equivalent time domain model, which is not used due to the computational expense of simulating a large number of multiple time steps [71].

This mathematical derivation will be used to determine the stability lobes based on the robot frequency response functions. While the formula presented in the source given is adaptable to drills of any flute number, the formulae given here are for a twist drill with two flutes.

Taking a simplified representation of the time domain solution for the structural dynamics of the drill (in this case also incorporating the simulated robot FRF from the dynamic model) gives a frequency response function matrix (where $\Phi_{jk}(i\omega)$ describes FRFs and is equivalent with $H_{jk}(i\omega)$):

$$[\Phi(i\omega)] = \begin{bmatrix} \Phi_{\mathrm{xx}} & 0 & 0 & 0 \\ 0 & \Phi_{\mathrm{yy}} & 0 & 0 \\ 0 & 0 & \Phi_{\mathrm{zz}} & \Phi_{\mathrm{z\theta}} \\ 0 & 0 & \Phi_{\mathrm{\theta z}} & \Phi_{\mathrm{\theta\theta}} \end{bmatrix} \qquad [17]$$

Axial-torsional coupling is represented by the terms $\Phi_{\mathrm{\theta z}}$ and $\Phi_{\mathrm{z\theta}}$.

Critical stability occurs when harmonic regenerative displacements $\{\Delta r\}$ occur at chatter frequency ω_c with a constant amplitude, described by the following eigenvalue problem:

$$\{F\}e^{i\omega_c t} = -2k_{tc}b_{\mathrm{lim}}\left(1 - e^{-i\omega_c T}\right)[B_0][\Phi(i\omega)]\{F\}e^{i\omega_c t} \qquad [18]$$

Where:

- $\{F(t)\} = \begin{Bmatrix} F_x \\ F_y \\ F_z \\ T_c \end{Bmatrix}$, $\{r\Delta\} = \begin{Bmatrix} dx \\ dy \\ dz \\ d\theta \end{Bmatrix}$,
- b_{lim} represents the maximum stable depth of cut in the radial direction, referring to the radius of material removed by the cutting lips, as determined by size of the pilot hole, thus b_{lim} informs pilot hole size for the process (pilot hole radius is visualised in Figure 20).

$$\begin{bmatrix} \frac{+k_{rc}}{2tan\kappa_t} & \frac{+1}{2tan\kappa_t} & 0 & 0 \\ \frac{-1}{2tan\kappa_t} & \frac{k_{rc}}{2tan\kappa_t} & 0 & 0 \\ 0 & 0 & k_{ac} & \frac{f_r}{2\pi}k_{ac} \\ 0 & 0 & (1-k_{rc})R_t & \frac{f_r}{2\pi}(1-k_{rc})R_t \end{bmatrix} = [B_0]$$

Directional cutting force coefficient matrix term definition definitions:

- (k_{tc}, k_{rc}, k_{ac}) represent average cutting force coefficients (tangential, radial, axial) of the process.
- R_t represents the tool diameter.
- f_r represents axial feed per revolution.

It should be noted that because the directional factor $[B_0]$ matrix shown has several zero values in off-diagonal terms, the lateral dynamic cutting forces (F_x, F_y) and axial cutting forces (F_z, T_c) are decoupled from each other, and from the corresponding vibrations connected to those decoupled forces lateral (dx, dy) and axial/torsional $(dz, d\theta)$.

Through eigenvalue derivation, this gives a formula for b_{lim} in known terms:

$$b_{lim} = \Lambda_R \frac{[1+\chi^2]}{4k_{tc}} \quad [19]$$

Where the corresponding vibrations (connected to spindle speeds (n)) can then be derived from the eigenvalues $(\Lambda_\mathrm{I}, \Lambda_\mathrm{R})$:

$$\chi = \frac{\Lambda_I}{\Lambda_R} = \frac{\sin(\omega_c T)}{1-\cos(\omega_c T)}, \; T = \frac{\epsilon + 2k\pi}{\omega_c}, \qquad \epsilon = \pi - 2\tan^{-1}\frac{\Lambda_\mathrm{I}}{\Lambda_\mathrm{R}} \quad \rightarrow \quad n = \frac{60}{2T} \quad [20]$$

Stability lobes can then be plotted using the method also outlined by Altintas. Lateral vibrations are evaluated by using Λ_{xy}, while torsional/axial vibrations consider eigenvalues $\Lambda_{z\theta}$. Altintas states that different parts of structural dynamics will affect productivity differently, and it is possible to determine which part has a greater effect on productivity.

4.3.3 Roukema's Method

Roukema, in his doctoral dissertation [72], "Mechanics and Dynamics of Drilling," has presented a numerical method to predict the static cutting force coefficients of a drilling process if given the cutting lip and chisel edge geometries of the drill, the cutting speed and feed rate of the process, and also including known material properties obtained from an orthogonal cutting database built up of experimental two-dimensional cutting tests [72]. These include the shear stress of the material, yielding shear angle and friction angle as functions of cutting conditions [72]. Edge force constants are also determined experimentally (K_{te}, K_{fe}, K_{re}) [72]. The method used for determining cutting coefficients (K_{tc}, K_{fc}, K_{rc}) involves discretising the cutting lips and chisel edge into smaller elements with calculated average cutting angles, then applying the orthogonal to oblique cutting transformation to calculate the forces on these elements, and finally summing the elements to estimate total force on the lip [72].

5 Evaluation and Comparison

5.1 Stiffness Matrix Accuracy

Joint stiffnesses, as the most flexible parts of the mass-spring series, are assumed to be dominant when predicting the end effector cartesian stiffness. which allows for comparison of the effectiveness of the MSA method applied here with measured values from the work of Celikag et al. In two machining robot configurations (Visualised in Figures 22 and 23), the following stiffnesses (Table 5) were predicted:

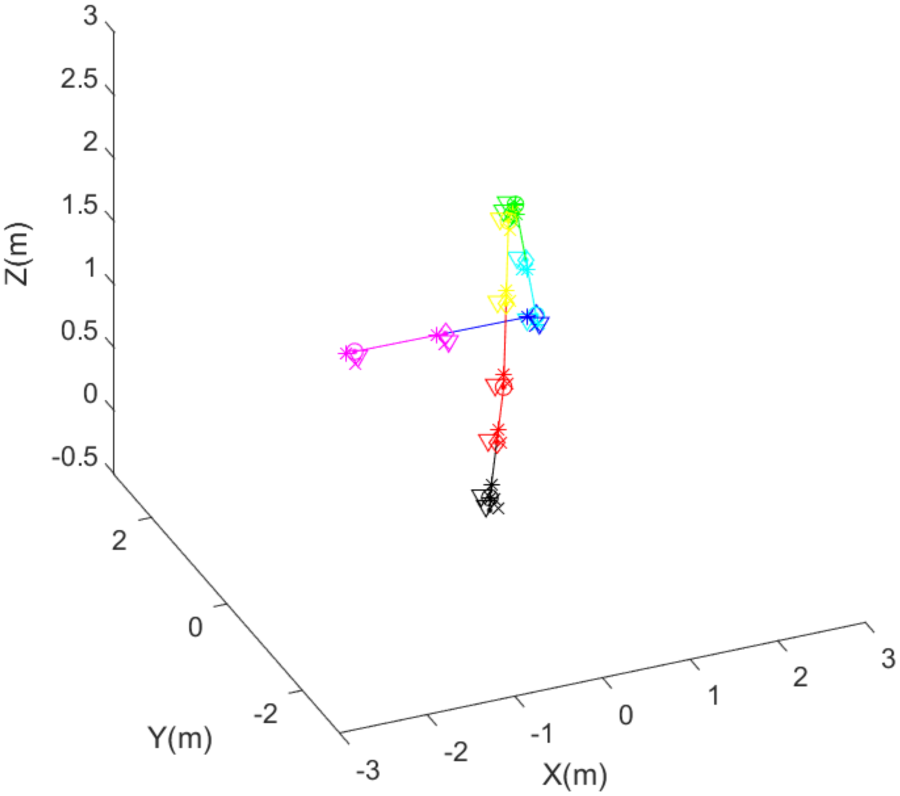

Figure 22: Matlab Visualisation of Robot Configuration A.

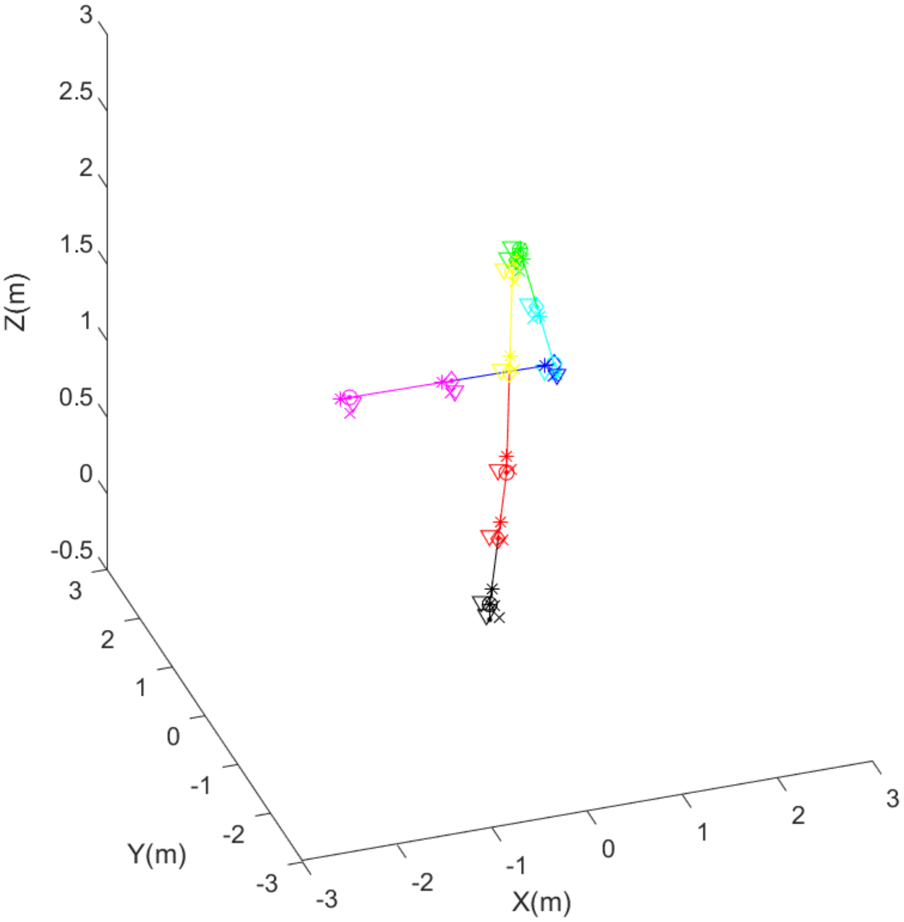

Figure 23: Matlab Visualisation of Robot Configuration B.

Joint variables (degrees)	K_x **(N/m)**	K_y **(N/m)**
Configuration A (q = [40, 5, 50, 40, -85, -30])	1.335 x 10^6	8.540 x 10^5
Configuration B (q = [40, 5, 60, 40, -85, -30])	1.410 x 10^6	9.709 x 10^5

Table 5: Measured ABB IRB 6640 Cartesian configurations and reported stiffness values.

With the elemental stiffness matrices for the same configurations, calculated and rotated through the steps outlined in Section 4.2.3, the Matlab program written as part of this project predicts the following stiffnesses in the X and Y directions when the robot is in the same configurations (Table 6).

Joint variables (degrees)	**K_x (N/m)**	**K_y (N/m)**
Configuration A (q = [40, 5, 50, 40, -85,-30])	1.3663 x 10^7 **(1023%)**	1.0595 x 10^6 **(124%)**
Configuration B (q = [40, 5, 60, 40, -85,-30])	1.3663 x 10^7 **(969%)**	1.0579 x 10^6 **(109%)**

Table 6: Measured ABB IRB 6640 Cartesian configurations and reported stiffness values, with percentage comparisons with previously measured data (presented in bold).

From comparing the MSA Matlab outputs for static stiffness with empirically measured values, K_x is much more poorly estimated than K_y, with those X axis stiffnesses appearing to be close to ten times larger than the values from K_y, within close proximity to 1000%.

This inaccuracy may be due to inaccurate rotation of stiffness elements, as the kinematic chain stiffness matrix has both high stiffnesses (from links) and low stiffnesses (from joints), and low stiffnesses were expected to dominate the aggregated stiffness of the end effector. The rotation stage of the program is where low and high stiffnesses become aligned, contrasted with no rotations where they do not, and hence where this dominance is established. It may be that the process is flawed for K_x but not for K_y, and the rotation operations should be revisited in future work.

For comparison with the Frequency Response Functions (FRF) measured from the robot, the simulated FRF of the robot in configurations approximating those of FRF measurement are also presented.

Next, the results of industrial software (Cutpro) applied to the measured FRF of the system. In the absence of drilling trials to generate measured stability lobes, this presents an alternative means of evaluating the accuracy of the Matlab simulation without empirical stability measurement during cutting. For evaluation of the simulations, a discussion is presented on the Matlab stability peaks in terms of frequency and magnitude as a proportion of the Cutpro, with notes on possible causes of differences.

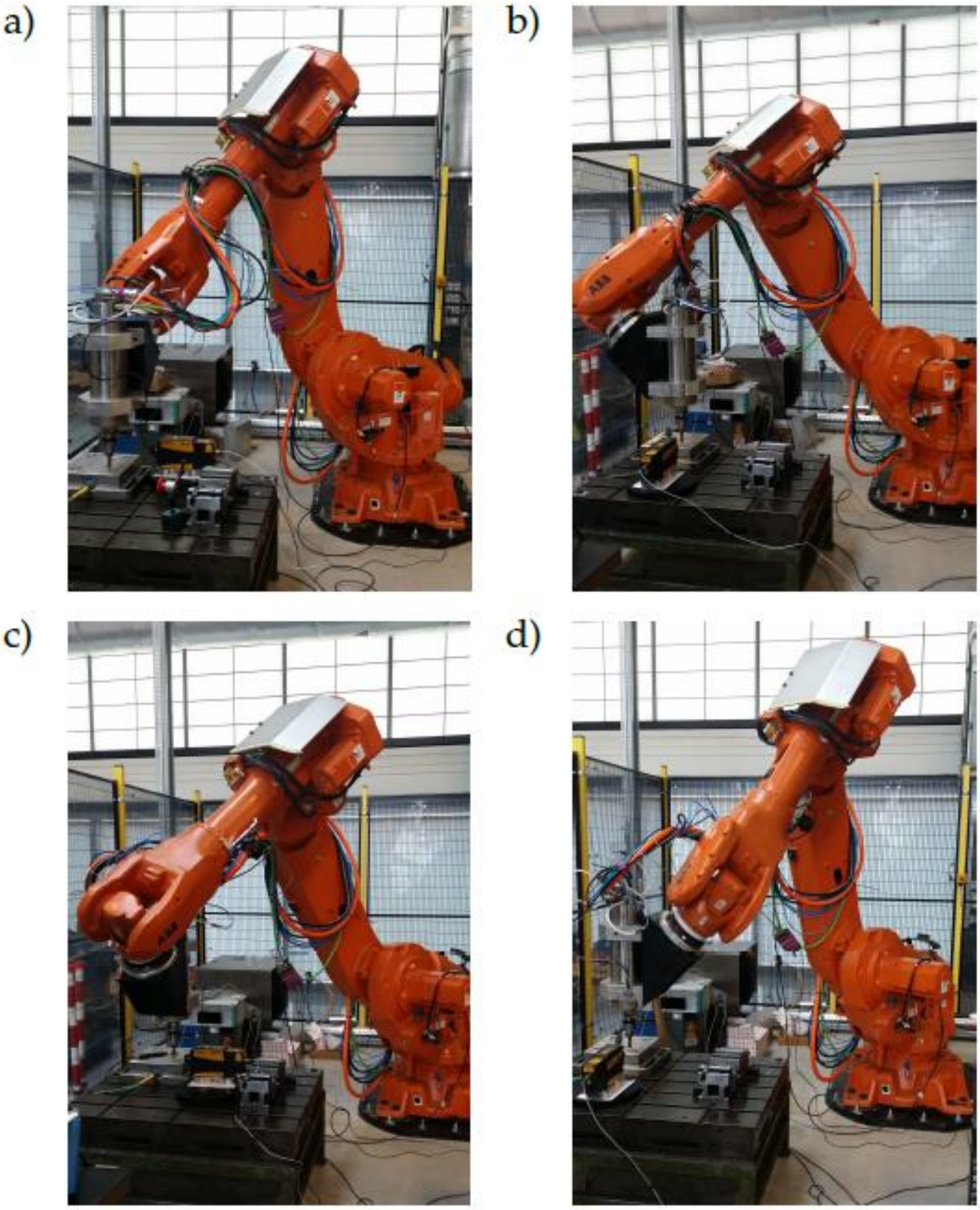

Figure 24: Configurations of the ABB IRB 6640 at 4 equidistant redundant angles, as described in Table 7 (Celikag et al. [64])

Figure Label	**Assigned Redundant Angle (Radian)**
a)	2π
b)	1.5π
c)	1π
d)	0.5π

Table 7: Configuration angle assignment (Figure 24 and 25).

The values shown in Table 7 are redundant angles of the drilling process and describe one of the orientation angles applied to the robot end effector which does not affect the machining trajectory. This trajectory is parallel to the tool axis for drilling and milling.

These configurations have been inserted into the program and are visualised below in Figure 25. Tool Centre Point (TCP) is visualised as a black dot representing the centre point, surrounded by dots representing the X (red), Y (green) and Z (blue) directional. The 6th joint target position and orientation (which is used by the robot controller) is represented by rings of the same colour scheme in close proximity. Visible in separate colours are the links, presented in terms of the joint which connects to the next link (one individual ring) and centre of mass coordinate system of the current link. Colours follow the convention included with Figure 25.

Link 1	**Link 2**	**Link 3**	**Link 4**	**Link 5**	**Link 6**
Red	Yellow	Green	Cyan	Blue	Magenta

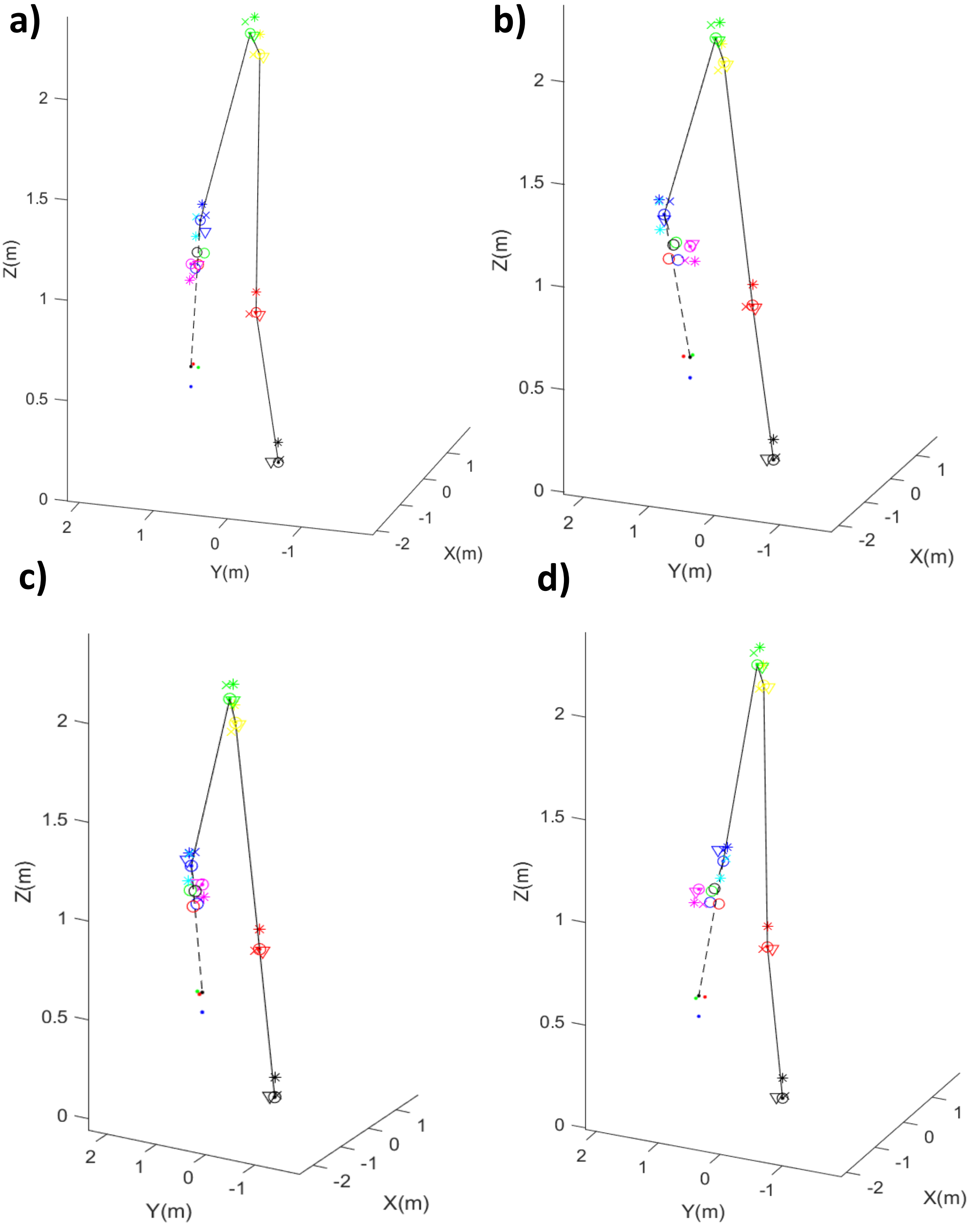

Figure 25: Matlab program internal kinematic model with visualised joints and centres of mass.

Table 8 shows the stiffnesses predicted by the Matlab program for each of these configurations.

Joint variables (degrees)	K_x **(N/m)**	K_y **(N/m)**
Configuration 1 (q = [135, -2, 53, 83, 30, -117])	67.535103 x 10^6	1.054190 x 10^6
Configuration 2 (q = [135, 20, 26, 30, 80, -150])	74.410177 x 10^6	1.050671 x 10^6
Configuration 3 (q = [153, 23, 20, -18, 87, 161])	91.772087 x 10^6	1,057965 x 10^6
Configuration 4 (q = [161, 3, 47, -68, 46, 123])	85.750878 x 10^6	1.059895 x 10^6

Table 8: Simulated static stiffness outputs for X and Y (Matlab) by configuration.

Considering the empirically measured results, and also considering the diversity of orientations for the robot end effector examined, it would be expected that K_x and K_y would have similar values or alternate between higher stiffness depending on XY orientation of the end effector, which is the most compliant part of the robot structure (normal to Y for configurations 1 and 3, normal to X configuration 2 and 4). This supports the earlier supposition that stiffness matrix rotations are not performed correctly for the X direction and should be revisited.

Before FRFs can be calculated, damping values for the robot structure are required.

5.2 Derivation of Damping Ratios from Experimental FRFs

The peak picking method may be used to extract the damping ratio of a given single-degree-of-freedom system from the FRF of that system. If there is sufficient separation between modes which are aligned in the same direction, a given mode of a multi-degree-of-freedom system may be treated as a single degree of freedom system. Damping ratio derivation is carried out with the following steps [73]:

- Identify the natural frequency of the peak (ω_r).
- Identify the magnitude of the peak (α_{max}) and calculate ($\frac{\alpha_{max}}{\sqrt{2}}$).
- Identify frequencies less and greater than the natural frequency at the half peak magnitude ($\omega_{1,}\omega_2$).
- Calculate damping ratio (ζ_r) from width of resonance peak:

$$\zeta_r = \frac{\omega_2 - \omega_1}{2\omega_r} \qquad [21]$$

These steps were programmed using Matlab with the following operations:

- Peaks (natural frequencies) are identified using the "localmax" function on the magnitude vector of the FRF to identify peak indices.
- By logging the sample number at which natural frequencies occur, the corresponding magnitudes can be accessed and $(\frac{\alpha_{max}}{\sqrt{2}})$ calculated for each.
- Samples can be queried for magnitude sequentially at ascending and descending frequencies, with the number of samples examined before the corresponding magnitude falls below $(\frac{\alpha_{max}}{\sqrt{2}})$ used to define estimates for $(\omega_{1,}\omega_2)$. The accuracy of this estimate is limited by the sampling frequency of the FRF. If a magnitude less than $(\frac{\alpha_{max}}{\sqrt{2}})$ is returned after only 1 sample is queried, $(\omega_2 - \omega_1)$ and therefore ζ_r would be equal to zero, in which case the peak is omitted from damping analysis by an "if" function.

This process has been performed for the experimental FRFs captured by Celikag et al, which have been imported into Matlab. Configuration 1 FRFs are presented here as examples (pictured in Figures 26 and 27), while results for all captured FRFs are included in Table 9. Visualisations of all FRFs can be found in Appendix I.

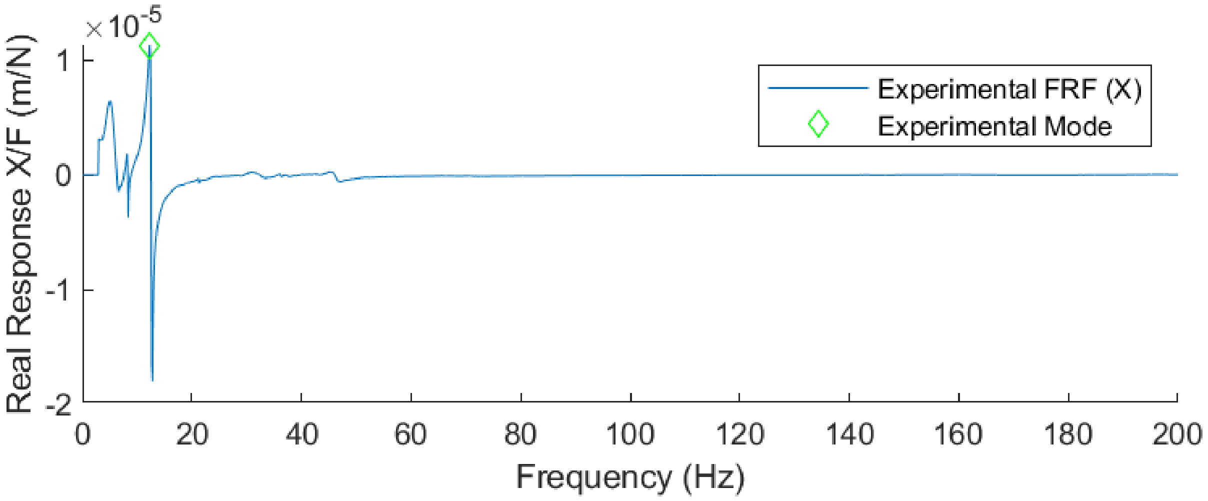

Figure 26: Measured ABB IRB 6640 (Configuration 1) Real FRF (Direct) (X).

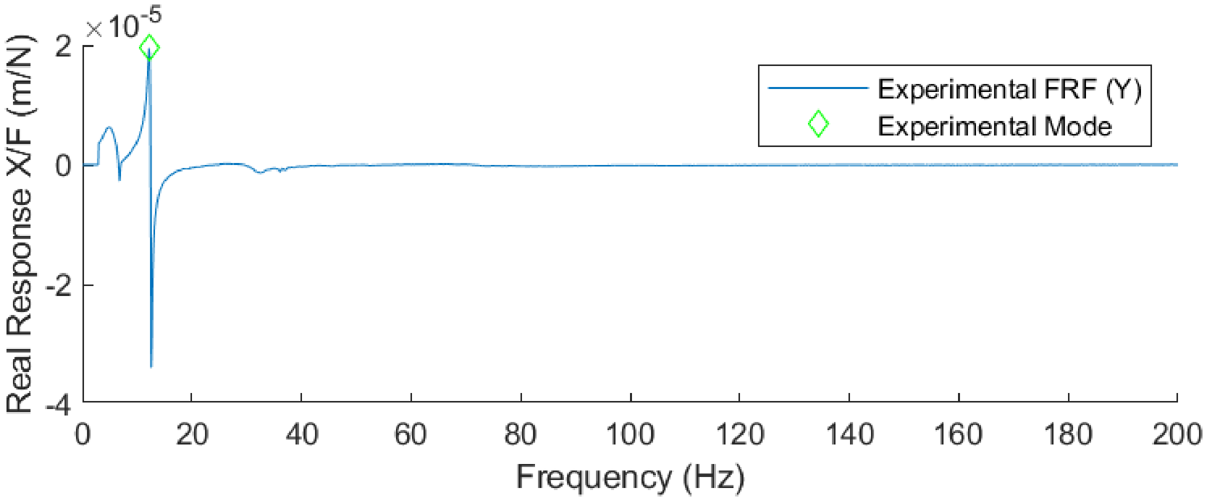

Figure 27: Measured ABB IRB 6640 (Configuration 1) Real FRF (Direct) (Y).

	Config. 1	**Config. 2**	**Config. 3**	**Config. 4**
Dominant Mode Frequency (X) (Hz)	12.3	14.5	14.7	11.9
Dominant Mode Response (X) (m/N)	1.132522e-05	1.037395e-05	9.606958e-06	1.244932e-05
Dominant Mode Damping Ratio (X)	**0.0284552845528455**	**0.0379310344827587**	**0.0442176870748299**	**0.0336134453781512**
Dominant Mode Frequency (Y) (Hz)	12.2	14.7	14.1	12
Dominant Mode Response (Y) (m/N)	1.953579e-05	1.758181e-05	1.365955e-05	1.131007e-05
Dominant Mode Damping Ratio (Y)	**0.0245901639344262**	**0.0204081632653061**	**0.0354609929078014**	**0.025**

Table 9: Properties modes of measured real FRFs for all 4 configurations.

From this table of properties of the 4 real FRFs, the damping ratios for the X direction range from approximately 0.028 to 0.045, while for the Y direction, the range is 0.020 to 0.036. As a damping ratio was required for simulated FRFs which must be consistent across configurations, the damping ratios of Configuration 1 were chosen arbitrarily (For X: ζ_r=0.0285; For Y: ζ_r=0.0246).

5.3 Matlab Simulated FRF Evaluation

In this section, the results of the Matlab program which implements the method described in previous sections will be evaluated. the Matlab simulated FRFs will be compared with FRFs measured under the same configurations.

For each of the 4 configurations, Appendix J includes:

- Full stiffness matrices (K_C)
- Non-diagonal mass matrices (M_C). Actual input (M_C) is diagonalised.
- Resulting Natural frequencies (ω) calculated using the Matlab “eig( )” function.
- Resulting mode shapes (ψ) calculated using the Matlab “eig( )” function.
- FRFs ($H_{jk}(\omega)$) generated by processing these natural frequencies and mode shapes along with the derived damping and mass matrix.

5.3.1 Stiffness and Mass Matrices

For configurations 1, 2, 3 and 4, the stiffness matrix constructed by the formulae in Section 4.2.3 shows only positive, non-zero terms on the diagonal.

The mass matrices are all diagonal matrices with positive, non-zero elements.

5.3.2 Natural Frequencies

Natural frequencies and mode shapes are generated through applying the Matlab eigenvalue function with K_C and M_C as inputs. An important observation when examining the natural frequencies is that some of them have negative imaginary values, rather than the expected positive real values. The mode numbers, frequencies and corresponding assignment of natural frequency is included in Table 10.

	Mode Number	Natural Frequency	Stiffness Representation
Config. 1	9	-1165.449i	Z axis translation of Mass 2
	24	-137.085i	Z axis rotation of Mass 4
Config. 2	9	-245.082i	Z axis translation of Mass 2
	25	-138.326i	X axis translation of Mass 5
Config. 3	10	-1150.006i	Z axis rotation of Mass 2
	26	-172.710i	Y axis translation of Mass 5
Config. 4	10	-1729.230i	X axis rotation of Mass 2
	22	-190.094i	X axis rotation of Mass 3

Table 10: Observed imaginary negative natural frequency outputs

The lack of a pattern in where these anomalies occur supports the idea that the stiffness rotations are incorrect, as these rotations would be expected to change with each differing configuration. It should be considered that these values are physically unfeasible, but these are likely not the cause of the anomalous profile shape of the X axis FRF of configuration 3, as there are two cases (Configuration 3, direction Y and Configuration 2 direction X) where both the dimension applies to the FRF being simulated the natural frequency is of a magnitude (172.710 Hz) that would fall within the frequency range being examined (0-200 Hz) and hence would be expected to give a visible effect in the FRF output. For this reason, it is recommended these be treated as problems with different sources.

The natural frequencies calculated for the presumed modes of interest (those affecting X and Y axis translation), are assumed respectively to be:

- Modes 1,7,13,19,25 and 31 (X axis translation).
- Modes 2,8,14,20,26 and 32 (Y axis translation).

These modes are also presented in Tables 10-14, in order of mass number from the robot base. Values in bold indicates this mode frequency is within the range visible on the FRF, and thus should be visible.

Configuration 1 (X direction)		**Configuration 1 (Y direction)**	
Mode Number	Natural Frequency	Mode Number	Natural Frequency
1	4042624.3	2	4042611.546
7	7806.624	8	2555.179
13	2038.215	14	2017.534
19	479.502	20	408.963
25	**134.862**	**26**	**136.173**
31	**69.828**	**32**	**41.753**

Table 11: Natural frequencies predicted for the robot end effector in Configuration 1.

Configuration 2 (X direction)		**Configuration 2 (Y direction)**	
Mode Number	Natural Frequency	Mode Number	Natural Frequency
1	4042651.618	2	116713.734
7	3504.463	8	2560.404
13	2016.501	14	1782.726
19	551.148	20	538.0667
25	138.326i	**26**	**118.390**
31	**71.260**	**32**	**29.071**

Table 12: Natural frequencies predicted for the robot end effector in Configuration 2.

Configuration 3 (X direction)		**Configuration 3 (Y direction)**	
Mode Number	Natural Frequency	Mode Number	Natural Frequency
1	4042633.041	2	4043047.450
7	3179.316	8	2577.224
13	1647.942	14	991.316
19	579.716	20	457.444
25	210.383	26	-172.710i
31	**72.522**	**32**	**30.961**

Table 13: Natural frequencies predicted for the robot end effector in Configuration 3.

Configuration 4 (X direction)		**Configuration 4 (Y direction)**	
Mode Number	Natural Frequency	Mode Number	Natural Frequency
1	4042601.445	2	4043062.493
7	4778.312	8	2570.696
13	1771.734	14	2060.868
19	410.655	20	358.491
25	225.314	**26**	**148.963**
31	**71.216**	**32**	**42.559**

Table 14: Natural frequencies predicted for the robot end effector in Configuration 4.

The lowest predicted modes are compared with actual measured robot FRF modes for all directions and configurations in Table 15.

	Simulated Natural Frequency (Hz)	**Measured Natural Frequency (Hz)**	**Simulated Natural Frequency as a Percentage of Measured (%)**
Configuration 1 (X)	69.828	12.3	**567.7073**
Configuration 1 (Y)	41.753	12.2	**342.2377**
Configuration 2 (X)	71.260	14.5	**491.4483**
Configuration 2 (Y)	29.071	14.7	**197.7619**
Configuration 3 (X)	72.522	14.7	**493.3469**
Configuration 3 (Y)	30.961	14.1	**219.5816**
Configuration 4 (X)	71.216	11.9	**598.4538**
Configuration 4 (Y)	42.559	12	**354.6583**

Table 15: Low Mode comparison of measured and simulated natural frequencies.

By comparing the lowest simulated natural frequencies with the most dominant modes observed at low frequency, the simulated natural frequencies are overestimated by approximately a factor of 4.9-6 for the X direction and overestimated by approximately a factor of 2-3.5 for the Y direction. It was expected that the result for the Y direction would be more accurate as the predicted static stiffness in the Y direction was closer than the X direction to that indicated by the experiment performed by Celikag et al.

5.3.3 Mode Shapes

The mode shapes are amongst the data presented for each configuration. They are 36x36 matrices, and no observations of their accuracy are made. The responses which result from the mode shape calculations are discussed in Section 5.3.4.

5.3.4 Frequency Response Function Analysis

The FRF profiles generated from these mode shapes are presented in Appendix J. Observed modes of this simulated FRF (real component), and correlations with the input natural frequencies are presented below in Table 16.

	Observed Mode Frequencies	Input Natural Frequency	Observed modes as Percentage of Input Frequency	Observed Response
Configuration 1 (X)	67.5	**69.828**	96.66609	3.77613e-13
	130.3	**134.862**	96.61728	5.5851e-13
Configuration 1 (Y)	40.7	**41.753**	97.47803	89193e-28
	132.9	**136.173**	97.59644	8.95563e-29
Configuration 2 (X)	69.2	**71.260**	97.10918	6.85289e-14
Configuration 2 (Y)	28.3	**29.071**	97.34787	4.20539e-28
	115	**118.390**	97.13658	8.27955e-29
Configuration 3 (X)	None	**72.522**	None	None
Configuration 3 (Y)	30.2	**30.961**	97.54207	6.03693e-30
Configuration 4 (X)	69.2	**71.216**	97.16918	9.41982e-14
Configuration 4 (Y)	41.5	**42.559**	97.51169	2.33839e-29
	145.5	**148.963**	97.67526	3.22126-30

Table 16: Comparison of FRF input and output frequencies, with corresponding responses.

From this data, it is found that simulations of the direct FRF in the X direction for Configuration 3 did not return the expected FRF-like profile, with visible modes that can be compared, instead returning a response which increased with frequency in an apparently exponential curve. It is not known what is causing this effect, however it is expected to be due to the specific interaction of the denominator terms ($\omega_r^2 - \omega^2 + 2\omega\omega_r\zeta_r i$) approaching zero as applied frequency (ω) increases for this configuration.

Besides this anomaly, the observed modal frequencies for are slightly lower than the input frequencies to the FRF formula (96-98% of input). This is expected in a damped system as the natural frequency is reduced the greater the damping effect.

Despite typically showing good agreement with the input frequencies, the modal response values are vastly different in the X and Y directions, with X direction modes of order 10^{-13} and Y direction modes of order 10^{-30} to 10^{-28}. This contradicts the simulated static stiffness, which suggested the robot was more compliant in the Y direction, and hence responses would be expected to be larger (greater displacement in response to force), not smaller than the X direction.

Overall, a comparison with the experimental FRF shows that the model is inaccurate in predicting response scale, to the point where comparing values as percentages is not useful, with experimental modal values being of the order of 10^{-5}, compared with 10^{-13} to 10^{-30}. This problem may be due to the numerator portion of the FRF formula ($\tilde{\varphi}_j^{(r)}\tilde{\varphi}_k^{(r)}$), (where specific mode shapes of the input and output directions are multiplied) not being performed correctly, as this limits the maximum (modal) response across the frequency spectrum.

5.3.5 FRF Evaluation Conclusions

There are multiple problems with the FRF simulation process which cannot be connected to incorrect stiffness, mass or damping values which the Matlab script was applied to. This problem likely stems either from the internal eigenvalue solver being improperly utilised for this application, or from errors in the coding of the FRF formula which utilises the resulting eigenvalues and eigenvectors.

5.4 Stability Lobe Program Evaluation

Evaluation of the stability lobe program will be carried out using Cutpro Machining Simulation, (specifically the Analytical Stability Lobe function). The following cutting parameters (see Table 17) were used for both simulations. Cutting Force Coefficients (CFCs) are taken from the milling of Aluminium 7075 [74]. These values have been applied to the formula for average directional factors in drilling for both Matlab and Cutpro to ensure the comparison is focused on stability lobe.

Process Input	**Value**
k_tc	1014.2 N/mm^2
k_fc	58.2 N/mm^2
k_rc	619.9 N/mm^2
Tool Radius	8 mm
Half Tip Angle	1.178 rad
Flute no	2
Feed per rev	0.1 mm

Table 17: Cutting conditions input to Cutpro and Matlab for comparison.

Additionally, a harmonic number of 10 (represented by "k" as described in Equation 20, Section 4.3.2) was applied to the Matlab stability lobe generation process, following the procedure described by Altintas [12], and demonstrated on frequency response functions of industrial robots by Mejri et al. [75]. A different set of stability data is generated for each mode of the FRF (see Figure 28), and these are then composited together, selecting from the minimum stability between all modes within each increment of spindle speed. In this case these increments have a resolution of 0.1 Hz or 6RPM.

It should be noted that no stability limits are captured for speeds below 150RPM due to an absence of negative response at very low frequencies, therefore stability predictions below this speed are unreliable.

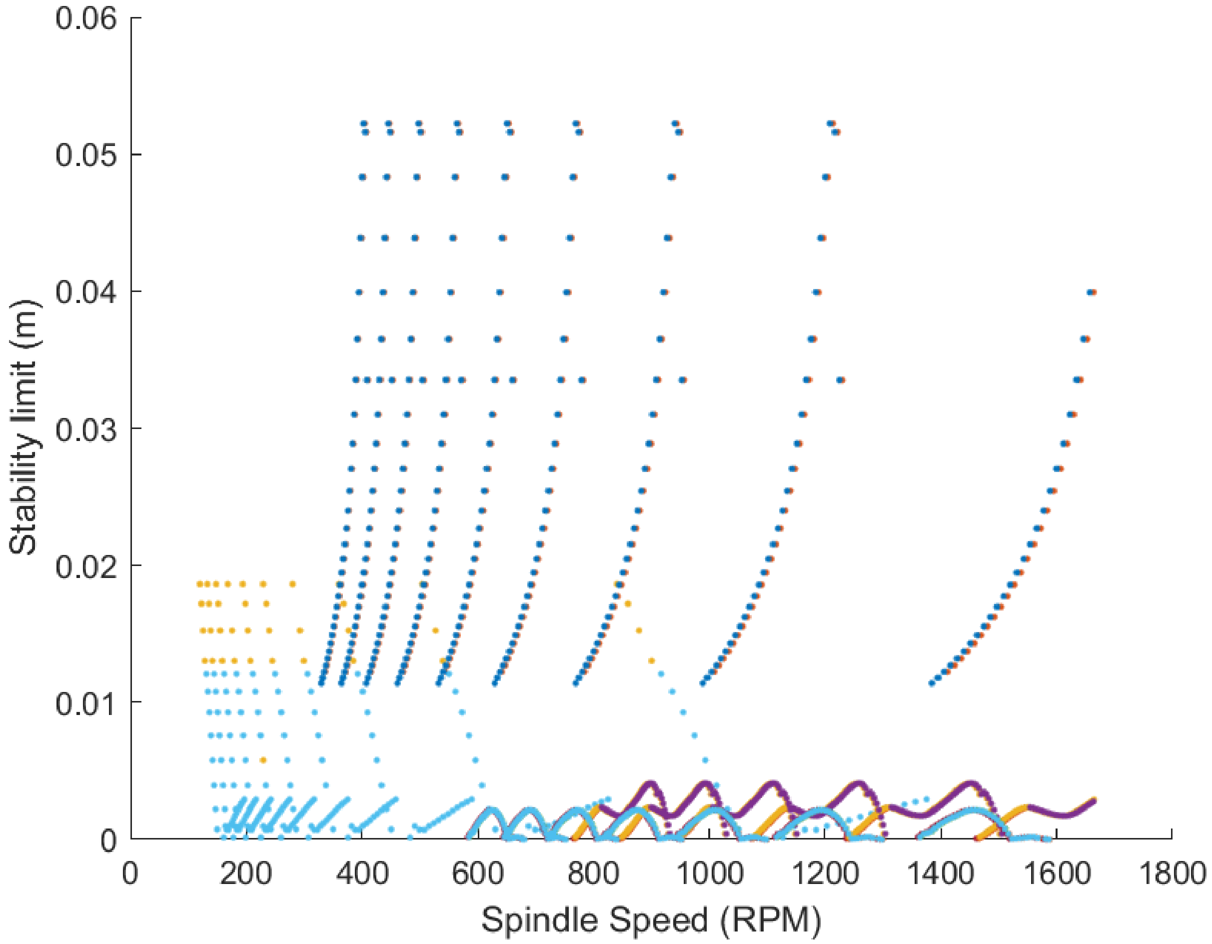

Figure 28: XY Stability lobes by negative FRF magnitude region.

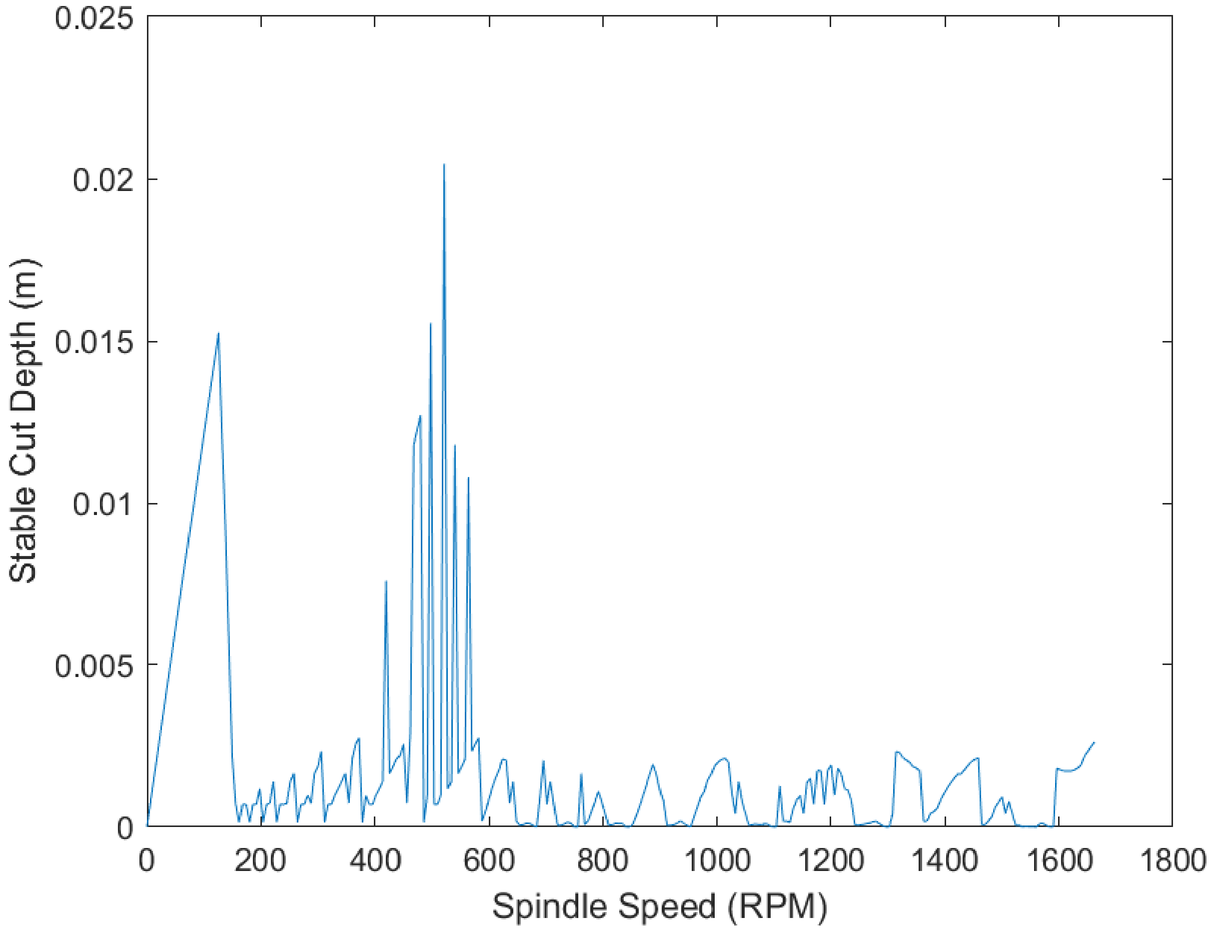

Figure 29: XY stability lobe composited into profile by filtering for minimum at each frequency.

Comparisons have been carried out by observing geometric similarities in both stability lobes, and comparing values, with bullet-pointed statements for any other observations that are either non-numerical or outside the comparable geometry. Graphs for each are included in Appendix K, with the following order:

- FRF Input.
- Cutpro Stability Lobes.
- Matlab Stability Lobes (Scatter of multiple modes and limits, as in Figure 28).
- Matlab Stability Lobes (Line plot of minimum limits for all modes at each speed, as in Figure 29).

Prominent stability peaks are tracked in Table 30, with the Matlab result given as a percentage of the Cutpro analogue.

FRF Configuration of measurement	Cutpro peak speed (RPM)	Cutpro peak stability limit (mm)	Matlab peak speed (RPM)	Matlab peak stability limit (mm)	**Matlab speed (as proportion of Cutpro value) (%)**	**Matlab stability limit (as proportion of Cutpro value) (%)**
Config. 1	259.108	0.2668	150	17.1264	**57.891**	**6419.190**
	679.283	0.197113	582	7.15799	**85.679**	**3631.414**
Config. 2	295.123	0.342378	126	15.2467	**42.694**	**4453.177**
	811.338	0.183911	522	20.4559	**64.3382**	**11122.717**
Config. 3	295.123	0.305383	132	13.8395	**44.727**	**4531.850**
	799.333	0.24464	510	22.806	**63.803**	**9322.269**
	none	None	1134	33.6097	**n/a**	**n/a**
	none	None	1590	35.7678	**n/a**	**n/a**
Config. 4	265.11	0.235321	162	23.3168	**61.107**	**9908.508**
	691.288	0.255449	618	35.1	**89.398**	**13740.512**

Figure 30: Comparison of Prominent Matlab and Cutpro Stability Peaks

From examining the output profiles of Cutpro and Matlab, the following observations are made:

- There are large differences in results, despite the same FRF data being used.
- Both sets of results show one cluster of stability peaks, followed by a low stability region, then a second high stability region, however the Matlab outputs give this stable region as a second cluster of peaks while the Cutpro output gives a single region.
- A 3rd and 4th stability peak were found in the Matlab output for configuration 3. This anomaly is observed, but no numerical comparison is performed as there is no analogous formation in the Cutpro output.
- By comparing the speeds at which the peaks of the stable regions occur, it is found that the Matlab predicted speed for the first stable region maximum is 44-57% of that predicted by Cutpro, suggesting the Matlab code is underestimating speeds.

- Comparing speeds for the peaks of the second stable region, the Matlab prediction is 63-90% of the Cutpro prediction, which is still an underestimate, but less so than for the first stable region.
- The stability lobes produced by the Matlab code are poorly scaled, returning stable cut depth values 100 times larger than those of the Cutpro output. Multiplying the results by 10^{-2} results in values of 45% to 138% proportion, which is a similar error level found in spindle speed. This is ascribed either to an error in unit conversion of the FRF (presented as m/N, compared with the average directional factors N/mm^2), or a flawed methodology used to composite the stability limits of multiple modes with multiple harmonics into a single lobe profile, which may incorrectly select for higher stabilities than are actually the case. Both of these components should be examined.

6 Suggestions for Future Research

Several potential next steps for this research will be outlined in the following sections. They have not been pursued beyond this outline due to time constraints.

6.1 Further Modelling

More detailed FEM modelling would be required to gather information to complete the model and reduce reliance on ratio scaling of simulated FRF:

- Conduct further CAD modelling of the robot for precise geometric measurements of the robot links.
  - Cross sectional area.
  - Polar moment of area.
  - Second moment of inertia.
- Conduct FEM modal analysis on CAD files of the tool to determine torsional axial FRF values (determine $FRF_{zz}, FRF_{z\theta}, FRF_{\theta z}, FRF_{\theta\theta}$) (see section 6.2).
- Conduct simulations using this information to generate 3-dimensional stability lobes and compare with measured FRF derived lobes to determine accuracy.

Huynh et al. presented a multi-body dynamics model with single degree of freedom joints to simulate an industrial machining robot, using rigid body model identification and experimental modal analysis [76]. They state they did not require a detailed model of link geometry, but that the SDOF representation can simulate the vibration modes accurately across postures [76]. They omitted the mode shape of deflections about the axis perpendicular to joint rotation, stating that these mode shapes vary by manipulator and posture [76]. For the 3DOF model, inertia tensors were obtained using CAD models, and tuned using rigid body model identification [76]. They stress joint stiffness and damping ratios are fitting parameters [76]. Identified elastic parameters were used to predict natural frequencies, damping ratios and mode shapes for other postures than those the model was built from [76]. These methods should be consulted to see if elements are preferable to the methodology discussed in this thesis.

6.2 Simulated FRF of Drilling Tool

Tool FRF profiles are required for the generation of drilling stability lobes but are not accounted for by the robot model considered in this research, particularly the torsional response, as measurement is more difficult than linear impact testing. For comprehensive testing of this modelling technique in hypothetical future research, the tool FRF should be included. If axial and torsional FRF data is already available for a given machine tool this could also be used. Building on previous work on modelling torsional axial response by Schmitz [77], Yang et al. have proposed a method by which the CAD file for a rotating machining tool can be analysed to predict frequency response under bending (x,y), axial (z) and torsional (θ) vibrations by modelling the tool as a series of Timoshenko beams [78] (described by Yokohama [79]) and considering the cross sectional geometry at intervals of the tool. They report from experimental validation that this process has an accuracy of within 5% [78].

Filiz and Ozdoganlar analysed the effectiveness of a 3D-ST (Spectral-Tchebychev) model for macro and micro drill dynamics, which provides both the bending and coupled torsional-axial modes of drills by use of the spectral-Tchebychev technique [80]. The model was compared with a measured FRF and solid element FE models. They judge the model to accurately predict frequencies and mode shapes for macro and micro drills [80].

6.3 Optimisation Stage

The 2D stability lobes (describing the relation of spindle speed with stable depth of cut [12] for a given robot configuration) generated from the dynamics of each configuration can be placed along an axis which represents configuration redundant angle, resulting in a 3-dimensional function [33], in this case with the following formula:

$$b_{\text{lim}} = f(n, \theta) \qquad [22]$$

Where n represents spindle speed and theta represents redundant angle. The search variant decision problem [81] for selecting the parameters with the largest stable depth of cut within the valid and unobstructed orientations of the end effector for a given task location (the definition of which is beyond the scope of this project), can be written as [82]:

$$\max\{f(n,\theta)\}$$

$$\text{Subject to } (n,\theta) \in S \subset R^2 \qquad [23]$$

The range of candidate speeds for the optimum solution are expected to be equal to the range of feasible spindle speeds for drilling (integer values of RPM), further bounded by the range of frequencies the dynamic model is able to capture. The range of candidate angles is limited by the robot axis resolution (described as 0.001° – 0.005° for the ABB IRB 6640 [83]). Candidate angles will also be limited by obstructions to the drilling process in restricted access spaces. This is expected to result in bands across the function where angles are unfeasible and therefore dynamic analysis is not required, resulting in no stable depth of cut. More realistically the angle increment number will be further limited by the computing time required for FRF simulation, limiting the resolution of the function along the angle axis. It should be mentioned that the function will not be interpolated.

Several optimisation methods have been considered and the decision of which to use will be made according to the volume and complexity of output data.

6.3.1 Enumeration Method

The optimisation method at this time is expected to use the enumeration method [81], specifically a comprehensive value comparison sweep along the two variable axes (n,θ) of the objective function using the Matlab “max” function. Firstly, a comparison of maxima amongst spindle speed for each angle spectrum, and then a comparison of the maxima between angles. Depending on the number of data points in the function, this approach could be computationally expensive. In this case, a particle swarm optimisation process would be added to the Matlab code.

6.3.2 Gradient Optimisation Algorithm

The use of a gradient optimisation algorithm [84] was considered, however as the global maximum is expected to be at a discrete point which can be input as a process parameter, rather than at a point on a continuous topology, it was rejected as unsuitable for this purpose.

6.3.3 Particle Swarm Optimisation

Particle swarm optimisation was selected as a further optimisation method for its simplicity and ease of application to the problem of locating maxima across a 2-dimensional path without having to compare all possible function outputs [82]. PSO is reported to be the most prevalent type of swarm intelligence-based optimisation algorithm [85]. Specifically, the Kennedy and Eberhart variation will be used ([86] cited by [82]) for its simplicity and compatibility with a discrete dataset.

During the simulation, multiple "particles" or cells are generated across the 2-dimensional matrix which describes the function at regular or randomised intervals, described by their two index values within the matrix. A simplified explanation of the PSO process is given below [82]:

For each iteration loop:

- If there is a positive difference between the largest value of the surrounding points and the current point, the particle moves a random number of cells in that direction, otherwise the particle remains in place.
- Each particle keeps track of its own maximum encountered value and the indices of its position, comparing it with each new value and adopting a larger value (and the corresponding index) if encountered.

When all particles have stopped changing their maximum value for a given number of consecutive loops, convergence is considered to be reached and the maximum amongst all logged cells (those being the local maxima) is taken as the global maximum.

7 Conclusions and Discussion

This project has found the following conclusions:

- From the case study information and further investigation, it was found that improved robotic drilling accuracy in restricted access drilling is linked to simpler and cheaper manufacturing of large aerospace components.
- A set of required tolerances and current state of technology have been recorded as references for the project moving forward.
- From experimental mini-projects and review of existing literature it was found that industrial robots do not usually possess the static or dynamic stiffness to carry out milling to aerospace tolerances without methods of compensation to improve the effective stiffness of the end effector.
- Several methods of optimising or augmenting the robot cell to improve machining accuracy have been explored and discussed.
- It was determined that machining cell optimisation is more versatile than machining cell augmentation in terms of application to existing serial robots.
- Limitations of optimisation compared with augmentation methods have been acknowledged. Additional methods have been identified in the event optimisation of the manipulator is insufficient to meet requirements.
- Examples were provided for how a robot arm may be simulated and how this then allows the robot's commands to be modified to mitigate compliance induced errors.
- The theoretical framework required for producing simulated robotic drilling stability lobes from complete robot and drilling parameters, has been collected.
- Simulations of robot dynamics and resulting frequency response functions have been carried out and compared with measured FRFs. While the static stiffness of the robot can be well predicted in some directions with the method used, other directions are less successful, and stiffness rotations should be revisited to fix the issue.
- Outputs of the Eigenproblem solving method used here included anomalous results that cannot be explained by the stiffness and mass inputs and result in

poor quality simulations of frequency response. This should be revisited to find a more accurate method of predicting natural frequencies and mode shapes.

- Even in the case where predicted static stiffness is close to agreement with previously measured values, natural frequencies are not accurately calculated, with overestimated frequencies and negative, imaginary terms occurring. The eigenproblem should be revisited.
- From evaluating the conversion of dynamic values to FRFs it is found that magnitude values of dominant modes are poorly predicted and orders of magnitude smaller than the expected response, while modal frequency prediction is more reliable compared with the damping and natural frequencies being input.
- Alongside simulating FRFs, the potential to process them into stability lobes within a Matlab environment has also been explored, with the goal of multiplexing the 2D stability lobes of the configuration range into 3D stability lobes describing all configurations. Some Matlab derived stable speeds (which are linked with frequencies), show similarity with Cutpro Stability Lobe outputs however the depth of cut at these speeds deviate strongly from the Cutpro prediction, and operations where units of FRF and average directional factors are converted should be audited for errors. The method of compositing the stability lobes of multiple modes together into one profile should also be reviewed.
- At the conclusion of the project, the presented method is not yet feasible for predicting the dynamic behaviour of a real robot with the accuracy required to predict stable cutting configurations for robotic drilling. There has been some success in prediction of static cartesian stiffness of the end effector in some directions, which is favourable, as it shows that the MSA method applied can simulate joint stiffness as dominant, even when higher stiffness links are included as part of the Kinematic chain (as opposed to the VJM method described, where these are omitted).
- While this program may become viable with further rewriting and troubleshooting, there is no time or funding remaining for this project to

implement those actions. The project should therefore not continue and be left to future work.

8 References

[1] E. J. A. Armarego and R. H. Brown, The Machining of Metals, Englewood Cliffs, New Jersey: Prentice-Hall, Inc., 1969.

[2] *BAE Systems Project Proposals,* 2020.

[3] S. Neculai-Eugen and C. Dragoş-Florin, "Dynamic Behaviour Study of the Drill Bush Guide Plates from the Fixtures Structure," *Applied Mechanics and Materials,* Vols. 809-810, no. 1662-7482, pp. 760-765, 2015.

[4] G. Gardiner, "One-shot dry drilling of stacked materials," *High Performance Composites,* vol. 22, no. 3, pp. 48-54, 2014.

[5] BSI Standards, "British Standards Online; Bibliographic Data; BS EN ISO 286-2:2010, ISO 286-2:1988," 2013 August 2013. [Online]. Available: https://bsol.bsigroup.com/Bibliographic/BibliographicInfoData/000000000030288633. [Accessed 27 04 2020].

[6] *BAE Systems Robotic PHD Final Project,* 2020.

[7] Kuka, "KMR iiwa," 2020. [Online]. Available: https://www.kuka.com/-/media/kuka-downloads/imported/9cb8e311bfd744b4b0eab25ca883f6d3/kuka_kmriiwa_en.pdf?rev=c6fb2cb7aa704b00a89124bf271dc17d. [Accessed 26 05 2020].

[8] E. Appleton and D. Williams, "Industrial robot applicatons," Halsted Press, New York, 1987.

[9] W. Ji and L. Wang, "Industrial Robotic Machining: A Review," *International Journal of Advanced Manufacturing Technology,* vol. 103, pp. 1239-1255, 2019.

[10] I. Iglesias, M. A. Sebastián and J. E. Ares, "Overview of the state of robotic machining: Current situation and future potential," *Procedia Engineering,* vol. 132, pp. 911-917, 2015.

[11] J. Padremenos, C. Doukas, P. Stavropoulos and G. Chryssolouris, "Machining With Robots: A Critical Review," in *7th International Conference on Digital Enterprise Technology*, Athens, Greece, 2011.

[12] Y. Altintas, Manufacturing automation: metal cutting mechanics, machine tool vibrations, and CNC design, New York: Cambridge university press, 2012.

[13] S. H. Kim, E. Nam, T. I. Ha, S.-H. Hwang, J. H. Lee, S.-H. Park and B.-K. Min, "Robotic Machining: A Review of Recent Progress," *International Journal of Precision Engineering and Manufacturing,* vol. 10, pp. 1629-1642, 2019.

[14] E. Ozturk and E. Budak, "Modelling of 5-Axis Milling Processes," *Machining Science and Technology,* vol. 11, no. 3, pp. 287-311, 2007.

[15] Y. Chen and F. Dong, “Robot Machining: recent development and future research issues,” *International Journal of Advanced Manufacturing Technology,* vol. 66, no. 9-12, pp. 1489-1497, 2012.

[16] A. Verl, A. Valente, S. Melkote, C. Brecher, E. Ozturk and L. T. Tunc, “Robots in machining,” *CIRP Annals - Manufacturing Technology,* vol. 68, pp. 799-822, 2019.

[17] T. Bo, Z. XingWei and D. Han, “Mobile-Robotic machining for large complex components: A review study,” *Science China Technological Sciences,* vol. 62, no. 8, pp. 1388-1400, 2019.

[18] A. Grau, M. Indri, L. L. Bello and T. Sauter, “Industrial Robotics in Factory Automation: from the Early Stage to the Internet of Things,” in *Proceedings IECON 2017 - 43rd Annual Conference of the IEEE Industrial Electronics Society*, Beijing, China, 2017.

[19] J. DePree and C. Gesswein, “Robotic Machining White Paper Project,” 31 10 2008. [Online]. Available: https://www.robotics.org/robotics/halcyon-development-ria. [Accessed 12 11 2018].

[20] H. Celikag, N. D. Sims and E. Ozturk, “Cartesian Stiffness Optimization for Serial Arm Robots,” *Procedia CIRP 77 (2018) 566-569,* vol. 77, pp. 566-569, 2018.

[21] A. Klimchik, A. Ambiehl, S. Garnier, B. Furet and A. Pashkevich, “Efficiency evaluation of robots in machining applications using industrial performance measure,” *Robotics and Computer–Integrated Manufacturing,* vol. 48, no. October 2015, pp. 12-29, 2017.

[22] H. N. Huynh, O. Verlinden and E. Riviere-Lorphevre, “Robotic Machining Simulation Using a Simplified Multibody Model,” in *Annals of DAAAM and Proceedings of the International DAAAM Symposium*, Vienna, Austria, 2017.

[23] C. Dumas, S. Caro, C. Mehdi, S. Garnier and B. Furet, “Joint Stiffness Identification of Industrial Serial Robots,” Robotica, Cambridge University Press, 2011.

[24] M. Cordes, W. Hintze and Y. Altintas, “Chatter Stability in Robotic Milling,” *Robotics and Computer Integrated Manufacturing,* vol. 55, no. February 2018, pp. 11-18, 2018.

[25] H. Celikag, E. Ozturk and N. D. Sims, “Can mode coupling chatter happen in milling?,” *International Journal of Machine Tools and Manufacture,* vol. 165, no. 103738, 2021.

[26] A. Klimchik, D. Bondarenko, A. Pashkevich, S. Briot and B. Furet, “Compliance error compensation in robotic-based milling,” Nantes, France.

[27] M. Gautier, A. Janot and P. O. Vandanjon, “A New Closed-Loop Output Error Method for Parameter Identification of Robot Dynamics,” *IEEE Transactions on Control Systems Technology,* vol. 21, no. 2, pp. 428 - 444, 2013.

[28] H. Huynh, H. Assadi, V. Dambly, E. Rivière-Lorphèvre and O. and Verlinden, “Direct method for updating flexible multibody systems applied to a milling robot,” *Robotics and Computer Integrated Manufacturing,* vol. 68, p. 102049, 2021.

[29] H. N. Huynh, E. Rivi`ere-Lorph`evre, F. Ducobu, A. Ozcan and O. Verlinden, “Dystamill: a framework dedicated to the dynamic simulation of milling,” *The International Journal of Advanced Manufacturing Technology,* vol. 98, p. 2109–2126, 2018.

[30] K. Burn, E. Robinson and D. Dixon, “Introducing fundamental concepts of control: A case study in robot force control,” *International Journal of Mechanical Engineering Education.,* vol. 24, no. 4, pp. 320-339, 2014.

[31] C. Chen, F. Peng, R. Yan, Y. Li, D. Wei, Z. Fan, X. Tang and Z. Zhu, “Stiffness performance index based posture and feed orientation optimization in robotic milling process,” *Robotics and Computer Integrated Manufacturing,* vol. 55, pp. 29-40, 2019.

[32] L. F. F. Furtado, E. Villani, L. G. Trabasso and R. Suterio, “A method to improve the use of 6-dof robots as machine tools,” *International Journal of Advanced Manufacturing Technology,* vol. 92, no. 5-8, pp. 2487-2502, 2017.

[33] S. Mousavi, V. Gagnol, B. C. Bouzgarrou and P. Ray, “Stability optimization in robotic milling through the control of functional redundancies,” *Robotics and Computer–Integrated Manufacturing,* vol. 50, no. July, pp. 181-192, 2017.

[34] L. T. Tunc and J. Shaw, “Investigation of the effects of Stewart platform-type industrial,” *International Journal of Advanced Manufacturing Techology,* vol. 87, pp. 189-199, 2016.

[35] L. T. Tunc and J. Shaw, “Experimental study on investigation of dynamics of hexapod robot for mobile machining,” *International Journal of Advanced Manufacturing Technology,* vol. 84, pp. 817-830, 2016.

[36] U. Schneider, M. Drust, M. Ansaloni, C. Lehmann, M. Pellicciari, F. Leali, J. Gunnink and A. Verl, “Improving robotic machining accuracy through experimental error investigation and modular compensation,” *The International Journal of Advanced Manufacturing Technology,* vol. 85, no. 1-4, pp. 3-15, 2014.

[37] C. Y. Lai, V. Chavez, D. Ernesto and S. Ding, “Transformable parallel-serial manipulator for robotic machining,” *International Journal of Advanced Manufacturing Technology,* vol. 97, no. 5-8, pp. 2987-2996, 2018.

[38] L. Yuan, S. Sun, Z. Pan, D. Ding, O. Gienke and W. Li., “Mode coupling chatter suppression for robotic machining using semi-active magnetorheological elastomers absorber,” *Mechanical Systems and Signal Processing,* vol. 117, pp. 221-237, 2019.

[39] Y. Guo, H. Dong, G. Wang and Y. Ke, “Vibration analysis and supression in robotic boring process,” *International Journal of Machine Tools and Manufacture,* vol. 101, pp. 102-110, 2016.

[40] M. G. Her and H. Kazerooni, “Automated Robotic Deburring of Parts Using Compliance Control,” *Journal of Dynamic Systems, Measurement and Control,* vol. 113, no. March, pp. 60-66, 1991.

[41] Z. Wang and P. Keogh, “Active Vibration Control for Robotic Machining,” in *Proceedings of the ASME 2017 International Mechanical Engineering Congress and Exposition*, Tampa, Florida, USA, 2017.

[42] S. Engin and Y. Altintas, “Mechanics and dynamics of general milling cutters. Part I: helical end mills,” *International Journal of Machine Tools & Manufacture,* vol. 41, p. 2195–2212, 2001.

[43] Y. Altintas, J. Yang and Z. M. Kilic, “Virtual prediction and constraint of contour errors induced by cutting force disturbances on multiaxis CNC machine tools,” *CIRP Annals - Manufacturing Technology,* vol. 68, pp. 377-380, 2019.

[44] B. Marguet, F. Wiegert, O. Lebahar, B. Bretagnol, F. Okcu and E. Ingvar, “Advanced Portable Hole Drilling,” *SAE Transactions, Section 1: JOURNAL OF AEROSPACE (2007),* vol. 116, pp. 897-903, 2007.

[45] S. A. Voronov, A. M. Gouskov, A. S. Kvashnin, E. A. Butcher and S. C. Sinha, “Influence of Torsional Motion on the Axial Vibrations of a Drilling Tool,” *Transactions of the ASME,* vol. 2, no. January, pp. 58-64, 2007.

[46] W. Polini and A. Corrado, “A kinematic approach for error modelling in drilling,” *Engineering Computations,* vol. 36, no. 4, pp. 1364-1383, 2019.

[47] A. Jiménez, M. Arizmendi and W. E. Cumbicus, “Model for the prediction of whirling vibrations in drilling processesthrough semi-discretization of the drill motion equation,” *International Journal of Advanced Manufacturing Technology,* pp. 2831-2855, 2019.

[48] A. Hohl, M. Tergeist, H. Oueslati, J. R. Jain, C. Herbig, G.-P. Ostermeyer and H. Reckmann, “Derivation and experimental validation of an analytical criterion for the identification of self-excited modes in drilling systems,” *Journal of Sound and Vibration,* vol. 342, pp. 290-302, 2015.

[49] P. V. Bayly, M. T. Lamar and S. G. Calvert, “Low-Frequency Regenerative Vibration and the Formation of Lobed Holes in Drilling,” *Journal of Manufacturing Science and Engineering,* vol. 124, no. May 2002, pp. 275-285, 2002.

[50] K. Ahmadi and Y. Altintas, “Stability of lateral, torsional and axial vibrations in drilling,” *International Journal of Machine Tools and Manufacture,* vol. 68, pp. 63-74, 2013.

[51] S. Ema, H. Fujii and E. Marui, “Whirling Vibration in Drilling; Vibration Analysis in Drilling Workpiece with a Pilot Hole.,” *Journal of Engineering for Industry,* vol. 110, pp. 315-321, 1988.

[52] M. Wan, Z. M. Kilic and Y. Altintas, “Mechanics and Dynamics of Multifunctional Tools,” *Journal of Manufacturing Science and Engineering,* vol. 137, no. 011019, pp. 1-10, 2015.

[53] Z. M. Kilic and Y. Altintas, “Generalized mechanics and dynamics of metal cutting operations for unified simulations,” *International Journal of Machine Tools and Manufacture,* vol. 104, pp. 1-13, 2016.

[54] S. Bi and J. Liang, “Robotic drilling system for titanium structures,” vol. 54, pp. 767-774, 2011.

[55] J. Zhang, W. Liao, Y. Bu, W. Tian and J. Hu, “Stiffness properties analysis and enhancement in robotic drilling application,” *International Journal of Advanced Manufacturing Technology,* 2020.

[56] N. Shen, Z. Guo, J. Li, L. Tong and K. Zhu, “A practical method of improving hole position accuracy in the robotic drilling process,” *The International Journal of Advanced Manufacturing Technology,* vol. 96, pp. 2973-2987, 2018.

[57] D. Busson, R. Bearee and A. Olabi, “Task-oriented rigidity optimization for 7 DOF redundant manipulators,” *International Federation of Automatic Control,* vol. 50, no. 1, pp. 14588-14593, 2017.

[58] A. Klimchik, D. Chablat and A. Pashkevich, “Stiffness modeling for perfect and non-perfect parallelmanipulators under internal and external loadings,” *Mechanism and Machine Theory,* vol. 79, pp. 1-28, 2014.

[59] J. E. Akin, Finite Element Analysis with Error Estimators, Burlington,MA: Elsevier Butterworth Heinemann, 2005.

[60] A. Klimchik, A. Pashkevich and D. Chablat, “CAD-based approach for identification of elasto-static parameters of robotic manipulators,” *Finite Elements in Analysis and Design,* vol. 75, pp. 19-30, 2011.

[61] G. D. L. Soares J´unior, J. M. Carvalho and R. S. Gonc¸alves, “Stiffness analysis of multibody systems using matrix structural analysis—MSA,” *Robotica,* vol. 34, pp. 2368-2385, 2016.

[62] A. Klimchik, A. Pashkevich and D. Chablat, “Fundamentals of manipulator stiffness modeling using matrix structural analysis,” *Mechanism and Machine Theory,* vol. 133, pp. 365-394, 2018.

[63] Y. Guo, H. Dong and Y. Ke, “Robotics and Computer-Integrated Manufacturing Stiffness-oriented posture optimization in robotic machining applications,” *Robotics and Computer Integrated Manufacturing,* vol. 35, pp. 69-76, 2015.

[64] H. Celikag, *On the dynamics of robotic machining,* Sheffield: University of Sheffield, 2020.

[65] J. Denavit and R. S. Hartenberg, “A kinematic notation for lower-pair mechanism based on matrices,” *Trans. ASME Journal of App1ied Mechanics,* vol. 22, pp. 215-221, 1955.

[66] S. Baglioni, F. Cianetti, C. Braccesi and D. M. D. Micheli, “Multibody modelling of N DOF robot arm assigned to milling manufacturing. Dynamic analysis and position

errors evaluation," *Journal of Mechanical Science and Technology,* vol. 30, no. 1, pp. 405-420, 2015.

[67] P. Corke, Robotics, Vision and Control, Berlin Heidelberg: Springer Tracts in Advanced Robotics, 2013.

[68] ABB, "IRB 6640 CAD Models.," [Online]. Available: https://new.abb.com/products/robotics/industrial-robots/irb-6640/irb-6640-cad.

[69] ABB, "ABB/Products/Robotics/Industrial-Robots/IRB 6640/IRB 6640 CAD," 09 2007. [Online]. Available: https://library.e.abb.com/public/1f1bf834a16985d5c12573670031be29/IRB%206640%20External%20%20Product%20presentation.pdf. [Accessed 24 02 2022].

[70] S. Mousavi, V. Gagnol and P. R. e. al., "Dynamic behaviour model of a machining robot Dynamic behaviour model of a machining robot," in *ECCOMAS Multibody Dynamics 2013*, Zagreb, Croatia, 2013.

[71] J. C. Roukema and Y. Altintas, "Generalized modeling of drilling vibrations. Part II: Chatter stability in frequency domain," *International Journal of Machine Tools and Manufacture,* vol. 47, pp. 1474-1485, 2007.

[72] J. C. Roukema, *Mechanics and Dynamics of Drilling,* The University of British Columbia, 2006.

[73] J. He and Z.-F. Fu, Modal Analysis, Oxford; Boston: Butterworth-Heinemann, 2001.

[74] L. Berglind and E. Ozturk, "Chapter 4; Modelling of Machining Processes," in *Twin-Control; A Digital Twin Approach to Improve Machine Tools Lifecycle*, Cham, Switzerland, Springer Nature Switzerland AG, 2019, pp. 57-93.

[75] S. Mejri, V. Gagnol, T.-p. L. Laurent, P. Ray and P. Paultre, "Dynamic characterization of machining robot and stability analysis," *International Journal of Advanced Manufacturing Technology,* vol. 82, pp. 351-359, 2016.

[76] H. N. Huynh, H. Assadi, E. Riviere-Lorphevre and O. Verlinden, "Modelling the dynamics of industrial robots for milling operations," *Robotics and Computer Integrated Manufacturing,* vol. 61, no. 101852, pp. 1-16, 2020.

[77] T. L. Schmitz, "Predicting High-Speed Machining Dynamics by Substructure Analysis," *National Institute of Standards and Technology, Automated Production Technology Division,* vol. 49, pp. 303-308, 2000.

[78] Y. Yang, W.-H. Zhang, Y.-C. Ma and M. Wan, "Generalized method for the analysis of bending, torsional and axial receptances of tool–holder–spindle assembly," *International Journal of Machine Tools & Manufacture,* vol. 99, p. 48–67, 2015.

[79] T. Yokoyama, "Vibrations of a hanging timoshenko beam under gravity," *Journal of Sound and Vibration,* vol. 141, no. 2, pp. 245-258, 1990.

[80] S. Filiz and O. B. Ozdoganlar, "A Model for Bending, Torsional, Axial Vibrations of Micro- and Macro-Drills, Including Actual Drill Geometry - Part II: Model Validation and Application," *Transactions of the ASME,* vol. 132, no. 041018, pp. 1-10, 2010.

[81] H. H. Hoos and T. Stutzle, Stochastic Local Search, San Francico: Morgan Kaufmann Publishers, 2005.

[82] J. Sun, C.-H. Lai and X.-J. Wu, Particle Swarm Optimisation: Classical and Quantum Perspectives, London: CRC Press, Taylor and Francis Group, 2012.

[83] ABB, "Product Specification: IRB 6640," 2020. [Online]. Available: https://library.e.abb.com/public/1c8cd7d860ec46f7b4254c03dd238dd8/3HAC028284%20PS%20IRB%206640-en.pdf. [Accessed 26 02 2021].

[84] H. B. Curry, "The Method of Steepest Descent for Non-Linear Minimization Problems," *Quarterly of Applied Mathematics,* vol. 2, no. 3, pp. 258-261, 1944.

[85] Y. Zhang, S. Wang and G. Ji, "A Comprehensive Survey on Particle Swarm Optimization Algorithm and Its Applications," *Mathematical Problems in Engineering,* vol. 2015, 2015.

[86] J. Kennedy and R. Eberhart, "Particle Swarm Optimization," in *Proceedings of the IEEE International Conference on Neural Networks*, Piscataway, NJ, 1995.

[87] S. Ramanjaneyulu, D. K. N. S. Suman, S. P. Kumar and V. S. Babu, "Design and Development of Graphine reinforced Acetal copolymer plastic gears and its performance evaluation," in *Materials Today: Proceedings 4*, 2017.

[88] L. Urena, E. Ozturk and N. Sims, "Convergence Analysis of the Multi-Frequency Approach around aVariable-Helix Instability Island," in *17th CIRP Conference on Modelling of Machining Operations*, Sheffield, 2019.

[89] K. S. S. Tony L Schmitz, "Updated Force Model," in *Machining Dynamics; Frequency Response to Improved Productivity*, New York, Springer Science+Business Media LLC, 2009, p. 161.

[90] A. J. L. George A. F. Seber, *Linear Regression Analysis,* Aukland, New Zealand: John Wiley and Sons, 2003.

[91] Sandvik Coromant, "316-16FL642-16005L 1745," [Online]. Available: https://www.sandvik.coromant.com/en-gb/products/pages/productdetails.aspx?c=316-16FL642-16005L%20%201745. [Accessed 01 01 2020].

[92] Sandvik Coromant, "EH16-A16-SH-130," [Online]. Available: https://www.sandvik.coromant.com/en-gb/products/Pages/productdetails.aspx?c=EH16-A16-SH-130. [Accessed 01 01 2020].

[93] Sanvik Coromant, "392.41014-63 40 120B," [Online]. Available: https://www.sandvik.coromant.com/en-

gb/products/Pages/productdetails.aspx?c=392.41014-63%2040%20120B. [Accessed 01 01 2020].

[94] O. Ozkrimli, *FlatEnd_MechanisticCFC_160212.xls,* Sheffield: Advanced Manufacturing Research Centre, 2014.

[95] E. Budak, Y. Altintas and E. J. A. Armarego, “Prediction of Milling Force Coefficients From Orthogonal Cutting Data,” *Transactionsof the ASME,* Vols. 118, May, p. 216, 1996.

[96] M. Nouari and H. Makich, “On the Physics of Machining Titanium Alloys: Interactions,” *metals,* vol. 4, pp. 335-358, 2014.

[97] B. Wu, Z. Pan, D. Ding, D. Cuiuri, H. Li, J. Xu and J. Norrish, “A review of the wire arc additive manufacturing of metals: properties, defects and quality improvement,” *Journal of Manufacturing Processes,* vol. 35, pp. 127-139, 2018.

[98] M. Wang, L. Gao and Y. Zheng, “An examination of the fundamental mechanics of cutting force coefficients,” *International Journal of Machine Tools and Manufacture,* vol. 78, pp. 1-7, 2014.

[99] K. McMullen, “Mini-Project 2: Experimental Report - Machinability of Plastic Workpiece with Robotic Machining Cell,” Sheffield, 2019.

[100] C. M. Taylor, S. G. A. Hernandez, M. Marshall and M. Broderick, “Cutting fluid application for titanium alloys Ti-6Al-4V and Ti-10V-2Fe-3Al in a finish turning process,” in *8th CIRP Conference on High Performance Cutting (HPC 2018)*, 2018.

[101] GrégoirePeigne, HenriParis, DanielBrissaud and A. Gouskov, “Impact of the cutting dynamics of small radial immersion milling operations on machined surface roughness,” *International Journal of Machine Tools and Manufacture,* vol. 44, no. 11, pp. 1133-1142, 2004.

[102] O. Ozkrimli, *FlatEnd_MechanisticCFC_160212,* Sheffield: AMRC with Boeing, 2014.

[103] Timetal, “IMETAL®6-4, 6-4 ELI & 6-4-.1RU,” 2000. [Online]. Available: https://www.timet.com/assets/local/documents/datasheets/alphaandbetaalloys/6-4.pdf. [Accessed 07 01 2020].

[104] X. Shi, S. Ma, C. Liu, Q. Wu, J. Lu, Y. Liu and W. Shi, “Selective laser melting-wire arc additive manufacturing hybrid fabrication of Ti-6Al-4V alloy: Microstructure and mechanical properties,” *Materials Science and Engineering: A,* vol. 684, pp. 196-204, 2017.

9 Appendix A

Mini-Project 2: Robotic Milling Cutting Force Coefficient Capture

This section will describe the theoretical background and application of an experimental process and subsequent data processing method to produce the cutting force coefficients of a robotic milling process, with data presented and discussed.

9.1 Introduction

The goal of this experiment is to yield cutting force coefficients from analysis of cutting force data acquired from variations of a cutting operation to which are applicable to that operation. The workpiece is composed of Acetal copolymer. The operation to be carried out is slot milling using an end mill tool, rotated by a spindle mounted to the end effector of an ABB serial robot (Model number ABB IRB 6640, located in the KTC building of the Advanced Manufacturing Research Centre, Sheffield). Experiment parameters are provided in Section 9.5.1. This experiment is based largely on a previous investigation into stability in robotic milling by Huseyin Celikag, who provided invaluable support in the planning and preparation for this experiment.

Acetal Copolymer was selected for use in the experiment due to availability and preference for previous experiments. Ramananeyulu et al describe Acetyl resins as "among the strongest and stiffest of all thermoplastics, and are characterized by good fatigue life, low moisture sensitivity, high resistance to solvents and chemicals, and good electrical properties [87]." Acetal is also described as competitive for the same applications as nylon [87].

Previous experimentation on milling with the Acetal copolymer material at a cutting speed of 78.41m/min assumed the following cutting constant values ($K_{tc} = 142.2\ N/mm^2$, $K_{rc} = 18.9\ N/mm^2$, which may be taken as a guideline for validation of the results of this experimentation [88]. The robotic milling operation was reported by Celikag to produce discontinuous chips at and above the minimum depths of cut achievable with the IRB6640, which it is observed may introduce inaccuracies to the mechanistic modelling of cutting forces, which would be incorporated into the cutting force coefficients being identified [64].

A plate dynamometer will be used for force measurement, with additional data provided by a microphone. The cutting trajectories have been programmed to make good use of existing work pieces.

9.2 Theoretical Basis

9.2.1 Cutting Coefficients and Slotting

During a slotting procedure, the tool movement occurs in a feed direction, with the tool edge engaging at a point close to tangent parallel with feed direction and disengaging at another point roughly on the opposite side of the tool circumference from the point of engagement [12].

Forces on a milling tool may be measured in directions tangential, radial and axial to the cutting edge as the tool rotates [12]. One or more of these may be described as “flow” to indicate the direction aligned with tool motion and chip removal. Cutting coefficients (K_{tc}, K_{rc} and K_{ac}) are proportionate to change in cutting force on the cutting edge with change in feed per tooth, as feed per tooth determines nominal chip thickness, and chip thickness determines the cross-sectional area of the chip [12].

K_{ac} coefficients are derived from change in axial force on the tool with increasing feed per tooth [12]. It is expected to be low as ideally the cutting edge would not move in the axial direction during the identification process, however, material is pushed upward from the workpiece during cutting by the tool rake face, with some shearing taking place, therefore some axial force is expected.

Edge constants (K_{te}, K_{re} and K_{ae}) represent the forces on the 1 dimensional length of the cutting edge which do not contribute to material shearing [12] and are derived mathematically from regression analysis of the forces which would occur in a hypothetical cutting process with zero feed per tooth, estimated from the intercepts of lines of best fit estimating the relationships between cutting forces and feed per tooth. Cutting forces are assumed to be directly proportional to chip thickness and axial depth, independent of other factors [89], therefore linear relationships are expected between feed per tooth and cutting force.

CFCs are derived by removing the effect of most of the cutting parameters from the average measured cutting forces to give generalised constants which can then be reapplied to varied cutting parameters for force prediction. The mathematical process which achieves this is described in the next section.

9.3 Derivation of Average Force to CFC Equation

The data acquired during this experiment will be manipulated using the mechanistic cutting force coefficient identification method [12] (Equations 1-22).

The generalised formula for the average force on an engaged cutting edge is equal to the integral of the instantaneous force in a given direction at each angle the tool is immersed in the material, with respect to the angle over which the force is applied, divided by the pitch angle where more than one tooth is used [12].

$$\bar{F}_q = \frac{1}{\varphi_p}\int_{\varphi_{st}}^{\varphi_{ex}} F_q(\varphi)d\varphi \qquad [24]$$

The cutting force at a particular time is dependent on the instantaneous depth of cut (h), the cutting constants, and some forces which are frictional in nature, these are called edge constants [12].

$$dF_{t,j}(\varphi, z) = [K_{tc}h_j\left(\varphi_j(z)\right) + K_{te}]dz \qquad [25]$$

$$dF_{r,j}(\varphi, z) = [K_{rc}h_j\left(\varphi_j(z)\right) + K_{re}]dz \qquad [26]$$

$$dF_{a,j}(\varphi, z) = [K_{ac}h_j\left(\varphi_j(z)\right) + K_{ae}]dz \qquad [27]$$

When converting from the cutting edge coordinate system to the tool axis coordinate system, the following formulae describing the trigonometric relationship is used:

$$dF_{x,j}\left(\varphi_j(z)\right) = -dF_{t,j}cos\left(\varphi_j(z)\right) - dF_{r,j}\sin\left(\varphi_j(z)\right) \qquad [28]$$

$$dF_{y,j}\left(\varphi_j(z)\right) = +dF_{t,j}cos\left(\varphi_j(z)\right) - dF_{r,j}\sin\left(\varphi_j(z)\right) \qquad [29]$$

$$dF_{z,j}\left(\varphi_j(z)\right) = dF_{a,j} \qquad [30]$$

Chip thickness increases, reaches a maximum (c) and then decreases during the immersion phase of π radians, as a sinusoid profile does. Substitute $c\ sin(\varphi)$ for h.

Substitute cutting force coefficient and chip thickness for tool edge coordinate system into the equation for Cartesian forces about tool axis.

$$dF_{x,j}\left(\varphi_j(z)\right) = -[K_{tc}c\ sin\left(\varphi_j(z)\right) + K_{te}]cos\left(\varphi_j(z)\right) - [K_{rc}c\ sin\left(\varphi_j(z)\right) + K_{re}]\sin\ (\varphi_j(z))dz$$

[31]

$$dF_{y,j}\left(\varphi_j(z)\right) = [K_{tc}c\ sin\left(\varphi_j(z)\right) + K_{te}]cos\left(\varphi_j(z)\right) - [K_{rc}c\ sin\left(\varphi_j(z)\right) + K_{re}]\sin\ (\varphi_j(z))dz$$

[32]

$$dF_{z,j}\left(\varphi_j(z)\right) = \left[K_{ac}h_j\left(\varphi_j(z)\right) + K_{ae}\right]dz$$

[33]

Simplifying down to give formulae which relate unit force to unit depth, cutting force coefficients and chip thickness.

$$dF_x = \{\frac{c}{2}\left[-K_{tc}\sin\ (2\varphi_j(z)) - K_{rc}\left[1 - \sin\ (2\varphi_j(z))\right]\right] + \left[-K_{te}\cos\left(\varphi_j(z)\right) - K_{re}sin(\varphi_j(z))\right]\Big\}dz$$

[34]

$$dF_y = \{\frac{c}{2}\left[-[K_{tc}cos2\varphi_j(z) - K_{rc}\left[1 - \sin\ (2\varphi_j(z))\right]\right] + \left[-K_{te}\sin\left(\varphi_j(z)\right) - K_{re}\cos\ (\varphi_j(z))\right]\Big\}dz$$

[35]

$$dF_{z,j}(\varphi, z) = [K_{ac}csin(\varphi_j(z)) + K_{ae}]dz$$

[36]

Integrating with respect to axial tool immersion (cut depth “a”) and factoring in the cutting parameters (Feed per tooth “c”) and flute number (“N”), yields a generalised equation connecting average force in a given direction to cutting coefficients with edge immersion conditions as boundaries. The following term definitions apply [12]:

$$\bar{F}_x = \left\{\left[\frac{Nac}{8\pi}[K_{tc}cos2\varphi - K_{rc}[2\varphi - sin2\varphi]\right] + \frac{Na}{2\pi}[-K_{re}sin\varphi + K_{re}cos\varphi]\right\}_{\varphi_{st}}^{\varphi_{ex}}$$

[37]

$$\bar{F}_y = \left\{\frac{Nac}{8\pi}\left[K_{tc}cos2\varphi - K_{rc}[2\varphi - sin2\varphi]\right] + \frac{Na}{2\pi}[-K_{re}sin\varphi + K_{re}cos\varphi]\right\}_{\varphi_{st}}^{\varphi_{ex}}$$

[38]

$$\bar{F}_z = \left\{\left[\frac{Na}{2\pi}\left[-K_{ae}sin\varphi + K_{ae}cos\varphi\right]\right]\right\}_{\varphi_{st}}^{\varphi_{ex}} \qquad [39]$$

Slotting is also referred to as full immersion milling, as the tool edge is immersed for the maximum angle possible while the tool is moving in a particular radial direction (between the angles of 0 and π). Under these conditions, the above formulae simplify to the following:

$$\bar{F}_x = -\frac{Na}{4}K_{rc}c - \frac{Na}{\pi}K_{re} \qquad [40]$$

$$\bar{F}_y = +\frac{Na}{4}K_{tc}c + \frac{Na}{\pi}K_{te} \qquad [41]$$

$$\bar{F}_z = +\frac{Na}{\pi}K_{ac}c + \frac{Na}{2}K_{ae} \qquad [42]$$

For slotting, cutting coefficients can be derived from the slopes (denoted by $\bar{F}_{qc}$) of the trend-lines estimating the relationship between feed per tooth and average cutting force in a Cartesian direction. Edge constants can be derived by the intercepts (denoted by $\bar{F}_{qe}$) of the trend-lines.

$$K_{tc} = \frac{4\bar{F}_{yc}}{Na}, \qquad K_{te} = \frac{\pi\bar{F}_{ye}}{Na} \qquad [43]$$

$$K_{rc} = -\frac{4\bar{F}_{xc}}{Na}, \qquad K_{re} = -\frac{\pi\bar{F}_{xe}}{Na} \qquad [44]$$

$$K_{ac} = \frac{\pi\bar{F}_{zc}}{Na}, \qquad K_{ae} = \frac{2\bar{F}_{ze}}{Na} \qquad [45]$$

These average forces can be processed using regression analysis with software as simple as a spreadsheet. The following section will detail the experimental process used to capture force data in this instance.

9.4 Regression Analysis Theory

Regression Analysis is a form of statistical modelling used “to construct mathematical models which describe or explain relationships that may exist between two variables [90].” It may be performed “to estimate the unknown constants, under the assumption of a valid model, and then use the model for prediction purposes [90],” and is therefore appropriate for identifying cutting force coefficients, which are assumed to fit a linear model. Linear regression analysis will be used to estimate coefficients based on Equations 17-19.

9.5 Methodology

9.5.1 Experimental Parameters

Cutting force coefficients are derived by performing a cutting operation using a range of different feed per tooth values, and then performing regression analysis on the average forces measured during cutting. A standard of four feed per tooth values was selected for input into regression analysis as four values was believed to be the absolute minimum number of data points needed to quickly infer whether a relationship is linear or non-linear.

No. of Flutes	6
Tool Helix angle (degrees)	42
Cut depth (mm)	2
Feed/tooth (mm)	0.5, 0.1, 0.15, 0.2
Spindle Speeds (RPM)	180, 230, 280, 330 (Low Range) 4800, 5400, 6000, 6600 (High Range)

Table 18: Cutting Parameters

Spindle speeds were selected to allow for comparison with previous experimentation on this material with the ABB6640 robotic machining cell. Lower spindle speeds were unchanged so that compatibility with other experiments could be judged. Higher spindle speeds were doubled to explore the effects of higher spindle speeds on the performance of this machining cell.

For this experiment, all cuts were performed with the following arrangement of equipment (Table 19):

Machine	ABB6640 Serial Robotic Manipulator with spindle mounted to end-effector.
Tool	End-Mill (316-16FL642-16005L 1745) (Sandvik Coromant) [91], compatible shank (EH16-A16-SH-130) (Sandvik Coromant) [92]
Back End	392.41014-63 40 120B (Sandvik Coromant) [93]
Collet	ER40, 16mm internal radius
Tool Length (gauge length, including tool holder)	229.373mm
Tool Radius (measured by optical tool setter, before installation to robot)	7.968-7.980mm
Maximum Tool Runout	12 μm
Tool Overhang/ Stick-out	112.82mm

Table 19: Equipment Specifications

Cutting trajectories were programmed using the ABB software package RobotStudio. Diagrams of these trajectories can be found in in Appendix D.

9.5.2 Experimental Process

This section will list and discuss the actions taken to perform the experiment.

Figure 31: End mill, shank and tool-holder installed into spindle.

- The tool assembly was built and installed into the robot spindle (see Figure 31).
- Dynamometer kit hardware and software were set up and initialised.
- A work object coordinate system was defined by the 3-point user definition method with a small plastic piece to protect the workpiece and dynamometer from damage.
- Using impact hammers and a laser vibrometer for impact testing (see Figure 32), a total of 32 frequency response functions were measured at the tool tip in the following variations:
  - 4 positions at the most extreme X and Y coordinates of the tool during planned trajectories.
  - Impacts applied both perpendicular and parallel to measuring direction.
  - Measurement in X and Y directions.
  - Measurement in high (100-1000Hz) (Sampling rate: 51200Hz resolution 0.5Hz) and low (0-100 Hz) (Sampling rate: 12800Hz resolution 0.1Hz) frequency ranges.

Figure 32: Tap testing equipment pictured alongside tool.

- FRF profiles were used to generate stability lobes for the cutting process, which suggested that cutting would not be stable due to the tool stick out length and chatter would be observed at all speeds for this cut depth.
- 8 cuts were performed in ascending RPM speeds for each of 4 increasing feed per tooth relations (All cut trajectories can be viewed in Appendix D).
- Microphone data was collected using a PCB – 378B20 microphone with MalDAQ software for data acquisition.
- Force data was collected using a Type 5070 Kistler Plate Dynamometer with Kistler Dynoware software for data acquisition.
- The process was filmed using a Go-pro miniature video camera. Cuts were performed in the positive X direction with reference to the robot coordinate frame.
- When one workpiece surface had been made full use of, it was removed from the dynamometer and replaced with the next, the work object coordinate system was redefined by the operator.
- The following program was then executed through the robot controller.
- The recording of cuts 7, 8, 11, 17 and 19 was unsuccessful.
- Cuts 7, 11, 17, 19 were attempted again, however cut 17 failed to cut the material on the second attempt, which may be due to the slower cutting speed

combined with high feed per tooth, or otherwise due to operator mistakes. Data was lost for cut 1 due to user inexperience with Dynoware software.

9.6 Dynamometer Technical Issues

The Kistler 9255 Table Dynamometer used during this experiment had experienced fluid intake during earlier use unrelated to this project. Significant drift issues were observed after maintenance. While drift compensation can be carried out to mitigate errors, this does not preclude the presence of other inaccuracies in the Dynamometer data. A particular problem would be any nonlinearity in Dynamometer output, which may be the cause of some anomalous values discussed in the following results section.

9.7 Results and Analysis

9.7.1 Preliminary Workpiece Examination

Cursory tactile examination of the workpiece by the researcher after cutting seems to indicate a general trend of resulting surface roughness decreasing with cutting speed but increasing with feed rate.

9.7.2 Force Data Analysis

The force data was captured using Dynoware software in the form of .dwd files. Technical issues with the Dynamometer caused drift to occur in the force data, as previously mentioned. Drift compensation was applied to each file to reduce this effect.

An average force was calculated across the period which was inferred to be stable cutting from the force profile using the Dynoware statistics tool. Figure 33 shows an example of a .dwd file after drift compensation and smoothing, with annotations for how the statistics function is used to derive mean forces.

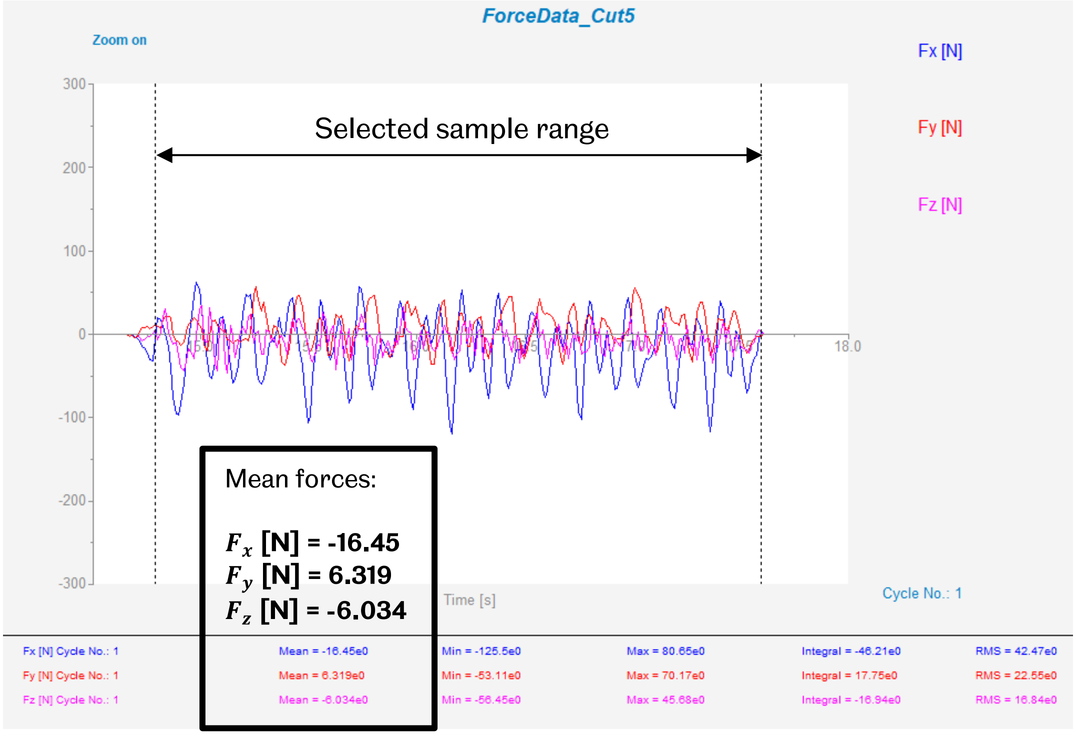

Mean forces:

F_x [N] = -16.45
F_y [N] = 6.319
F_z [N] = -6.034

```
Fx [N] Cycle No.: 1     Mean = -16.45e0     Min = -125.5e0     Max = 80.65e0     Integral = -46.21e0     RMS = 42.47e0
Fy [N] Cycle No.: 1     Mean = 6.319e0      Min = -53.11e0     Max = 70.17e0     Integral = 17.75e0      RMS = 22.55e0
Fz [N] Cycle No.: 1     Mean = -6.034e0     Min = -56.45e0     Max = 45.68e0     Integral = -16.94e0     RMS = 16.84e0
```

Figure 33: Annotated example of a set of force data undergoing statistical analysis.

Force data which appeared to result from non-immersion or transient cutting was omitted. Averages were entered into the experimental sheet.

9.7.3 Dynamometer to Tool Coordinate System Transform

It is necessary to convert from the dynamometer coordinate system used to capture forces being exerted on the workpiece to the tool coordinate system before cutting force coefficients are derived. Firstly, the coordinate system of the tool should be opposite (reversed X, Y and Z directions) to that of the workpiece, as assuming Newton's 3rd law applies to the tool-workpiece interaction, the force on the tool is assumed to be equal and opposite to that on the workpiece. Rotation in the XY plane must then be carried out to account for the feed direction (set as X). This transformation requires that the X and Y dimensions switch directions and are both reversed (See Equations 46-47 and Figure 34).

$$Fx_{tool} = -Fy_{tool} \qquad [46]$$

$$Fy_{tool} = -Fx_{tool} \qquad [47]$$

$$Fz_{tool} = Fz_{tool} \qquad [48]$$

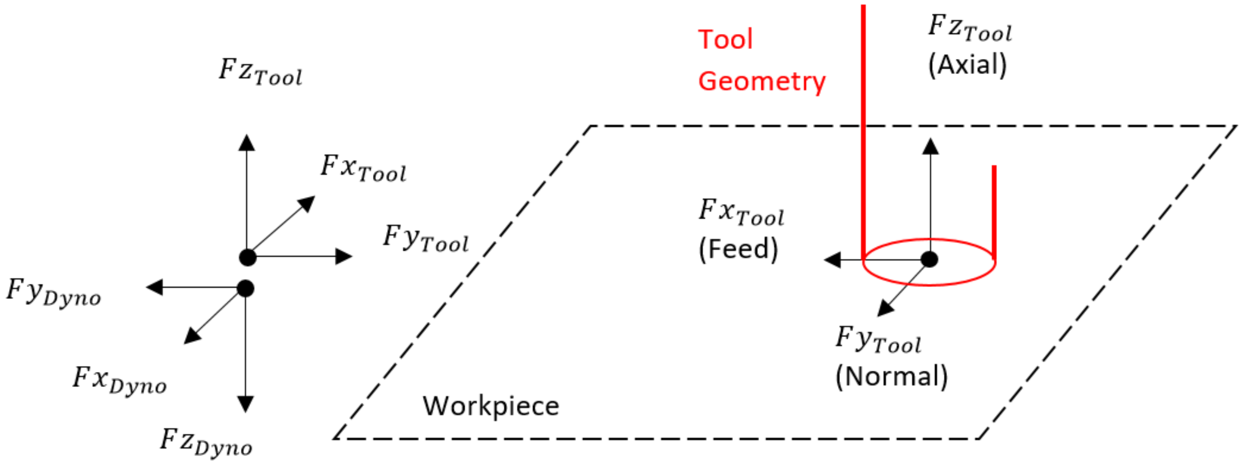

Figure 34: Graphical Representation of the two components of the tool coordinate system transformation.

9.7.4 Regression Analysis of Force Data

These average cutting forces were inserted into a pre-built spreadsheet [94] for regression analysis (wherein multiple data points from the same system to derive general descriptions of that system). Derivation of cutting force was carried out, based on the mechanistic cutting force coefficient identification method discussed in the Section 9.5.2. Lines of best fit were generated from which the coefficients of the process may be determined from gradients and intercepts (using the relations described in Equations 40-42). A more linear relationship should indicate a good fit with the expected linear model and therefore more reliable cutting force coefficient.

The graphs can be found labelled A through H in Appendix B. The corresponding speeds and cutting force coefficients are presented in Table 20.

Graph	**Cutting speed (m/min)**	**K_{tc}** (N/mm^2)	**K_{rc}** (N/mm^2)	**K_{ac}** (N/mm^2)	**K_{te}** (N/mm)	**K_{re}** (N/mm)	**K_{ae}** (N/mm)
A	**9.05**	29.07	50.8	-9.69	11.81	5.3	-1.94
B	**11.56**	75.12	45.27	0.94	5.89	1.96	0.35
C	**14.07**	50.31	8.13	6.77	13.54	9.53	-0.18
D	**16.59**	99.83	46.39	18.89	3.63	1.24	2.54
E	**241.27**	25.57	20.15	-34.42	8.73	3.2	2.92
F	**271.43**	33.85	26.4	-6.51	5.34	2.43	0.96
G	**301.59**	135.69	79.08	-64.3	-0.69	-1.75	-1.5
H	**331.75**	192.23	93.9	-108.78	-8.08	-3.92	-6.12

Table 20: Cutting Force Coefficients calculated from measured force data, with corresponding cutting speed and directory of corresponding graphs in Appendix B.

9.8 Discussion of Calculated Cutting Coefficient Values

Cutting force coefficients can be analysed to better understand the cutting process of the particular tool geometry, material and cutting speed. This section will examine the trends present in the data for a range of cutting speeds. It should be observed that the previously derived values for radial and tangential cutting constants [88] fall within the range of values seen in Table 20, for a cutting speed which falls within the range explored in that table, suggesting the values are plausible.

- The line of best fit of the graph for cuts performed at 9.04m/min is missing two data points representing cuts 1 and 17 performed at 0.05mm/tooth and 0.15mm/tooth respectively, as a result, the cutting force coefficients derived from the analysis of this data is unreliable. It should be observed that the cutting force coefficients calculated appear to defy the convention of K_{tc} having a greater value than K_{rc}. This may be attributed to the small number of data points.

- The cuts performed at 11.56m/min appear to exhibit a nonlinear relationship between feed per tooth and cutting force in the feed and normal directions (due to a larger force reading in both directions during cut 18 (0.15mm/tooth)), which means this data may not be reliable. The relationship in the normal direction appears closer to the trend-line, but still greater in in magnitude than that of the cut performed at 0.2mm/tooth, suggesting some factor has skewed the result.
- The graph for cutting at 14.07m/min indicates there is a highly nonlinear relationship between feed per tooth and cutting force, as the cuts performed at 0.1 and 0.15 mm/tooth are larger than suggesting that the cutting force coefficients derived are not reliable.
- Cuts performed at 16.59m/min show a feed/tooth - force profile which is very similar to that of cuts performed at a speed of 11.56m/min, implying a similar factor has affected both results, the anomaly again occurred at 0.15mm/tooth.
- Cuts performed at 241.27m/min exhibit a similar profile to that of cuts performed at 14.07m/min, with the effect being more pronounced in the axial direction at 241.27m/min. This may be because at higher cutting speeds the mass of the chips should experience greater acceleration when contacting the rake face, thus exerting greater force on the tool.
- Cuts performed at 271.43 m/min show a similar relationship to that of 16.59m/min, but the nonlinearity is less pronounced. A very high magnitude, negative axial cutting force was calculated for this speed, which is not expected in processes of this type.
- Cuts performed at 301.59 m/min show a very linear relationship between feed per tooth and cutting force.
- The force data collected at 331.75 m/min is less reliable due to the missing data points from cut 8, but nonetheless appears to show highly linear profiles in all axes, possibly indicating reliable cutting force coefficients. It is noted that the axial cutting coefficient is calculated to be greater than the radial cutting coefficient.

9.9 Discussion of Negative CFC Values

As cutting force coefficients are measured in terms of force exerted on the cutting edges as a result of the cutting process, and the edge is expected to face resistance while cutting even with zero feed, negative values are not expected for cutting coefficients, as this would suggest the edge was being accelerated during cutting. Negative values were found at some speeds for K_{ac}, K_{te}, K_{re} and K_{ae}.

In the case of K_{ac}, the negative values could result from non-ideal behaviour of the robot gravity compensation causing the trajectory to change in the axial direction between cuts, errors from force measurement, or simply from divergence in how the tool geometry exerts axial forces at different cutting speeds, or some combination of these factors.

9.10 Discussion of Negative Edge Constants

In the case of the edge constants, this may be due to the dynamometer issues causing nonlinearity in the sensitivity of the dynamometer, as this would skew the intercept of the cutting force trend-lines higher or lower. Due to the extrapolation used to derive edge constants, this could offset the edge constants by a small amount. As the edge constants only have small values relative to the cutting constants, this offset may explain the negative values, as well as why some values seem abnormally large compared to most results [95].

The funding and access to resources to repeat this experiment without this interference is not available within the course of this project, and no analogous data set has been found. Hence this data is not replaced during the course of this research.

9.11 Analysis of Change in Calculated CFC Values with Cutting Speed

This section will discuss the trends in the data relating cutting speed to each of the cutting force coefficients. Graphs depicting these trends can be found in Appendix F.

- Tangential cutting constants (K_{tc}) (Graph I) appear to increase with the low range of cutting speeds, and increase across the high range of cutting speeds, but the trends are not collinear and therefore there is not a consistent linear relationship.

- Radial cutting constants (K_{rc}) (Graph J) appear to cluster around 50N/mm^2 over the low range of cutting speeds with one anomalous low result of 8.13N/mm^2. The higher range appears to have a roughly linear relationship.
- Axial cutting constant (K_{ac}) (Graph K) increases across the low range, and decreases over the high range, suggesting that the relationship changes drastically between these two speed ranges.
- The tangential edge constant (K_{te}) (Graph L) appears to exhibit a loose clustering of data points around 8N/mm for the low-speed range, and a decreasing relationship over the high-speed range.
- The radial edge constant (K_{re}) (Graph M) shows a loose clustering of coefficients around 4N/mm for the low-speed range, and a shallow negative correlation over the high-speed range.
- The axial edge constant (K_{ae}) (Graph N) is clustered around 0 N/mm for the low-speed range. The higher speed range appears to be causing the axial edge constant to decrease but the median is close to that of the low-speed range at around -1N/mm.

According to results provided by Urena et al., for a cutting speed of 216.14 m/min, tangential cutting force coefficient for milling is approximately 100 N/mm^2. The values presented by Urena et al. for this speed do not appear to change drastically (less than a 3% tolerance) with tool helix angle (10°-25°) or flute number (1-3). Considering this, the coefficients determined from this experiment (with 6 teeth, helix angle 42°) vary heavily by comparison (with the minimum coefficient only 13.3% of the maximum).

One possible explanation for this behaviour is that chatter is occurring at low feed per tooth values, and systematically increasing the actual average chip area. A constant chip area is assumed when calculating CFCs, therefore the resulting CFCs would be inaccurately calculated.

9.12 Conclusions

Force data has been collected and processed to calculate average cutting forces, and regression analysis has been used to derive cutting force coefficients. The CFC values have been taken as calculated and analysed for the relationship between CFC values and cutting speed over the speed ranges discussed. Most of the values contain reliable and consistent data for the scope of the experiment, however errors due to equipment issues and user error have reduced the reliability of analysis based on cuts at some speeds.

There is an increase in tangential cutting coefficient with cutting speed which may be considered abnormal, this may be explained as a result of progressively greater regenerative chatter with cutting speed increasing the average chip thickness per tooth pass.

There are unexpected anomalies in some of the results, suggesting either the presence of other factors not considered in the scope of this experiment, or more errors occurred than this report considers, and the experiment may be worth repeating with the guidance of the lessons learnt to determine between the two possibilities.

The funding and access to resources required to repeat this experiment in order to find a resulting dataset without interference from the dynamometer is not available within the course of this project, and no analogous data set has been found. Hence this data is not replaced during the course of this research. This is also true of the milling trials described in Appendix B.

9.13 Lessons Learnt

A number of errors and delays occurred during the experimental process. These have been reflected on and a list of lessons learnt has been compiled to avoid these problems in future.

- Thorough auditing of documentation should be carried out prior to readiness gates to reduce the time spent on resulting gate actions.
- When intending to carry out comparisons with previous experimental work, it is difficult to achieve the same process parameters when a different tool geometry is used, even if tool diameters and cut depths are kept consistent.
- Tool stick-out/overhang has a large impact on the dynamics of the tool when cutting. During tap testing, accelerometers were found to be unsuitable to collect force data, and a laser vibrometer was substituted. A shorter shank should be used to reduce the dynamic effects.

- A detachable tool end and shank results in difficulties with tap testing as impacts will register twice, which makes data collection more difficult, as light hits need to be used to get around this. In future tools should ideally be a single structure.
- Impact testing must be performed systematically to avoid mistakes in usage of impact hammers, not in a procedural way to fill in data points, as mistakes can occur when switching between frequencies.
- Stability lobes produced from tap testing cannot reliably predict the outcome of cutting processes without adding simulation of process damping, which is not necessarily reliable.
- Time and material should be allotted for cuts which do not yield successful results the first time to be repeated. A new code with pre-programmed trajectories should be written before the experiment, with spaces for cutting parameters to be easily copied in from failed cuts.
- Because the existing trajectories associated with cuts may not be compatible with each other on the same workpiece, some cuts could not be performed in the short time available for repeats.
- Additional float time should be allotted between experiments to prevent complicated rescheduling.

9.14 Further Research

Robots are known to possess low stiffness and low modal frequencies which adversely affect stability in milling, which could increase or decrease cutting forces at certain speeds and distort the results of CFC identification, rendering the results of this experiment unreliable for applications using other machines. Future research could examine the modal frequencies of the robot and response to dynamic cutting forces at certain speeds to determine the extent of this effect. Analysis of sound data collected during this experiment, and performing Fourier transforms of the discussed force data may help with such an investigation by detecting the frequencies present in the data.

The experiment could also be repeated using a high stiffness CNC machine to better understand how the low stiffness may have affected the results. Further, alterations could be made to the robotic machining cell and this experiment could be repeated, with analysis of the force data used to benchmark how the alterations affect machining performance.

9.15 Significance

The activities carried out in the course of this mini-project has provided the following benefits:

- A greater understanding of how instability in robotic machining can result in chatter and the subsequent effect of chatter on part quality.
- Improved understanding of the process of modal analysis of tap test data. This information is useful for understanding the theoretical framework around frequency response functions and their use in generating stability lobes for machining processes (see Section 4.2, 4.3).
- Demonstrated how cutting force coefficients may be determined for later use in machining stability predictions (see Section 4.3).

10 Appendix B

Mini-Project 3: Wire Arc-Additive Manufactured Titanium Milling Trial Report

10.1 Preface

This experiment provided an opportunity to apply machining theory and examine the average forces required to machine aerospace metals, as well as the relation these forces have with the stability of the milling process. An understanding of these coefficients would be useful for the later theoretical background of the drilling simulation. These activities were not considered to be within the scope of the research activities directed toward the MPhil course, so have been placed in the Appendix.

This experimentation was novel in regard to the material used, which has restricted availability and is intellectual property of BAE Systems.

10.1.1 Abstract

Hybrid machining may be improved by the application of robotic machining, however there is little information on the machinability of additively manufactured titanium. In this report the machinability of cast Ti-6Al-4V was compared with a sample of additively manufactured titanium via milling trials. The machinability of the materials was assessed via cutting force data analysis. Additively manufactured titanium generally exhibited higher critical cutting force coefficients (tangential and radial) than cast titanium, as cutting forces increased more rapidly with feed per tooth, indicating increased material strength [96].

10.1.2 Introduction

BAE systems has approached AMRC with a request that machinability trials be carried out on a sample of wire arc additive manufactured (WAAM) titanium, to contribute to investigations into hybrid manufacturing of parts made from that material. There exists demand for additively manufactured titanium alloys in aerospace manufacturing due to potential cost savings over conventional subtractive manufacturing of titanium [97]. Cutting force coefficient identification was judged as a good measure of material machinability.

Originally, the CFC identification was intended to be carried out using robotic machining, however this was rejected as the available ABB6640 robotic machining cell exhibits significantly low stiffness, and therefore could not substantially resist the cutting forces inherent in machining of metals such as titanium. For this reason, a 3-axis milling machine (DMG Mori NVX 5080) was selected instead of the robot for its availability and stiffness. Samples of cast titanium (Ti6Al4V) and IP-protected WAAM titanium were provided by BAE Systems for use in the experiment.

Previous examinations at a speed of 1000 r/min (50.27/min) put the CFC values of titanium alloy (TA15) at (K_{tc}= 1820.3 N/mm^2, K_{rc}=563.6 N/mm^2) [98], which may provide a guideline with which to validate CFC values after this experiment.

10.2 Methodology

10.2.1 Theoretical Basis

The Altintas method of mechanistic identification of cutting coefficients [12] was used to calculate cutting force coefficient values for this cutting system at the specified cutting speeds. The mathematical procedure outlining this process has been described in a previous report on cutting force coefficient identification in robotic machining [99], and will be utilised here in the same way.

10.2.2 Preparation and Parameter Selection

- Titanium samples were faced to ensure surfaces were as flat as possible for cutting so that axial depth of cut would be consistent to simplify data analysis. A consistent depth of cut simplifies the data analysis process. The dimensions were measured manually in the case of the cast titanium sample, and the piece was cut down to a shorter length to fit within the boundaries of the dynamometer.
- The geometry of the WAAM titanium sample was highly irregular. This problem necessitated the use of GOM 3D imaging facilities at the NAMRC building and digital manipulation of the resulting files using Siemens NX software to determine how to cut the material into a more usable shape and what the approximate dimensions of this shape would be. This machining was then carried out by AMRC technicians, yielding a usable piece with regular faces.

- Feeds and speeds were selected to keep cutting speeds at a safe level for titanium [100] which carries a risk of fire when cut at high speeds. For additional safety, coolant was deployed during the experiment, requiring a protective cover to be placed over the dynamometer.

Table 21 describes the chosen cutting parameters of the experiment:

No. of Flutes	6
Axial cut depth (mm)	2
Feed/tooth (mm)	0.025, 0.05, 0.075, 0.1
Spindle Speeds (RPM)	90, 115, 140, 165 (Low Range) 1200, 1350, 1500, 1650 (High Range)

Table 21: Cutting Parameters

For this experiment, most cuts were performed with the equipment as listed in Table 22, with the replacement of the tool with an identical model and a similar shank after tool damage occurred:

Machine	DMG Mori NVX 5080
Tool	End-Mill (316-16FL642-16005L 1745) (Sandvik Coromant), compatible shank (EH16-A16-SH-130) (Sandvik Coromant), replacement shank used after first tool breakage (EH16-A16-SE-135 Sandvik Coromant)
Back End	NBT40-C20-70 (Nikken)
Collet	CG20, 16mm internal radius
Tool Length	152.246mm (157.314mm after end mill and shank replacement)
Tool Runout	0.06mm after end mill and shank replacement
Tool Overhang/ Stick-out	77.57mm (82.17mm after end mill and shank replacement)

Table 22: Equipment Specifications.

10.2.3 Experimental Process

The following section will discuss the process of experimentation used to acquire force data.

- Cutting trajectories, speeds and feeds for each of the 64 planned cuts were written in G-code as seven separate programmes corresponding to seven cutting surfaces and checked by a qualified CNC machine operator (trajectory diagrams can be found in Appendix G).
- Tap testing was carried out using a small nylon-tipped impact hammer (Model 9722A500) with, with measurements made using an accelerometer (3224A1) connected to the tool tip while the tool was mounted in the machine.
- Cutpro stability analysis with simulated process damping was used to estimate stability lobes for the intended milling process (See Figure 35). The lobes predicted that cutting would be stable at low speeds but may become unstable at higher speeds.

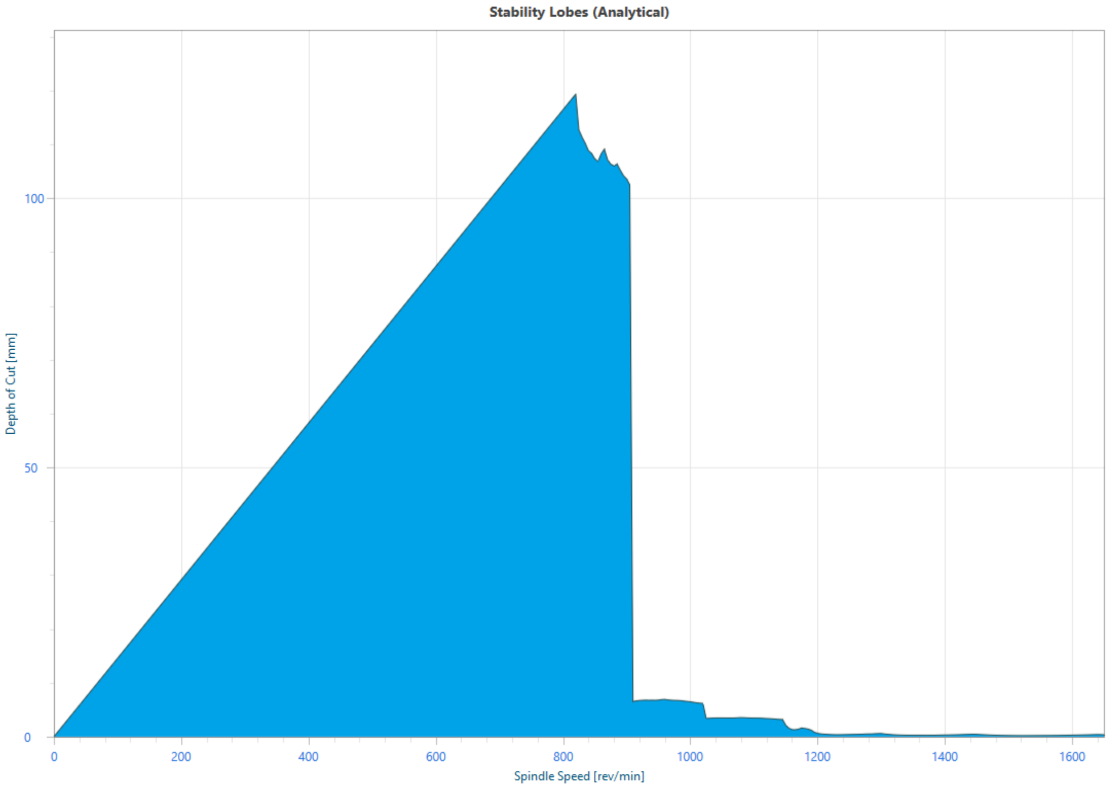

Figure 35: Screenshot of Cutpro Analytical Stability Lobes function, showing stability lobes for cutting Ti6Al4V with described cutting parameters.

- Force data collection was performed using a Kistler Type 5070 table Dynamometer kit with Dynoware software for data acquisition.
- Microphone data collection was performed using a PCB – 378B20 microphone with MalDAQ software for data acquisition.
- A Go-pro Miniature video camera was used to film the cutting procedure, however the use of coolant at high pressure conceals much of the process from view of the camera.
- The Dynamometer was fixed to the machine bed and a plastic cover was applied to prevent coolant from flooding the electronics.
- The work pieces were placed in a vice with the material exposed above the jaws at a greater height than 2mm to prevent tool contact with the vice. All cuts were performed on the cast titanium sample first, as this was considered to be more predictable and thus less likely to result in tool breakage. The workpiece was removed from the vice and rotated as required when each surface had

undergone the planned cuts, with the work object coordinate system redefined before each new surface (graphical representation in Appendix G).

- When the WAAM titanium piece was being cut, the datum point of the TCP would be set to one of two opposing corners depending on the direction of cut. This was planned to reduce the number of times the workpiece needed to be removed from the vice. These datum points can be seen in the cutting diagrams presented in Appendix G.
- Two tool breakages occurred when attempting to cut the WAAM at the lowest cutting speed with the two highest feed per tooth parameters (cuts 17 and 25). Damage was suspected to have occurred to the shank after the first breakage due to oscillations occurring after this breakage. The tool shank was replaced with a spare of similar dimensions and the cuts continued until the lowest speed was attempted again, and a second tool breakage occurred. The experiment was concluded after this breakage, and no data was acquired for cuts performed at 90 RPM at 0.75mm per tooth or greater and all speeds with 0.1mm.

10.3 Results and Analysis

10.3.1 Preliminary Workpiece Examination

A brief examination of the workpiece suggested that chatter was not occurring in significant magnitudes until a feed per tooth of 0.075 mm was used, at which point surface roughness of the slots became noticeable at low speeds and pronounced at high speeds. Regenerative vibrations result in unstable cutting depth, leaving rougher surfaces [101]. It may be assumed from this examination that regenerative chatter increased significantly at 0.075 mm/tooth.

10.3.2 Dynamometer to Tool Coordinate System Transformation

Technical issues with the Dynamometer caused drift to occur in the force data. Drift compensation was used to filter the data.

An average force for each cut was calculated across the section of time which was inferred from the force profile to be stable cutting. Force data which appeared to result from transient cutting was omitted from the average. Averages were calculated using Kistler Dynoware as in the previous CFC identification report [99].

It is necessary to convert from the dynamometer coordinate system used to capture forces on the workpiece to the tool coordinate system before cutting force coefficients are derived. To do this, firstly, the coordinate system of the dynamometer should be opposite to that of the workpiece (reversed X, Y and Z directions), as the force on the tool is assumed to be equal and opposite to that of the workpiece. For cuts performed in direction 1 as specified in Figure 36, X and Y must switch orientations (Equations 46 and 47), and for those performed in direction 2 as specified these directions must also be reversed (Equations 49 and 50).

$$Fx_{tool} = Fy_{tool} \qquad [46]$$

$$Fy_{tool} = Fx_{tool} \qquad [47]$$

$$Fz_{tool} = Fz_{tool} \qquad [48]$$

$$Fx_{tool} = -Fy_{tool} \qquad [49]$$

$$Fy_{tool} = -Fx_{tool} \qquad [50]$$

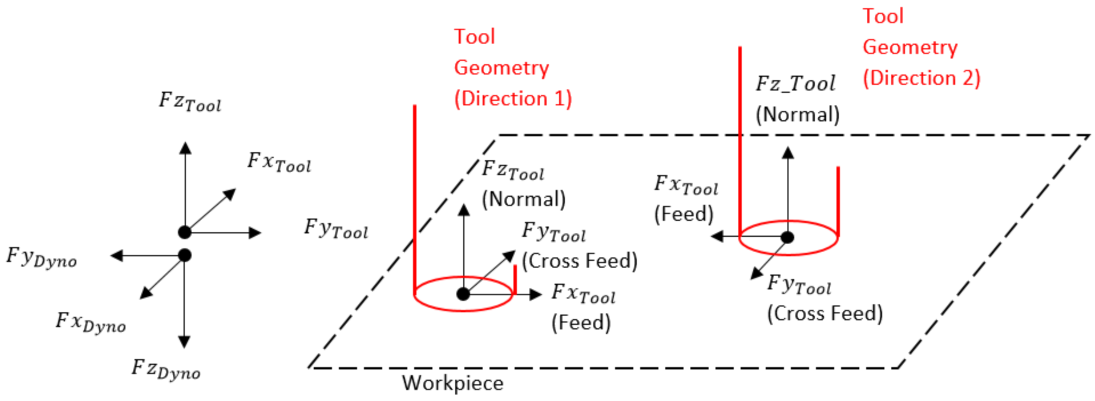

Figure 36: Graphical Representation of the two components of the tool coordinate system transformation.

Much like in the previous report, the average cutting forces derived from the experiment were inserted into a prepared spreadsheet [102] which was utilised in the previous report, yielding estimates of the cutting force coefficients of this material and process. A more linear relationship should indicate a more reliable cutting force coefficient estimate.

10.3.3 Effects of Missing Data Points on Regression Analysis

Due to a tool breakage at WAAM material cut 17, there is no stable cutting data for cuts 17-21, so these results were not carried forward. The tool was then replaced, however a second breakage occurred at cut 25, meaning there is no data for cuts 26-32 for that material.

Regression analysis was carried out on six cutting speeds with only three data points instead of four, reducing the confidence of CFC values calculated for speeds 7.037168-82.93805 m/min.

10.3.4 Effect of Dynamometer Technical Issues

As stated in a previous report [99], cutting force measurements may be distorted due to the poor condition of the dynamometer used. This may explain some anomalies visible in the output of the regression analysis, particularly for coefficients derived from analysis of smaller forces (edge constants and axial cutting constants).

10.3.5 Discussion of Regression Analysis

There is a near universal trend of linear relationships exhibited by the graphs visualising the relationship between feed per tooth and resulting cutting force with low R^2 values (with the exception of graphs O and P, both describing cuts performed at 82.93805 m/min, which have noticeably higher R^2 values across the three axes, suggesting the anomalies are most likely due to cut 16 (feed per tooth = 0.05 mm, cutting speed = 82.93805 m/min).

10.3.6 Analysis of Calculated Cutting Force Coefficient Values

The calculated cutting force coefficient data has been placed in Table 23, which contains the cutting speeds, materials and an index of graphed data found in Appendix E.

Cutting speed (m/min)	**Graph Index**	**Material**	**K_{tc}** (N/mm^2)	**K_{rc}** (N/mm^2)	**K_{ac}** (N/mm^2)	**K_{te}** (N/mm)	**K_{re}** (N/mm)	**K_{ae}** (N/mm)
4.52389	A	Ti6Al4V	**2610**	**2280**	**968**	19.9	-3.68	-10.3
	B	WAAM-Ti	**3320**	**2460**	**1320**	49.9	105	-10.7
5.78053	C	Ti6Al4V	**2580**	**2230**	**908**	16.0	-4.44	-7.35
	D	WAAM Ti	**3340**	**2610**	**1300**	43.0	93.7	-9.87
7.037168	E	Ti6Al4V	**2580**	**2180**	**858**	13.4	-4.95	-5.86
	F	WAAM Ti	**3290**	**2730**	**1300**	40.6	87.1	-10.5
8.293805	G	Ti6Al4V	**2480**	**2190**	**807**	15.9	-5.59	-4.07
	H	WAAM Ti	**3240**	**2710**	**1220**	39.0	82.8	-9.30
60.31858	I	Ti6Al4V	**2240**	**2130**	**913**	12.1	-1.51	-8.40
	J	WAAM Ti	**2610**	**3070**	**1300**	25.9	65.8	-10.4
67.8584	K	Ti6Al4V	**2280**	**2170**	**970**	13.9	8.43	-9.92
	L	WAAM Ti	**2100**	**1400**	**1160**	41.4	112	-9.60
75.39822	M	Ti6Al4V	**2280**	**2090**	**933**	13.7	18.5	-9.07
	N	WAAM Ti	**2880**	**3050**	**754**	2.83	52.0	-7.06
82.93805	O	Ti6Al4V	**2310**	**2060**	**951**	15.6	27.9	-9.07
	P	WAAM Ti	**3490**	**4350**	**1190**	12.4	47.8	-3.63

Table 23: Cutting speeds, index of graphs in Appendix E and calculated CFC values.

CFC values in general are higher for both materials than the values described in the study on TA15 previously mentioned [98].

From examination of graphs (Q) and (R) it can be seen that there is a general trend of the WAAM material exhibiting higher tangential and radial cutting constants (K_{tc}, K_{rc}) than the cast titanium sample for the low cutting speed range and most of the high cutting speed range. This trend could be due to the higher hardness inherent in some WAAM materials compared with Ti6Al4 [103] [104]. However, there was an exception at 67.8584 m/min, the tangential and radial cutting constants seem abnormally low for the WAAM titanium compared to the adjacent speeds, even being lower than those of the cast titanium. It is believed that this is a result of extrapolation from a low number of data points.

According to graph (Q), for both materials, the tangential cutting constant appears to be decreasing slightly across the low range, while for the high range the K_{tc} of the WAAM titanium appears to vary strongly with cutting speed. Conversely, across the high-speed range, the cast titanium exhibits fairly consistent values.

From graph (R), across the low-speed range, the K_{rc} value of the cast titanium appears to be decreasing, while the value of the WAAM titanium seems to be increasing. Across the high-speed range, the WAAM titanium values appear to change drastically, much like the K_{tc} values, while the cast titanium values appear to again be fairly consistent.

Looking at graph (S), it can be seen that the axial cutting constant (K_{ac}) is consistently higher for the WAAM titanium than for the cast titanium in the low-speed range and most of the higher range. The constant also appears to be decreasing across the low-speed range for both materials. Across the high-speed range, the cast titanium value appears to be very steadily increasing, while the WAAM titanium value appears to be slowly decreasing. At 75.39822 m/min there is an apparent anomaly, as the axial cutting constant (K_{ac}) is lower than the adjacent speeds, and lower than that of the cast titanium for that speed. This could again be due to extrapolation from few data points, or possibly due to the issues outlined in Section 9.3.4.

The relationships for the edge constants (graphs T, U and V) appear to be more complicated than those of the cutting constants, possibly due to higher sensitivity to the accuracy of regression analysis.

According to graph (T) the tangential edge constant (K_{te}) for the cast titanium appears to be clustered between 10 and 20 N/mm, for both the high and low range of cutting speeds. The K_{te} values for the WAAM titanium at low cutting speed appear to decrease in what resembles a curve, but for the high cutting speed range, the values seem widely distributed across a relatively broad range between 0 and 45 N/mm with no relationship that can be easily perceived.

For the radial edge coefficient (K_{re}) relationships (graph U), the WAAM material has consistently higher values, and an anomalous high value is present at the cut for cutting WAAM titanium at 67.8584 m/min. Both materials appear to exhibit decreasing values over the low range (again a curve may be seen for WAAM titanium). Over the higher speed range, the values are decreasing for the WAAM titanium and increasing for the cast titanium.

The axial edge coefficient (K_{ae}) seems to be increasing over the low-speed range and falling over the high-speed range for the cast titanium. The K_{ae} relation for the WAAM titanium appears to cluster around -10N/mm for the low range of speeds and increase over the high range of speeds.

10.3.7 Tool Breakage

At the present time, it is unknown to what extent tool wear during the experiment may have contributed to tool breakage. It should be noted that both breakages occurred when cutting the WAAM titanium at low spindle speeds, indicating cutting forces were high at this time. Similarity was expected between the two material samples, yet there is no evidence of any tool damage during cuts performed on the cast titanium sample, even at the feed rates and speeds at which the breakage occurred for the WAAM Titanium.

10.4 Conclusion

The experimental process described in the methodology has been carried out to yield cutting force data, and this cutting force data was fed into a regression analysis to identify the cutting force coefficients of the specified cutting process.

The final CFC values do not appear to fit the pattern expected for milling processes, particularly the edge constants, at this point this is ascribed to the technical issues with the dynamometer disrupting the findings of the regression analysis, and to fully remove this issue, the experiment would need to be repeated with fully tested and calibrated dynamometer.

The relationships between cutting force coefficients and cutting speed have been plotted and described in this report, with comparisons made between the two materials, indicating that generally the WAAM material could be expected to exhibit higher tangential and radial cutting constants than the cast titanium, which may fit with the previously mentioned higher strength observed from some WAAM titanium [103] [104]. Lessons learnt while carrying out this experiment have been compiled to advise on this form of machining trial if it is repeated.

10.4.1 Lessons Learnt

Applicable advice for future experiments of this kind is listed below.

- Preparations for the experiment should conclude sooner to leave more time for auditing the experiment plan, and adequate time should be left between experiments to prevent delays from interfering with sensitive schedules.
- Some CNC machines require decimal points in all numerical values or will default to registering all integers as micrometres.
- A specialised microphone may greatly improve sound data collection as sound is damped by the door of the CNC machine.
- Cutting speeds which are too low risk damage to tools as they are not designed to operate below a certain speed threshold. Minimum cutting speeds should be reported as a matter of safety alongside maximum cutting speeds.
- Depth of cut may have been changeable without significantly altering the experiment beyond comparison with other CFCs.

10.4.2 Future Research

The presumed impact of the damaged dynamometer on these results makes it difficult to draw reliable conclusions and renders the CFC values unreliable to use for predictions about milling processes using tools and materials of this type. Ideally the experiment should be repeated with a more reliable method of force measurement.

Dynamic analysis of force and sound data may provide more information about the behaviour of the WAAM titanium sample.

Hardness testing on the WAAM titanium may explain the causation behind the difference in critical cutting force coefficients. Scanning Electron Microscopy may reveal microstructural differences.

11 Appendix C

Graphical Representation of Regression Analysis for Robotic Machining of Acetal Copolymer

Graph	**Cutting speed (m/min)**	**K_{tc}** (N/mm^2)	**K_{rc}** (N/mm^2)	**K_{ac}** (N/mm^2)	**K_{te}** (N/mm)	**K_{re}** (N/mm)	**K_{ae}** (N/mm)
A	**9.05**	29.07	50.8	-9.69	11.81	5.3	-1.94
B	**11.56**	75.12	45.27	0.94	5.89	1.96	0.35
C	**14.07**	50.31	8.13	6.77	13.54	9.53	-0.18
D	**16.59**	99.83	46.39	18.89	3.63	1.24	2.54
E	**241.27**	25.57	20.15	-34.42	8.73	3.2	2.92
F	**271.43**	33.85	26.4	-6.51	5.34	2.43	0.96
G	**301.59**	135.69	79.08	-64.3	-0.69	-1.75	-1.5
H	**331.75**	192.23	93.9	-108.78	-8.08	-3.92	-6.12

Table 24: Cutting Force Coefficients calculated from measured force data, with corresponding cutting speed and directory of corresponding graphs in Appendix E.

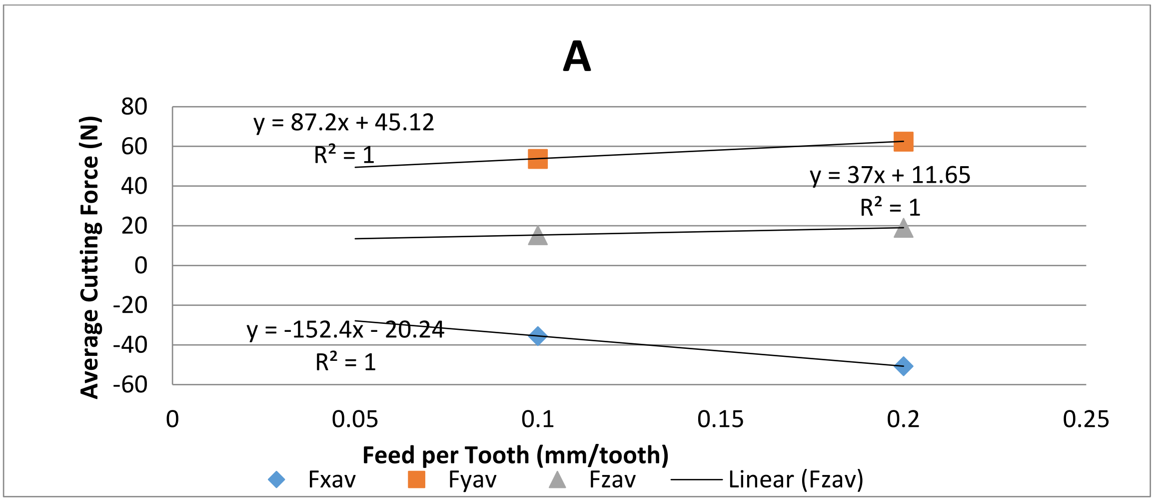

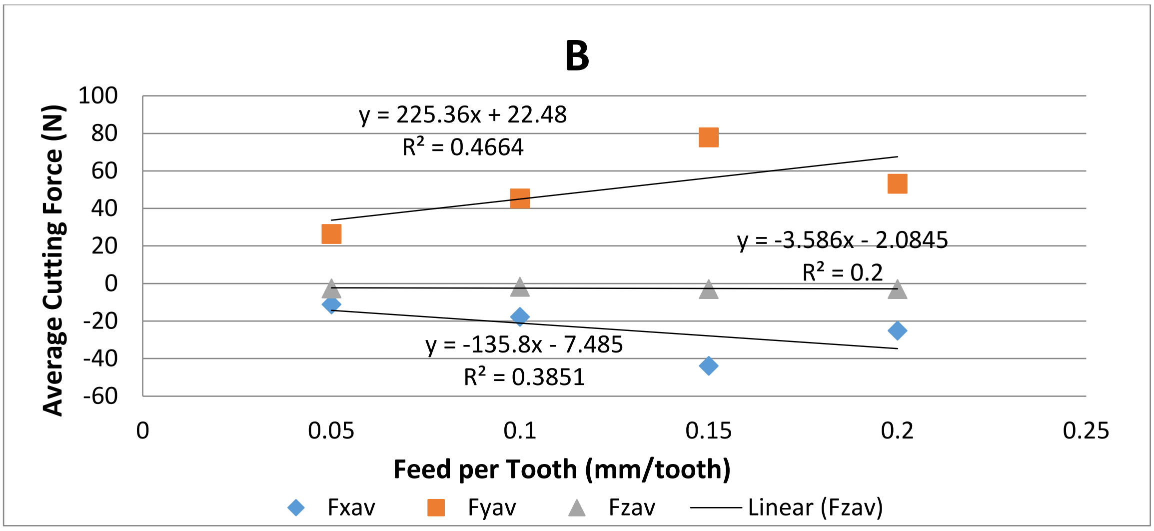
B
Average Cutting Force (N)
100
80
60
40
20
0
-20
-40
-60
y = 225.36x + 22.48
R² = 0.4664
y = -3.586x - 2.0845
R² = 0.2
y = -135.8x - 7.485
R² = 0.3851
0
0.05
0.1
0.15
0.2
0.25
Feed per Tooth (mm/tooth)
Fxav
Fyav
Fzav
Linear (Fzav)

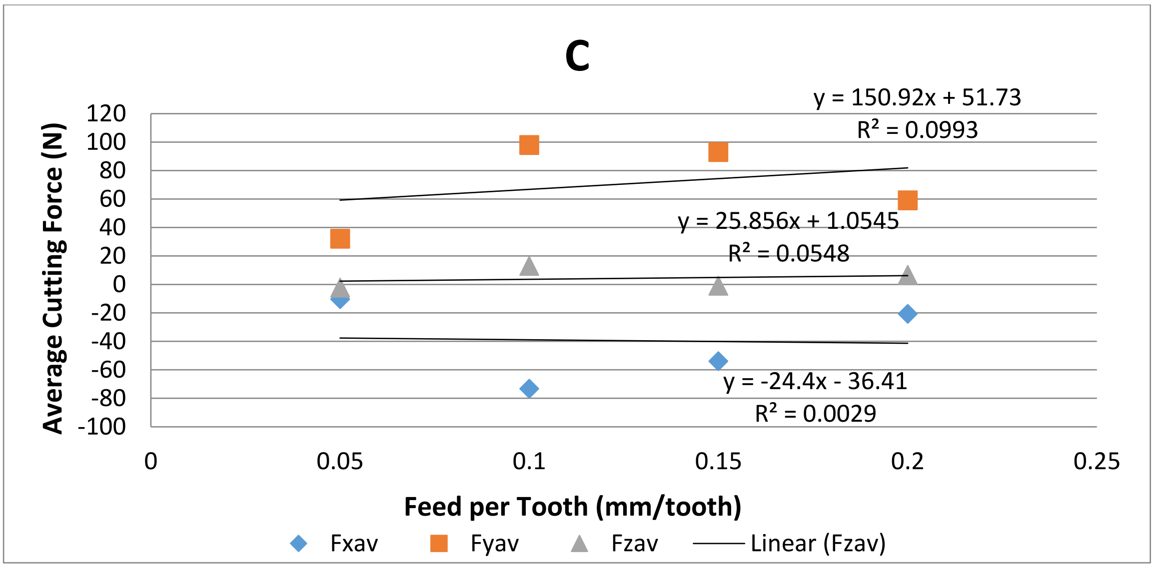
C
Average Cutting Force (N)
120
100
80
60
40
20
0
-20
-40
-60
-80
-100
y = 150.92x + 51.73
R² = 0.0993
y = 25.856x + 1.0545
R² = 0.0548
y = -24.4x - 36.41
R² = 0.0029
0
0.05
0.1
0.15
0.2
0.25
Feed per Tooth (mm/tooth)
Fxav
Fyav
Fzav
Linear (Fzav)

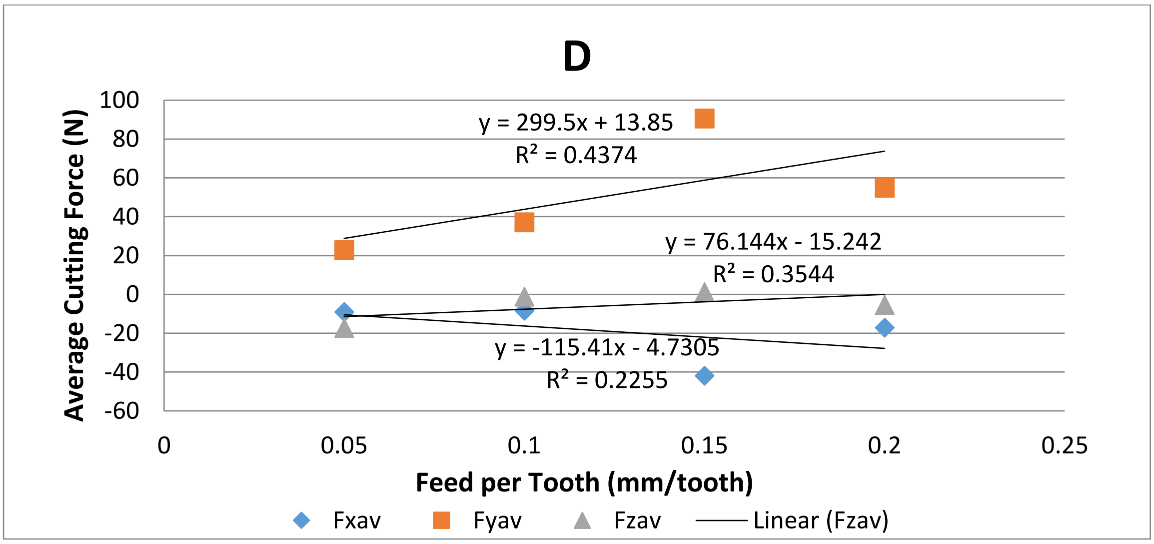
D
Average Cutting Force (N)
100
80
60
40
20
0
-20
-40
-60
y = 299.5x + 13.85
R² = 0.4374
y = 76.144x - 15.242
R² = 0.3544
y = -115.41x - 4.7305
R² = 0.2255
0
0.05
0.1
0.15
0.2
0.25
Feed per Tooth (mm/tooth)
Fxav
Fyav
Fzav
Linear (Fzav)

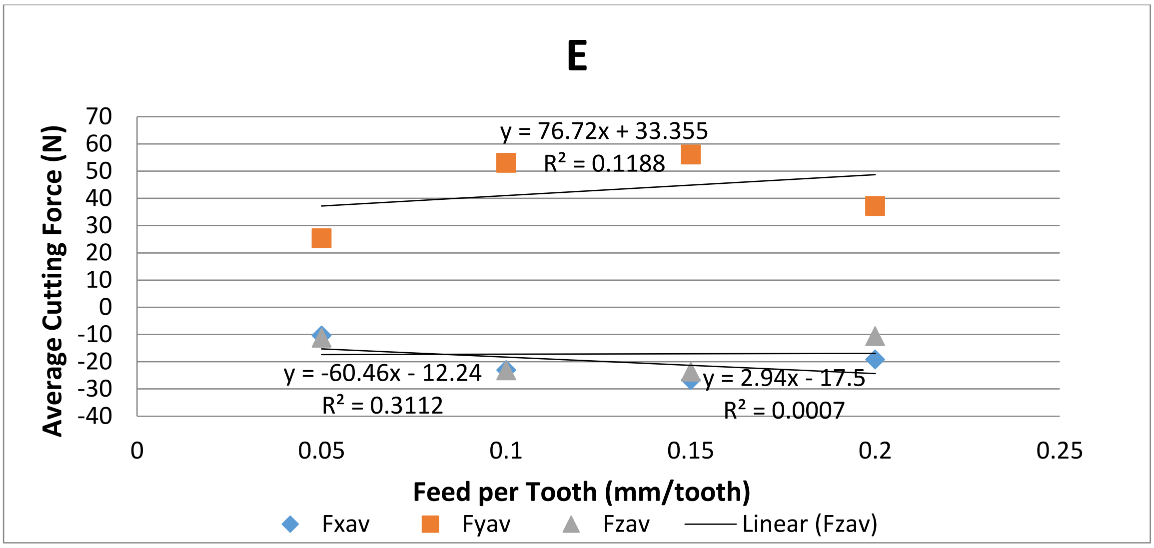
E
Average Cutting Force (N)
70
60
50
40
30
20
10
0
-10
-20
-30
-40
y = 76.72x + 33.355
R² = 0.1188
y = -60.46x - 12.24
R² = 0.3112
y = 2.94x - 17.5
R² = 0.0007
0
0.05
0.1
0.15
0.2
0.25
Feed per Tooth (mm/tooth)
◆ Fxav
■ Fyav
▲ Fzav
—— Linear (Fzav)

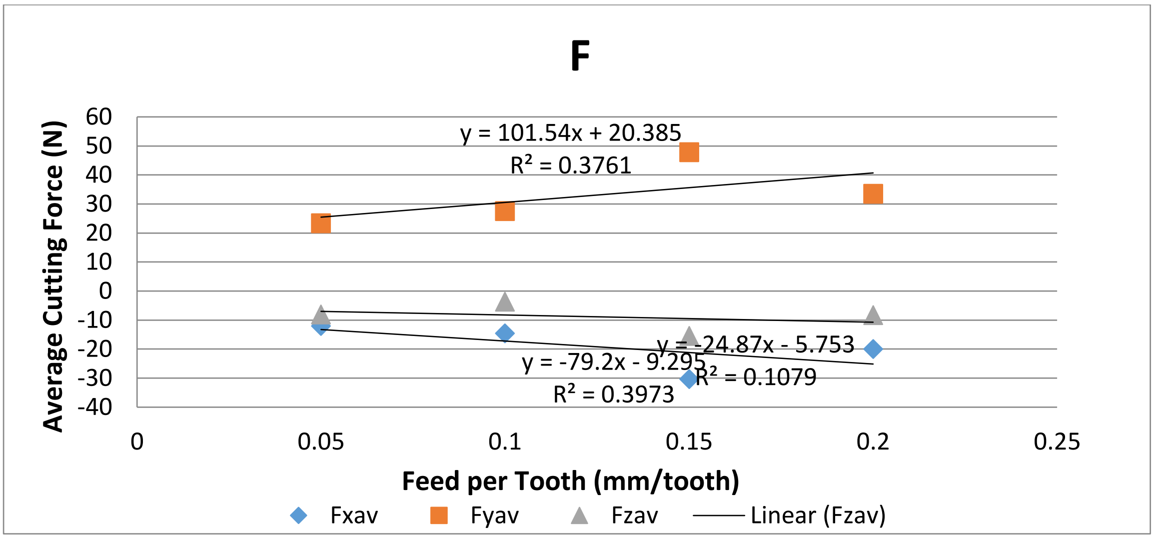
F
Average Cutting Force (N)
60
50
40
30
20
10
0
-10
-20
-30
-40
y = 101.54x + 20.385
R² = 0.3761
y = -24.87x - 5.753
R² = 0.1079
y = -79.2x - 9.295
R² = 0.3973
0
0.05
0.1
0.15
0.2
0.25
Feed per Tooth (mm/tooth)
◆ Fxav
■ Fyav
▲ Fzav
—— Linear (Fzav)

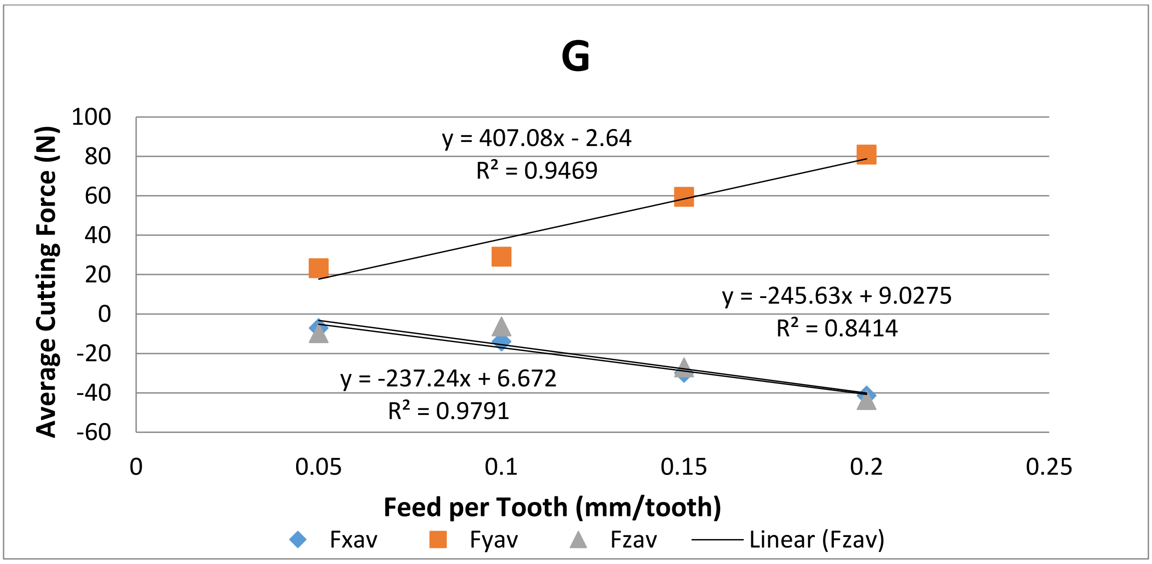
G
Average Cutting Force (N)
100
80
60
40
20
0
-20
-40
-60
y = 407.08x - 2.64
R² = 0.9469
y = -245.63x + 9.0275
R² = 0.8414
y = -237.24x + 6.672
R² = 0.9791
0
0.05
0.1
0.15
0.2
0.25
Feed per Tooth (mm/tooth)
◆ Fxav
■ Fyav
▲ Fzav
—— Linear (Fzav)

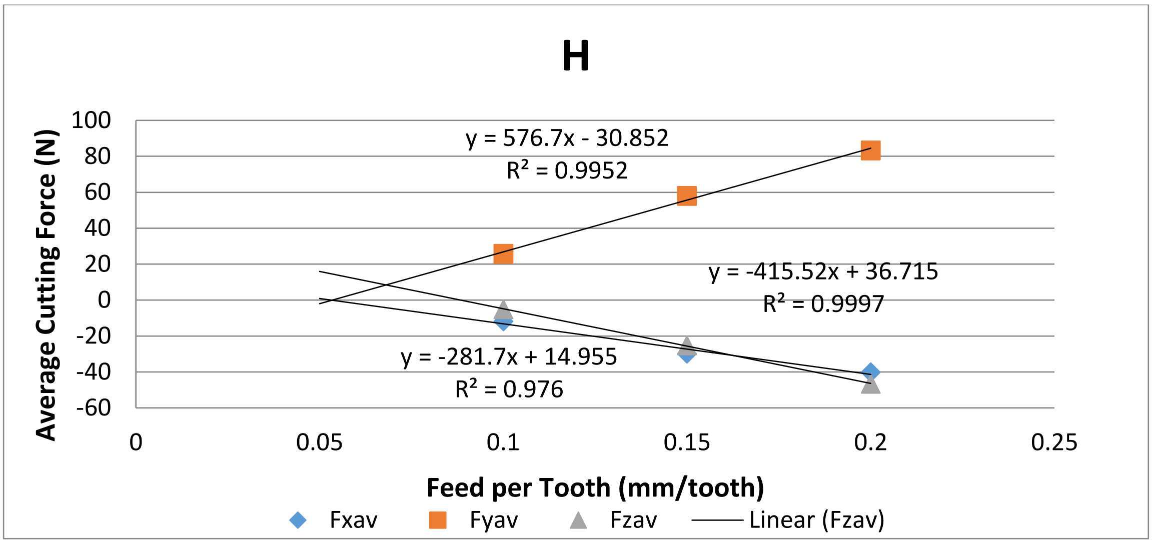
H
Average Cutting Force (N)
100
80
60
40
20
0
-20
-40
-60
0
0.05
0.1
0.15
0.2
0.25
Feed per Tooth (mm/tooth)
y = 576.7x - 30.852
R² = 0.9952
y = -415.52x + 36.715
R² = 0.9997
y = -281.7x + 14.955
R² = 0.976
Fxav
Fyav
Fzav
Linear (Fzav)

12 Appendix D

C.1 Graphical Representations of Relationships between Cutting Speed and Cutting Force Coefficients in Robotic Milling of Acetal Copolymer.

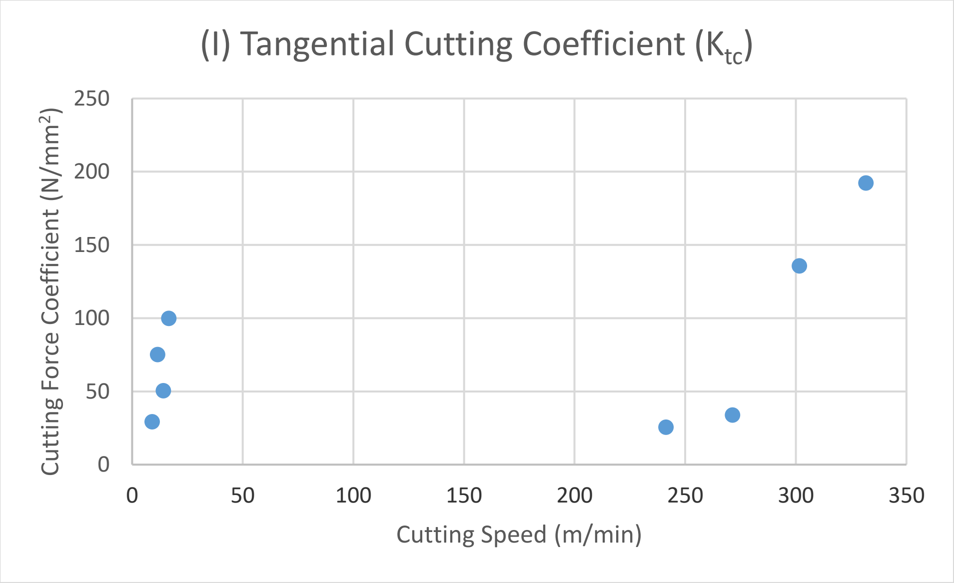

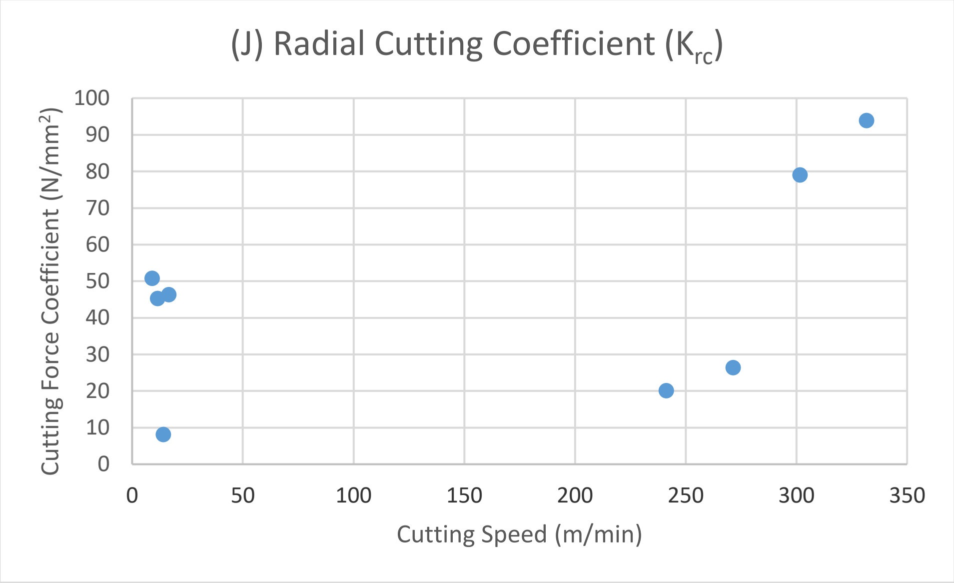

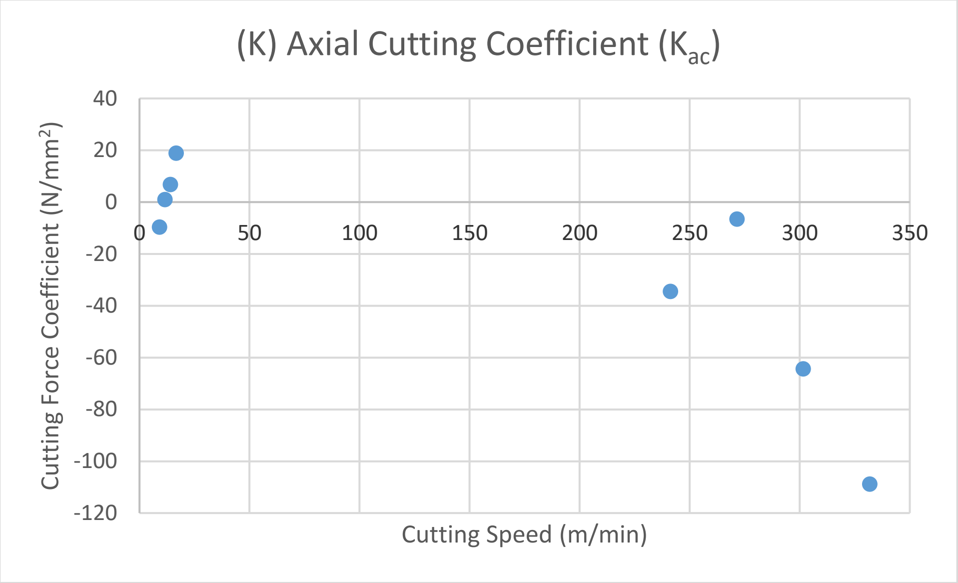
(K) Axial Cutting Coefficient (K_{ac})
Cutting Force Coefficient (N/mm^2)
40
20
0
-20
-40
-60
-80
-100
-120
0
50
100
150
200
250
300
350
Cutting Speed (m/min)


(L) Tangential Edge Coefficient (K_{te})
Cutting Force Coefficient (N/mm)
15
10
5
0
-5
-10
0
50
100
150
200
250
300
350
Cutting Speed (m/min)

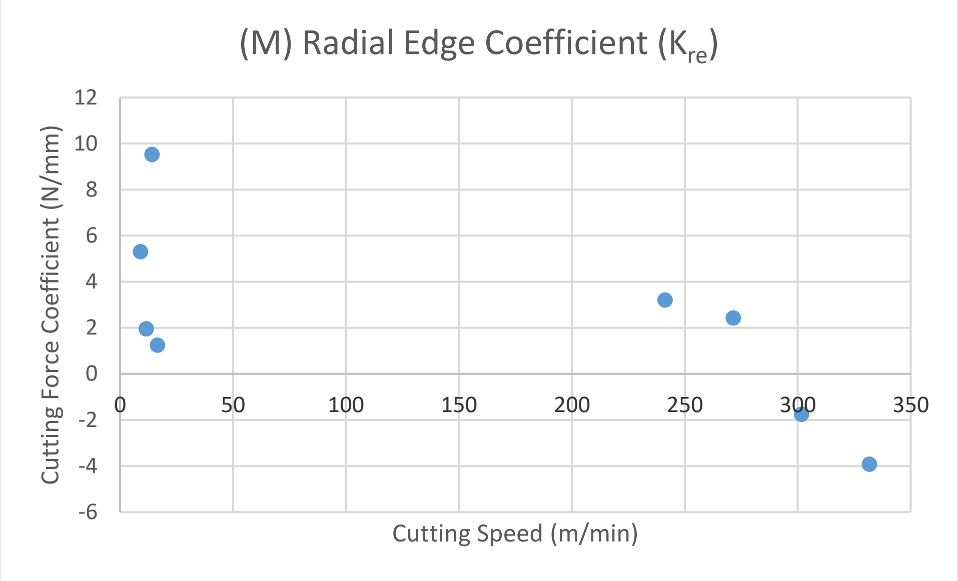
(M) Radial Edge Coefficient (K_{re})
Cutting Force Coefficient (N/mm)
Cutting Speed (m/min)
12
10
8
6
4
2
0
-2
-4
-6
0
50
100
150
200
250
300
350

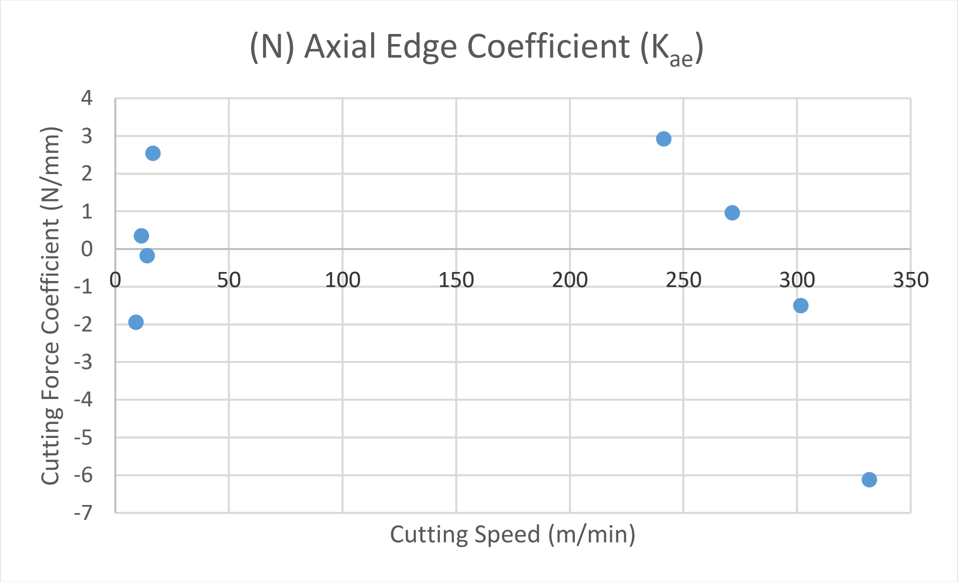
(N) Axial Edge Coefficient (K_{ae})
Cutting Force Coefficient (N/mm)
Cutting Speed (m/min)
4
3
2
1
0
-1
-2
-3
-4
-5
-6
-7
0
50
100
150
200
250
300
350

13 Appendix E

D.1 Robot Cutting Trajectory Diagrams

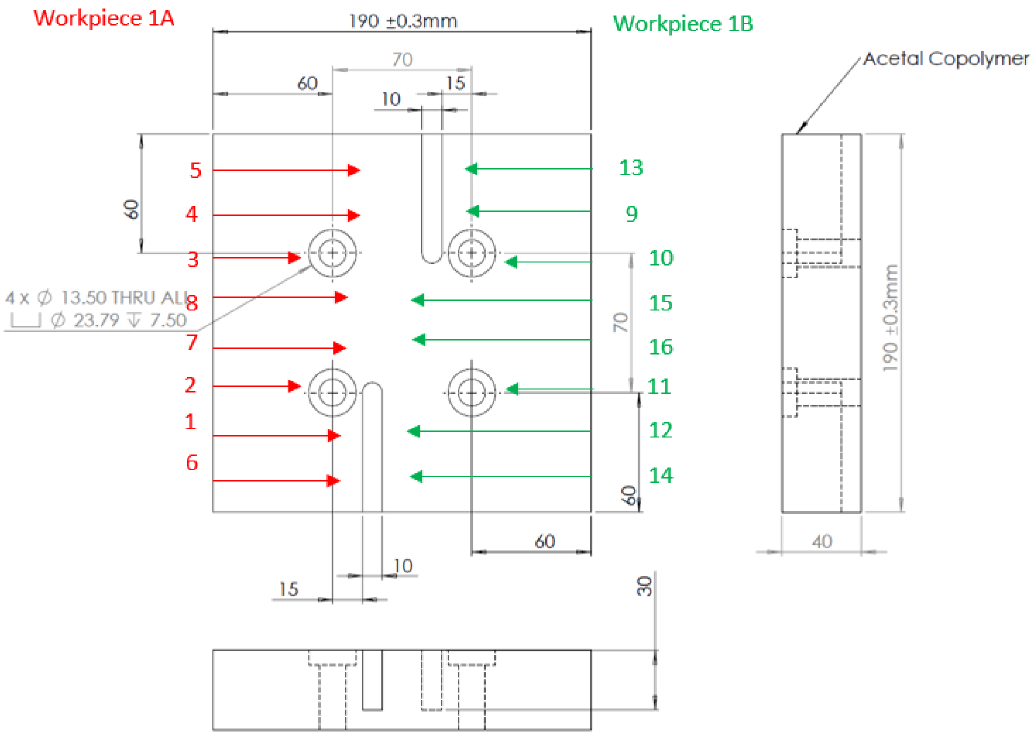

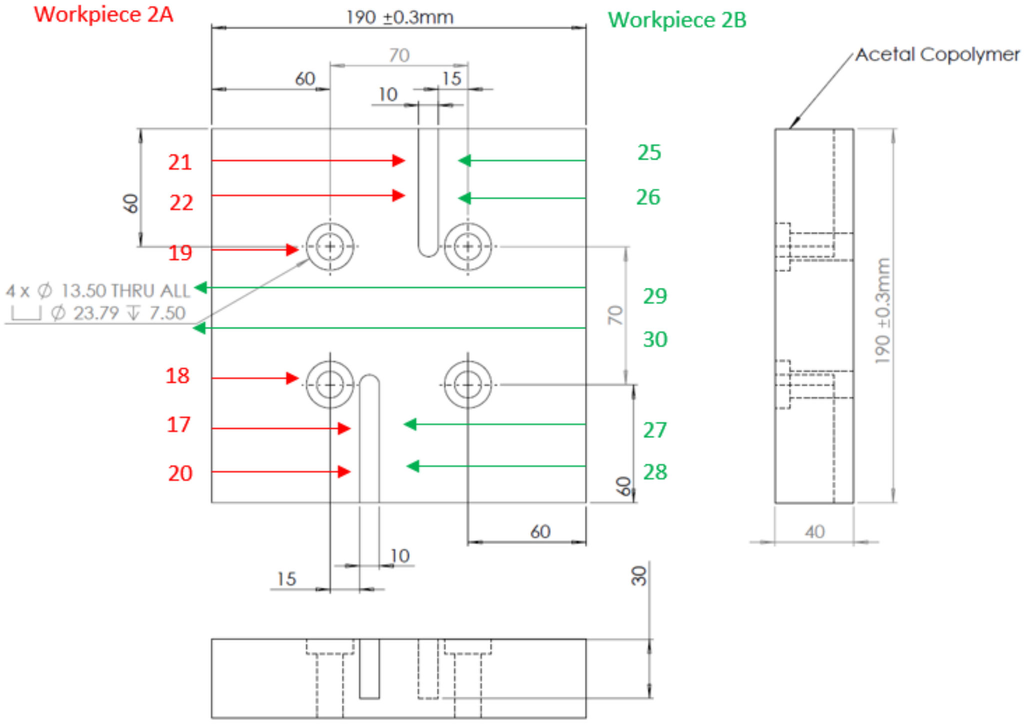

Workpiece 3C

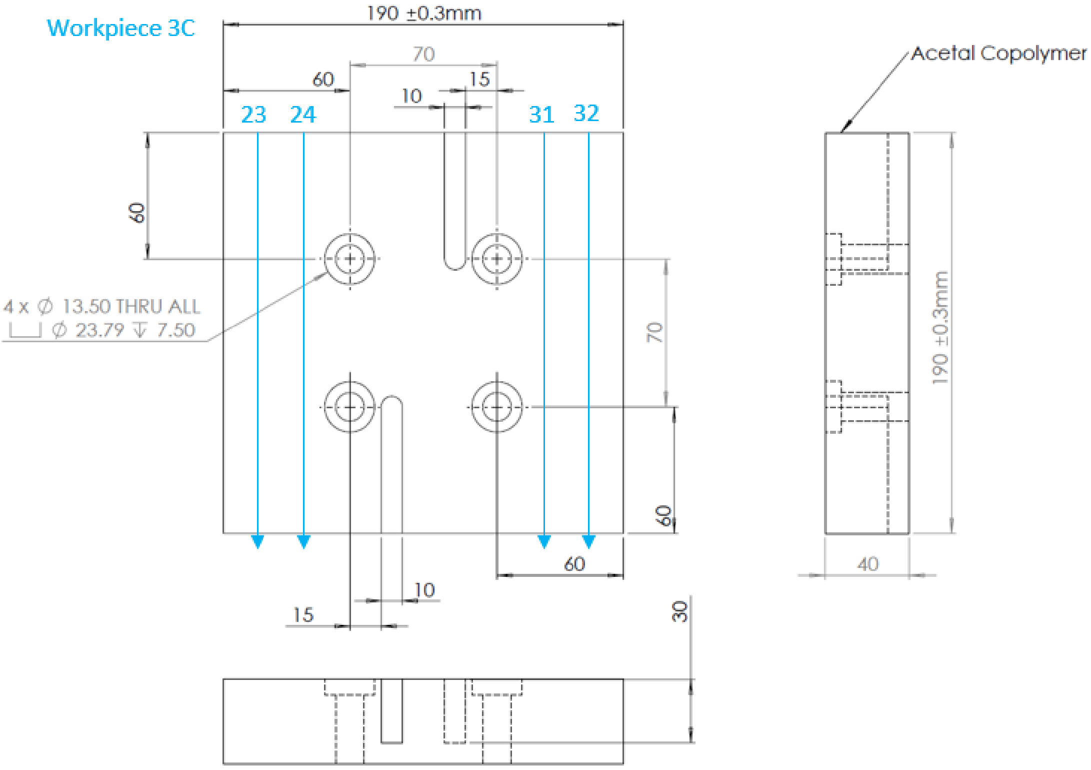

14 Appendix F

E.1 Graphical Representation of Regression Analysis in CNC Milling of WAAM Titanium

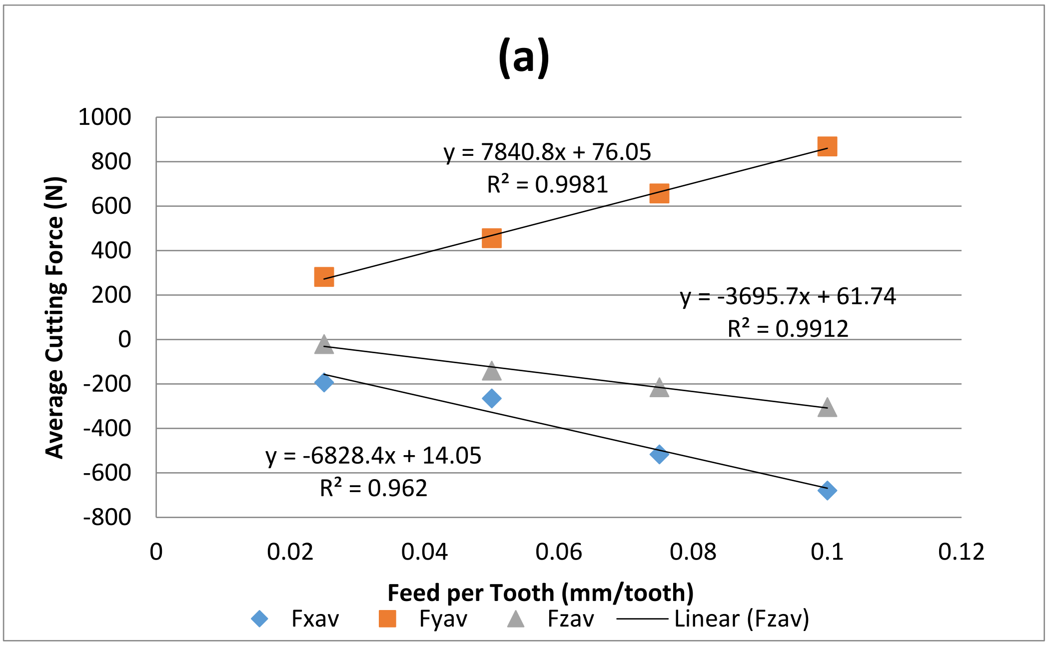

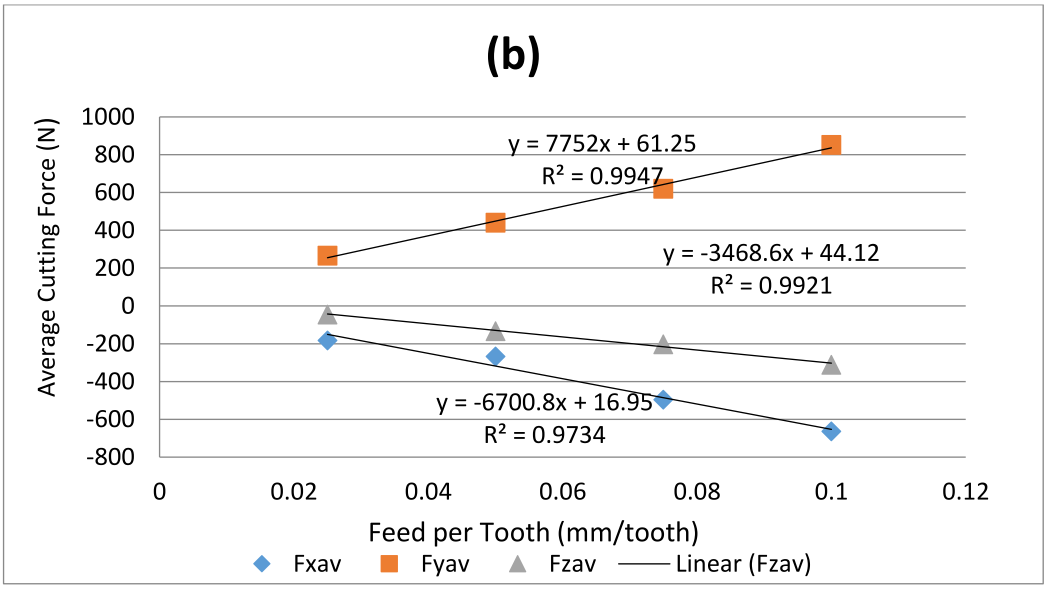

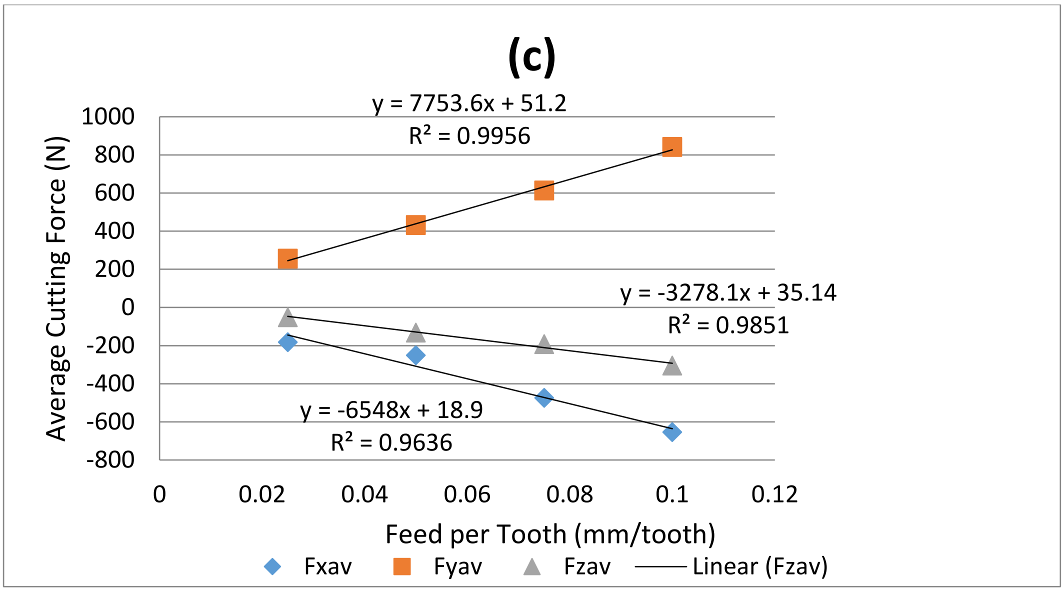
(c)
y = 7753.6x + 51.2
R² = 0.9956
y = -3278.1x + 35.14
R² = 0.9851
y = -6548x + 18.9
R² = 0.9636
Average Cutting Force (N)
1000
800
600
400
200
0
-200
-400
-600
-800
0
0.02
0.04
0.06
0.08
0.1
0.12
Feed per Tooth (mm/tooth)
Fxav
Fyav
Fzav
Linear (Fzav)

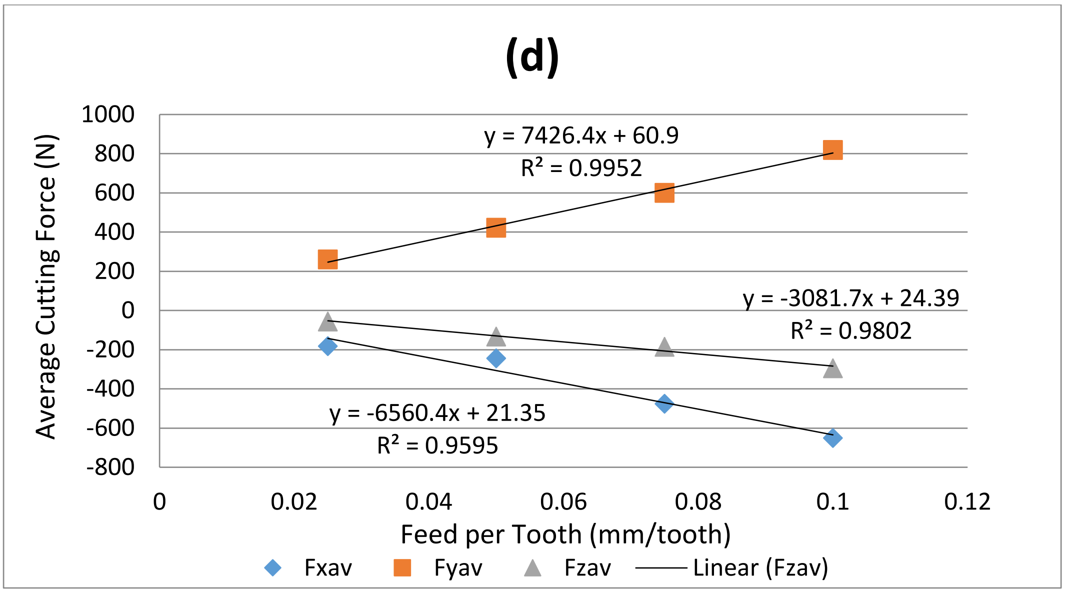
(d)
y = 7426.4x + 60.9
R² = 0.9952
y = -3081.7x + 24.39
R² = 0.9802
y = -6560.4x + 21.35
R² = 0.9595
Average Cutting Force (N)
1000
800
600
400
200
0
-200
-400
-600
-800
0
0.02
0.04
0.06
0.08
0.1
0.12
Feed per Tooth (mm/tooth)
Fxav
Fyav
Fzav
Linear (Fzav)

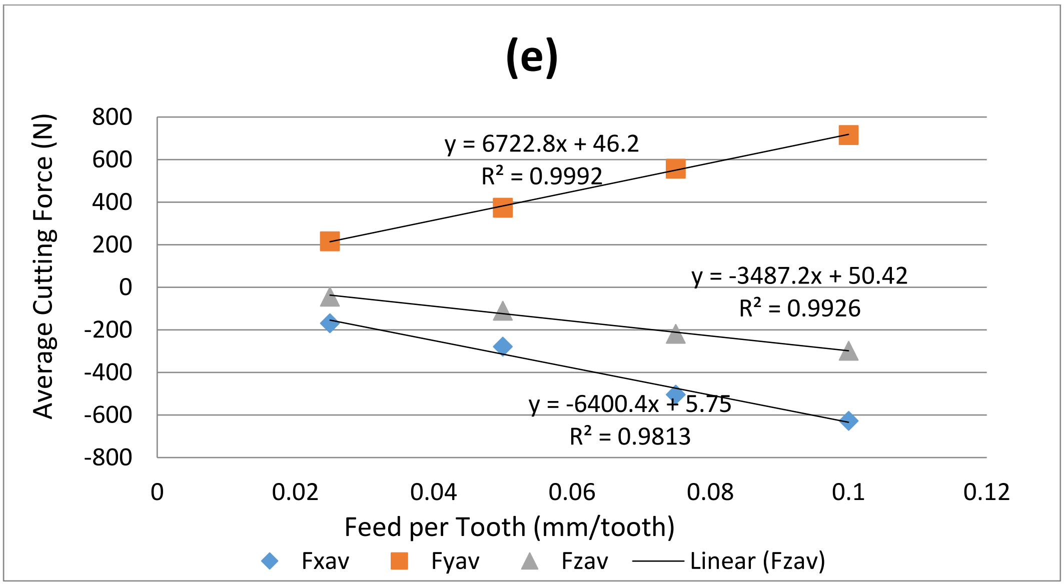
(e)
y = 6722.8x + 46.2
R² = 0.9992
y = -3487.2x + 50.42
R² = 0.9926
y = -6400.4x + 5.75
R² = 0.9813
Average Cutting Force (N)
800
600
400
200
0
-200
-400
-600
-800
0
0.02
0.04
0.06
0.08
0.1
0.12
Feed per Tooth (mm/tooth)
Fxav
Fyav
Fzav
Linear (Fzav)

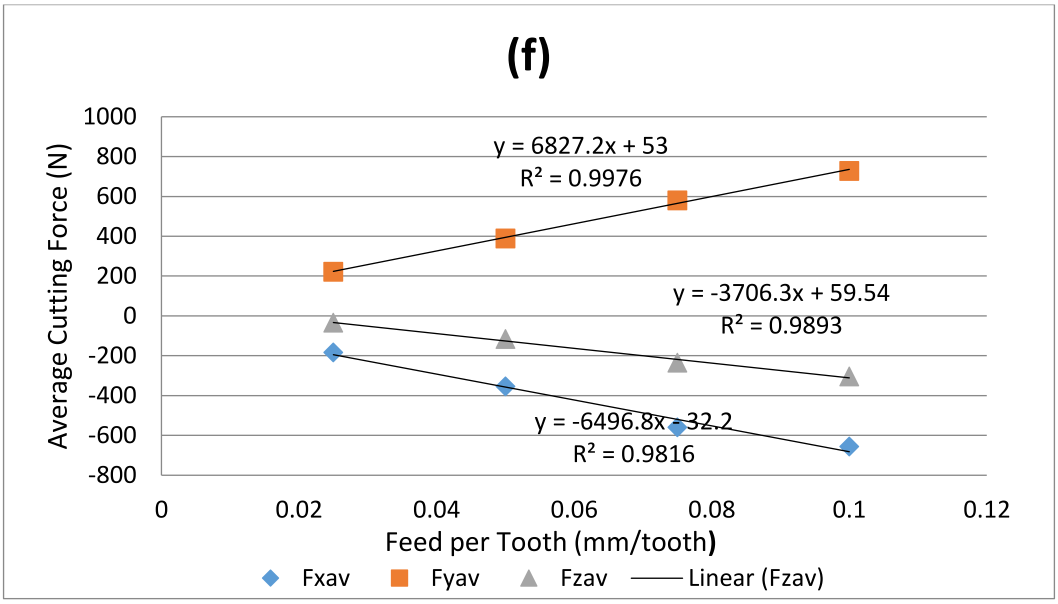
(f)
Average Cutting Force (N)
1000
800
600
400
200
0
-200
-400
-600
-800
0
0.02
0.04
0.06
0.08
0.1
0.12
Feed per Tooth (mm/tooth)
y = 6827.2x + 53
R² = 0.9976
y = -3706.3x + 59.54
R² = 0.9893
y = -6496.8x - 32.2
R² = 0.9816
◆ Fxav
■ Fyav
▲ Fzav
— Linear (Fzav)

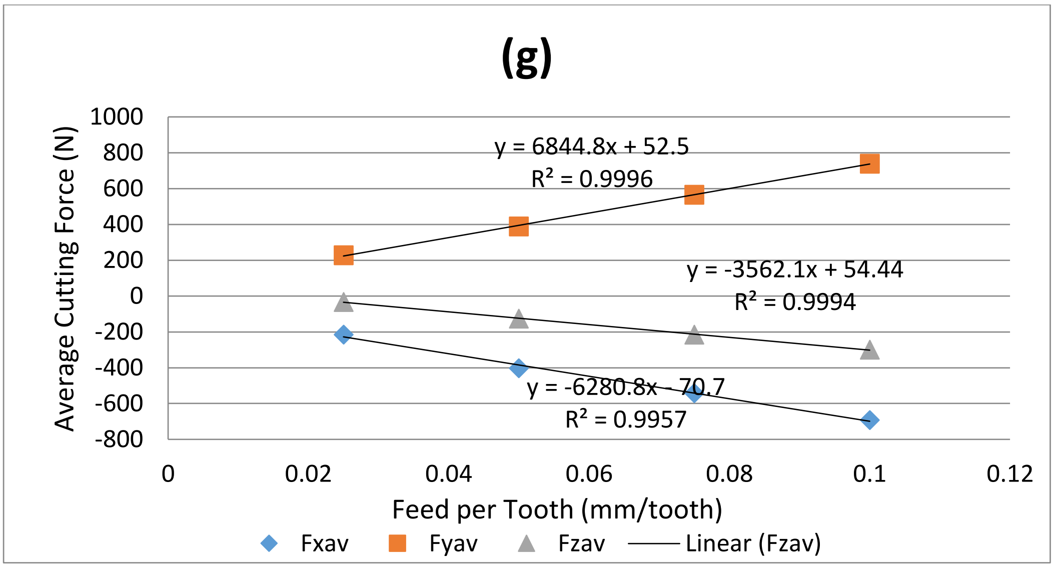
(g)
Average Cutting Force (N)
1000
800
600
400
200
0
-200
-400
-600
-800
0
0.02
0.04
0.06
0.08
0.1
0.12
Feed per Tooth (mm/tooth)
y = 6844.8x + 52.5
R² = 0.9996
y = -3562.1x + 54.44
R² = 0.9994
y = -6280.8x - 70.7
R² = 0.9957
◆ Fxav
■ Fyav
▲ Fzav
— Linear (Fzav)

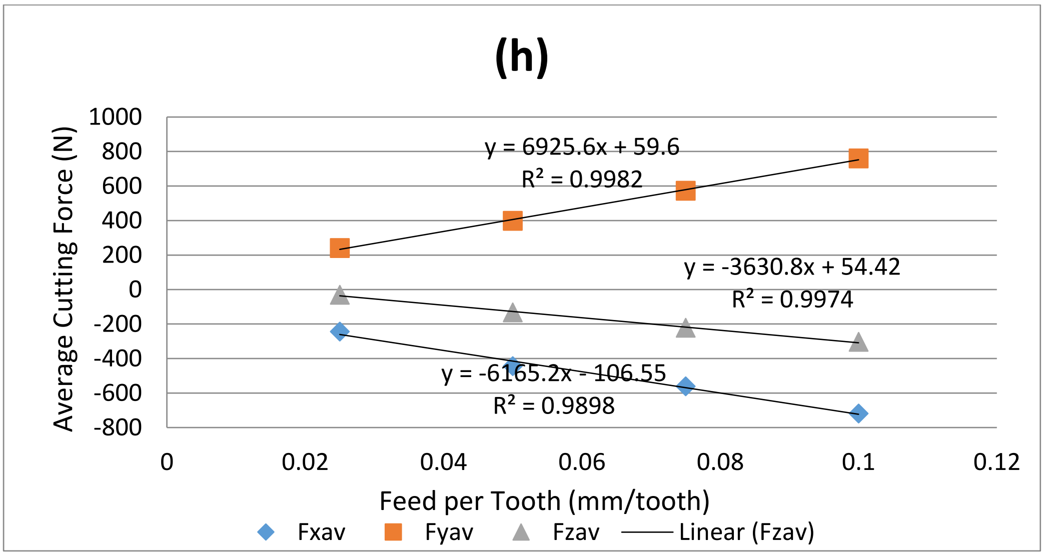
(h)
Average Cutting Force (N)
1000
800
600
400
200
0
-200
-400
-600
-800
0
0.02
0.04
0.06
0.08
0.1
0.12
Feed per Tooth (mm/tooth)
y = 6925.6x + 59.6
R² = 0.9982
y = -3630.8x + 54.42
R² = 0.9974
y = -6165.2x - 106.55
R² = 0.9898
◆ Fxav
■ Fyav
▲ Fzav
— Linear (Fzav)

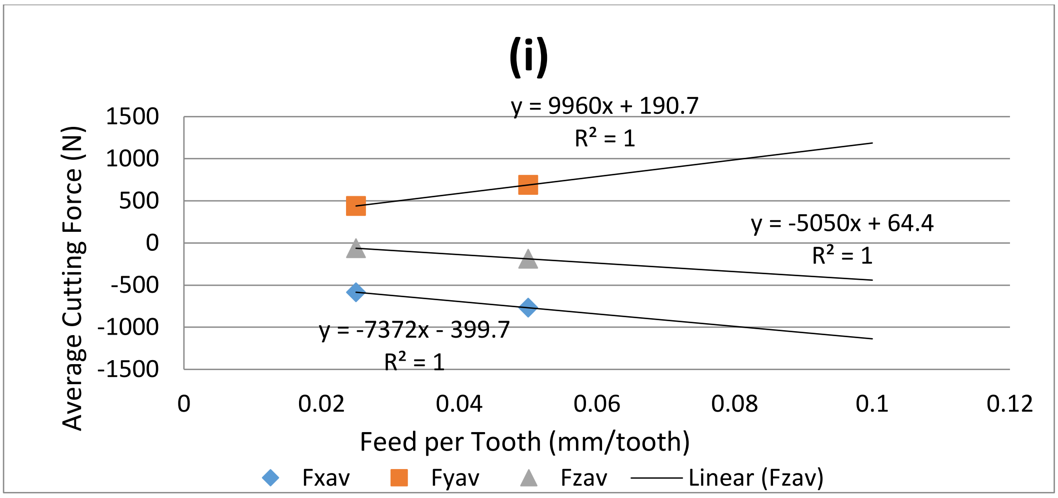
(i)
y = 9960x + 190.7
R² = 1
y = -5050x + 64.4
R² = 1
y = -7372x - 399.7
R² = 1
Average Cutting Force (N)
1500
1000
500
0
-500
-1000
-1500
0
0.02
0.04
0.06
0.08
0.1
0.12
Feed per Tooth (mm/tooth)
◆ Fxav
■ Fyav
▲ Fzav
Linear (Fzav)

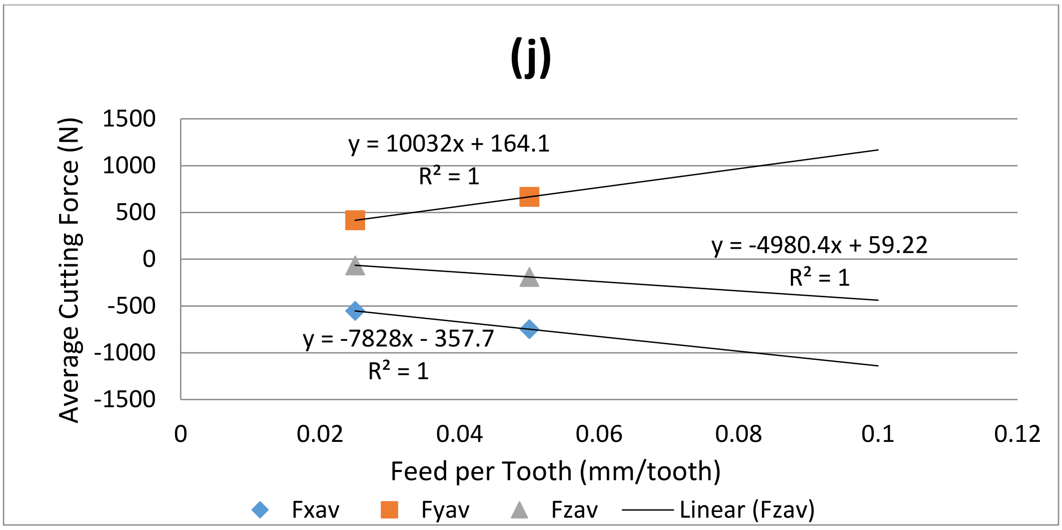
(j)
y = 10032x + 164.1
R² = 1
y = -4980.4x + 59.22
R² = 1
y = -7828x - 357.7
R² = 1
Average Cutting Force (N)
1500
1000
500
0
-500
-1000
-1500
0
0.02
0.04
0.06
0.08
0.1
0.12
Feed per Tooth (mm/tooth)
◆ Fxav
■ Fyav
▲ Fzav
Linear (Fzav)

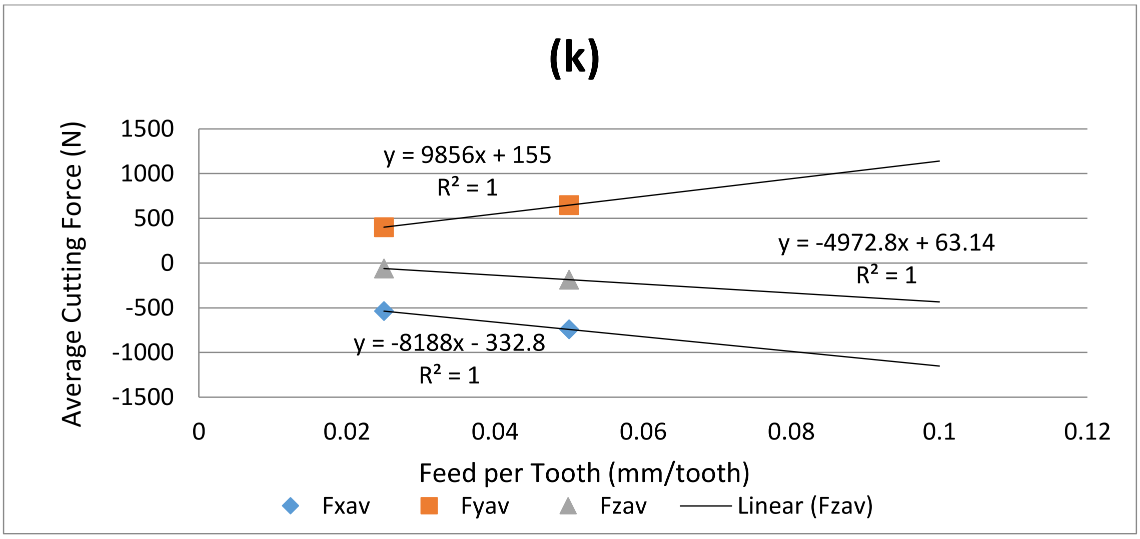
(k)
y = 9856x + 155
R² = 1
y = -4972.8x + 63.14
R² = 1
y = -8188x - 332.8
R² = 1
Average Cutting Force (N)
1500
1000
500
0
-500
-1000
-1500
0
0.02
0.04
0.06
0.08
0.1
0.12
Feed per Tooth (mm/tooth)
◆ Fxav
■ Fyav
▲ Fzav
Linear (Fzav)

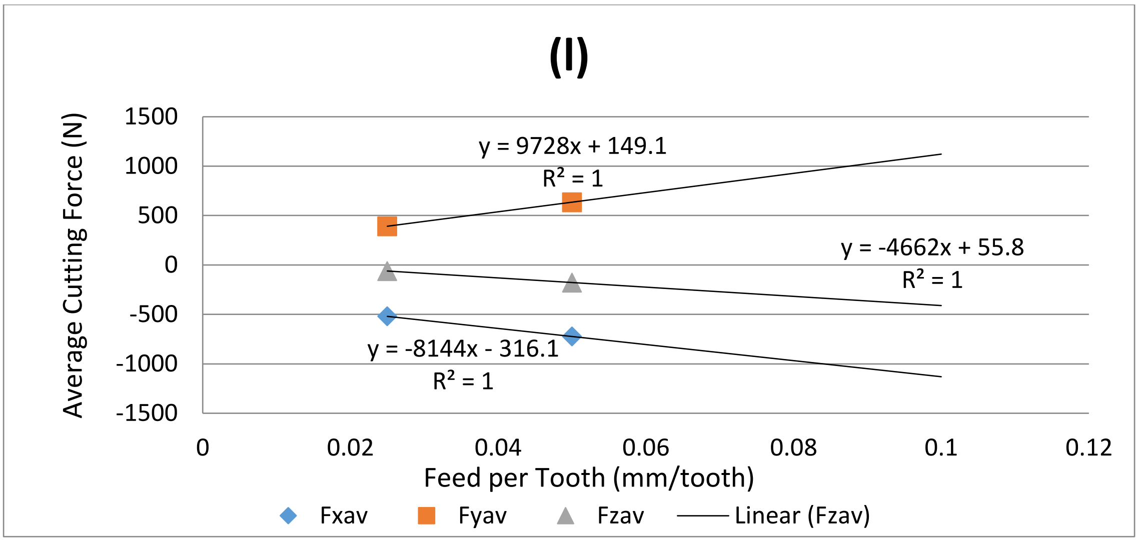
(l)
Average Cutting Force (N)
1500
1000
500
0
-500
-1000
-1500
y = 9728x + 149.1
R² = 1
y = -4662x + 55.8
R² = 1
y = -8144x - 316.1
R² = 1
0
0.02
0.04
0.06
0.08
0.1
0.12
Feed per Tooth (mm/tooth)
Fxav
Fyav
Fzav
Linear (Fzav)

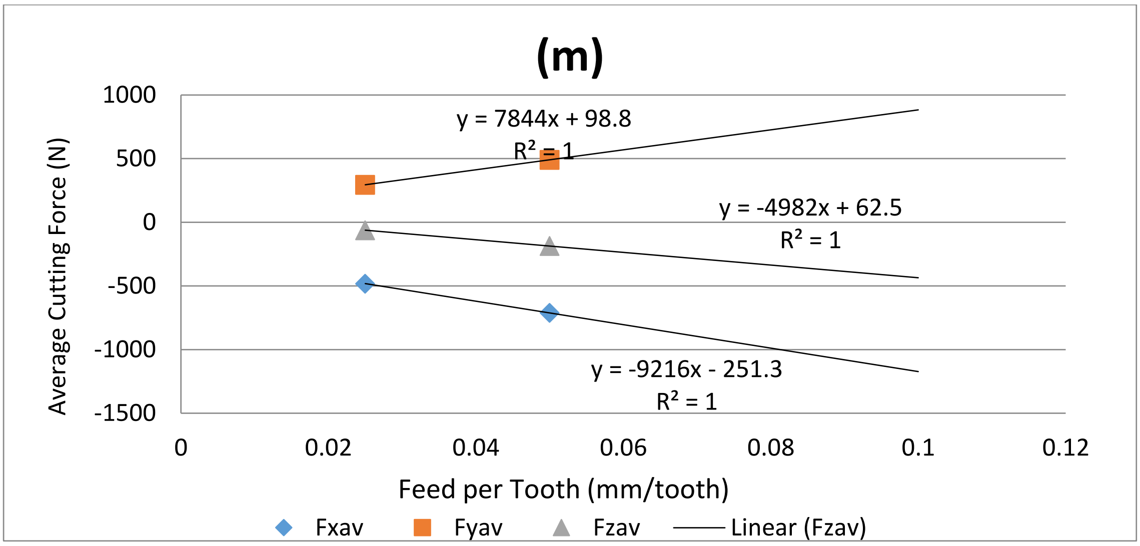
(m)
Average Cutting Force (N)
1000
500
0
-500
-1000
-1500
y = 7844x + 98.8
R² = 1
y = -4982x + 62.5
R² = 1
y = -9216x - 251.3
R² = 1
0
0.02
0.04
0.06
0.08
0.1
0.12
Feed per Tooth (mm/tooth)
Fxav
Fyav
Fzav
Linear (Fzav)

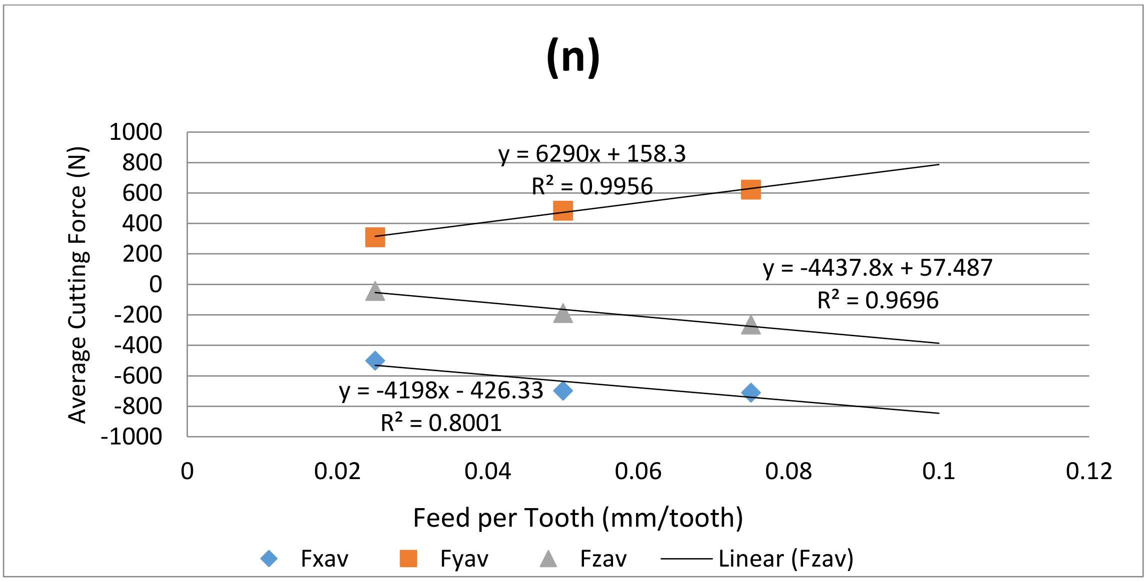
(n)
Average Cutting Force (N)
1000
800
600
400
200
0
-200
-400
-600
-800
-1000
y = 6290x + 158.3
R² = 0.9956
y = -4437.8x + 57.487
R² = 0.9696
y = -4198x - 426.33
R² = 0.8001
0
0.02
0.04
0.06
0.08
0.1
0.12
Feed per Tooth (mm/tooth)
Fxav
Fyav
Fzav
Linear (Fzav)

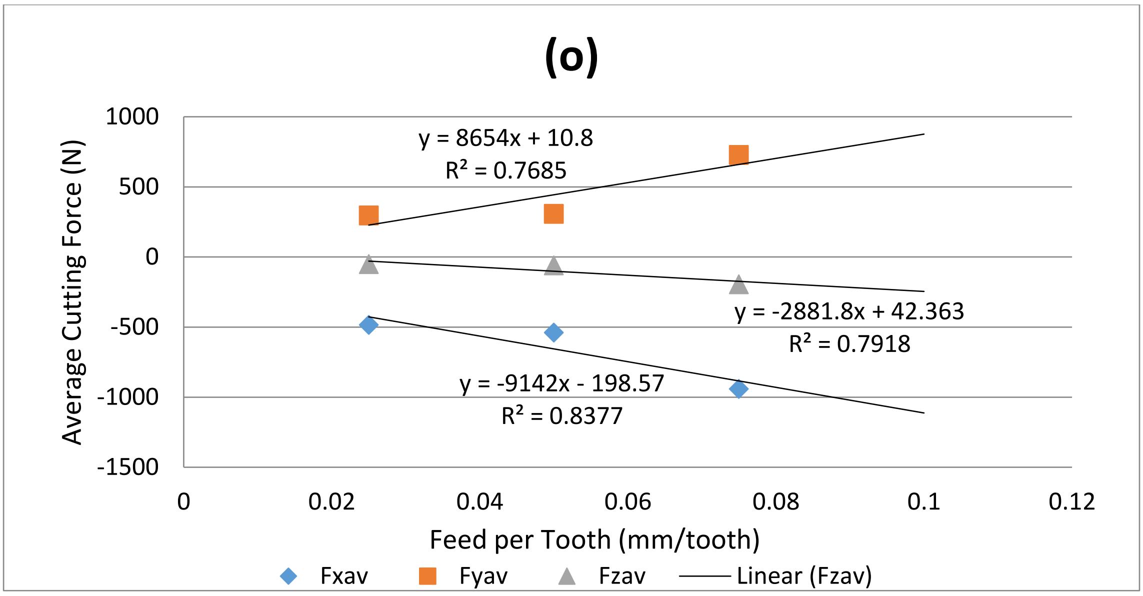
(o)
Average Cutting Force (N)
1000
500
0
-500
-1000
-1500
0
0.02
0.04
0.06
0.08
0.1
0.12
Feed per Tooth (mm/tooth)
y = 8654x + 10.8
R² = 0.7685
y = -2881.8x + 42.363
R² = 0.7918
y = -9142x - 198.57
R² = 0.8377
◆ Fxav
■ Fyav
▲ Fzav
—— Linear (Fzav)

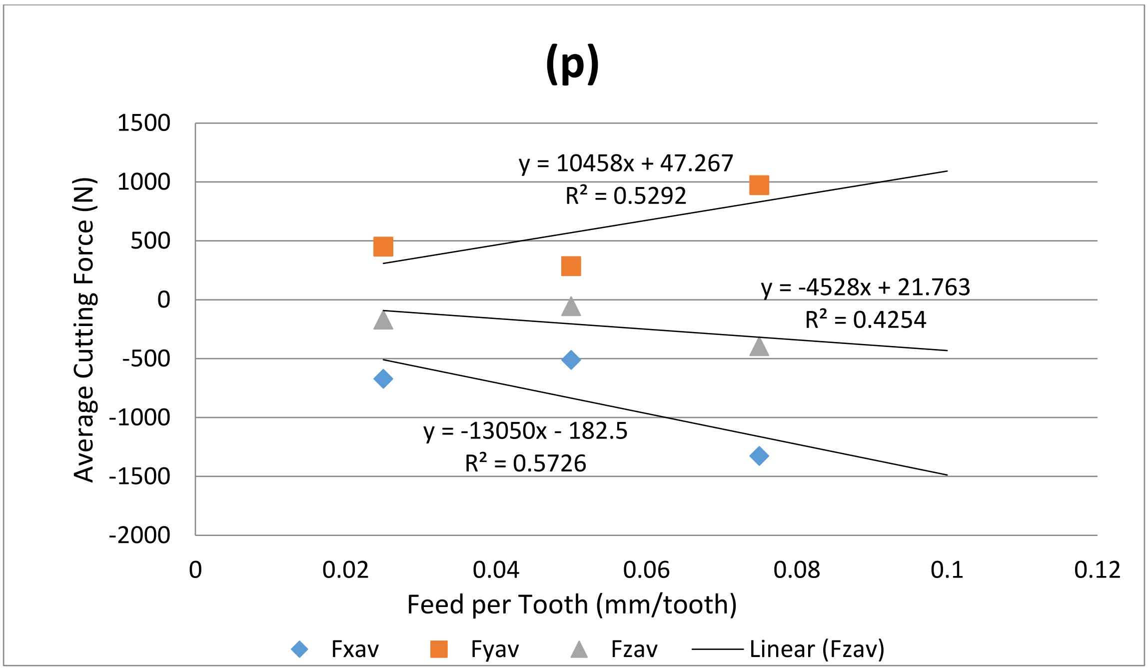
(p)
Average Cutting Force (N)
1500
1000
500
0
-500
-1000
-1500
-2000
0
0.02
0.04
0.06
0.08
0.1
0.12
Feed per Tooth (mm/tooth)
y = 10458x + 47.267
R² = 0.5292
y = -4528x + 21.763
R² = 0.4254
y = -13050x - 182.5
R² = 0.5726
◆ Fxav
■ Fyav
▲ Fzav
—— Linear (Fzav)

15 Appendix G

G.1 Graphical Representations of Relationships between Cutting Speed and Cutting Force Coefficients in CNC Milling of Titanium and WAAM Titanium

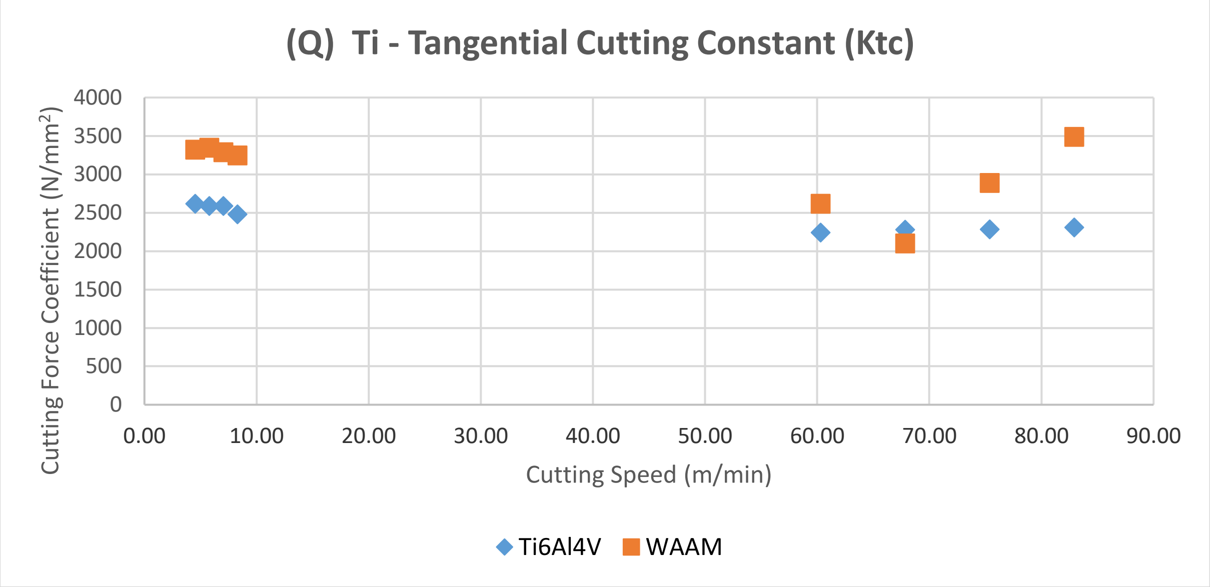

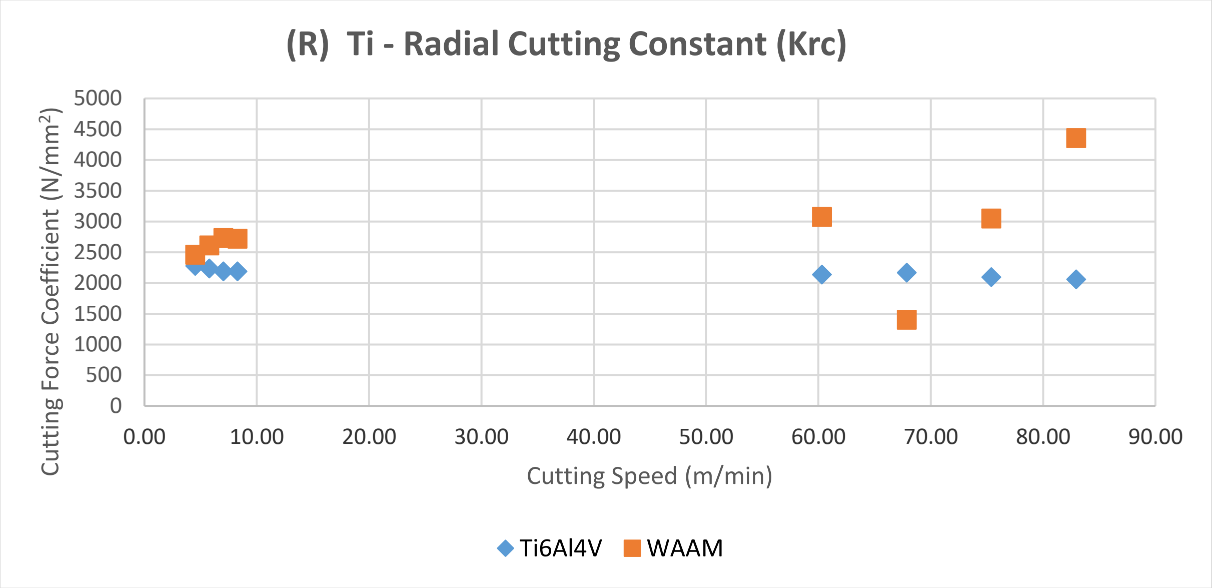

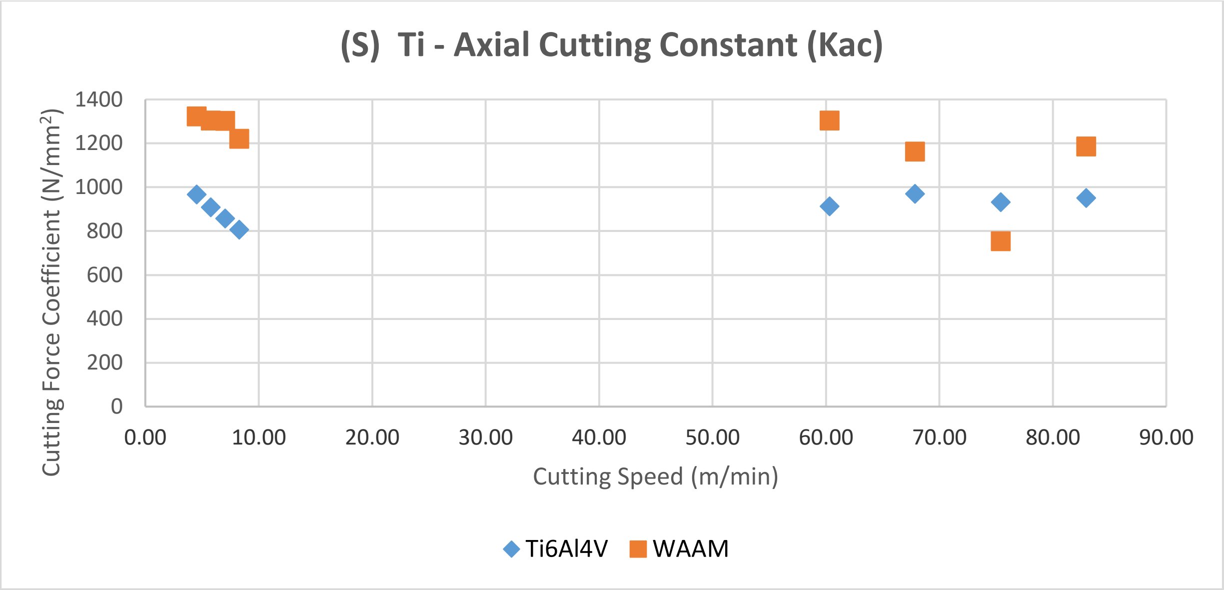
(S) Ti - Axial Cutting Constant (Kac)
Cutting Force Coefficient (N/mm²)
1400
1200
1000
800
600
400
200
0
0.00
10.00
20.00
30.00
40.00
50.00
60.00
70.00
80.00
90.00
Cutting Speed (m/min)
◆ Ti6Al4V
■ WAAM

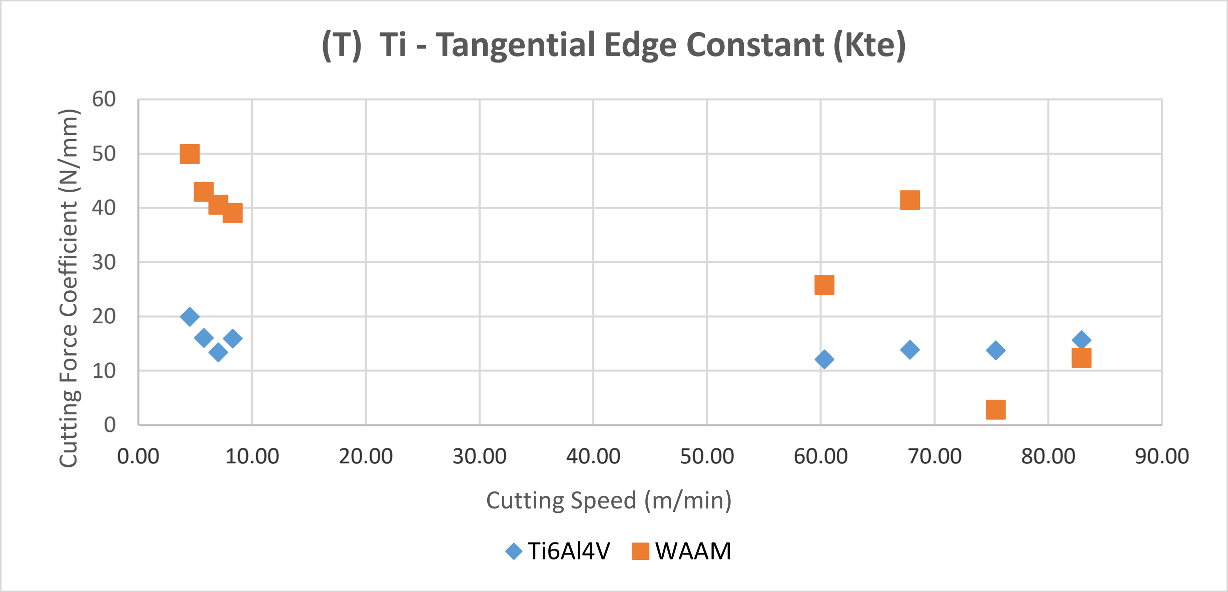
(T) Ti - Tangential Edge Constant (Kte)
Cutting Force Coefficient (N/mm)
60
50
40
30
20
10
0
0.00
10.00
20.00
30.00
40.00
50.00
60.00
70.00
80.00
90.00
Cutting Speed (m/min)
◆ Ti6Al4V
■ WAAM

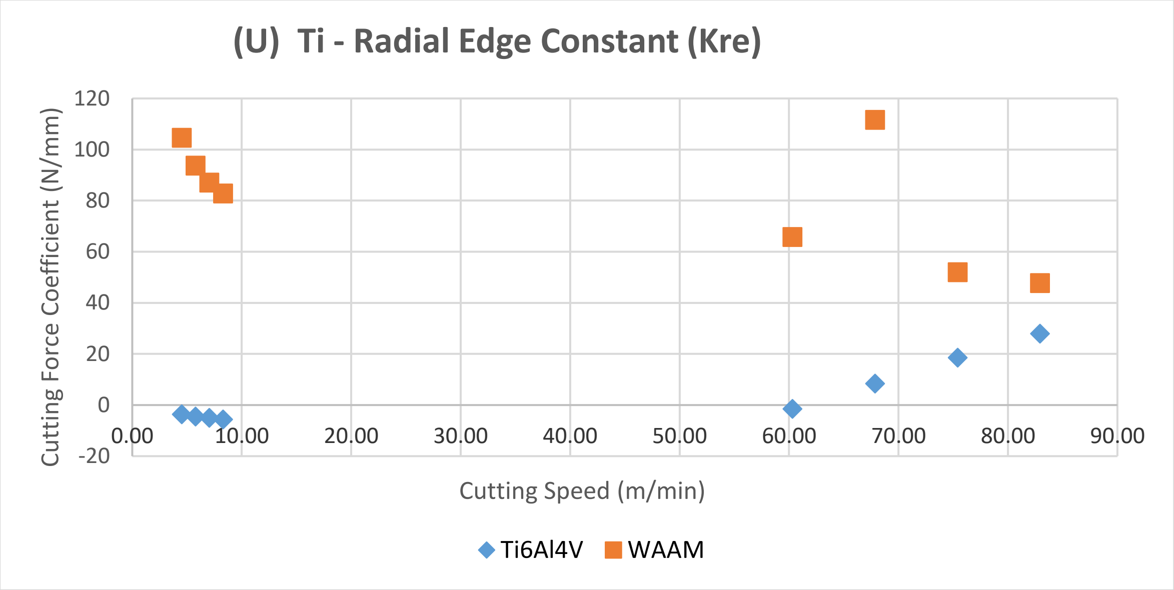
(U) Ti - Radial Edge Constant (Kre)
Cutting Force Coefficient (N/mm)
120
100
80
60
40
20
0
-20
0.00
10.00
20.00
30.00
40.00
50.00
60.00
70.00
80.00
90.00
Cutting Speed (m/min)
◆ Ti6Al4V
■ WAAM

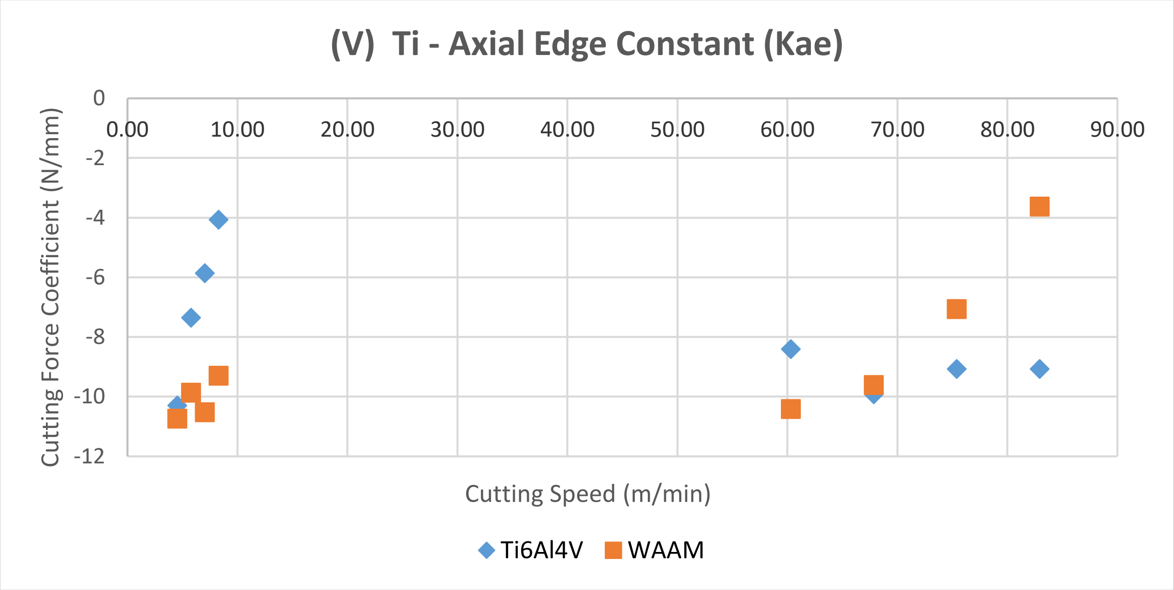
(V) Ti - Axial Edge Constant (Kae)
Cutting Force Coefficient (N/mm)
0
-2
-4
-6
-8
-10
-12
0.00
10.00
20.00
30.00
40.00
50.00
60.00
70.00
80.00
90.00
Cutting Speed (m/min)
◆ Ti6Al4V
■ WAAM

16 Appendix H

G.1 Graphical Representation of CNC Cutting Trajectories

G.1.1 Cast Titanium Cutting Trajectories

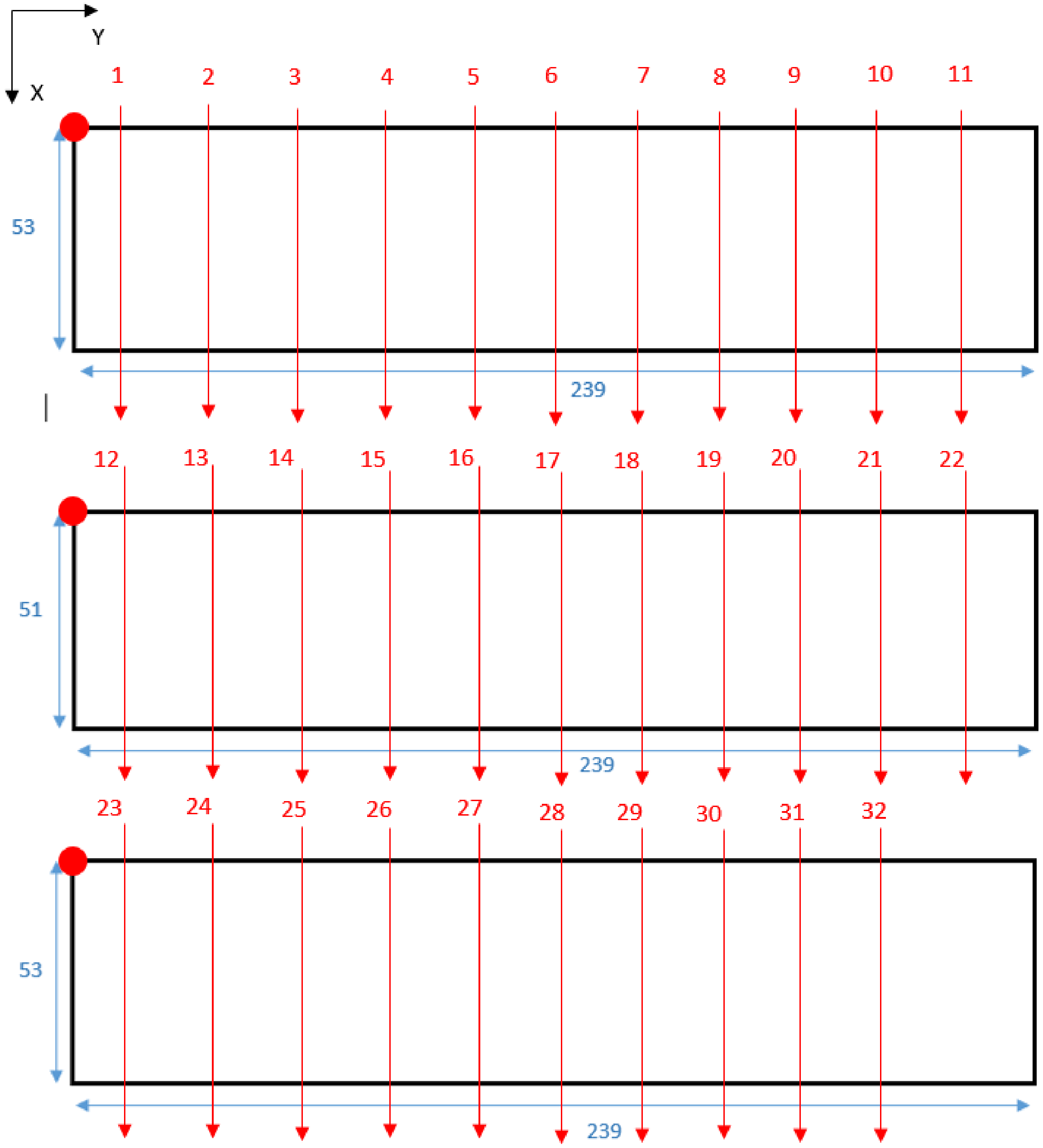

G.1.2 WAAM Titanium Cutting Trajectories

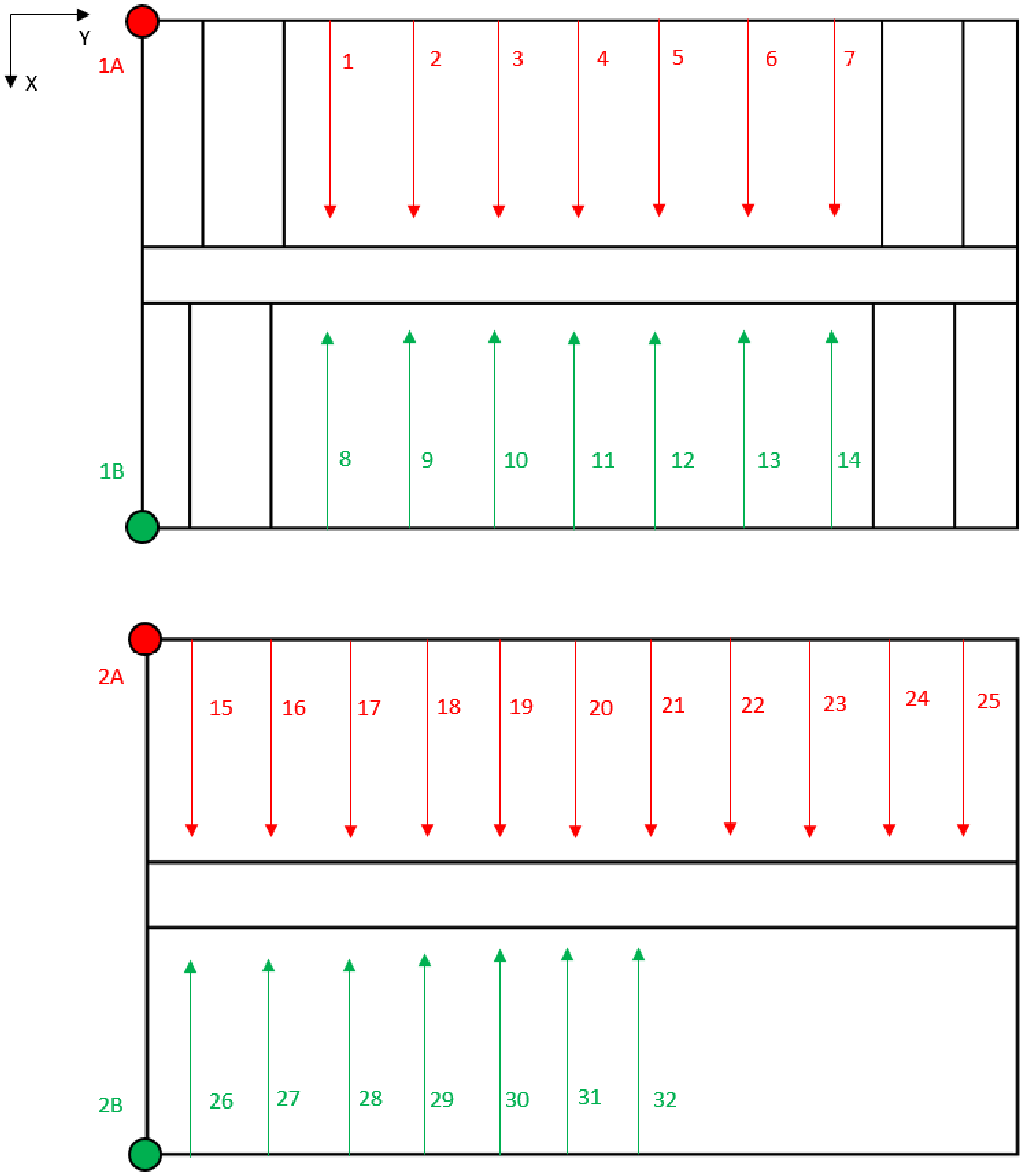

17 Appendix I

I.1 Experimental FRFs for Damping Derivations

I.1.1 Experimental FRF Damping Analysis – Configuration 1

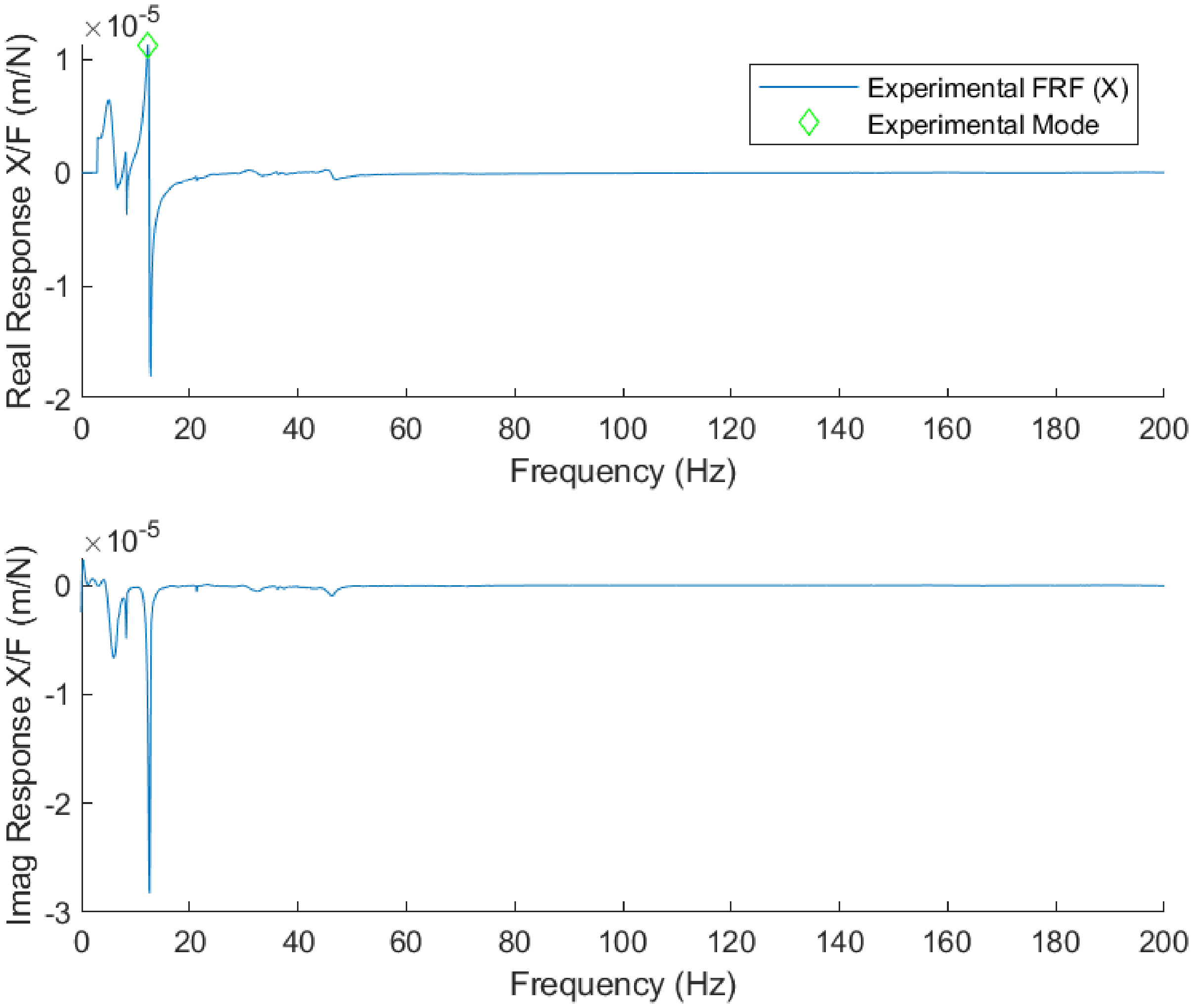

Frequency (Hz)	Response (m/N)	Damping Ratio
12.3	1.132522e-05	0.0284552845528455

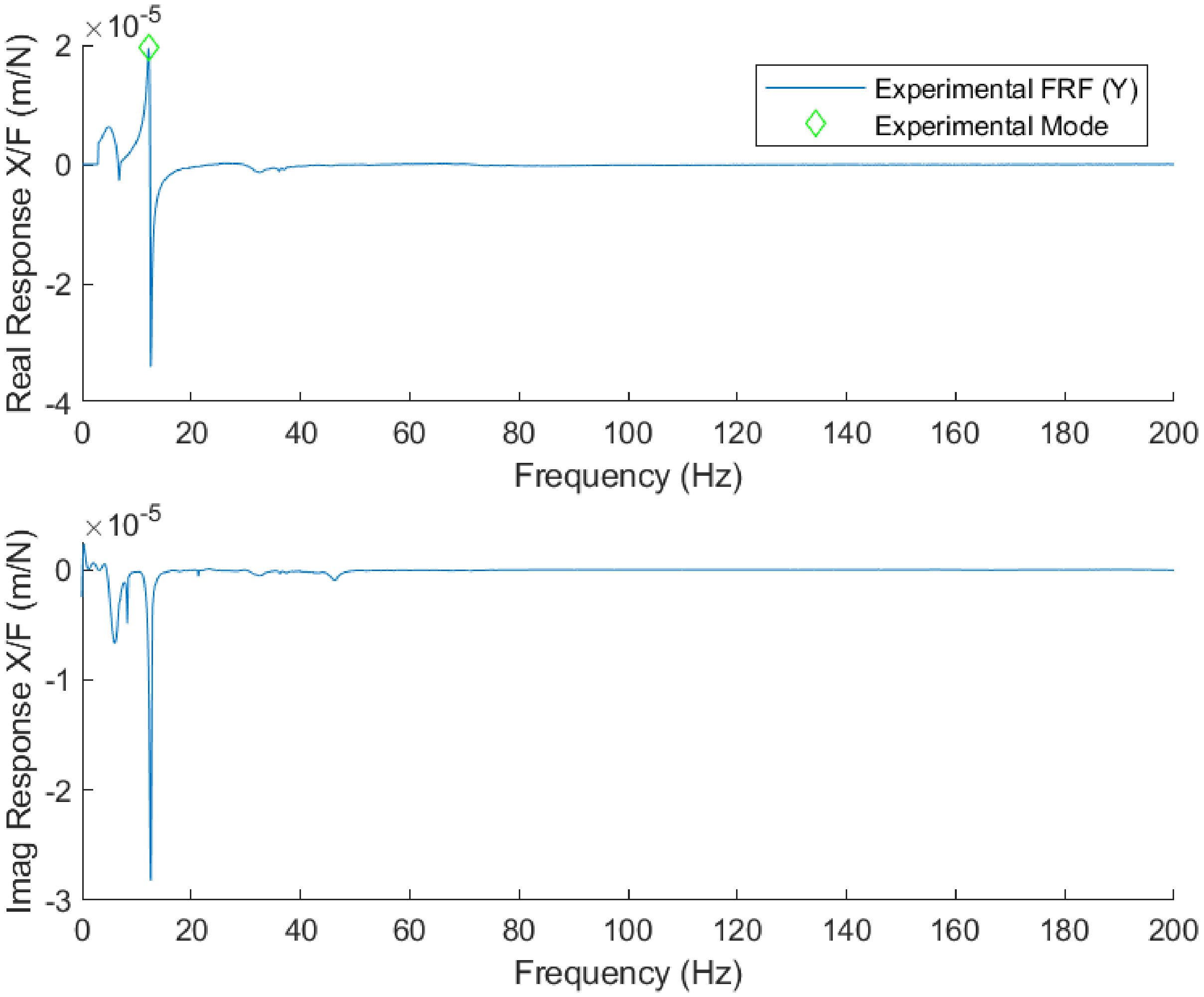

Frequency (Hz)	Response (m/N)	Damping Ratio
12.2	Response: 1.953579e-05	0.0245901639344262

I.1.2 Experimental FRF Damping Analysis – Configuration 2

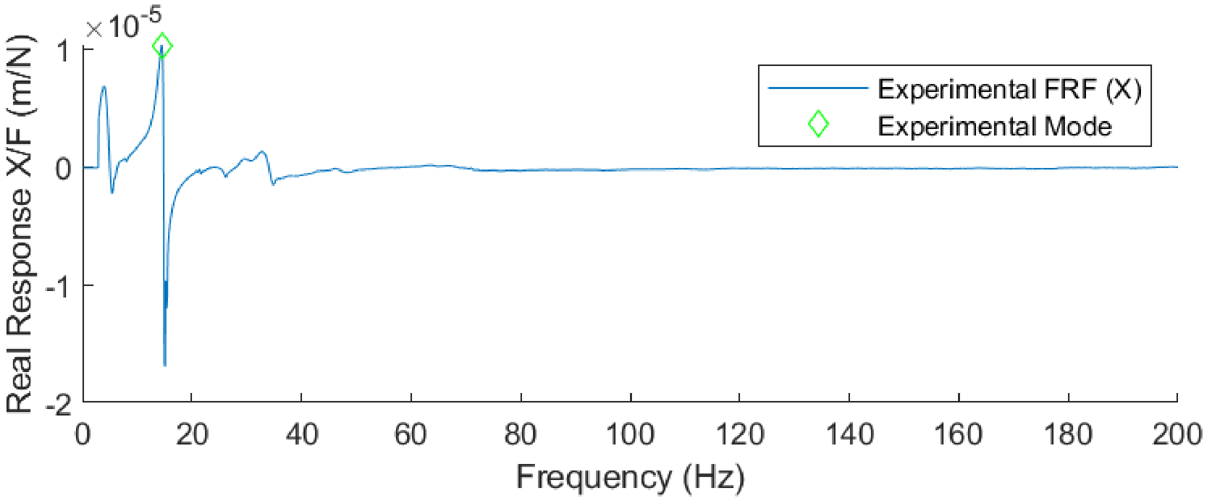

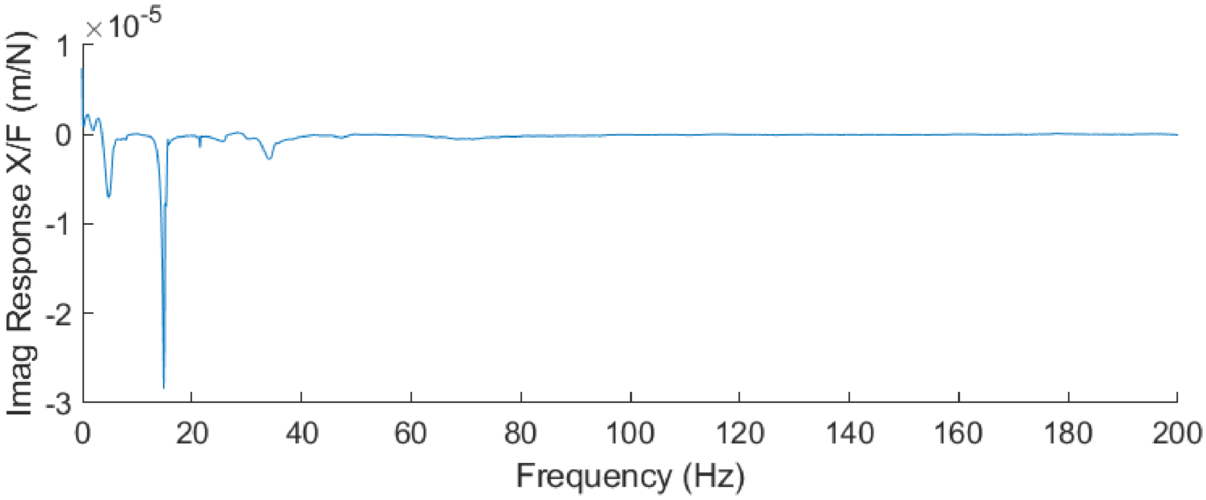

Frequency (Hz)	Response (m/N)	Damping Ratio
14.5	1.0373950e-05	0.0379310344827587

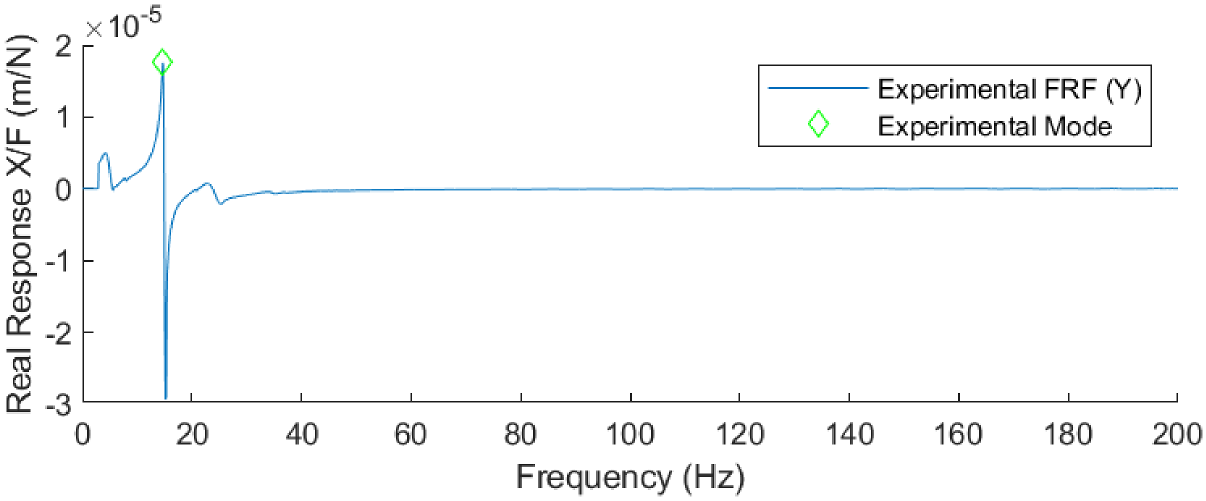

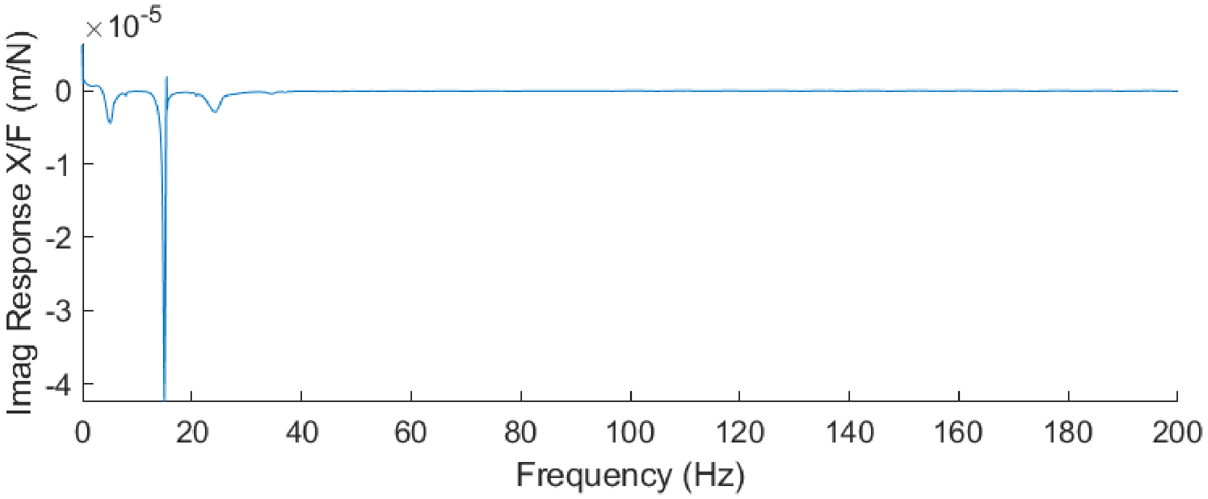

Frequency (Hz)	Response (m/N)	Damping Ratio
14.7	1.758181e-05	0.0204081632653061

I.1.3 Experimental FRF Damping Analysis – Configuration 3

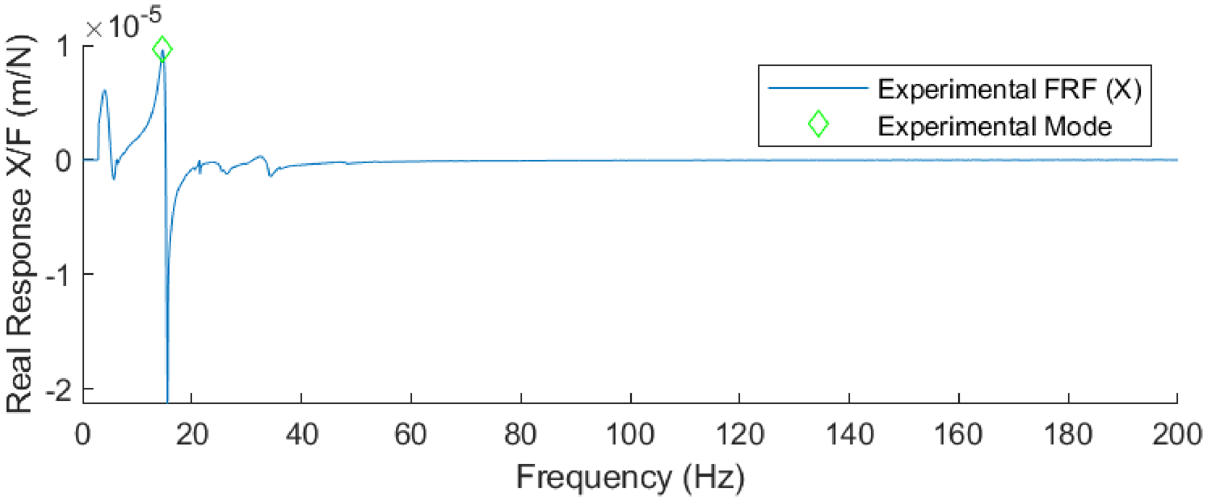

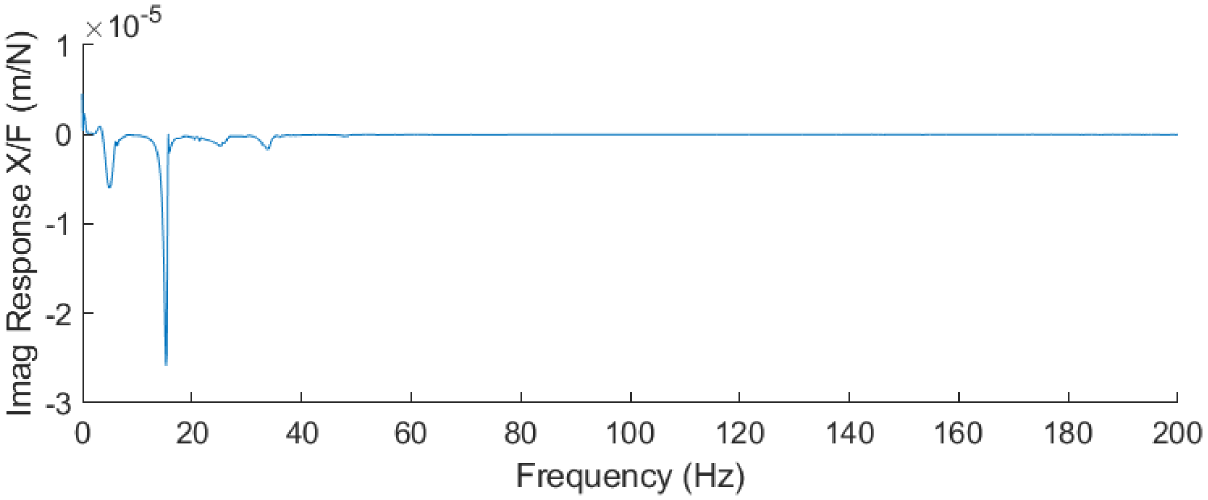

Frequency (Hz)	Response (m/N)	Damping Ratio
14.7	9.606958e-06	0.0442176870748299

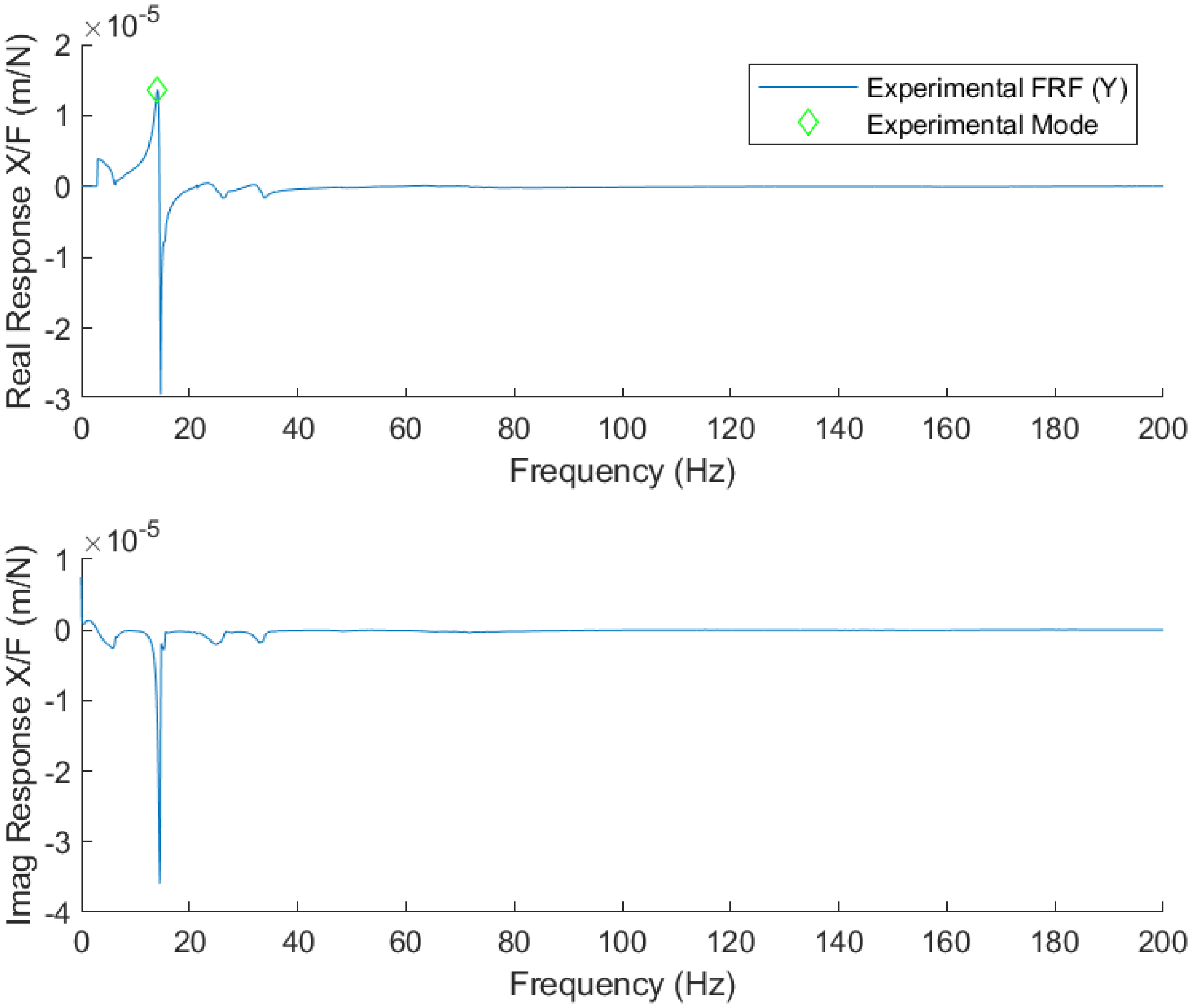

Frequency (Hz)	Response (m/N)	Damping Ratio
14.1	1.3659550e-05	0.0354609929078014

I.1.4 Experimental FRF Damping Analysis – Configuration 4

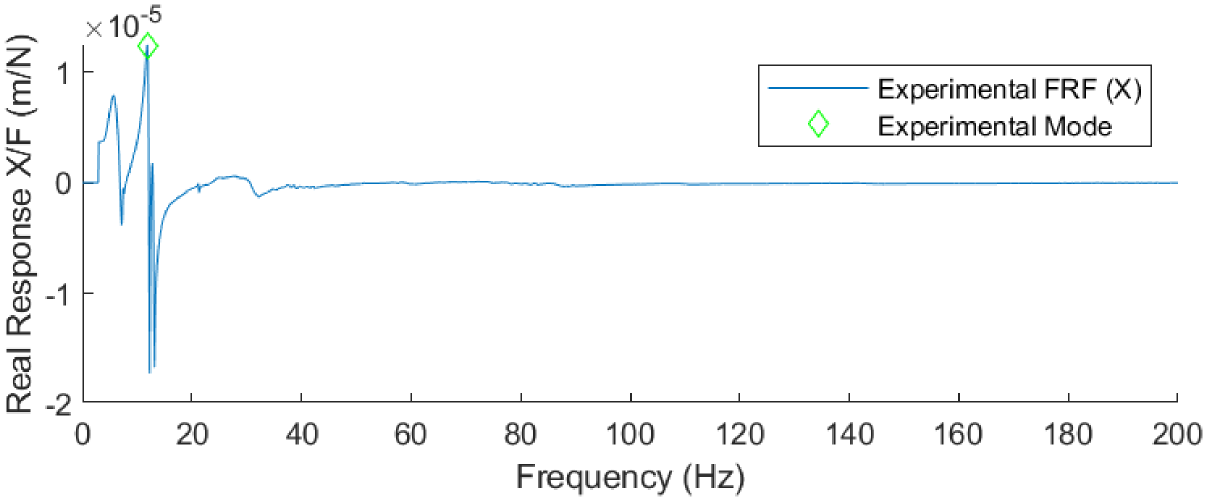

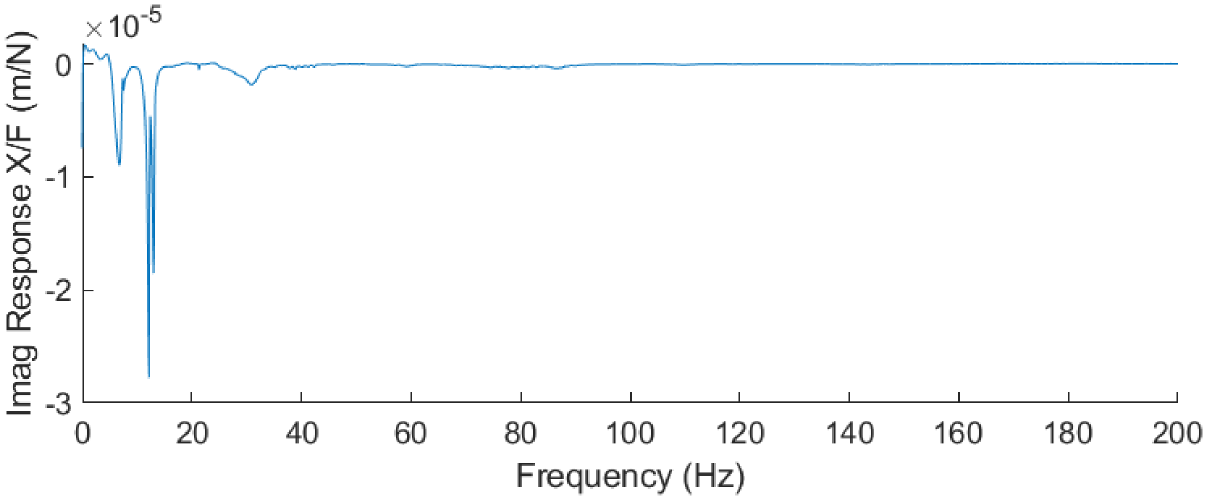

Frequency (Hz)	Response (m/N)	Damping Ratio
11.9	1.244932e-05	0.0336134453781512

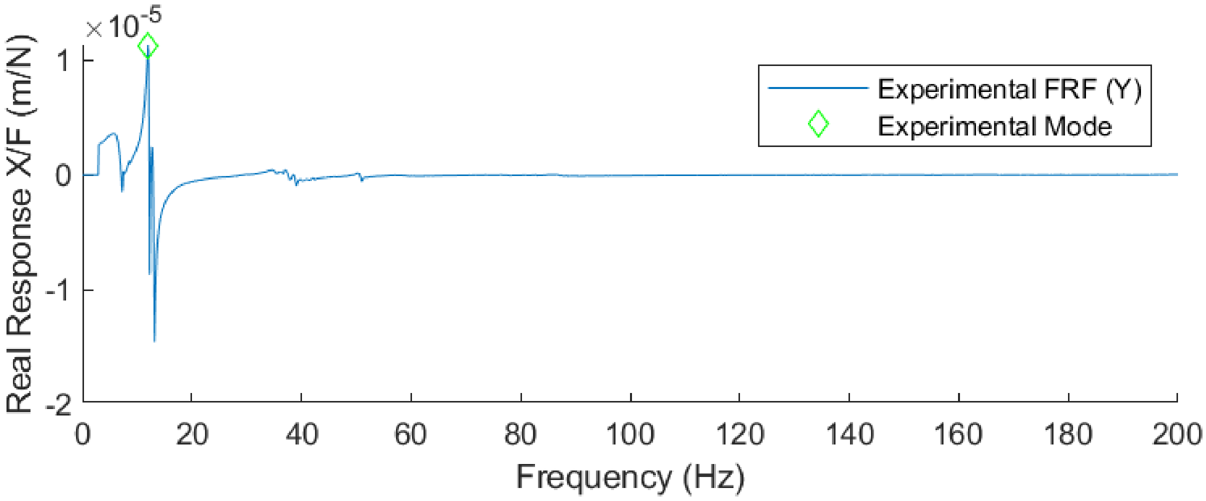

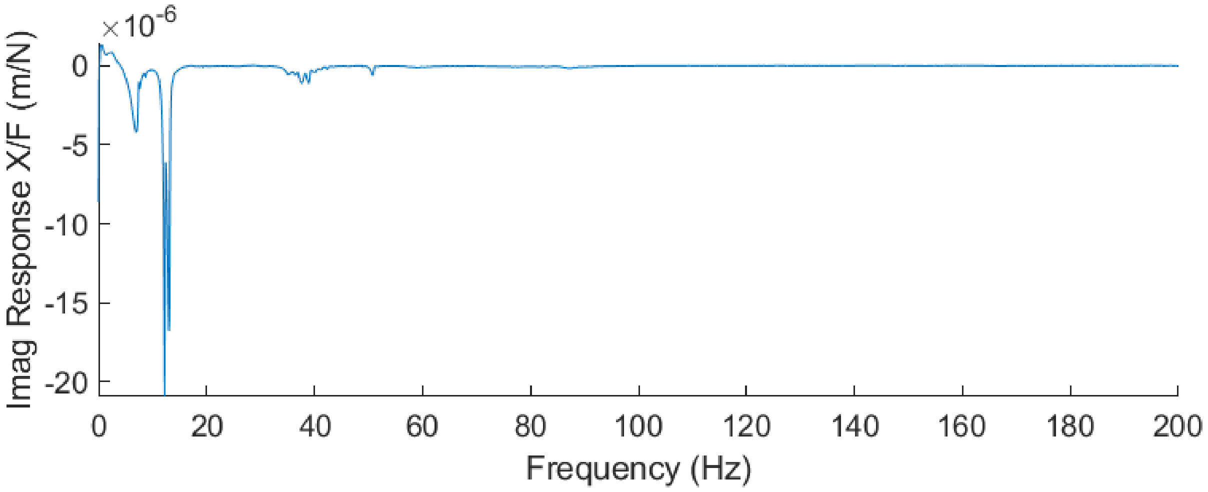

Frequency (Hz)	Response (m/N)	Damping Ratio
12	0.025	1.131007e-05

18 Appendix J

J.1 FRF Simulation Program Evaluation - Configuration 1

K_C	1	2	3	4	5	6	7	8	9	10	11	12	13	14	15	16	17	18
1	1.09E+10	-1.57E-06	1.73E-06	-5.72E-07	-3.10E-07	-4.36E-09	-1.53E+09	-3.35E-07	-1.02E-06	1.31E-08	-2.72E-07	8.48E-08	0.00E+00	0.00E+00	0.00E+00	0.00E+00	0.00E+00	0.00E+00
2	1.83E-06	4.13E+08	-3.29E-06	2.14E-08	-3.57E-07	-1.74E+08	-1.31E-07	-6.95E+06	-1.70E-08	9.24E-10	-6.98E-10	4.46E+06	0.00E+00	0.00E+00	0.00E+00	0.00E+00	0.00E+00	0.00E+00
3	1.38E-06	4.42E-06	4.13E+08	4.50E-08	1.74E+08	-8.03E-07	-7.22E-07	5.59E-09	-6.95E+06	-2.62E-10	-4.46E+06	-2.10E-09	0.00E+00	0.00E+00	0.00E+00	0.00E+00	0.00E+00	0.00E+00
4	5.83E-08	2.24E-08	-1.35E-07	1.83E+06	-1.58E+06	-6.21E+05	8.94E-10	-2.25E-09	7.78E-10	-7.58E+04	-2.20E+03	5.60E+02	0.00E+00	0.00E+00	0.00E+00	0.00E+00	0.00E+00	0.00E+00
5	1.75E-07	8.51E-07	1.74E+08	-1.58E+06	7.73E+07	-8.65E+06	-2.60E-08	-1.40E-09	-4.46E+06	-2.20E+03	-4.67E+06	2.17E+05	0.00E+00	0.00E+00	0.00E+00	0.00E+00	0.00E+00	0.00E+00
6	-1.53E-07	-1.74E+08	6.21E-07	-6.21E+05	-8.65E+06	9.48E+07	4.28E-09	4.46E+06	6.98E-10	5.60E+02	2.17E+05	-3.88E+06	0.00E+00	0.00E+00	0.00E+00	0.00E+00	0.00E+00	0.00E+00
7	-1.53E+09	-3.35E-07	-1.02E-06	1.31E-08	-2.72E-07	8.48E-08	5.49E+09	1.77E-06	6.02E-06	-2.93E-08	4.63E-07	-1.36E-07	-3.96E+09	-1.43E-06	-5.01E-06	1.61E-08	-1.91E-07	5.16E-08
8	-1.31E-07	-6.95E+06	-1.70E-08	9.24E-10	-6.98E-10	4.46E+06	-7.48E-07	3.43E+08	8.63E-06	-1.39E-09	3.49E-07	-3.44E+07	8.79E-07	-3.36E+08	-8.61E-06	4.66E-10	-3.48E-07	3.00E+07
9	-7.22E-07	5.59E-09	-6.95E+06	-2.62E-10	-4.46E+06	-2.10E-09	5.43E-07	1.43E-07	3.43E+08	-6.69E-10	3.44E+07	3.96E-09	1.79E-07	-1.49E-07	-3.36E+08	9.31E-10	-3.00E+07	-1.86E-09
10	8.94E-10	-2.25E-09	7.78E-10	-7.58E+04	-2.20E+03	5.60E+02	-3.39E-09	-2.60E-08	1.35E-08	1.47E+05	9.44E+03	-5.13E+03	2.50E-09	2.83E-08	-1.42E-08	-7.08E+04	-7.24E+03	4.57E+03
11	-2.60E-08	-1.40E-09	-4.46E+06	-2.20E+03	-4.67E+06	2.17E+05	2.60E-08	-2.47E-08	3.44E+07	9.44E+03	8.69E+06	-5.04E+05	0.00E+00	2.61E-08	-3.00E+07	-7.24E+03	-4.02E+06	2.87E+05
12	4.28E-09	4.46E+06	6.98E-10	5.60E+02	2.17E+05	-3.88E+06	2.79E-08	-3.44E+07	-2.99E-07	-5.13E+03	-5.04E+05	7.62E+06	-3.21E-08	3.00E+07	2.98E-07	4.57E+03	2.87E+05	-3.75E+06
13	0.00E+00	0.00E+00	0.00E+00	0.00E+00	0.00E+00	0.00E+00	-3.96E+09	-1.43E-06	-5.01E-06	1.61E-08	-1.91E-07	5.16E-08	4.58E+09	1.19E-06	4.74E-06	-5.38E-08	1.56E-07	8.59E-09
14	0.00E+00	0.00E+00	0.00E+00	0.00E+00	0.00E+00	0.00E+00	8.79E-07	-3.36E+08	-8.61E-06	4.66E-10	-3.48E-07	3.00E+07	-1.84E-06	3.37E+08	8.66E-06	-8.73E-10	3.59E-07	-3.07E+07
15	0.00E+00	0.00E+00	0.00E+00	0.00E+00	0.00E+00	0.00E+00	1.79E-07	-1.49E-07	-3.36E+08	9.31E-10	-3.00E+07	-1.86E-09	-8.14E-08	1.32E-07	3.37E+08	-1.37E-09	3.07E+07	2.21E-09
16	0.00E+00	0.00E+00	0.00E+00	0.00E+00	0.00E+00	0.00E+00	2.50E-09	2.83E-08	-1.42E-08	-7.08E+04	-7.24E+03	4.57E+03	-3.82E-09	-3.19E-08	1.41E-08	8.19E+04	8.09E+03	-5.78E+03
17	0.00E+00	0.00E+00	0.00E+00	0.00E+00	0.00E+00	0.00E+00	0.00E+00	2.61E-08	-3.00E+07	-7.24E+03	-4.02E+06	2.87E+05	-8.15E-10	-2.86E-08	3.07E+07	8.09E+03	4.59E+06	-3.02E+05
18	0.00E+00	0.00E+00	0.00E+00	0.00E+00	0.00E+00	0.00E+00	-3.21E-08	3.00E+07	2.98E-07	4.57E+03	2.87E+05	-3.75E+06	3.92E-08	-3.07E+07	-3.04E-07	-5.78E+03	-3.02E+05	4.32E+06
19	0.00E+00	0.00E+00	0.00E+00	0.00E+00	0.00E+00	0.00E+00	0.00E+00	0.00E+00	0.00E+00	0.00E+00	0.00E+00	0.00E+00	-6.17E+08	2.38E-07	2.68E-07	3.76E-08	3.55E-08	-6.02E-08
20	0.00E+00	0.00E+00	0.00E+00	0.00E+00	0.00E+00	0.00E+00	0.00E+00	0.00E+00	0.00E+00	0.00E+00	0.00E+00	0.00E+00	9.65E-07	-1.27E+06	-4.54E-08	4.07E-10	-1.11E-08	7.27E+05
21	0.00E+00	0.00E+00	0.00E+00	0.00E+00	0.00E+00	0.00E+00	0.00E+00	0.00E+00	0.00E+00	0.00E+00	0.00E+00	0.00E+00	-9.74E-08	1.67E-08	-1.27E+06	4.37E-10	-7.27E+05	-3.49E-10
22	0.00E+00	0.00E+00	0.00E+00	0.00E+00	0.00E+00	0.00E+00	0.00E+00	0.00E+00	0.00E+00	0.00E+00	0.00E+00	0.00E+00	1.33E-09	3.67E-09	1.09E-10	-1.11E+04	-8.48E+02	1.20E+03
23	0.00E+00	0.00E+00	0.00E+00	0.00E+00	0.00E+00	0.00E+00	0.00E+00	0.00E+00	0.00E+00	0.00E+00	0.00E+00	0.00E+00	8.15E-10	2.50E-09	-7.27E+05	-8.48E+02	-5.66E+05	1.52E+04
24	0.00E+00	0.00E+00	0.00E+00	0.00E+00	0.00E+00	0.00E+00	0.00E+00	0.00E+00	0.00E+00	0.00E+00	0.00E+00	0.00E+00	-7.04E-09	7.27E+05	5.79E-09	1.20E+03	1.52E+04	-5.77E+05
25	0.00E+00	0.00E+00	0.00E+00	0.00E+00	0.00E+00	0.00E+00	0.00E+00	0.00E+00	0.00E+00	0.00E+00	0.00E+00	0.00E+00	0.00E+00	0.00E+00	0.00E+00	0.00E+00	0.00E+00	0.00E+00
26	0.00E+00	0.00E+00	0.00E+00	0.00E+00	0.00E+00	0.00E+00	0.00E+00	0.00E+00	0.00E+00	0.00E+00	0.00E+00	0.00E+00	0.00E+00	0.00E+00	0.00E+00	0.00E+00	0.00E+00	0.00E+00
27	0.00E+00	0.00E+00	0.00E+00	0.00E+00	0.00E+00	0.00E+00	0.00E+00	0.00E+00	0.00E+00	0.00E+00	0.00E+00	0.00E+00	0.00E+00	0.00E+00	0.00E+00	0.00E+00	0.00E+00	0.00E+00
28	0.00E+00	0.00E+00	0.00E+00	0.00E+00	0.00E+00	0.00E+00	0.00E+00	0.00E+00	0.00E+00	0.00E+00	0.00E+00	0.00E+00	0.00E+00	0.00E+00	0.00E+00	0.00E+00	0.00E+00	0.00E+00
29	0.00E+00	0.00E+00	0.00E+00	0.00E+00	0.00E+00	0.00E+00	0.00E+00	0.00E+00	0.00E+00	0.00E+00	0.00E+00	0.00E+00	0.00E+00	0.00E+00	0.00E+00	0.00E+00	0.00E+00	0.00E+00
30	0.00E+00	0.00E+00	0.00E+00	0.00E+00	0.00E+00	0.00E+00	0.00E+00	0.00E+00	0.00E+00	0.00E+00	0.00E+00	0.00E+00	0.00E+00	0.00E+00	0.00E+00	0.00E+00	0.00E+00	0.00E+00
31	0.00E+00	0.00E+00	0.00E+00	0.00E+00	0.00E+00	0.00E+00	0.00E+00	0.00E+00	0.00E+00	0.00E+00	0.00E+00	0.00E+00	0.00E+00	0.00E+00	0.00E+00	0.00E+00	0.00E+00	0.00E+00
32	0.00E+00	0.00E+00	0.00E+00	0.00E+00	0.00E+00	0.00E+00	0.00E+00	0.00E+00	0.00E+00	0.00E+00	0.00E+00	0.00E+00	0.00E+00	0.00E+00	0.00E+00	0.00E+00	0.00E+00	0.00E+00
33	0.00E+00	0.00E+00	0.00E+00	0.00E+00	0.00E+00	0.00E+00	0.00E+00	0.00E+00	0.00E+00	0.00E+00	0.00E+00	0.00E+00	0.00E+00	0.00E+00	0.00E+00	0.00E+00	0.00E+00	0.00E+00
34	0.00E+00	0.00E+00	0.00E+00	0.00E+00	0.00E+00	0.00E+00	0.00E+00	0.00E+00	0.00E+00	0.00E+00	0.00E+00	0.00E+00	0.00E+00	0.00E+00	0.00E+00	0.00E+00	0.00E+00	0.00E+00
35	0.00E+00	0.00E+00	0.00E+00	0.00E+00	0.00E+00	0.00E+00	0.00E+00	0.00E+00	0.00E+00	0.00E+00	0.00E+00	0.00E+00	0.00E+00	0.00E+00	0.00E+00	0.00E+00	0.00E+00	0.00E+00
36	0.00E+00	0.00E+00	0.00E+00	0.00E+00	0.00E+00	0.00E+00	0.00E+00	0.00E+00	0.00E+00	0.00E+00	0.00E+00	0.00E+00	0.00E+00	0.00E+00	0.00E+00	0.00E+00	0.00E+00	0.00E+00

19	20	21	22	23	24	25	26	27	28	29	30	31	32	33	34	35	36
0.00E+00	0.00E+00	0.00E+00	0.00E+00	0.00E+00	0.00E+00	0.00E+00	0.00E+00	0.00E+00	0.00E+00	0.00E+00	0.00E+00	0.00E+00	0.00E+00	0.00E+00	0.00E+00	0.00E+00	0.00E+00
0.00E+00	0.00E+00	0.00E+00	0.00E+00	0.00E+00	0.00E+00	0.00E+00	0.00E+00	0.00E+00	0.00E+00	0.00E+00	0.00E+00	0.00E+00	0.00E+00	0.00E+00	0.00E+00	0.00E+00	0.00E+00
0.00E+00	0.00E+00	0.00E+00	0.00E+00	0.00E+00	0.00E+00	0.00E+00	0.00E+00	0.00E+00	0.00E+00	0.00E+00	0.00E+00	0.00E+00	0.00E+00	0.00E+00	0.00E+00	0.00E+00	0.00E+00
0.00E+00	0.00E+00	0.00E+00	0.00E+00	0.00E+00	0.00E+00	0.00E+00	0.00E+00	0.00E+00	0.00E+00	0.00E+00	0.00E+00	0.00E+00	0.00E+00	0.00E+00	0.00E+00	0.00E+00	0.00E+00
0.00E+00	0.00E+00	0.00E+00	0.00E+00	0.00E+00	0.00E+00	0.00E+00	0.00E+00	0.00E+00	0.00E+00	0.00E+00	0.00E+00	0.00E+00	0.00E+00	0.00E+00	0.00E+00	0.00E+00	0.00E+00
0.00E+00	0.00E+00	0.00E+00	0.00E+00	0.00E+00	0.00E+00	0.00E+00	0.00E+00	0.00E+00	0.00E+00	0.00E+00	0.00E+00	0.00E+00	0.00E+00	0.00E+00	0.00E+00	0.00E+00	0.00E+00
0.00E+00	0.00E+00	0.00E+00	0.00E+00	0.00E+00	0.00E+00	0.00E+00	0.00E+00	0.00E+00	0.00E+00	0.00E+00	0.00E+00	0.00E+00	0.00E+00	0.00E+00	0.00E+00	0.00E+00	0.00E+00
0.00E+00	0.00E+00	0.00E+00	0.00E+00	0.00E+00	0.00E+00	0.00E+00	0.00E+00	0.00E+00	0.00E+00	0.00E+00	0.00E+00	0.00E+00	0.00E+00	0.00E+00	0.00E+00	0.00E+00	0.00E+00
0.00E+00	0.00E+00	0.00E+00	0.00E+00	0.00E+00	0.00E+00	0.00E+00	0.00E+00	0.00E+00	0.00E+00	0.00E+00	0.00E+00	0.00E+00	0.00E+00	0.00E+00	0.00E+00	0.00E+00	0.00E+00
0.00E+00	0.00E+00	0.00E+00	0.00E+00	0.00E+00	0.00E+00	0.00E+00	0.00E+00	0.00E+00	0.00E+00	0.00E+00	0.00E+00	0.00E+00	0.00E+00	0.00E+00	0.00E+00	0.00E+00	0.00E+00
0.00E+00	0.00E+00	0.00E+00	0.00E+00	0.00E+00	0.00E+00	0.00E+00	0.00E+00	0.00E+00	0.00E+00	0.00E+00	0.00E+00	0.00E+00	0.00E+00	0.00E+00	0.00E+00	0.00E+00	0.00E+00
0.00E+00	0.00E+00	0.00E+00	0.00E+00	0.00E+00	0.00E+00	0.00E+00	0.00E+00	0.00E+00	0.00E+00	0.00E+00	0.00E+00	0.00E+00	0.00E+00	0.00E+00	0.00E+00	0.00E+00	0.00E+00
-6.17E+08	2.38E-07	2.68E-07	3.76E-08	3.55E-08	-6.02E-08	0.00E+00	0.00E+00	0.00E+00	0.00E+00	0.00E+00	0.00E+00	0.00E+00	0.00E+00	0.00E+00	0.00E+00	0.00E+00	0.00E+00
9.65E-07	-1.27E+06	-4.54E-08	4.07E-10	-1.11E-08	7.27E+05	0.00E+00	0.00E+00	0.00E+00	0.00E+00	0.00E+00	0.00E+00	0.00E+00	0.00E+00	0.00E+00	0.00E+00	0.00E+00	0.00E+00
-9.74E-08	1.67E-08	-1.27E+06	4.37E-10	-7.27E+05	-3.49E-10	0.00E+00	0.00E+00	0.00E+00	0.00E+00	0.00E+00	0.00E+00	0.00E+00	0.00E+00	0.00E+00	0.00E+00	0.00E+00	0.00E+00
1.33E-09	3.67E-09	1.09E-10	-1.11E+04	-8.48E+02	1.20E+03	0.00E+00	0.00E+00	0.00E+00	0.00E+00	0.00E+00	0.00E+00	0.00E+00	0.00E+00	0.00E+00	0.00E+00	0.00E+00	0.00E+00
8.15E-10	2.50E-09	-7.27E+05	-8.48E+02	-5.66E+05	1.52E+04	0.00E+00	0.00E+00	0.00E+00	0.00E+00	0.00E+00	0.00E+00	0.00E+00	0.00E+00	0.00E+00	0.00E+00	0.00E+00	0.00E+00
-7.04E-09	7.27E+05	5.79E-09	1.20E+03	1.52E+04	-5.77E+05	0.00E+00	0.00E+00	0.00E+00	0.00E+00	0.00E+00	0.00E+00	0.00E+00	0.00E+00	0.00E+00	0.00E+00	0.00E+00	0.00E+00
3.15E+11	-4.11E+01	-4.73E+01	4.05E-05	-1.18E-02	1.03E-02	-3.14E+11	4.11E+01	4.73E+01	-4.06E-05	1.18E-02	-1.03E-02	0.00E+00	0.00E+00	0.00E+00	0.00E+00	0.00E+00	0.00E+00
1.95E-01	3.77E+14	7.17E+01	-4.58E-05	1.81E-02	-1.88E+11	-1.95E-01	-3.77E+14	-7.17E+01	4.58E-05	-1.81E-02	1.88E+11	0.00E+00	0.00E+00	0.00E+00	0.00E+00	0.00E+00	0.00E+00
2.81E-01	1.64E+02	3.77E+14	-1.64E-04	1.88E+11	-4.12E-02	-2.81E-01	-1.64E+02	-3.77E+14	1.64E-04	-1.88E+11	4.12E-02	0.00E+00	0.00E+00	0.00E+00	0.00E+00	0.00E+00	0.00E+00
1.31E-05	1.71E-03	1.17E-02	2.40E+06	-6.48E+05	1.65E+06	-1.31E-05	-1.71E-03	-1.17E-02	-2.39E+06	6.48E+05	-1.65E+06	0.00E+00	0.00E+00	0.00E+00	0.00E+00	0.00E+00	0.00E+00
-6.10E-05	2.44E-02	1.88E+11	-6.48E+05	1.22E+08	1.03E+07	6.10E-05	-2.44E-02	-1.88E+11	6.48E+05	-1.22E+08	-1.04E+07	0.00E+00	0.00E+00	0.00E+00	0.00E+00	0.00E+00	0.00E+00
-4.96E-05	-1.88E+11	-1.33E-02	1.65E+06	1.03E+07	9.98E+07	4.96E-05	1.88E+11	1.33E-02	-1.65E+06	-1.04E+07	-9.93E+07	0.00E+00	0.00E+00	0.00E+00	0.00E+00	0.00E+00	0.00E+00
-3.14E+11	4.11E+01	4.73E+01	-4.06E-05	1.18E-02	-1.03E-02	3.14E+11	-4.11E+01	-4.73E+01	4.06E-05	-6.38E+04	1.03E-02	-8.22E+07	0.00E+00	-3.54E-09	2.29E-10	6.38E+04	3.64E-11
-1.95E-01	-3.77E+14	-7.17E+01	4.58E-05	-1.81E-02	1.88E+11	1.95E-01	3.77E+14	7.17E+01	6.38E+04	1.81E-02	-1.88E+11	0.00E+00	-8.39E+07	0.00E+00	-6.38E+04	-3.57E-10	-3.37E-12
-2.81E-01	-1.64E+02	-3.77E+14	1.64E-04	-1.88E+11	4.12E-02	2.81E-01	1.64E+02	3.77E+14	-1.64E-04	1.88E+11	-4.12E-02	-3.54E-09	0.00E+00	-1.40E+08	8.21E-09	-1.78E-08	6.26E-11
-1.31E-05	-1.71E-03	-1.17E-02	-2.39E+06	6.48E+05	-1.65E+06	1.31E-05	6.38E+04	1.17E-02	2.41E+06	-6.48E+05	1.65E+06	2.73E-10	-6.38E+04	-1.04E-09	-1.83E+04	-4.52E+00	1.62E+00
6.10E-05	-2.44E-02	-1.88E+11	6.48E+05	-1.22E+08	-1.04E+07	-6.38E+04	2.44E-02	1.88E+11	-6.48E+05	1.22E+08	1.04E+07	6.38E+04	-1.09E-11	7.27E-10	-4.52E+00	-1.83E+04	3.63E-01
4.96E-05	1.88E+11	1.33E-02	-1.65E+06	-1.04E+07	-9.93E+07	-4.96E-05	-1.88E+11	-1.33E-02	1.65E+06	1.04E+07	9.93E+07	-7.96E-11	1.39E-10	-1.34E-09	1.62E+00	3.63E-01	-3.63E+02
0.00E+00	0.00E+00	0.00E+00	0.00E+00	0.00E+00	0.00E+00	-8.22E+07	0.00E+00	-3.54E-09	2.29E-10	6.38E+04	3.64E-11	8.22E+07	0.00E+00	3.54E-09	-2.29E-10	-6.38E+04	-3.64E-11
0.00E+00	0.00E+00	0.00E+00	0.00E+00	0.00E+00	0.00E+00	0.00E+00	-8.39E+07	0.00E+00	-6.38E+04	-3.57E-10	-3.37E-12	0.00E+00	8.39E+07	0.00E+00	6.38E+04	3.57E-10	3.37E-12
0.00E+00	0.00E+00	0.00E+00	0.00E+00	0.00E+00	0.00E+00	-3.54E-09	0.00E+00	-1.40E+08	8.21E-09	-1.78E-08	6.26E-11	3.54E-09	0.00E+00	1.40E+08	-8.21E-09	1.78E-08	-6.26E-11
0.00E+00	0.00E+00	0.00E+00	0.00E+00	0.00E+00	0.00E+00	2.73E-10	-6.38E+04	-1.04E-09	-1.83E+04	-4.52E+00	1.62E+00	-2.73E-10	6.38E+04	1.04E-09	1.83E+04	4.52E+00	-1.62E+00
0.00E+00	0.00E+00	0.00E+00	0.00E+00	0.00E+00	0.00E+00	6.38E+04	-1.09E-11	7.27E-10	-4.52E+00	-1.83E+04	3.63E-01	-6.38E+04	1.09E-11	-7.27E-10	4.52E+00	1.83E+04	-3.63E-01
0.00E+00	0.00E+00	0.00E+00	0.00E+00	0.00E+00	0.00E+00	-7.96E-11	1.39E-10	-1.34E-09	1.62E+00	3.63E-01	-3.63E+02	7.96E-11	-1.39E-10	1.34E-09	-1.62E+00	-3.63E-01	3.63E+02

M_C (convert to diagonal)	
1	478.1478155
2	478.1478155
3	478.1478155
4	29.36039406
5	24.17664146
6	37.76596901
7	154.2855258
8	154.2855258
9	154.2855258
10	55.19087379
11	16.99580638
12	48.027989
13	213.9519076
14	213.9519076
15	213.9519076
16	4.849618093
17	6.119578187
18	9.395927147
19	186.6735005
20	186.6735005
21	186.6735005
22	5.025017531
23	38.56197643
24	20.24739215
25	26.32104143
26	26.32104143
27	26.32104143
28	0.043599443
29	0.195111447
30	0.251141214
31	60
32	60
33	60
34	2.7375
35	2.7375
36	1.875

Natural Frequencies	
1	4042624.83265247 + 0.00000000000000i
2	4042611.54555017 + 0.00000000000000i
3	116712.249649545 + 0.00000000000000i
4	12540.4869766846 + 0.00000000000000i
5	7224.94428978476 + 0.00000000000000i
6	4778.29019914116 + 0.00000000000000i
7	7806.62404635618 + 0.00000000000000i
8	2555.17914915990 + 0.00000000000000i
9	0.00000000000000 - 1165.44923853596i
10	1451.42046456196 + 0.00000000000000i
11	2120.50922603192 + 0.00000000000000i
12	935.285132653042 + 0.00000000000000i
13	2038.21495280806 + 0.00000000000000i
14	2017.53361541387 + 0.00000000000000i
15	1730.08001295831 + 0.00000000000000i
16	1779.55289412791 + 0.00000000000000i
17	1339.55405993875 + 0.00000000000000i
18	613.510104809971 + 0.00000000000000i
19	479.502018684871 + 0.00000000000000i
20	408.962503440078 + 0.00000000000000i
21	420.714291459057 + 0.00000000000000i
22	305.759121606995 + 0.00000000000000i
23	269.063027017495 + 0.00000000000000i
24	0.00000000000000 - 137.084900338241i
25	134.862279373165 + 0.00000000000000i
26	136.172794216298 + 0.00000000000000i
27	115.363516921200 + 0.00000000000000i
28	105.226726371824 + 0.00000000000000i
29	91.2560520789636 + 0.00000000000000i
30	79.4354393738056 + 0.00000000000000i
31	69.8283691240151 + 0.00000000000000i
32	41.7528768950851 + 0.00000000000000i
33	13.8852946428864 + 0.00000000000000i
34	31.0035712437801 + 0.00000000000000i
35	28.2351675913757 + 0.00000000000000i
36	28.7928038975152 + 0.00000000000000i

Mode shapes	1	2	3	4	5	6	7	8	9	10	11	12	13	14	15	16	17	18
1	-1.60E-17	1.68E-17	1.33E-11	-2.18E-10	1.09E-01	-1.00E+00	2.72E-09	-1.85E-01	4.80E-07	-4.35E-02	-8.64E-08	1.87E-02	-6.33E-08	-1.61E-08	1.66E-07	8.79E-09	5.63E-07	-1.51E-07
2	3.05E-28	1.93E-26	2.02E-25	3.32E-13	1.94E-15	1.12E-13	2.65E-12	-7.50E-10	-5.67E-08	7.85E-08	-5.49E-03	6.73E-08	2.11E-02	2.36E-02	1.11E-04	1.58E-01	-3.65E-05	6.41E-03
3	-2.99E-26	-7.70E-27	2.60E-26	-8.42E-13	-8.68E-15	-3.98E-13	8.21E-13	7.31E-09	3.28E-08	-1.80E-07	-3.68E-02	-2.26E-07	3.13E-02	1.13E-01	-1.31E-04	-4.81E-02	6.60E-06	2.70E-02
4	-9.17E-29	3.17E-29	1.18E-27	2.31E-15	1.20E-16	1.30E-14	-4.66E-16	-6.50E-10	-1.22E-08	3.10E-08	3.87E-03	4.47E-08	-2.94E-03	-1.23E-02	2.18E-05	1.21E-02	-2.86E-06	2.65E-03
5	-4.77E-25	-1.15E-25	4.18E-25	-1.31E-11	-1.31E-13	-5.56E-12	1.34E-11	7.79E-08	-7.38E-07	-1.02E-06	-3.40E-01	-6.28E-07	2.85E-01	1.00E+00	-9.27E-04	-3.04E-01	1.76E-05	-1.97E-02
6	5.42E-27	-1.65E-25	-1.74E-24	-2.62E-12	-1.38E-14	-7.98E-13	-2.28E-11	2.66E-09	1.12E-06	-3.66E-07	5.41E-02	-1.12E-07	-1.59E-01	-2.11E-01	-6.52E-04	-1.00E+00	1.90E-04	7.85E-03
7	-1.19E-17	-2.12E-17	-5.65E-08	9.18E-09	-1.00E+00	-2.03E-02	-3.24E-08	-9.47E-01	3.64E-06	-2.83E-01	-4.97E-07	1.29E-01	-3.71E-07	-9.47E-08	1.03E-06	5.43E-08	3.71E-06	-1.06E-06
8	2.28E-22	-1.48E-17	-9.30E-20	-2.91E-09	-5.44E-12	-1.24E-10	-8.42E-09	1.89E-07	-2.82E-05	2.02E-06	1.12E-02	1.81E-06	-6.54E-01	5.85E-02	3.62E-07	2.08E-02	-2.05E-03	-1.90E-02
9	1.91E-17	-1.35E-21	-1.20E-19	5.18E-09	1.63E-11	2.75E-10	-1.63E-09	-5.49E-07	-5.50E-06	-6.74E-06	4.10E-01	-1.40E-05	4.37E-02	8.10E-02	-2.53E-03	-7.25E-03	-3.40E-05	-9.11E-02
10	8.25E-21	-3.40E-21	-7.23E-23	1.64E-12	3.48E-15	7.28E-14	3.81E-12	-9.69E-11	-5.10E-08	1.68E-09	4.80E-05	2.08E-08	-2.33E-05	3.47E-06	1.42E-07	-3.96E-06	4.97E-07	8.06E-04
11	2.04E-17	-6.94E-19	-1.29E-19	5.52E-09	1.75E-11	2.90E-10	-2.22E-09	-5.57E-07	-1.24E-05	-5.41E-06	4.23E-01	-2.47E-06	1.58E-02	6.67E-03	-2.24E-03	1.86E-02	8.15E-05	7.86E-01
12	-3.76E-19	5.16E-18	3.52E-20	9.26E-10	1.59E-12	3.85E-11	3.02E-09	-5.70E-08	1.33E-05	-6.59E-07	-7.34E-03	-1.45E-06	2.14E-01	-1.38E-02	1.28E-05	2.02E-02	5.68E-04	-5.88E-02
13	9.21E-19	-1.77E-19	2.99E-05	-4.34E-08	6.05E-01	3.76E-01	3.09E-08	-1.00E+00	5.05E-06	-3.52E-01	-5.68E-07	1.67E-01	-4.30E-07	-1.10E-07	1.25E-06	6.51E-08	4.67E-06	-1.40E-06
14	5.92E-16	5.14E-11	2.26E-16	8.21E-08	5.13E-11	5.08E-10	9.05E-08	-2.16E-07	-7.81E-06	-6.86E-07	-7.74E-03	2.70E-08	4.66E-01	-4.31E-02	-6.52E-06	-2.32E-02	4.73E-04	1.29E-02
15	-5.13E-11	5.89E-16	3.39E-16	-1.11E-07	-1.17E-10	-8.79E-10	1.23E-08	5.42E-07	-4.97E-07	2.77E-06	-2.90E-01	4.29E-06	-3.29E-02	-6.40E-02	1.22E-03	7.82E-03	2.42E-05	9.21E-02
16	-3.65E-15	9.86E-15	3.88E-17	4.45E-09	1.00E-10	2.01E-10	-3.16E-07	-2.72E-08	-1.65E-05	1.59E-07	-5.22E-04	-1.97E-07	2.93E-04	-1.24E-04	-2.56E-06	-8.07E-06	-1.96E-05	-8.98E-03
17	-1.03E-09	1.11E-13	4.69E-15	-2.89E-06	-2.86E-09	-1.90E-08	3.52E-07	5.45E-06	-1.10E-04	-4.11E-05	-1.00E+00	-1.48E-04	-9.69E-02	-2.19E-01	-6.11E-03	2.53E-02	-2.57E-04	-1.00E+00
18	2.62E-14	-6.70E-10	-3.94E-15	-1.40E-06	-8.22E-10	-7.46E-09	-1.53E-06	1.68E-06	4.47E-04	-9.59E-06	2.71E-02	-1.39E-05	-1.00E+00	9.43E-02	6.58E-05	4.94E-02	1.04E-02	2.58E-01
19	-1.87E-14	1.54E-14	-1.41E-01	1.99E-06	-3.58E-02	-5.57E-02	-2.16E-07	9.22E-01	1.65E-05	-5.39E-01	-1.41E-07	3.61E-01	-1.88E-07	-5.31E-08	1.33E-06	6.33E-08	7.90E-06	-3.37E-06
20	-1.62E-06	-1.41E-01	4.61E-12	1.85E-05	5.07E-09	1.54E-08	2.12E-06	-9.01E-07	7.02E-05	8.48E-06	3.56E-05	-9.17E-07	-1.75E-03	1.68E-04	-2.30E-06	1.26E-04	2.83E-01	1.71E-03
21	1.41E-01	-1.62E-06	-1.50E-09	-6.01E-05	-4.91E-09	-1.82E-09	2.28E-06	-1.31E-07	5.50E-05	4.92E-06	1.65E-03	5.23E-06	1.99E-04	4.50E-04	2.82E-01	-2.02E-04	2.09E-06	6.02E-03
22	-5.35E-10	1.07E-09	-2.29E-10	-2.90E-04	-2.34E-06	-2.06E-06	8.62E-03	8.57E-05	-8.77E-03	-2.06E-04	4.68E-05	-8.48E-05	-1.06E-04	2.13E-05	1.45E-04	5.61E-06	9.20E-03	6.73E-04
23	3.41E-04	-3.05E-09	1.26E-09	5.06E-03	1.62E-06	4.56E-06	-2.03E-04	-2.83E-04	-2.12E-03	1.16E-03	4.49E-03	1.20E-03	3.83E-04	1.10E-03	1.83E-03	-1.58E-04	-2.51E-05	3.63E-02
24	9.61E-09	6.50E-04	9.13E-10	3.73E-03	7.36E-07	2.83E-06	1.51E-03	-1.56E-04	1.22E-02	4.62E-04	-4.14E-04	3.02E-04	1.09E-02	-1.09E-03	-3.03E-04	-7.05E-04	-5.61E-03	-2.20E-02
25	1.01E-11	-1.09E-13	1.00E+00	1.80E-06	-3.60E-02	-5.58E-02	-2.08E-07	9.22E-01	1.65E-05	-5.38E-01	-1.40E-07	3.61E-01	-1.87E-07	-5.29E-08	1.33E-06	6.32E-08	7.90E-06	-3.37E-06
26	1.15E-05	1.00E+00	-3.27E-11	-1.34E-04	-2.49E-08	-1.00E-07	-5.97E-05	5.45E-06	-4.36E-04	-1.02E-05	3.62E-05	-1.29E-05	-1.76E-03	1.69E-04	9.84E-06	1.26E-04	2.83E-01	1.71E-03
27	-1.00E+00	1.15E-05	1.06E-08	4.42E-04	3.99E-08	2.49E-08	-1.79E-05	1.10E-06	-1.44E-04	-7.84E-07	1.65E-03	1.18E-06	1.98E-04	4.50E-04	2.82E-01	-2.02E-04	-1.09E-06	6.02E-03
28	6.17E-08	-3.35E-08	2.64E-08	3.35E-02	2.72E-04	2.42E-04	-1.00E+00	-1.06E-02	7.74E-01	2.96E-02	-9.17E-04	1.89E-02	5.57E-03	-7.26E-04	-1.94E-02	-3.01E-04	-1.14E-02	-3.54E-03
29	-6.75E-02	6.02E-07	-2.43E-05	-1.00E+00	-8.80E-05	-4.88E-05	4.01E-02	-2.75E-03	3.96E-01	1.26E-02	4.16E-03	9.28E-03	3.07E-03	7.75E-04	-5.05E-03	-3.08E-04	6.35E-03	3.42E-02
30	-7.75E-07	-5.24E-02	-7.36E-08	-3.01E-01	-5.93E-05	-2.28E-04	-1.22E-01	1.25E-02	-1.00E+00	-3.68E-02	7.49E-04	-2.37E-02	4.42E-03	-2.15E-04	2.40E-02	-3.51E-04	-2.35E-02	-1.67E-02
31	-4.39E-12	3.80E-17	-1.01E-04	-6.84E-06	9.69E-04	3.56E-03	7.21E-07	-2.45E-01	-1.45E-04	1.00E+00	1.48E-06	1.00E+00	1.26E-06	3.32E-07	-4.43E-06	-2.31E-07	-9.52E-06	-4.20E-05
32	-9.86E-13	-8.56E-08	1.30E-15	9.73E-07	-5.00E-09	-5.49E-09	1.93E-05	7.03E-07	7.61E-05	-2.45E-05	-1.60E-05	4.11E-06	8.89E-04	-8.80E-05	4.36E-06	-9.97E-05	-1.00E+00	2.33E-03
33	1.43E-07	-1.64E-12	-1.82E-12	-6.67E-06	-1.87E-09	-2.83E-09	7.12E-07	-6.14E-07	-9.10E-05	-8.04E-06	-1.78E-03	1.89E-06	-2.54E-04	-6.05E-04	-1.00E+00	5.67E-04	-4.73E-06	7.17E-03
34	-9.64E-15	-1.43E-09	-9.75E-15	-1.39E-06	-3.48E-08	-7.08E-08	1.10E-04	1.08E-05	3.79E-03	-9.45E-05	1.09E-06	-1.45E-04	5.90E-06	-2.77E-07	4.35E-05	-1.03E-06	-1.67E-02	1.03E-04
35	2.76E-11	-6.71E-16	1.71E-06	4.25E-05	-1.65E-05	-6.07E-05	-4.37E-06	4.17E-03	1.93E-03	-1.71E-02	-6.19E-06	-1.72E-02	-4.95E-06	-1.27E-06	1.14E-05	6.52E-07	-2.35E-05	-6.16E-04
36	-7.90E-16	6.20E-13	6.77E-16	3.69E-07	2.24E-10	1.94E-09	3.73E-07	-3.73E-07	-1.43E-04	3.40E-06	-3.22E-08	5.26E-06	-2.04E-07	1.01E-08	-1.55E-06	2.14E-08	2.54E-06	8.59E-06

19	20	21	22	23	24	25	26	27	28	29	30	31	32	33	34	35	36
-1.30E-07	6.35E-08	-2.19E-09	1.10E-08	-8.91E-09	-9.73E-09	-2.32E-08	-2.32E-09	1.35E-07	-2.10E-09	5.23E-08	-2.99E-08	7.10E-09	1.20E-11	4.32E-13	5.78E-10	1.13E-10	-1.01E-10
-2.34E-02	-5.66E-02	-3.22E-01	-3.50E-02	-3.30E-02	-1.59E-01	-2.86E-03	-1.40E-04	1.70E-02	3.42E-04	-1.34E-02	-4.00E-04	1.15E-03	-1.36E-03	-1.55E-06	-6.11E-03	-3.09E-04	1.86E-03
-3.97E-02	-1.87E-02	-1.15E-01	-5.78E-02	7.14E-02	4.07E-01	-1.64E-03	-6.79E-04	-3.51E-02	-6.95E-04	2.32E-02	2.17E-04	-3.94E-02	3.61E-03	2.43E-05	5.59E-03	1.01E-03	-5.41E-03
-1.18E-02	1.33E-03	3.67E-03	-1.42E-01	1.00E+00	-7.69E-01	2.59E-03	-3.07E-03	1.06E-01	7.08E-04	-7.11E-02	-1.28E-03	9.22E-02	8.53E-03	-5.44E-05	-8.08E-03	-1.34E-02	3.30E-03
5.33E-02	3.95E-02	2.28E-01	1.23E-01	-1.58E-01	-1.00E+00	4.31E-03	1.66E-03	8.16E-02	1.67E-03	-5.97E-02	-1.06E-03	9.55E-02	-8.62E-03	-5.84E-05	-1.43E-02	-2.65E-03	1.32E-02
-4.06E-02	-1.08E-01	-6.03E-01	-1.06E-01	-7.47E-02	-3.89E-01	-1.08E-02	-7.54E-04	3.91E-02	8.04E-04	-3.13E-02	-8.96E-04	9.08E-03	-3.28E-03	-4.49E-06	-1.31E-02	-8.81E-04	4.66E-03
-9.23E-07	4.51E-07	-1.56E-08	7.86E-08	-6.36E-08	-6.97E-08	-1.66E-07	-1.66E-08	9.65E-07	-1.50E-08	3.75E-07	-2.14E-07	5.09E-08	8.67E-11	2.89E-12	4.10E-09	8.21E-10	-7.33E-10
-1.97E-02	-7.71E-02	6.38E-02	1.49E-01	1.36E-02	-5.55E-03	4.80E-02	4.29E-03	2.28E-02	4.44E-04	-3.20E-02	-5.95E-03	-7.66E-01	7.55E-04	3.22E-04	-1.61E-01	1.76E-02	-2.32E-02
-6.64E-02	3.86E-02	-6.26E-04	7.72E-03	-1.17E-02	9.02E-02	-9.09E-03	-1.49E-03	7.98E-02	2.63E-03	-2.61E-01	-2.26E-02	1.17E-01	4.67E-03	-1.89E-05	-5.03E-02	-1.80E-02	1.10E-02
3.90E-04	2.45E-04	-3.84E-04	2.54E-03	-1.98E-02	-5.07E-02	4.11E-02	-8.06E-02	-1.19E-02	-2.74E-02	1.40E-02	1.17E-03	-2.39E-02	4.07E-01	-4.72E-05	2.13E-01	-2.58E-01	-2.35E-01
-5.16E-01	8.02E-02	4.14E-01	1.96E-02	-9.87E-02	-6.11E-01	3.38E-02	5.46E-03	-1.47E-01	-2.50E-03	2.08E-01	1.40E-02	-9.47E-02	-9.78E-03	5.67E-06	3.68E-02	1.83E-02	-5.21E-03
-1.85E-02	-9.47E-02	3.45E-01	-1.00E+00	-8.93E-02	-1.49E-01	-8.67E-02	-9.99E-03	5.57E-03	7.48E-04	-4.41E-02	-7.42E-03	-9.45E-01	-8.25E-04	4.70E-04	-1.96E-01	2.16E-02	-2.63E-02
-1.22E-06	5.98E-07	-2.06E-08	1.04E-07	-8.46E-08	-9.29E-08	-2.21E-07	-2.21E-08	1.29E-06	-2.00E-08	4.99E-07	-2.85E-07	6.77E-08	1.16E-10	3.03E-12	5.46E-09	1.10E-09	-9.78E-10
8.20E-03	2.59E-02	-6.59E-02	2.02E-01	2.00E-02	2.41E-04	1.59E-02	1.29E-03	5.62E-03	4.08E-04	-3.30E-02	-6.60E-03	-7.72E-01	7.73E-04	3.56E-04	-1.64E-01	1.82E-02	-2.40E-02
-2.44E-02	-1.92E-04	4.43E-02	-7.70E-04	-1.65E-02	7.65E-02	-8.56E-03	-1.09E-03	1.14E-01	3.02E-03	-2.62E-01	-2.10E-02	1.18E-01	4.62E-03	-2.66E-05	-5.29E-02	-1.90E-02	1.18E-02
-5.97E-03	-4.06E-03	5.58E-03	-1.64E-03	5.47E-03	-2.41E-02	-5.23E-01	1.00E+00	6.66E-03	1.79E-01	2.27E-02	1.88E-04	-5.87E-02	2.80E-01	-1.81E-05	2.88E-01	-3.59E-01	-3.38E-01
-1.00E+00	5.01E-01	-3.48E-02	1.11E-01	-5.03E-02	-4.63E-01	3.14E-02	1.59E-03	-5.47E-01	-6.85E-03	2.01E-01	-6.52E-03	-9.91E-02	-9.16E-03	9.14E-05	6.13E-02	2.80E-02	-1.30E-02
2.74E-01	1.00E+00	-1.00E+00	-5.07E-01	-2.55E-02	-8.28E-02	-4.65E-01	-4.57E-02	-1.92E-01	3.42E-04	-5.45E-02	-1.46E-02	-1.00E+00	-7.43E-04	8.54E-04	-2.29E-01	2.76E-02	-3.45E-02
-3.03E-06	1.51E-06	-5.18E-08	2.67E-07	-2.17E-07	-2.42E-07	-5.74E-07	-5.72E-08	3.33E-06	-5.20E-08	1.29E-06	-7.41E-07	1.76E-07	3.13E-10	-2.02E-12	1.43E-08	2.87E-09	-2.54E-09
3.40E-03	1.83E-02	-1.59E-02	-3.57E-02	-3.68E-03	4.79E-03	9.95E-02	1.08E-02	3.49E-02	-5.24E-04	1.20E-02	3.05E-03	2.32E-01	6.79E-03	2.02E-03	-7.64E-01	8.59E-02	-1.27E-01
1.29E-02	-8.81E-03	-7.19E-04	-4.02E-03	3.84E-03	-2.09E-02	2.79E-02	3.93E-03	-1.96E-01	-2.36E-03	8.54E-03	-2.39E-02	1.96E-02	-1.59E-03	-2.38E-04	-5.40E-01	-1.53E-01	1.27E-01
1.11E-03	8.52E-04	-1.33E-03	-1.64E-03	-1.17E-04	-3.90E-03	1.22E-01	-2.06E-01	-7.32E-02	6.28E-01	3.40E-02	-1.20E-02	-7.80E-03	-7.44E-01	3.39E-04	5.44E-01	-8.82E-01	-8.79E-01
7.18E-02	-4.61E-02	-4.95E-03	-2.57E-02	1.91E-02	-1.46E-01	1.58E-01	2.02E-02	-9.84E-01	-7.31E-03	-2.44E-01	-5.81E-02	1.08E-01	6.38E-04	4.44E-04	7.17E-01	2.16E-01	-1.75E-01
-4.14E-02	-1.98E-01	1.77E-01	3.50E-01	3.41E-02	-4.11E-02	-1.00E+00	-1.04E-01	-3.15E-01	-2.30E-04	-1.35E-02	-5.01E-03	3.29E-01	5.29E-03	3.61E-03	-1.00E+00	1.20E-01	-1.74E-01
-3.04E-06	1.51E-06	-5.18E-08	2.67E-07	-2.17E-07	-2.43E-07	-5.74E-07	-5.73E-08	3.34E-06	-5.20E-08	1.30E-06	-7.42E-07	1.76E-07	3.13E-10	-2.03E-12	1.43E-08	2.88E-09	-2.54E-09
3.41E-03	1.83E-02	-1.59E-02	-3.57E-02	-3.68E-03	4.79E-03	9.95E-02	1.08E-02	3.49E-02	-5.52E-04	1.20E-02	3.05E-03	2.32E-01	6.79E-03	2.02E-03	-7.64E-01	8.59E-02	-1.27E-01
1.29E-02	-8.80E-03	-7.22E-04	-4.02E-03	3.84E-03	-2.09E-02	2.79E-02	3.93E-03	-1.96E-01	-2.38E-03	8.55E-03	-2.39E-02	1.96E-02	-1.59E-03	-2.39E-04	-5.40E-01	-1.53E-01	1.27E-01
-3.87E-03	-1.28E-02	1.19E-02	1.27E-02	1.08E-03	-5.44E-03	1.21E-01	-2.12E-01	-1.04E-01	6.61E-01	1.95E-02	4.05E-04	-1.04E-02	-7.38E-01	1.01E-03	5.40E-01	-8.80E-01	-8.76E-01
6.94E-02	-5.29E-02	1.69E-03	-1.85E-02	1.97E-02	-1.47E-01	1.58E-01	1.57E-02	-9.98E-01	1.47E-02	-2.51E-01	-5.25E-02	1.07E-01	4.16E-03	7.79E-04	7.15E-01	2.17E-01	-1.73E-01
-3.51E-02	-1.81E-01	1.61E-01	3.32E-01	3.26E-02	-3.91E-02	-1.00E+00	-9.26E-02	-2.74E-01	-5.65E-02	4.03E-03	-2.07E-02	3.32E-01	-3.69E-03	2.77E-03	-9.95E-01	1.17E-01	-1.79E-01
-7.03E-05	5.05E-05	-1.63E-06	1.69E-05	-1.80E-05	8.27E-05	-1.97E-04	-1.93E-05	1.57E-03	-2.95E-05	9.78E-04	-7.40E-04	2.28E-04	1.22E-06	3.46E-08	9.37E-05	2.30E-05	-1.91E-05
4.07E-03	2.08E-02	-1.82E-02	-3.83E-02	-3.88E-03	4.72E-03	1.01E-01	1.07E-02	3.51E-02	7.16E-04	1.21E-02	3.05E-03	2.33E-01	7.00E-03	2.02E-03	-7.65E-01	8.61E-02	-1.26E-01
1.43E-02	-9.48E-03	-7.82E-04	-4.19E-03	3.96E-03	-2.08E-02	2.81E-02	3.97E-03	-1.97E-01	-2.39E-03	8.58E-03	-2.40E-02	1.96E-02	-1.60E-03	-2.39E-04	-5.40E-01	-1.53E-01	1.27E-01
1.85E-04	8.91E-04	-7.81E-04	-1.66E-03	-1.80E-04	-1.37E-03	-6.73E-02	1.20E-01	1.06E-01	-1.00E+00	-7.59E-02	1.10E-02	-4.98E-02	-1.00E+00	1.13E-03	6.34E-01	-1.00E+00	-1.00E+00
-2.07E-03	2.19E-03	-6.61E-05	1.42E-03	-2.00E-03	-3.84E-02	-9.15E-02	-8.74E-03	1.00E+00	-2.29E-02	1.00E+00	-1.00E+00	3.99E-01	5.73E-03	8.23E-04	8.35E-01	2.47E-01	-1.98E-01
2.96E-05	2.09E-04	-1.76E-04	-6.87E-04	-8.73E-05	-3.97E-04	1.08E-02	9.60E-04	4.00E-03	1.14E-03	-1.15E-04	6.82E-04	-1.37E-02	6.06E-04	1.00E+00	2.50E-01	-3.72E-02	5.46E-02

FRF Output – X Direction

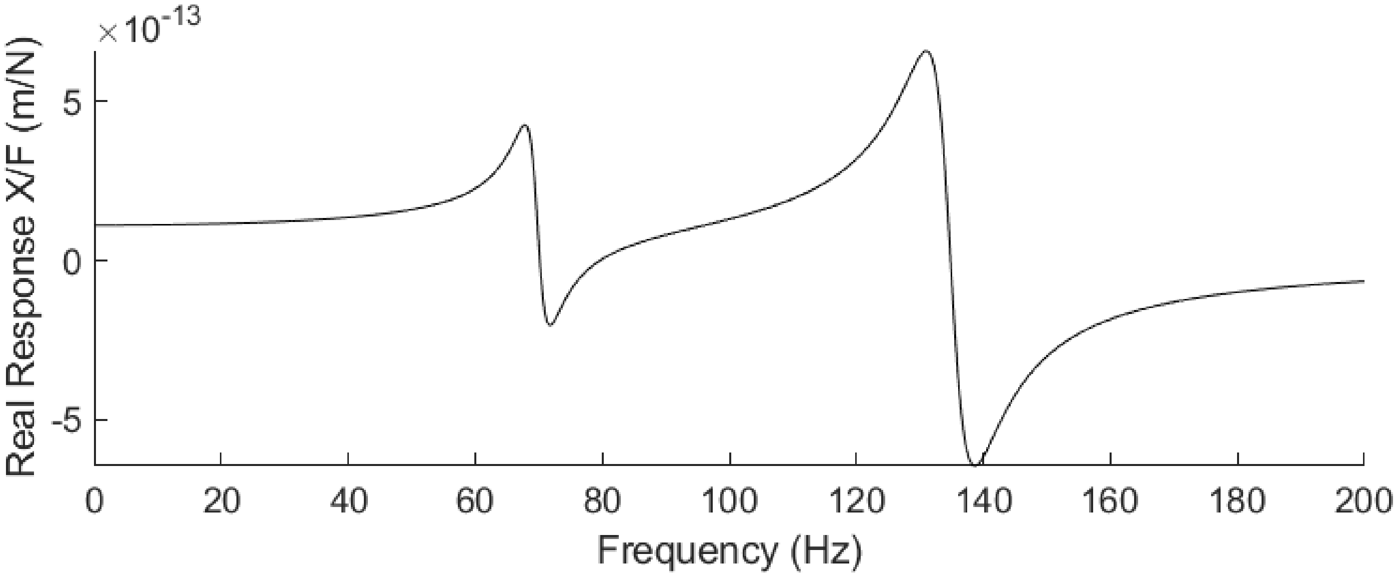

Modes: [67.5, 3.77613e-13; 130.3, 5.5851e-13]

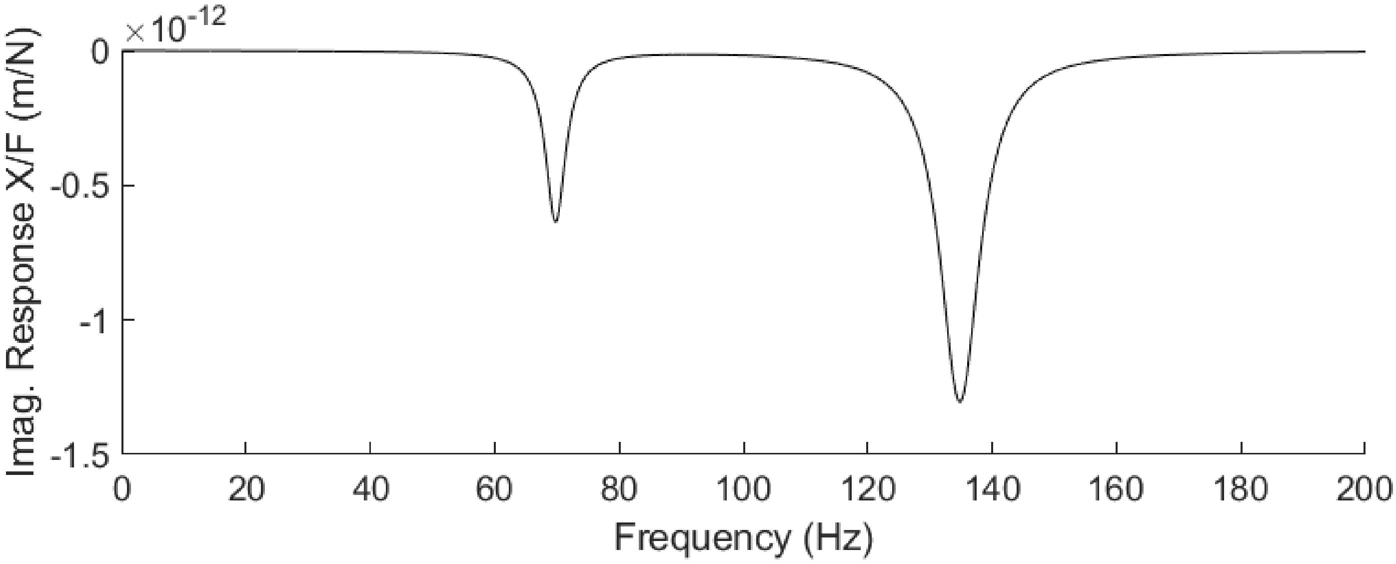

FRF Output – Y Direction

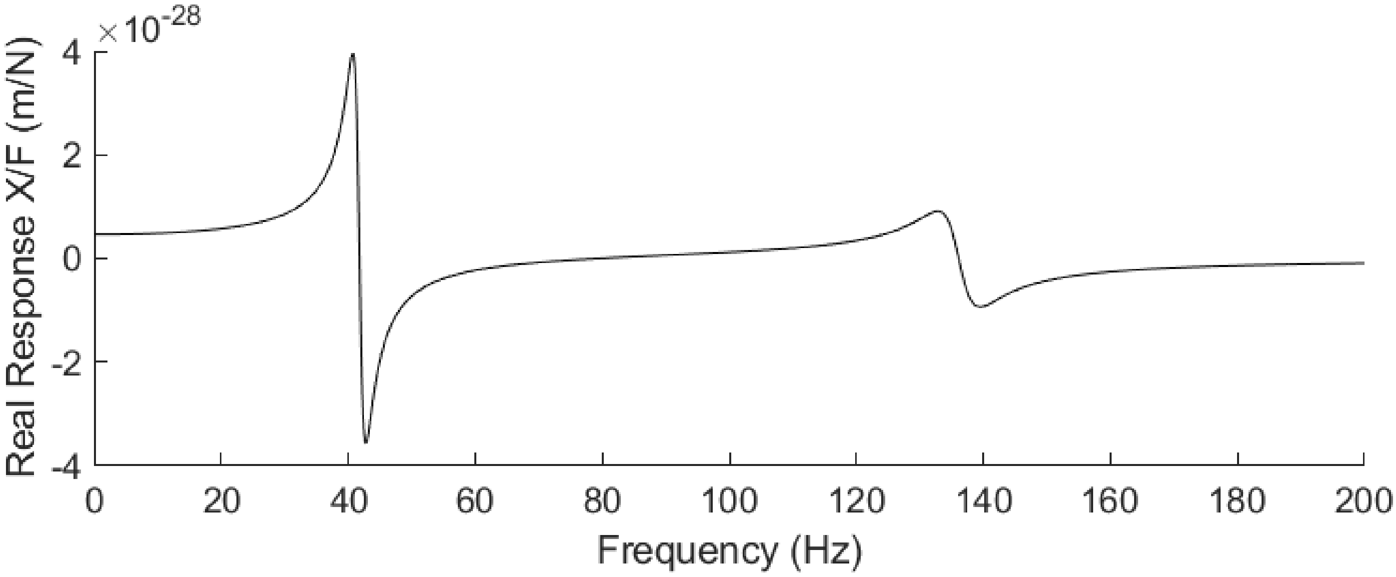

Modes: [40.7,3.89193e-28; 132.9, 8.95563e-29]

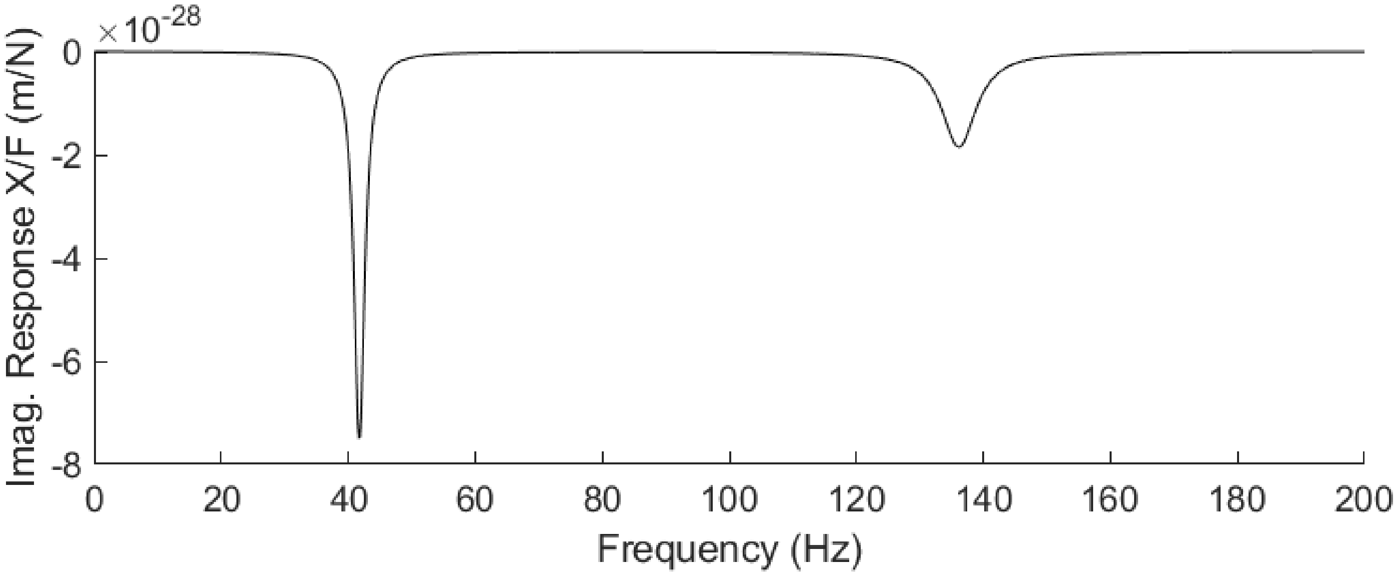

J.2 FRF Generator Program Evaluation - Configuration 2

K_C	1	2	3	4	5	6	7	8	9	10	11	12	13	14	15	16	17	18
1	1.09E+10	4.59E-06	1.60E-06	3.21E-07	-1.39E-06	-1.12E-06	-1.53E+09	1.77E-07	3.41E-06	-8.64E-10	1.61E-06	-5.39E-08	0.00E+00	0.00E+00	0.00E+00	0.00E+00	0.00E+00	0.00E+00
2	1.45E-07	4.13E+08	5.29E-06	-3.91E-09	8.86E-07	-1.74E+08	6.34E-08	-6.95E+06	1.34E-09	1.87E-10	1.75E-10	4.46E+06	0.00E+00	0.00E+00	0.00E+00	0.00E+00	0.00E+00	0.00E+00
3	2.33E-06	3.08E-06	4.13E+08	-4.49E-08	1.74E+08	-7.04E-07	-2.24E-08	9.90E-10	-6.95E+06	1.80E-10	-4.46E+06	-2.04E-10	0.00E+00	0.00E+00	0.00E+00	0.00E+00	0.00E+00	0.00E+00
4	1.61E-07	-5.96E-08	-7.47E-08	1.83E+06	-1.58E+06	-6.16E+05	-1.71E-12	1.20E-10	1.77E-10	-7.58E+04	-4.06E+01	1.36E+00	0.00E+00	0.00E+00	0.00E+00	0.00E+00	0.00E+00	0.00E+00
5	1.74E-07	6.37E-07	1.74E+08	-1.58E+06	7.73E+07	-8.45E+06	1.01E-09	1.46E-10	-4.46E+06	-4.06E+01	-4.73E+06	3.04E+04	0.00E+00	0.00E+00	0.00E+00	0.00E+00	0.00E+00	0.00E+00
6	-1.49E-07	-1.74E+08	-7.56E-07	-6.16E+05	-8.45E+06	9.47E+07	-2.15E-10	4.46E+06	-8.73E-11	1.36E+00	3.04E+04	-3.82E+06	0.00E+00	0.00E+00	0.00E+00	0.00E+00	0.00E+00	0.00E+00
7	-1.53E+09	1.77E-07	3.41E-06	-8.64E-10	1.61E-06	-5.39E-08	5.49E+09	-8.74E-08	-3.90E-06	-7.15E-09	-1.62E-06	7.06E-08	-3.96E+09	-8.94E-08	4.92E-07	8.01E-09	6.37E-09	-1.67E-08
8	6.34E-08	-6.95E+06	1.34E-09	1.87E-10	1.75E-10	4.46E+06	6.02E-07	3.43E+08	7.88E-07	6.91E-09	2.40E-08	-3.44E+07	-6.65E-07	-3.36E+08	-7.90E-07	-7.10E-09	-2.42E-08	3.00E+07
9	-2.24E-08	9.90E-10	-6.95E+06	1.80E-10	-4.46E+06	-2.04E-10	-1.03E-06	8.78E-07	3.43E+08	4.71E-09	3.44E+07	-2.40E-08	1.06E-06	-8.79E-07	-3.36E+08	-4.89E-09	-3.00E+07	2.42E-08
10	-1.71E-12	1.20E-10	1.77E-10	-7.58E+04	-4.06E+01	1.36E+00	6.73E-10	1.08E-08	4.72E-09	1.46E+05	2.51E+03	7.90E+02	-6.71E-10	-1.09E-08	-4.90E-09	-7.07E+04	-2.46E+03	-7.91E+02
11	1.01E-09	1.46E-10	-4.46E+06	-4.06E+01	-4.73E+06	3.04E+04	-1.42E-08	-3.87E-09	3.44E+07	2.51E+03	8.90E+06	1.63E+05	1.32E-08	3.73E-09	-3.00E+07	-2.46E+03	-4.17E+06	-1.93E+05
12	-2.15E-10	4.46E+06	-8.73E-11	1.36E+00	3.04E+04	-3.82E+06	-3.98E-09	-3.44E+07	-3.64E-09	7.90E+02	1.63E+05	7.45E+06	4.19E-09	3.00E+07	3.73E-09	-7.91E+02	-1.93E+05	-3.63E+06
13	0.00E+00	0.00E+00	0.00E+00	0.00E+00	0.00E+00	0.00E+00	-3.96E+09	-8.94E-08	4.92E-07	8.01E-09	6.37E-09	-1.67E-08	4.58E+09	3.87E-07	-6.71E-07	2.34E-08	-6.44E-08	-3.56E-08
14	0.00E+00	0.00E+00	0.00E+00	0.00E+00	0.00E+00	0.00E+00	-6.65E-07	-3.36E+08	-7.90E-07	-7.10E-09	-2.42E-08	3.00E+07	6.63E-07	3.37E+08	7.46E-07	7.01E-09	2.82E-08	-3.07E+07
15	0.00E+00	0.00E+00	0.00E+00	0.00E+00	0.00E+00	0.00E+00	1.06E-06	-8.79E-07	-3.36E+08	-4.89E-09	-3.00E+07	2.42E-08	-8.81E-07	8.47E-07	3.37E+08	5.53E-09	3.07E+07	-2.60E-08
16	0.00E+00	0.00E+00	0.00E+00	0.00E+00	0.00E+00	0.00E+00	-6.71E-10	-1.09E-08	-4.90E-09	-7.07E+04	-2.46E+03	-7.91E+02	-5.74E-09	1.29E-08	5.40E-09	8.18E+04	3.31E+03	-4.13E+02
17	0.00E+00	0.00E+00	0.00E+00	0.00E+00	0.00E+00	0.00E+00	1.32E-08	3.73E-09	-3.00E+07	-2.46E+03	-4.17E+06	-1.93E+05	-1.27E-08	-2.07E-09	3.07E+07	3.31E+03	4.73E+06	1.78E+05
18	0.00E+00	0.00E+00	0.00E+00	0.00E+00	0.00E+00	0.00E+00	4.19E-09	3.00E+07	3.73E-09	-7.91E+02	-1.93E+05	-3.63E+06	-2.53E-09	-3.07E+07	-8.59E-09	-4.13E+02	1.78E+05	4.20E+06
19	0.00E+00	0.00E+00	0.00E+00	0.00E+00	0.00E+00	0.00E+00	0.00E+00	0.00E+00	0.00E+00	0.00E+00	0.00E+00	0.00E+00	-6.17E+08	-2.98E-07	1.79E-07	-3.14E-08	5.80E-08	5.22E-08
20	0.00E+00	0.00E+00	0.00E+00	0.00E+00	0.00E+00	0.00E+00	0.00E+00	0.00E+00	0.00E+00	0.00E+00	0.00E+00	0.00E+00	1.98E-09	-1.27E+06	4.37E-08	8.73E-11	-4.02E-09	7.27E+05
21	0.00E+00	0.00E+00	0.00E+00	0.00E+00	0.00E+00	0.00E+00	0.00E+00	0.00E+00	0.00E+00	0.00E+00	0.00E+00	0.00E+00	-1.76E-07	3.23E-08	-1.27E+06	-6.40E-10	-7.27E+05	1.75E-09
22	0.00E+00	0.00E+00	0.00E+00	0.00E+00	0.00E+00	0.00E+00	0.00E+00	0.00E+00	0.00E+00	0.00E+00	0.00E+00	0.00E+00	6.41E-09	-1.95E-09	-5.05E-10	-1.11E+04	-8.50E+02	1.20E+03
23	0.00E+00	0.00E+00	0.00E+00	0.00E+00	0.00E+00	0.00E+00	0.00E+00	0.00E+00	0.00E+00	0.00E+00	0.00E+00	0.00E+00	-4.95E-10	-1.66E-09	-7.27E+05	-8.50E+02	-5.66E+05	1.52E+04
24	0.00E+00	0.00E+00	0.00E+00	0.00E+00	0.00E+00	0.00E+00	0.00E+00	0.00E+00	0.00E+00	0.00E+00	0.00E+00	0.00E+00	-1.66E-09	7.27E+05	4.86E-09	1.20E+03	1.52E+04	-5.77E+05
25	0.00E+00	0.00E+00	0.00E+00	0.00E+00	0.00E+00	0.00E+00	0.00E+00	0.00E+00	0.00E+00	0.00E+00	0.00E+00	0.00E+00	0.00E+00	0.00E+00	0.00E+00	0.00E+00	0.00E+00	0.00E+00
26	0.00E+00	0.00E+00	0.00E+00	0.00E+00	0.00E+00	0.00E+00	0.00E+00	0.00E+00	0.00E+00	0.00E+00	0.00E+00	0.00E+00	0.00E+00	0.00E+00	0.00E+00	0.00E+00	0.00E+00	0.00E+00
27	0.00E+00	0.00E+00	0.00E+00	0.00E+00	0.00E+00	0.00E+00	0.00E+00	0.00E+00	0.00E+00	0.00E+00	0.00E+00	0.00E+00	0.00E+00	0.00E+00	0.00E+00	0.00E+00	0.00E+00	0.00E+00
28	0.00E+00	0.00E+00	0.00E+00	0.00E+00	0.00E+00	0.00E+00	0.00E+00	0.00E+00	0.00E+00	0.00E+00	0.00E+00	0.00E+00	0.00E+00	0.00E+00	0.00E+00	0.00E+00	0.00E+00	0.00E+00
29	0.00E+00	0.00E+00	0.00E+00	0.00E+00	0.00E+00	0.00E+00	0.00E+00	0.00E+00	0.00E+00	0.00E+00	0.00E+00	0.00E+00	0.00E+00	0.00E+00	0.00E+00	0.00E+00	0.00E+00	0.00E+00
30	0.00E+00	0.00E+00	0.00E+00	0.00E+00	0.00E+00	0.00E+00	0.00E+00	0.00E+00	0.00E+00	0.00E+00	0.00E+00	0.00E+00	0.00E+00	0.00E+00	0.00E+00	0.00E+00	0.00E+00	0.00E+00
31	0.00E+00	0.00E+00	0.00E+00	0.00E+00	0.00E+00	0.00E+00	0.00E+00	0.00E+00	0.00E+00	0.00E+00	0.00E+00	0.00E+00	0.00E+00	0.00E+00	0.00E+00	0.00E+00	0.00E+00	0.00E+00
32	0.00E+00	0.00E+00	0.00E+00	0.00E+00	0.00E+00	0.00E+00	0.00E+00	0.00E+00	0.00E+00	0.00E+00	0.00E+00	0.00E+00	0.00E+00	0.00E+00	0.00E+00	0.00E+00	0.00E+00	0.00E+00
33	0.00E+00	0.00E+00	0.00E+00	0.00E+00	0.00E+00	0.00E+00	0.00E+00	0.00E+00	0.00E+00	0.00E+00	0.00E+00	0.00E+00	0.00E+00	0.00E+00	0.00E+00	0.00E+00	0.00E+00	0.00E+00
34	0.00E+00	0.00E+00	0.00E+00	0.00E+00	0.00E+00	0.00E+00	0.00E+00	0.00E+00	0.00E+00	0.00E+00	0.00E+00	0.00E+00	0.00E+00	0.00E+00	0.00E+00	0.00E+00	0.00E+00	0.00E+00
35	0.00E+00	0.00E+00	0.00E+00	0.00E+00	0.00E+00	0.00E+00	0.00E+00	0.00E+00	0.00E+00	0.00E+00	0.00E+00	0.00E+00	0.00E+00	0.00E+00	0.00E+00	0.00E+00	0.00E+00	0.00E+00
36	0.00E+00	0.00E+00	0.00E+00	0.00E+00	0.00E+00	0.00E+00	0.00E+00	0.00E+00	0.00E+00	0.00E+00	0.00E+00	0.00E+00	0.00E+00	0.00E+00	0.00E+00	0.00E+00	0.00E+00	0.00E+00

19	20	21	22	23	24	25	26	27	28	29	30	31	32	33	34	35	36
0.00E+00	0.00E+00	0.00E+00	0.00E+00	0.00E+00	0.00E+00	0.00E+00	0.00E+00	0.00E+00	0.00E+00	0.00E+00	0.00E+00	0.00E+00	0.00E+00	0.00E+00	0.00E+00	0.00E+00	0.00E+00
0.00E+00	0.00E+00	0.00E+00	0.00E+00	0.00E+00	0.00E+00	0.00E+00	0.00E+00	0.00E+00	0.00E+00	0.00E+00	0.00E+00	0.00E+00	0.00E+00	0.00E+00	0.00E+00	0.00E+00	0.00E+00
0.00E+00	0.00E+00	0.00E+00	0.00E+00	0.00E+00	0.00E+00	0.00E+00	0.00E+00	0.00E+00	0.00E+00	0.00E+00	0.00E+00	0.00E+00	0.00E+00	0.00E+00	0.00E+00	0.00E+00	0.00E+00
0.00E+00	0.00E+00	0.00E+00	0.00E+00	0.00E+00	0.00E+00	0.00E+00	0.00E+00	0.00E+00	0.00E+00	0.00E+00	0.00E+00	0.00E+00	0.00E+00	0.00E+00	0.00E+00	0.00E+00	0.00E+00
0.00E+00	0.00E+00	0.00E+00	0.00E+00	0.00E+00	0.00E+00	0.00E+00	0.00E+00	0.00E+00	0.00E+00	0.00E+00	0.00E+00	0.00E+00	0.00E+00	0.00E+00	0.00E+00	0.00E+00	0.00E+00
0.00E+00	0.00E+00	0.00E+00	0.00E+00	0.00E+00	0.00E+00	0.00E+00	0.00E+00	0.00E+00	0.00E+00	0.00E+00	0.00E+00	0.00E+00	0.00E+00	0.00E+00	0.00E+00	0.00E+00	0.00E+00
0.00E+00	0.00E+00	0.00E+00	0.00E+00	0.00E+00	0.00E+00	0.00E+00	0.00E+00	0.00E+00	0.00E+00	0.00E+00	0.00E+00	0.00E+00	0.00E+00	0.00E+00	0.00E+00	0.00E+00	0.00E+00
0.00E+00	0.00E+00	0.00E+00	0.00E+00	0.00E+00	0.00E+00	0.00E+00	0.00E+00	0.00E+00	0.00E+00	0.00E+00	0.00E+00	0.00E+00	0.00E+00	0.00E+00	0.00E+00	0.00E+00	0.00E+00
0.00E+00	0.00E+00	0.00E+00	0.00E+00	0.00E+00	0.00E+00	0.00E+00	0.00E+00	0.00E+00	0.00E+00	0.00E+00	0.00E+00	0.00E+00	0.00E+00	0.00E+00	0.00E+00	0.00E+00	0.00E+00
0.00E+00	0.00E+00	0.00E+00	0.00E+00	0.00E+00	0.00E+00	0.00E+00	0.00E+00	0.00E+00	0.00E+00	0.00E+00	0.00E+00	0.00E+00	0.00E+00	0.00E+00	0.00E+00	0.00E+00	0.00E+00
0.00E+00	0.00E+00	0.00E+00	0.00E+00	0.00E+00	0.00E+00	0.00E+00	0.00E+00	0.00E+00	0.00E+00	0.00E+00	0.00E+00	0.00E+00	0.00E+00	0.00E+00	0.00E+00	0.00E+00	0.00E+00
0.00E+00	0.00E+00	0.00E+00	0.00E+00	0.00E+00	0.00E+00	0.00E+00	0.00E+00	0.00E+00	0.00E+00	0.00E+00	0.00E+00	0.00E+00	0.00E+00	0.00E+00	0.00E+00	0.00E+00	0.00E+00
-6.17E+08	-2.98E-07	1.79E-07	-3.14E-08	5.80E-08	5.22E-08	0.00E+00	0.00E+00	0.00E+00	0.00E+00	0.00E+00	0.00E+00	0.00E+00	0.00E+00	0.00E+00	0.00E+00	0.00E+00	0.00E+00
1.98E-09	-1.27E+06	4.37E-08	8.73E-11	-4.02E-09	7.27E+05	0.00E+00	0.00E+00	0.00E+00	0.00E+00	0.00E+00	0.00E+00	0.00E+00	0.00E+00	0.00E+00	0.00E+00	0.00E+00	0.00E+00
-1.76E-07	3.23E-08	-1.27E+06	-6.40E-10	-7.27E+05	1.75E-09	0.00E+00	0.00E+00	0.00E+00	0.00E+00	0.00E+00	0.00E+00	0.00E+00	0.00E+00	0.00E+00	0.00E+00	0.00E+00	0.00E+00
6.41E-09	-1.95E-09	-5.05E-10	-1.11E+04	-8.50E+02	1.20E+03	0.00E+00	0.00E+00	0.00E+00	0.00E+00	0.00E+00	0.00E+00	0.00E+00	0.00E+00	0.00E+00	0.00E+00	0.00E+00	0.00E+00
-4.95E-10	-1.66E-09	-7.27E+05	-8.50E+02	-5.66E+05	1.52E+04	0.00E+00	0.00E+00	0.00E+00	0.00E+00	0.00E+00	0.00E+00	0.00E+00	0.00E+00	0.00E+00	0.00E+00	0.00E+00	0.00E+00
-1.66E-09	7.27E+05	4.86E-09	1.20E+03	1.52E+04	-5.77E+05	0.00E+00	0.00E+00	0.00E+00	0.00E+00	0.00E+00	0.00E+00	0.00E+00	0.00E+00	0.00E+00	0.00E+00	0.00E+00	0.00E+00
3.15E+11	-1.48E+01	-1.80E+01	8.97E-06	-4.48E-03	3.71E-03	-3.14E+11	1.48E+01	1.80E+01	-8.94E-06	4.48E-03	-3.71E-03	0.00E+00	0.00E+00	0.00E+00	0.00E+00	0.00E+00	0.00E+00
-1.98E-09	3.77E+14	-2.20E+01	7.63E-06	-5.56E-03	-1.88E+11	0.00E+00	-3.77E+14	2.20E+01	-7.63E-06	5.56E-03	1.88E+11	0.00E+00	0.00E+00	0.00E+00	0.00E+00	0.00E+00	0.00E+00
-3.91E-02	-4.64E+00	3.77E+14	-9.16E-05	1.88E+11	1.08E-03	3.91E-02	4.64E+00	-3.77E+14	9.16E-05	-1.88E+11	-1.08E-03	0.00E+00	0.00E+00	0.00E+00	0.00E+00	0.00E+00	0.00E+00
6.88E-06	-3.77E-03	-1.59E-03	2.48E+06	-8.23E+05	2.74E+05	-6.89E-06	3.77E-03	1.59E-03	-2.47E+06	8.24E+05	-2.75E+05	0.00E+00	0.00E+00	0.00E+00	0.00E+00	0.00E+00	0.00E+00
3.43E-05	-3.28E-02	1.88E+11	-8.23E+05	9.80E+07	9.41E+06	-3.43E-05	3.28E-02	-1.88E+11	8.24E+05	-9.74E+07	-9.43E+06	0.00E+00	0.00E+00	0.00E+00	0.00E+00	0.00E+00	0.00E+00
6.87E-05	-1.88E+11	-2.01E-02	2.74E+05	9.41E+06	1.23E+08	-6.87E-05	1.88E+11	2.01E-02	-2.75E+05	-9.43E+06	-1.23E+08	0.00E+00	0.00E+00	0.00E+00	0.00E+00	0.00E+00	0.00E+00
-3.14E+11	1.48E+01	1.80E+01	-8.94E-06	4.48E-03	-3.71E-03	3.14E+11	-1.48E+01	-1.80E+01	8.94E-06	-6.70E+04	3.71E-03	-9.26E+07	0.00E+00	-3.44E-09	9.28E-11	6.70E+04	-5.82E-11
0.00E+00	-3.77E+14	2.20E+01	-7.63E-06	5.56E-03	1.88E+11	0.00E+00	3.77E+14	-2.20E+01	6.70E+04	-5.56E-03	-1.88E+11	0.00E+00	-6.63E+07	0.00E+00	-6.70E+04	-8.88E-10	2.96E-11
3.91E-02	4.64E+00	-3.77E+14	9.16E-05	-1.88E+11	-1.08E-03	-3.91E-02	-4.64E+00	3.77E+14	-9.16E-05	1.88E+11	1.08E-03	-3.44E-09	0.00E+00	-1.49E+08	1.62E-08	-1.18E-08	-2.77E-09
-6.89E-06	3.77E-03	1.59E-03	-2.47E+06	8.24E+05	-2.75E+05	6.89E-06	6.70E+04	-1.59E-03	2.49E+06	-8.24E+05	2.75E+05	1.06E-09	-6.70E+04	1.35E-09	-1.87E+04	1.41E+01	4.25E-01
-3.43E-05	3.28E-02	-1.88E+11	8.24E+05	-9.74E+07	-9.43E+06	-6.70E+04	-3.28E-02	1.88E+11	-8.24E+05	9.75E+07	9.43E+06	6.70E+04	4.55E-11	5.77E-11	1.41E+01	-1.88E+04	-1.01E+00
-6.87E-05	1.88E+11	2.01E-02	-2.75E+05	-9.43E+06	-1.23E+08	6.87E-05	-1.88E+11	-2.01E-02	2.75E+05	9.43E+06	1.23E+08	1.08E-11	-5.38E-11	-5.17E-10	4.25E-01	-1.01E+00	-3.71E+02
0.00E+00	0.00E+00	0.00E+00	0.00E+00	0.00E+00	0.00E+00	-9.26E+07	0.00E+00	-3.44E-09	9.28E-11	6.70E+04	-5.82E-11	9.26E+07	0.00E+00	3.44E-09	-9.28E-11	-6.70E+04	5.82E-11
0.00E+00	0.00E+00	0.00E+00	0.00E+00	0.00E+00	0.00E+00	0.00E+00	-6.63E+07	0.00E+00	-6.70E+04	-8.88E-10	2.96E-11	0.00E+00	6.63E+07	0.00E+00	6.70E+04	8.88E-10	-2.96E-11
0.00E+00	0.00E+00	0.00E+00	0.00E+00	0.00E+00	0.00E+00	-3.44E-09	0.00E+00	-1.49E+08	1.62E-08	-1.18E-08	-2.77E-09	3.44E-09	0.00E+00	1.49E+08	-1.62E-08	1.18E-08	2.77E-09
0.00E+00	0.00E+00	0.00E+00	0.00E+00	0.00E+00	0.00E+00	1.06E-09	-6.70E+04	1.35E-09	-1.87E+04	1.41E+01	4.25E-01	-1.06E-09	6.70E+04	-1.35E-09	1.87E+04	-1.41E+01	-4.25E-01
0.00E+00	0.00E+00	0.00E+00	0.00E+00	0.00E+00	0.00E+00	6.70E+04	4.55E-11	5.77E-11	1.41E+01	-1.88E+04	-1.01E+00	-6.70E+04	-4.55E-11	-5.77E-11	-1.41E+01	1.88E+04	1.01E+00
0.00E+00	0.00E+00	0.00E+00	0.00E+00	0.00E+00	0.00E+00	1.08E-11	-5.38E-11	-5.17E-10	4.25E-01	-1.01E+00	-3.71E+02	-1.08E-11	5.38E-11	5.17E-10	-4.25E-01	1.01E+00	3.71E+02

M_C (convert to diagonal)	
1	478.1478155
2	478.1478155
3	478.1478155
4	29.31827143
5	24.22770505
6	37.76596901
7	154.2855258
8	154.2855258
9	154.2855258
10	66.79881305
11	5.348412269
12	33.92478109
13	213.9519076
14	213.9519076
15	213.9519076
16	5.437793314
17	5.534949941
18	9.436430088
19	186.6735005
20	186.6735005
21	186.6735005
22	19.13084547
23	39.37084489
24	2.486169891
25	26.32104143
26	26.32104143
27	26.32104143
28	0.243464151
29	0.134758736
30	0.160020586
31	60
32	60
33	60
34	2.7375
35	2.7375
36	1.875

Natural Frequencies	
1	4042651.61842316 + 0.00000000000000i
2	116713.734272212 + 0.00000000000000i
3	4042642.01671646 + 0.00000000000000i
4	14542.6055194804 + 0.00000000000000i
5	7224.94842481382 + 0.00000000000000i
6	4778.29783058044 + 0.00000000000000i
7	3504.46344632432 + 0.00000000000000i
8	2560.40420712155 + 0.00000000000000i
9	0.00000000000000 - 1245.08176173863i
10	2272.89461766791 + 0.00000000000000i
11	1504.38942756699 + 0.00000000000000i
12	2045.06437059452 + 0.00000000000000i
13	2016.50071672957 + 0.00000000000000i
14	1782.72594402762 + 0.00000000000000i
15	1780.40532397782 + 0.00000000000000i
16	955.854676975869 + 0.00000000000000i
17	1190.40065136398 + 0.00000000000000i
18	939.738900227670 + 0.00000000000000i
19	551.148152221280 + 0.00000000000000i
20	538.066739963717 + 0.00000000000000i
21	425.494878206218 + 0.00000000000000i
22	367.068485731981 + 0.00000000000000i
23	270.452337401746 + 0.00000000000000i
24	244.508836453373 + 0.00000000000000i
25	0.00000000000000 - 138.326193295759i
26	118.389625332388 + 0.00000000000000i
27	126.921886233904 + 0.00000000000000i
28	82.1353355805617 + 0.00000000000000i
29	93.2191609925586 + 0.00000000000000i
30	88.6600032863289 + 0.00000000000000i
31	71.2603853315762 + 0.00000000000000i
32	29.0712719030132 + 0.00000000000000i
33	31.8239912180145 + 0.00000000000000i
34	35.4662221744481 + 0.00000000000000i
35	18.8283123550378 + 0.00000000000000i
36	14.0475281878552 + 0.00000000000000i

Mode shapes	1	2	3	4	5	6	7	8	9	10	11	12	13	14	15	16	17	18
1	-1.60E-17	1.68E-17	1.33E-11	-2.18E-10	1.09E-01	-1.00E+00	2.72E-09	-1.85E-01	4.80E-07	-4.35E-02	-8.64E-08	1.87E-02	-6.33E-08	-1.61E-08	1.66E-07	8.79E-09	5.63E-07	-1.51E-07
2	3.05E-28	1.93E-26	2.02E-25	3.32E-13	1.94E-15	1.12E-13	2.65E-12	-7.50E-10	-5.67E-08	7.85E-08	-5.49E-03	6.73E-08	2.11E-02	2.36E-02	1.11E-04	1.58E-01	-3.65E-05	6.41E-03
3	-2.99E-26	-7.70E-27	2.60E-26	-8.42E-13	-8.68E-15	-3.98E-13	8.21E-13	7.31E-09	3.28E-08	-1.80E-07	-3.68E-02	-2.26E-07	3.13E-02	1.13E-01	-1.31E-04	-4.81E-02	6.60E-06	2.70E-02
4	-9.17E-29	3.17E-29	1.18E-27	2.31E-15	1.20E-16	1.30E-14	-4.66E-16	-6.50E-10	-1.22E-08	3.10E-08	3.87E-03	4.47E-08	-2.94E-03	-1.23E-02	2.18E-05	1.21E-02	-2.86E-06	2.65E-03
5	-4.77E-25	-1.15E-25	4.18E-25	-1.31E-11	-1.31E-13	-5.56E-12	1.34E-11	7.79E-08	-7.38E-07	-1.02E-06	-3.40E-01	-6.28E-07	2.85E-01	1.00E+00	-9.27E-04	-3.04E-01	1.76E-05	-1.97E-02
6	5.42E-27	-1.65E-25	-1.74E-24	-2.62E-12	-1.38E-14	-7.98E-13	-2.28E-11	2.66E-09	1.12E-06	-3.66E-07	5.41E-02	-1.12E-07	-1.59E-01	-2.11E-01	-6.52E-04	-1.00E+00	1.90E-04	7.85E-03
7	-1.19E-17	-2.12E-17	-5.65E-08	9.18E-09	-1.00E+00	-2.03E-02	-3.24E-08	-9.47E-01	3.64E-06	-2.83E-01	-4.97E-07	1.29E-01	-3.71E-07	-9.47E-08	1.03E-06	5.43E-08	3.71E-06	-1.06E-06
8	2.28E-22	-1.48E-17	-9.30E-20	-2.91E-09	-5.44E-12	-1.24E-10	-8.42E-09	1.89E-07	-2.82E-05	2.02E-06	1.12E-02	1.81E-06	-6.54E-01	5.85E-02	3.62E-07	2.08E-02	-2.05E-03	-1.90E-02
9	1.91E-17	-1.35E-21	-1.20E-19	5.18E-09	1.63E-11	2.75E-10	-1.63E-09	-5.49E-07	-5.50E-06	-6.74E-06	4.10E-01	-1.40E-05	4.37E-02	8.10E-02	-2.53E-03	-7.25E-03	-3.40E-05	-9.11E-02
10	8.25E-21	-3.40E-21	-7.23E-23	1.64E-12	3.48E-15	7.28E-14	3.81E-12	-9.69E-11	-5.10E-08	1.68E-09	4.80E-05	2.08E-08	-2.33E-05	3.47E-06	1.42E-07	-3.96E-06	4.97E-07	8.06E-04
11	2.04E-17	-6.94E-19	-1.29E-19	5.52E-09	1.75E-11	2.90E-10	-2.22E-09	-5.57E-07	-1.24E-05	-5.41E-06	4.23E-01	-2.47E-06	1.58E-02	6.67E-03	-2.24E-03	1.86E-02	8.15E-05	7.86E-01
12	-3.76E-19	5.16E-18	3.52E-20	9.26E-10	1.59E-12	3.85E-11	3.02E-09	-5.70E-08	1.33E-05	-6.59E-07	-7.34E-03	-1.45E-06	2.14E-01	-1.38E-02	1.28E-05	2.02E-02	5.68E-04	-5.88E-02
13	9.21E-19	-1.77E-19	2.99E-05	-4.34E-08	6.05E-01	3.76E-01	3.09E-08	-1.00E+00	5.05E-06	-3.52E-01	-5.68E-07	1.67E-01	-4.30E-07	-1.10E-07	1.25E-06	6.51E-08	4.67E-06	-1.40E-06
14	5.92E-16	5.14E-11	2.26E-16	8.21E-08	5.13E-11	5.08E-10	9.05E-08	-2.16E-07	-7.81E-06	-6.86E-07	-7.74E-03	2.70E-08	4.66E-01	-4.31E-02	-6.52E-06	-2.32E-02	4.73E-04	1.29E-02
15	-5.13E-11	5.89E-16	3.39E-16	-1.11E-07	-1.17E-10	-8.79E-10	1.23E-08	5.42E-07	-4.97E-07	2.77E-06	-2.90E-01	4.29E-06	-3.29E-02	-6.40E-02	1.22E-03	7.82E-03	2.42E-05	9.21E-02
16	-3.65E-15	9.86E-15	3.88E-17	4.45E-09	1.00E-10	2.01E-10	-3.16E-07	-2.72E-08	-1.65E-05	1.59E-07	-5.22E-04	-1.97E-07	2.93E-04	-1.24E-04	-2.56E-06	-8.07E-06	-1.96E-05	-8.98E-03
17	-1.03E-09	1.11E-13	4.69E-15	-2.89E-06	-2.86E-09	-1.90E-08	3.52E-07	5.45E-06	-1.10E-04	-4.11E-05	-1.00E+00	-1.48E-04	-9.69E-02	-2.19E-01	-6.11E-03	2.53E-02	-2.57E-04	-1.00E+00
18	2.62E-14	-6.70E-10	-3.94E-15	-1.40E-06	-8.22E-10	-7.46E-09	-1.53E-06	1.68E-06	4.47E-04	-9.59E-06	2.71E-02	-1.39E-05	-1.00E+00	9.43E-02	6.58E-05	4.94E-02	1.04E-02	2.58E-01
19	-1.87E-14	1.54E-14	-1.41E-01	1.99E-06	-3.58E-02	-5.57E-02	-2.16E-07	9.22E-01	1.65E-05	-5.39E-01	-1.41E-07	3.61E-01	-1.88E-07	-5.31E-08	1.33E-06	6.33E-08	7.90E-06	-3.37E-06
20	-1.62E-06	-1.41E-01	4.61E-12	1.85E-05	5.07E-09	1.54E-08	2.12E-06	-9.01E-07	7.02E-05	8.48E-06	3.56E-05	-9.17E-07	-1.75E-03	1.68E-04	-2.30E-06	1.26E-04	2.83E-01	1.71E-03
21	1.41E-01	-1.62E-06	-1.50E-09	-6.01E-05	-4.91E-09	-1.82E-09	2.28E-06	-1.31E-07	5.50E-05	4.92E-06	1.65E-03	5.23E-06	1.99E-04	4.50E-04	2.82E-01	-2.02E-04	2.09E-06	6.02E-03
22	-5.35E-10	1.07E-09	-2.29E-10	-2.90E-04	-2.34E-06	-2.06E-06	8.62E-03	8.57E-05	-8.77E-03	-2.06E-04	4.68E-05	-8.48E-05	-1.06E-04	2.13E-05	1.45E-04	5.61E-06	9.20E-03	6.73E-04
23	3.41E-04	-3.05E-09	1.26E-09	5.06E-03	1.62E-06	4.56E-06	-2.03E-04	-2.83E-04	-2.12E-03	1.16E-03	4.49E-03	1.20E-03	3.83E-04	1.10E-03	1.83E-03	-1.58E-04	-2.51E-05	3.63E-02
24	9.61E-09	6.50E-04	9.13E-10	3.73E-03	7.36E-07	2.83E-06	1.51E-03	-1.56E-04	1.22E-02	4.62E-04	-4.14E-04	3.02E-04	1.09E-02	-1.09E-03	-3.03E-04	-7.05E-04	-5.61E-03	-2.20E-02
25	1.01E-11	-1.09E-13	1.00E+00	1.80E-06	-3.60E-02	-5.58E-02	-2.08E-07	9.22E-01	1.65E-05	-5.38E-01	-1.40E-07	3.61E-01	-1.87E-07	-5.29E-08	1.33E-06	6.32E-08	7.90E-06	-3.37E-06
26	1.15E-05	1.00E+00	-3.27E-11	-1.34E-04	-2.49E-08	-1.00E-07	-5.97E-05	5.45E-06	-4.36E-04	-1.02E-05	3.62E-05	-1.29E-05	-1.76E-03	1.69E-04	9.84E-06	1.26E-04	2.83E-01	1.71E-03
27	-1.00E+00	1.15E-05	1.06E-08	4.42E-04	3.99E-08	2.49E-08	-1.79E-05	1.10E-06	-1.44E-04	-7.84E-07	1.65E-03	1.18E-06	1.98E-04	4.50E-04	2.82E-01	-2.02E-04	-1.09E-06	6.02E-03
28	6.17E-08	-3.35E-08	2.64E-08	3.35E-02	2.72E-04	2.42E-04	-1.00E+00	-1.06E-02	7.74E-01	2.96E-02	-9.17E-04	1.89E-02	5.57E-03	-7.26E-04	-1.94E-02	-3.01E-04	-1.14E-02	-3.54E-03
29	-6.75E-02	6.02E-07	-2.43E-05	-1.00E+00	-8.80E-05	-4.88E-05	4.01E-02	-2.75E-03	3.96E-01	1.26E-02	4.16E-03	9.28E-03	3.07E-03	7.75E-04	-5.05E-03	-3.08E-04	6.35E-03	3.42E-02
30	-7.75E-07	-5.24E-02	-7.36E-08	-3.01E-01	-5.93E-05	-2.28E-04	-1.22E-01	1.25E-02	-1.00E+00	-3.68E-02	7.49E-04	-2.37E-02	4.42E-03	-2.15E-04	2.40E-02	-3.51E-04	-2.35E-02	-1.67E-02
31	-4.39E-12	3.80E-17	-1.01E-04	-6.84E-06	9.69E-04	3.56E-03	7.21E-07	-2.45E-01	-1.45E-04	1.00E+00	1.48E-06	1.00E+00	1.26E-06	3.32E-07	-4.43E-06	-2.31E-07	-9.52E-06	-4.20E-05
32	-9.86E-13	-8.56E-08	1.30E-15	9.73E-07	-5.00E-09	-5.49E-09	1.93E-05	7.03E-07	7.61E-05	-2.45E-05	-1.60E-05	4.11E-06	8.89E-04	-8.80E-05	4.36E-06	-9.97E-05	-1.00E+00	2.33E-03
33	1.43E-07	-1.64E-12	-1.82E-12	-6.67E-06	-1.87E-09	-2.83E-09	7.12E-07	-6.14E-07	-9.10E-05	-8.04E-06	-1.78E-03	1.89E-06	-2.54E-04	-6.05E-04	-1.00E+00	5.67E-04	-4.73E-06	7.17E-03
34	-9.64E-15	-1.43E-09	-9.75E-15	-1.39E-06	-3.48E-08	-7.08E-08	1.10E-04	1.08E-05	3.79E-03	-9.45E-05	1.09E-06	-1.45E-04	5.90E-06	-2.77E-07	4.35E-05	-1.03E-06	-1.67E-02	1.03E-04
35	2.76E-11	-6.71E-16	1.71E-06	4.25E-05	-1.65E-05	-6.07E-05	-4.37E-06	4.17E-03	1.93E-03	-1.71E-02	-6.19E-06	-1.72E-02	-4.95E-06	-1.27E-06	1.14E-05	6.52E-07	-2.35E-05	-6.16E-04
36	-7.90E-16	6.20E-13	6.77E-16	3.69E-07	2.24E-10	1.94E-09	3.73E-07	-3.73E-07	-1.43E-04	3.40E-06	-3.22E-08	5.26E-06	-2.04E-07	1.01E-08	-1.55E-06	2.14E-08	2.54E-06	8.59E-06

19	20	21	22	23	24	25	26	27	28	29	30	31	32	33	34	35	36
-1.30E-07	6.35E-08	-2.19E-09	1.10E-08	-8.91E-09	-9.73E-09	-2.32E-08	-2.32E-09	1.35E-07	-2.10E-09	5.23E-08	-2.99E-08	7.10E-09	1.20E-11	4.32E-13	5.78E-10	1.13E-10	-1.01E-10
-2.34E-02	-5.66E-02	-3.22E-01	-3.50E-02	-3.30E-02	-1.59E-01	-2.86E-03	-1.40E-04	1.70E-02	3.42E-04	-1.34E-02	-4.00E-04	1.15E-03	-1.36E-03	-1.55E-06	-6.11E-03	-3.09E-04	1.86E-03
-3.97E-02	-1.87E-02	-1.15E-01	-5.78E-02	7.14E-02	4.07E-01	-1.64E-03	-6.79E-04	-3.51E-02	-6.95E-04	2.32E-02	2.17E-04	-3.94E-02	3.61E-03	2.43E-05	5.59E-03	1.01E-03	-5.41E-03
-1.18E-02	1.33E-03	3.67E-03	-1.42E-01	1.00E+00	-7.69E-01	2.59E-03	-3.07E-03	1.06E-01	7.08E-04	-7.11E-02	-1.28E-03	9.22E-02	8.53E-03	-5.44E-05	-8.08E-03	-1.34E-02	3.30E-03
5.33E-02	3.95E-02	2.28E-01	1.23E-01	-1.58E-01	-1.00E+00	4.31E-03	1.66E-03	8.16E-02	1.67E-03	-5.97E-02	-1.06E-03	9.55E-02	-8.62E-03	-5.84E-05	-1.43E-02	-2.65E-03	1.32E-02
-4.06E-02	-1.08E-01	-6.03E-01	-1.06E-01	-7.47E-02	-3.89E-01	-1.08E-02	-7.54E-04	3.91E-02	8.04E-04	-3.13E-02	-8.96E-04	9.08E-03	-3.28E-03	-4.49E-06	-1.31E-02	-8.81E-04	4.66E-03
-9.23E-07	4.51E-07	-1.56E-08	7.86E-08	-6.36E-08	-6.97E-08	-1.66E-07	-1.66E-08	9.65E-07	-1.50E-08	3.75E-07	-2.14E-07	5.09E-08	8.67E-11	2.89E-12	4.10E-09	8.21E-10	-7.33E-10
-1.97E-02	-7.71E-02	6.38E-02	1.49E-01	1.36E-02	-5.55E-03	4.80E-02	4.29E-03	2.28E-02	4.44E-04	-3.20E-02	-5.95E-03	-7.66E-01	7.55E-04	3.22E-04	-1.61E-01	1.76E-02	-2.32E-02
-6.64E-02	3.86E-02	-6.26E-04	7.72E-03	-1.17E-02	9.02E-02	-9.09E-03	-1.49E-03	7.98E-02	2.63E-03	-2.61E-01	-2.26E-02	1.17E-01	4.67E-03	-1.89E-05	-5.03E-02	-1.80E-02	1.10E-02
3.90E-04	2.45E-04	-3.84E-04	2.54E-03	-1.98E-02	-5.07E-02	4.11E-02	-8.06E-02	-1.19E-02	-2.74E-02	1.40E-02	1.17E-03	-2.39E-02	4.07E-01	-4.72E-05	2.13E-01	-2.58E-01	-2.35E-01
-5.16E-01	8.02E-02	4.14E-01	1.96E-02	-9.87E-02	-6.11E-01	3.38E-02	5.46E-03	-1.47E-01	-2.50E-03	2.08E-01	1.40E-02	-9.47E-02	-9.78E-03	5.67E-06	3.68E-02	1.83E-02	-5.21E-03
-1.85E-02	-9.47E-02	3.45E-01	-1.00E+00	-8.93E-02	-1.49E-01	-8.67E-02	-9.99E-03	5.57E-03	7.48E-04	-4.41E-02	-7.42E-03	-9.45E-01	-8.25E-04	4.70E-04	-1.96E-01	2.16E-02	-2.63E-02
-1.22E-06	5.98E-07	-2.06E-08	1.04E-07	-8.46E-08	-9.29E-08	-2.21E-07	-2.21E-08	1.29E-06	-2.00E-08	4.99E-07	-2.85E-07	6.77E-08	1.16E-10	3.03E-12	5.46E-09	1.10E-09	-9.78E-10
8.20E-03	2.59E-02	-6.59E-02	2.02E-01	2.00E-02	2.41E-04	1.59E-02	1.29E-03	5.62E-03	4.08E-04	-3.30E-02	-6.60E-03	-7.72E-01	7.73E-04	3.56E-04	-1.64E-01	1.82E-02	-2.40E-02
-2.44E-02	-1.92E-04	4.43E-02	-7.70E-04	-1.65E-02	7.65E-02	-8.56E-03	-1.09E-03	1.14E-01	3.02E-03	-2.62E-01	-2.10E-02	1.18E-01	4.62E-03	-2.66E-05	-5.29E-02	-1.90E-02	1.18E-02
-5.97E-03	-4.06E-03	5.58E-03	-1.64E-03	5.47E-03	-2.41E-02	-5.23E-01	1.00E+00	6.66E-03	1.79E-01	2.27E-02	1.88E-04	-5.87E-02	2.80E-01	-1.81E-05	2.88E-01	-3.59E-01	-3.38E-01
-1.00E+00	5.01E-01	-3.48E-02	1.11E-01	-5.03E-02	-4.63E-01	3.14E-02	1.59E-03	-5.47E-01	-6.85E-03	2.01E-01	-6.52E-03	-9.91E-02	-9.16E-03	9.14E-05	6.13E-02	2.80E-02	-1.30E-02
2.74E-01	1.00E+00	-1.00E+00	-5.07E-01	-2.55E-02	-8.28E-02	-4.65E-01	-4.57E-02	-1.92E-01	3.42E-04	-5.45E-02	-1.46E-02	-1.00E+00	-7.43E-04	8.54E-04	-2.29E-01	2.76E-02	-3.45E-02
-3.03E-06	1.51E-06	-5.18E-08	2.67E-07	-2.17E-07	-2.42E-07	-5.74E-07	-5.72E-08	3.33E-06	-5.20E-08	1.29E-06	-7.41E-07	1.76E-07	3.13E-10	-2.02E-12	1.43E-08	2.87E-09	-2.54E-09
3.40E-03	1.83E-02	-1.59E-02	-3.57E-02	-3.68E-03	4.79E-03	9.95E-02	1.08E-02	3.49E-02	-5.24E-04	1.20E-02	3.05E-03	2.32E-01	6.79E-03	2.02E-03	-7.64E-01	8.59E-02	-1.27E-01
1.29E-02	-8.81E-03	-7.19E-04	-4.02E-03	3.84E-03	-2.09E-02	2.79E-02	3.93E-03	-1.96E-01	-2.36E-03	8.54E-03	-2.39E-02	1.96E-02	-1.59E-03	-2.38E-04	-5.40E-01	-1.53E-01	1.27E-01
1.11E-03	8.52E-04	-1.33E-03	-1.64E-03	-1.17E-04	-3.90E-03	1.22E-01	-2.06E-01	-7.32E-02	6.28E-01	3.40E-02	-1.20E-02	-7.80E-03	-7.44E-01	3.39E-04	5.44E-01	-8.82E-01	-8.79E-01
7.18E-02	-4.61E-02	-4.95E-03	-2.57E-02	1.91E-02	-1.46E-01	1.58E-01	2.02E-02	-9.84E-01	-7.31E-03	-2.44E-01	-5.81E-02	1.08E-01	6.38E-04	4.44E-04	7.17E-01	2.16E-01	-1.75E-01
-4.14E-02	-1.98E-01	1.77E-01	3.50E-01	3.41E-02	-4.11E-02	-1.00E+00	-1.04E-01	-3.15E-01	-2.30E-04	-1.35E-02	-5.01E-03	3.29E-01	5.29E-03	3.61E-03	-1.00E+00	1.20E-01	-1.74E-01
-3.04E-06	1.51E-06	-5.18E-08	2.67E-07	-2.17E-07	-2.43E-07	-5.74E-07	-5.73E-08	3.34E-06	-5.20E-08	1.30E-06	-7.42E-07	1.76E-07	3.13E-10	-2.03E-12	1.43E-08	2.88E-09	-2.54E-09
3.41E-03	1.83E-02	-1.59E-02	-3.57E-02	-3.68E-03	4.79E-03	9.95E-02	1.08E-02	3.49E-02	-5.52E-04	1.20E-02	3.05E-03	2.32E-01	6.79E-03	2.02E-03	-7.64E-01	8.59E-02	-1.27E-01
1.29E-02	-8.80E-03	-7.22E-04	-4.02E-03	3.84E-03	-2.09E-02	2.79E-02	3.93E-03	-1.96E-01	-2.38E-03	8.55E-03	-2.39E-02	1.96E-02	-1.59E-03	-2.39E-04	-5.40E-01	-1.53E-01	1.27E-01
-3.87E-03	-1.28E-02	1.19E-02	1.27E-02	1.08E-03	-5.44E-03	1.21E-01	-2.12E-01	-1.04E-01	6.61E-01	1.95E-02	4.05E-04	-1.04E-02	-7.38E-01	1.01E-03	5.40E-01	-8.80E-01	-8.76E-01
6.94E-02	-5.29E-02	1.69E-03	-1.85E-02	1.97E-02	-1.47E-01	1.58E-01	1.57E-02	-9.98E-01	1.47E-02	-2.51E-01	-5.25E-02	1.07E-01	4.16E-03	7.79E-04	7.15E-01	2.17E-01	-1.73E-01
-3.51E-02	-1.81E-01	1.61E-01	3.32E-01	3.26E-02	-3.91E-02	-1.00E+00	-9.26E-02	-2.74E-01	-5.65E-02	4.03E-03	-2.07E-02	3.32E-01	-3.69E-03	2.77E-03	-9.95E-01	1.17E-01	-1.79E-01
-7.03E-05	5.05E-05	-1.63E-06	1.69E-05	-1.80E-05	8.27E-05	-1.97E-04	-1.93E-05	1.57E-03	-2.95E-05	9.78E-04	-7.40E-04	2.28E-04	1.22E-06	3.46E-08	9.37E-05	2.30E-05	-1.91E-05
4.07E-03	2.08E-02	-1.82E-02	-3.83E-02	-3.88E-03	4.72E-03	1.01E-01	1.07E-02	3.51E-02	7.16E-04	1.21E-02	3.05E-03	2.33E-01	7.00E-03	2.02E-03	-7.65E-01	8.61E-02	-1.26E-01
1.43E-02	-9.48E-03	-7.82E-04	-4.19E-03	3.96E-03	-2.08E-02	2.81E-02	3.97E-03	-1.97E-01	-2.39E-03	8.58E-03	-2.40E-02	1.96E-02	-1.60E-03	-2.39E-04	-5.40E-01	-1.53E-01	1.27E-01
1.85E-04	8.91E-04	-7.81E-04	-1.66E-03	-1.80E-04	-1.37E-03	-6.73E-02	1.20E-01	1.06E-01	-1.00E+00	-7.59E-02	1.10E-02	-4.98E-02	-1.00E+00	1.13E-03	6.34E-01	-1.00E+00	-1.00E+00
-2.07E-03	2.19E-03	-6.61E-05	1.42E-03	-2.00E-03	-3.84E-02	-9.15E-02	-8.74E-03	1.00E+00	-2.29E-02	1.00E+00	-1.00E+00	3.99E-01	5.73E-03	8.23E-04	8.35E-01	2.47E-01	-1.98E-01
2.96E-05	2.09E-04	-1.76E-04	-6.87E-04	-8.73E-05	-3.97E-04	1.08E-02	9.60E-04	4.00E-03	1.14E-03	-1.15E-04	6.82E-04	-1.37E-02	6.06E-04	1.00E+00	2.50E-01	-3.72E-02	5.46E-02

FRF Output – X Direction

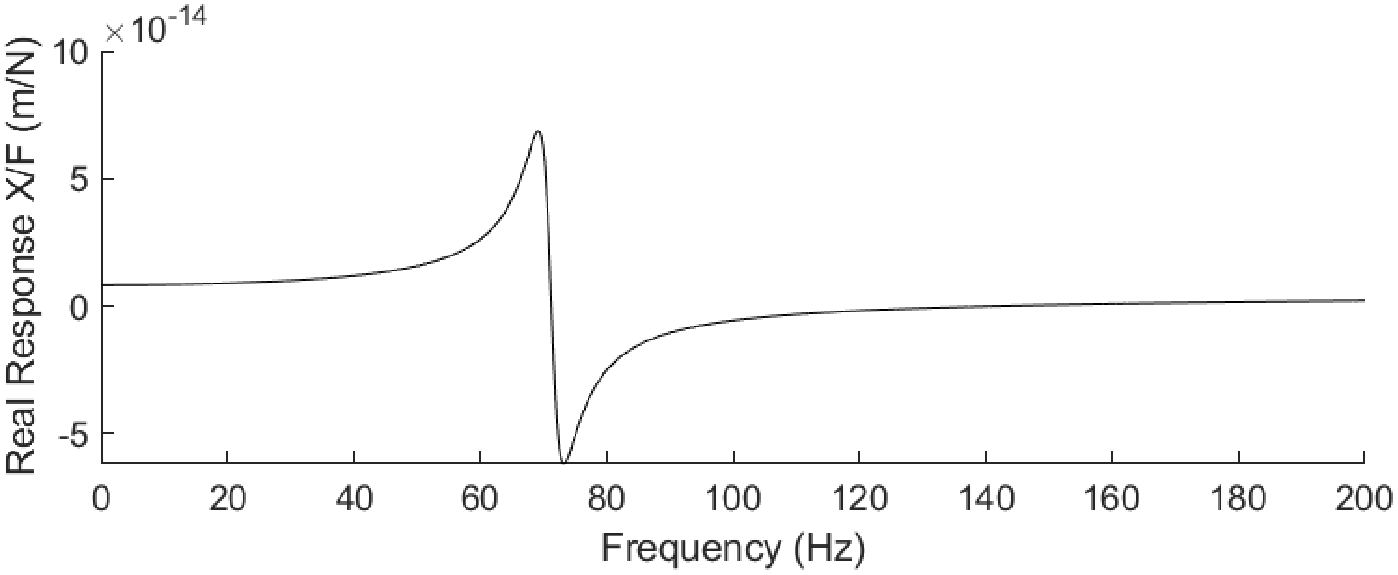

Modes: [69.2, 6.85289e-14]

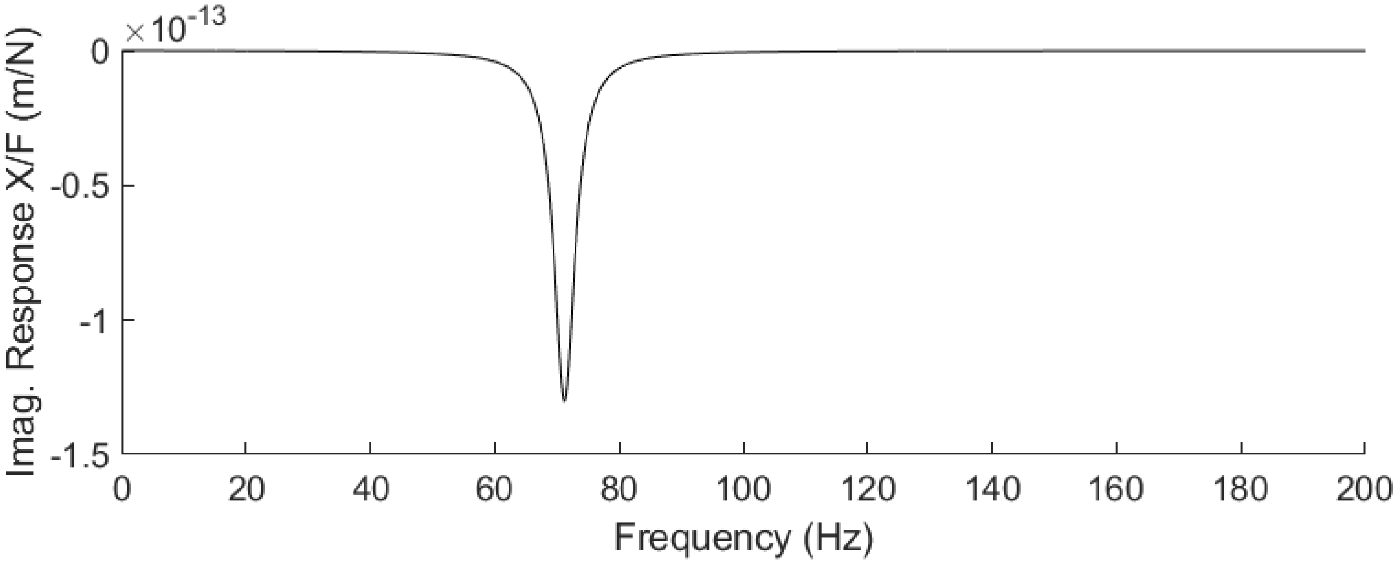

FRF Output – Y Direction

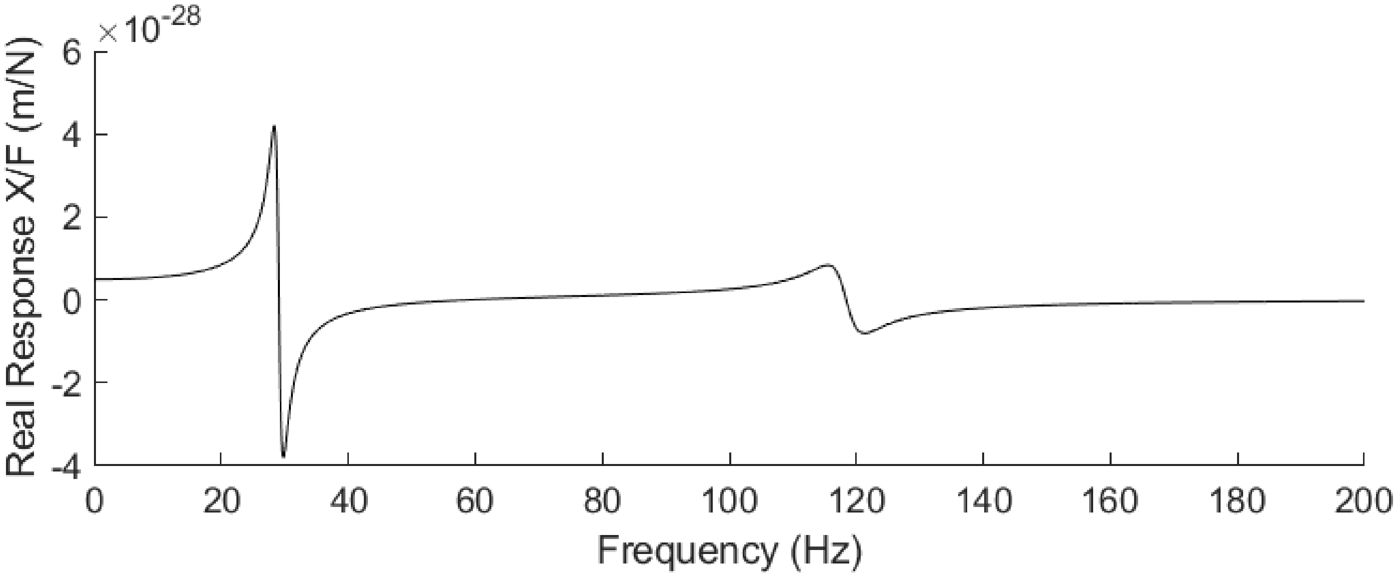

Modes: [28.3,4.20539e-28;115,8.27955e-29]

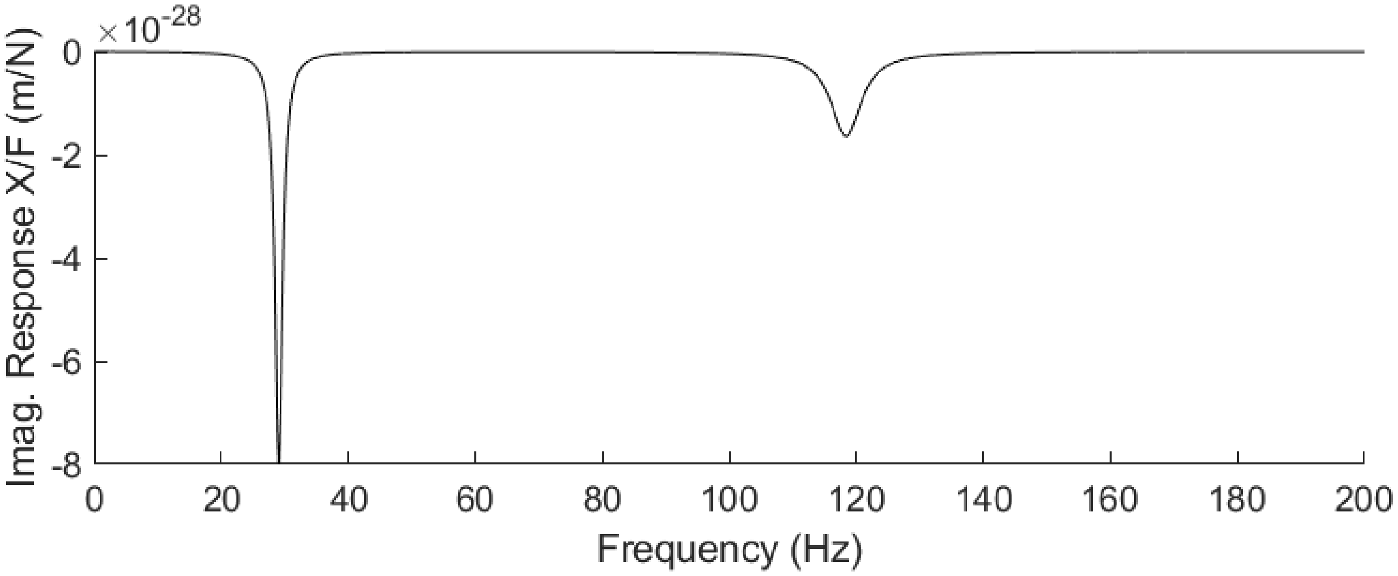

J.3 FRF Generator Program Evaluation - Configuration 3

K_C	1	2	3	4	5	6	7	8	9	10	11	12	13	14	15	16	17	18
1	1.09E+10	-3.66E-06	-4.30E-05	1.16E-07	-1.83E-06	8.40E-07	-1.53E+09	-1.53E-07	3.90E-05	4.89E-11	1.08E-06	5.76E-09	0.00E+00	0.00E+00	0.00E+00	0.00E+00	0.00E+00	0.00E+00
2	-1.67E-06	4.13E+08	2.92E-06	2.43E-08	6.56E-07	-1.74E+08	6.30E-08	-6.95E+06	0.00E+00	-1.27E-10	4.00E-11	4.46E+06	0.00E+00	0.00E+00	0.00E+00	0.00E+00	0.00E+00	0.00E+00
3	5.21E-07	2.18E-06	4.13E+08	-5.23E-08	1.74E+08	-3.99E-07	3.40E-08	-1.38E-10	-6.95E+06	1.83E-10	-4.46E+06	-3.64E-12	0.00E+00	0.00E+00	0.00E+00	0.00E+00	0.00E+00	0.00E+00
4	-7.01E-08	1.14E-07	-3.20E-08	1.62E+06	-2.22E+06	-1.72E+06	7.89E-14	-1.33E-10	1.83E-10	-7.58E+04	-2.20E+00	-1.22E-02	0.00E+00	0.00E+00	0.00E+00	0.00E+00	0.00E+00	0.00E+00
5	2.21E-07	1.16E-07	1.74E+08	-2.22E+06	8.37E+07	-1.18E+07	-1.45E-09	-2.18E-11	-4.46E+06	-2.20E+00	-4.73E+06	-5.03E+03	0.00E+00	0.00E+00	0.00E+00	0.00E+00	0.00E+00	0.00E+00
6	-2.08E-07	-1.74E+08	-1.90E-07	-1.72E+06	-1.18E+07	8.89E+07	-1.93E-10	4.46E+06	-3.64E-12	-1.22E-02	-5.03E+03	-3.82E+06	0.00E+00	0.00E+00	0.00E+00	0.00E+00	0.00E+00	0.00E+00
7	-1.53E+09	-1.53E-07	3.90E-05	4.89E-11	1.08E-06	5.76E-09	5.49E+09	-4.13E-07	-3.71E-05	-3.45E-09	-9.47E-07	2.52E-08	-3.96E+09	5.66E-07	-1.97E-06	3.40E-09	-1.31E-07	-3.10E-08
8	6.30E-08	-6.95E+06	0.00E+00	-1.27E-10	4.00E-11	4.46E+06	2.74E-08	3.43E+08	-2.98E-08	-3.68E-10	-9.71E-10	-3.44E+07	-9.03E-08	-3.36E+08	2.98E-08	4.95E-10	9.31E-10	3.00E+07
9	3.40E-08	-1.38E-10	-6.95E+06	1.83E-10	-4.46E+06	-3.64E-12	-5.89E-07	-1.49E-07	3.43E+08	-1.58E-09	3.44E+07	6.52E-09	5.55E-07	1.49E-07	-3.36E+08	1.40E-09	-3.00E+07	-6.52E-09
10	7.89E-14	-1.33E-10	1.83E-10	-7.58E+04	-2.20E+00	-1.22E-02	-1.66E-11	-1.72E-08	-2.65E-09	1.46E+05	1.32E+03	2.08E+02	1.65E-11	1.73E-08	2.47E-09	-7.07E+04	-1.31E+03	-2.08E+02
11	-1.45E-09	-2.18E-11	-4.46E+06	-2.20E+00	-4.73E+06	-5.03E+03	-1.53E-08	-1.67E-08	3.44E+07	1.32E+03	8.95E+06	1.08E+05	1.68E-08	1.68E-08	-3.00E+07	-1.31E+03	-4.22E+06	-1.03E+05
12	-1.93E-10	4.46E+06	-3.64E-12	-1.22E-02	-5.03E+03	-3.82E+06	-2.48E-09	-3.44E+07	9.32E-09	2.08E+02	1.08E+05	7.40E+06	2.68E-09	3.00E+07	-9.31E-09	-2.08E+02	-1.03E+05	-3.58E+06
13	0.00E+00	0.00E+00	0.00E+00	0.00E+00	0.00E+00	0.00E+00	-3.96E+09	5.66E-07	-1.97E-06	3.40E-09	-1.31E-07	-3.10E-08	4.58E+09	-8.94E-08	2.18E-06	-2.06E-08	1.67E-07	-9.21E-08
14	0.00E+00	0.00E+00	0.00E+00	0.00E+00	0.00E+00	0.00E+00	-9.03E-08	-3.36E+08	2.98E-08	4.95E-10	9.31E-10	3.00E+07	-1.10E-07	3.37E+08	-3.27E-08	-5.97E-10	-2.01E-09	-3.07E+07
15	0.00E+00	0.00E+00	0.00E+00	0.00E+00	0.00E+00	0.00E+00	5.55E-07	1.49E-07	-3.36E+08	1.40E-09	-3.00E+07	-6.52E-09	-6.40E-07	-1.92E-07	3.37E+08	-7.86E-10	3.07E+07	1.43E-08
16	0.00E+00	0.00E+00	0.00E+00	0.00E+00	0.00E+00	0.00E+00	1.65E-11	1.73E-08	2.47E-09	-7.07E+04	-1.31E+03	-2.08E+02	2.41E-09	-1.77E-08	-3.02E-09	8.17E+04	1.61E+03	-4.43E+02
17	0.00E+00	0.00E+00	0.00E+00	0.00E+00	0.00E+00	0.00E+00	1.68E-08	1.68E-08	-3.00E+07	-1.31E+03	-4.22E+06	-1.03E+05	-1.48E-08	-2.35E-08	3.07E+07	1.61E+03	4.78E+06	8.66E+04
18	0.00E+00	0.00E+00	0.00E+00	0.00E+00	0.00E+00	0.00E+00	2.68E-09	3.00E+07	-9.31E-09	-2.08E+02	-1.03E+05	-3.58E+06	1.43E-09	-3.07E+07	1.09E-08	-4.43E+02	8.66E+04	4.17E+06
19	0.00E+00	0.00E+00	0.00E+00	0.00E+00	0.00E+00	0.00E+00	0.00E+00	0.00E+00	0.00E+00	0.00E+00	0.00E+00	0.00E+00	-6.17E+08	-4.77E-07	-2.09E-07	1.73E-08	-3.67E-08	1.23E-07
20	0.00E+00	0.00E+00	0.00E+00	0.00E+00	0.00E+00	0.00E+00	0.00E+00	0.00E+00	0.00E+00	0.00E+00	0.00E+00	0.00E+00	2.01E-07	-1.27E+06	2.91E-09	1.02E-10	1.08E-09	7.27E+05
21	0.00E+00	0.00E+00	0.00E+00	0.00E+00	0.00E+00	0.00E+00	0.00E+00	0.00E+00	0.00E+00	0.00E+00	0.00E+00	0.00E+00	8.54E-08	4.25E-08	-1.27E+06	-6.11E-10	-7.27E+05	-7.77E-09
22	0.00E+00	0.00E+00	0.00E+00	0.00E+00	0.00E+00	0.00E+00	0.00E+00	0.00E+00	0.00E+00	0.00E+00	0.00E+00	0.00E+00	-2.42E-09	4.04E-10	5.50E-10	-1.10E+04	-2.92E+02	6.51E+02
23	0.00E+00	0.00E+00	0.00E+00	0.00E+00	0.00E+00	0.00E+00	0.00E+00	0.00E+00	0.00E+00	0.00E+00	0.00E+00	0.00E+00	-1.96E-09	6.69E-09	-7.27E+05	-2.92E+02	-5.63E+05	1.64E+04
24	0.00E+00	0.00E+00	0.00E+00	0.00E+00	0.00E+00	0.00E+00	0.00E+00	0.00E+00	0.00E+00	0.00E+00	0.00E+00	0.00E+00	-4.10E-09	7.27E+05	-1.63E-09	6.51E+02	1.64E+04	-5.92E+05
25	0.00E+00	0.00E+00	0.00E+00	0.00E+00	0.00E+00	0.00E+00	0.00E+00	0.00E+00	0.00E+00	0.00E+00	0.00E+00	0.00E+00	0.00E+00	0.00E+00	0.00E+00	0.00E+00	0.00E+00	0.00E+00
26	0.00E+00	0.00E+00	0.00E+00	0.00E+00	0.00E+00	0.00E+00	0.00E+00	0.00E+00	0.00E+00	0.00E+00	0.00E+00	0.00E+00	0.00E+00	0.00E+00	0.00E+00	0.00E+00	0.00E+00	0.00E+00
27	0.00E+00	0.00E+00	0.00E+00	0.00E+00	0.00E+00	0.00E+00	0.00E+00	0.00E+00	0.00E+00	0.00E+00	0.00E+00	0.00E+00	0.00E+00	0.00E+00	0.00E+00	0.00E+00	0.00E+00	0.00E+00
28	0.00E+00	0.00E+00	0.00E+00	0.00E+00	0.00E+00	0.00E+00	0.00E+00	0.00E+00	0.00E+00	0.00E+00	0.00E+00	0.00E+00	0.00E+00	0.00E+00	0.00E+00	0.00E+00	0.00E+00	0.00E+00
29	0.00E+00	0.00E+00	0.00E+00	0.00E+00	0.00E+00	0.00E+00	0.00E+00	0.00E+00	0.00E+00	0.00E+00	0.00E+00	0.00E+00	0.00E+00	0.00E+00	0.00E+00	0.00E+00	0.00E+00	0.00E+00
30	0.00E+00	0.00E+00	0.00E+00	0.00E+00	0.00E+00	0.00E+00	0.00E+00	0.00E+00	0.00E+00	0.00E+00	0.00E+00	0.00E+00	0.00E+00	0.00E+00	0.00E+00	0.00E+00	0.00E+00	0.00E+00
31	0.00E+00	0.00E+00	0.00E+00	0.00E+00	0.00E+00	0.00E+00	0.00E+00	0.00E+00	0.00E+00	0.00E+00	0.00E+00	0.00E+00	0.00E+00	0.00E+00	0.00E+00	0.00E+00	0.00E+00	0.00E+00
32	0.00E+00	0.00E+00	0.00E+00	0.00E+00	0.00E+00	0.00E+00	0.00E+00	0.00E+00	0.00E+00	0.00E+00	0.00E+00	0.00E+00	0.00E+00	0.00E+00	0.00E+00	0.00E+00	0.00E+00	0.00E+00
33	0.00E+00	0.00E+00	0.00E+00	0.00E+00	0.00E+00	0.00E+00	0.00E+00	0.00E+00	0.00E+00	0.00E+00	0.00E+00	0.00E+00	0.00E+00	0.00E+00	0.00E+00	0.00E+00	0.00E+00	0.00E+00
34	0.00E+00	0.00E+00	0.00E+00	0.00E+00	0.00E+00	0.00E+00	0.00E+00	0.00E+00	0.00E+00	0.00E+00	0.00E+00	0.00E+00	0.00E+00	0.00E+00	0.00E+00	0.00E+00	0.00E+00	0.00E+00
35	0.00E+00	0.00E+00	0.00E+00	0.00E+00	0.00E+00	0.00E+00	0.00E+00	0.00E+00	0.00E+00	0.00E+00	0.00E+00	0.00E+00	0.00E+00	0.00E+00	0.00E+00	0.00E+00	0.00E+00	0.00E+00
36	0.00E+00	0.00E+00	0.00E+00	0.00E+00	0.00E+00	0.00E+00	0.00E+00	0.00E+00	0.00E+00	0.00E+00	0.00E+00	0.00E+00	0.00E+00	0.00E+00	0.00E+00	0.00E+00	0.00E+00	0.00E+00

19	**20**	**21**	**22**	**23**	**24**	**25**	**26**	**27**	**28**	**29**	**30**	**31**	**32**	**33**	**34**	**35**	**36**
0.00E+00	0.00E+00	0.00E+00	0.00E+00	0.00E+00	0.00E+00	0.00E+00	0.00E+00	0.00E+00	0.00E+00	0.00E+00	0.00E+00	0.00E+00	0.00E+00	0.00E+00	0.00E+00	0.00E+00	0.00E+00
0.00E+00	0.00E+00	0.00E+00	0.00E+00	0.00E+00	0.00E+00	0.00E+00	0.00E+00	0.00E+00	0.00E+00	0.00E+00	0.00E+00	0.00E+00	0.00E+00	0.00E+00	0.00E+00	0.00E+00	0.00E+00
0.00E+00	0.00E+00	0.00E+00	0.00E+00	0.00E+00	0.00E+00	0.00E+00	0.00E+00	0.00E+00	0.00E+00	0.00E+00	0.00E+00	0.00E+00	0.00E+00	0.00E+00	0.00E+00	0.00E+00	0.00E+00
0.00E+00	0.00E+00	0.00E+00	0.00E+00	0.00E+00	0.00E+00	0.00E+00	0.00E+00	0.00E+00	0.00E+00	0.00E+00	0.00E+00	0.00E+00	0.00E+00	0.00E+00	0.00E+00	0.00E+00	0.00E+00
0.00E+00	0.00E+00	0.00E+00	0.00E+00	0.00E+00	0.00E+00	0.00E+00	0.00E+00	0.00E+00	0.00E+00	0.00E+00	0.00E+00	0.00E+00	0.00E+00	0.00E+00	0.00E+00	0.00E+00	0.00E+00
0.00E+00	0.00E+00	0.00E+00	0.00E+00	0.00E+00	0.00E+00	0.00E+00	0.00E+00	0.00E+00	0.00E+00	0.00E+00	0.00E+00	0.00E+00	0.00E+00	0.00E+00	0.00E+00	0.00E+00	0.00E+00
0.00E+00	0.00E+00	0.00E+00	0.00E+00	0.00E+00	0.00E+00	0.00E+00	0.00E+00	0.00E+00	0.00E+00	0.00E+00	0.00E+00	0.00E+00	0.00E+00	0.00E+00	0.00E+00	0.00E+00	0.00E+00
0.00E+00	0.00E+00	0.00E+00	0.00E+00	0.00E+00	0.00E+00	0.00E+00	0.00E+00	0.00E+00	0.00E+00	0.00E+00	0.00E+00	0.00E+00	0.00E+00	0.00E+00	0.00E+00	0.00E+00	0.00E+00
0.00E+00	0.00E+00	0.00E+00	0.00E+00	0.00E+00	0.00E+00	0.00E+00	0.00E+00	0.00E+00	0.00E+00	0.00E+00	0.00E+00	0.00E+00	0.00E+00	0.00E+00	0.00E+00	0.00E+00	0.00E+00
0.00E+00	0.00E+00	0.00E+00	0.00E+00	0.00E+00	0.00E+00	0.00E+00	0.00E+00	0.00E+00	0.00E+00	0.00E+00	0.00E+00	0.00E+00	0.00E+00	0.00E+00	0.00E+00	0.00E+00	0.00E+00
0.00E+00	0.00E+00	0.00E+00	0.00E+00	0.00E+00	0.00E+00	0.00E+00	0.00E+00	0.00E+00	0.00E+00	0.00E+00	0.00E+00	0.00E+00	0.00E+00	0.00E+00	0.00E+00	0.00E+00	0.00E+00
0.00E+00	0.00E+00	0.00E+00	0.00E+00	0.00E+00	0.00E+00	0.00E+00	0.00E+00	0.00E+00	0.00E+00	0.00E+00	0.00E+00	0.00E+00	0.00E+00	0.00E+00	0.00E+00	0.00E+00	0.00E+00
-6.17E+08	-4.77E-07	-2.09E-07	1.73E-08	-3.67E-08	1.23E-07	0.00E+00	0.00E+00	0.00E+00	0.00E+00	0.00E+00	0.00E+00	0.00E+00	0.00E+00	0.00E+00	0.00E+00	0.00E+00	0.00E+00
2.01E-07	-1.27E+06	2.91E-09	1.02E-10	1.08E-09	7.27E+05	0.00E+00	0.00E+00	0.00E+00	0.00E+00	0.00E+00	0.00E+00	0.00E+00	0.00E+00	0.00E+00	0.00E+00	0.00E+00	0.00E+00
8.54E-08	4.25E-08	-1.27E+06	-6.11E-10	-7.27E+05	-7.77E-09	0.00E+00	0.00E+00	0.00E+00	0.00E+00	0.00E+00	0.00E+00	0.00E+00	0.00E+00	0.00E+00	0.00E+00	0.00E+00	0.00E+00
-2.42E-09	4.04E-10	5.50E-10	-1.10E+04	-2.92E+02	6.51E+02	0.00E+00	0.00E+00	0.00E+00	0.00E+00	0.00E+00	0.00E+00	0.00E+00	0.00E+00	0.00E+00	0.00E+00	0.00E+00	0.00E+00
-1.96E-09	6.69E-09	-7.27E+05	-2.92E+02	-5.63E+05	1.64E+04	0.00E+00	0.00E+00	0.00E+00	0.00E+00	0.00E+00	0.00E+00	0.00E+00	0.00E+00	0.00E+00	0.00E+00	0.00E+00	0.00E+00
-4.10E-09	7.27E+05	-1.63E-09	6.51E+02	1.64E+04	-5.92E+05	0.00E+00	0.00E+00	0.00E+00	0.00E+00	0.00E+00	0.00E+00	0.00E+00	0.00E+00	0.00E+00	0.00E+00	0.00E+00	0.00E+00
3.15E+11	-1.20E+00	9.70E-01	-1.37E-06	2.47E-04	3.04E-04	-3.14E+11	1.20E+00	-9.70E-01	1.35E-06	-2.47E-04	-3.04E-04	0.00E+00	0.00E+00	0.00E+00	0.00E+00	0.00E+00	0.00E+00
-1.25E-01	3.77E+14	-2.02E+01	6.10E-05	-4.84E-03	-1.88E+11	1.25E-01	-3.77E+14	2.02E+01	-6.10E-05	4.84E-03	1.88E+11	0.00E+00	0.00E+00	0.00E+00	0.00E+00	0.00E+00	0.00E+00
-3.13E-02	2.34E+01	3.77E+14	1.22E-04	1.88E+11	-5.87E-03	3.13E-02	-2.34E+01	-3.77E+14	-1.22E-04	-1.88E+11	5.87E-03	0.00E+00	0.00E+00	0.00E+00	0.00E+00	0.00E+00	0.00E+00
-1.60E-07	-6.85E-04	-2.76E-04	2.49E+06	5.83E+05	1.17E+05	1.62E-07	6.85E-04	2.76E-04	-2.48E+06	-5.82E+05	-1.17E+05	0.00E+00	0.00E+00	0.00E+00	0.00E+00	0.00E+00	0.00E+00
-1.53E-05	3.46E-03	1.88E+11	5.83E+05	9.59E+07	-6.13E+06	1.53E-05	-3.46E-03	-1.88E+11	-5.82E+05	-9.54E+07	6.11E+06	0.00E+00	0.00E+00	0.00E+00	0.00E+00	0.00E+00	0.00E+00
3.05E-05	-1.88E+11	3.91E-03	1.17E+05	-6.13E+06	1.25E+08	-3.05E-05	1.88E+11	-3.91E-03	-1.17E+05	6.11E+06	-1.24E+08	0.00E+00	0.00E+00	0.00E+00	0.00E+00	0.00E+00	0.00E+00
-3.14E+11	1.20E+00	-9.70E-01	1.35E-06	-2.47E-04	-3.04E-04	3.14E+11	-1.20E+00	9.70E-01	-1.35E-06	-6.76E+04	3.04E-04	-1.21E+08	0.00E+00	2.29E-09	3.57E-10	6.76E+04	2.42E-25
1.25E-01	-3.77E+14	2.02E+01	-6.10E-05	4.84E-03	1.88E+11	-1.25E-01	3.77E+14	-2.02E+01	6.76E+04	-4.84E-03	-1.88E+11	0.00E+00	-1.17E+08	0.00E+00	-6.76E+04	3.27E-11	2.32E-12
3.13E-02	-2.34E+01	-3.77E+14	-1.22E-04	-1.88E+11	5.87E-03	-3.13E-02	2.34E+01	3.77E+14	1.22E-04	1.88E+11	-5.87E-03	2.29E-09	0.00E+00	-8.36E+07	-5.78E-11	1.23E-08	4.31E-09
1.62E-07	6.85E-04	2.76E-04	-2.48E+06	-5.82E+05	-1.17E+05	-1.62E-07	6.76E+04	-2.76E-04	2.50E+06	5.82E+05	1.17E+05	2.15E-10	-6.76E+04	7.60E-10	-1.88E+04	-9.71E+00	1.18E+00
1.53E-05	-3.46E-03	-1.88E+11	-5.82E+05	-9.54E+07	6.11E+06	-6.76E+04	3.46E-03	1.88E+11	5.82E+05	9.54E+07	-6.11E+06	6.76E+04	-3.55E-10	-3.84E-10	-9.71E+00	-1.88E+04	1.29E+00
-3.05E-05	1.88E+11	-3.91E-03	-1.17E+05	6.11E+06	-1.24E+08	3.05E-05	-1.88E+11	3.91E-03	1.17E+05	-6.11E+06	1.24E+08	-2.29E-11	1.09E-10	-8.01E-10	1.18E+00	1.29E+00	-3.73E+02
0.00E+00	0.00E+00	0.00E+00	0.00E+00	0.00E+00	0.00E+00	-1.21E+08	0.00E+00	2.29E-09	3.57E-10	6.76E+04	2.42E-25	1.21E+08	0.00E+00	-2.29E-09	-3.57E-10	-6.76E+04	-2.42E-25
0.00E+00	0.00E+00	0.00E+00	0.00E+00	0.00E+00	0.00E+00	0.00E+00	-1.17E+08	0.00E+00	-6.76E+04	3.27E-11	2.32E-12	0.00E+00	1.17E+08	0.00E+00	6.76E+04	-3.27E-11	-2.32E-12
0.00E+00	0.00E+00	0.00E+00	0.00E+00	0.00E+00	0.00E+00	2.29E-09	0.00E+00	-8.36E+07	-5.78E-11	1.23E-08	4.31E-09	-2.29E-09	0.00E+00	8.36E+07	5.78E-11	-1.23E-08	-4.31E-09
0.00E+00	0.00E+00	0.00E+00	0.00E+00	0.00E+00	0.00E+00	2.15E-10	-6.76E+04	7.60E-10	-1.88E+04	-9.71E+00	1.18E+00	-2.15E-10	6.76E+04	-7.60E-10	1.88E+04	9.71E+00	-1.18E+00
0.00E+00	0.00E+00	0.00E+00	0.00E+00	0.00E+00	0.00E+00	6.76E+04	-3.55E-10	-3.84E-10	-9.71E+00	-1.88E+04	1.29E+00	-6.76E+04	3.55E-10	3.84E-10	9.71E+00	1.88E+04	-1.29E+00
0.00E+00	0.00E+00	0.00E+00	0.00E+00	0.00E+00	0.00E+00	-2.29E-11	1.09E-10	-8.01E-10	1.18E+00	1.29E+00	-3.73E+02	2.29E-11	-1.09E-10	8.01E-10	-1.18E+00	-1.29E+00	3.73E+02

M_C (convert to diagonal)	
1	478.1478155
2	478.1478155
3	478.1478155
4	35.43979561
5	13.80447821
6	37.76596901
7	154.2855258
8	154.2855258
9	154.2855258
10	63.49119523
11	25.1634378
12	31.26095388
13	213.9519076
14	213.9519076
15	213.9519076
16	3.68405801
17	6.832403275
18	9.43384661
19	186.6735005
20	186.6735005
21	186.6735005
22	42.99257813
23	8.588944073
24	0.319345948
25	26.32104143
26	26.32104143
27	26.32104143
28	0.268714041
29	0.173642443
30	0.026122098
31	60
32	60
33	60
34	2.7375
35	2.7375
36	1.875

Natural Frequencies	
1	4042633.04133691 + 0.00000000000000i
2	4043047.44974124 + 0.00000000000000i
3	116717.799612054 + 0.00000000000000i
4	35455.7407413171 + 0.00000000000000i
5	7224.95993759381 + 0.00000000000000i
6	4778.31961153604 + 0.00000000000000i
7	3179.31576593781 + 0.00000000000000i
8	2577.22365175554 + 0.00000000000000i
9	2627.32736927672 + 0.00000000000000i
10	0.00000000000000 - 1150.00608753666i
11	2084.02177701643 + 0.00000000000000i
12	2048.27898071688 + 0.00000000000000i
13	1647.94209543978 + 0.00000000000000i
14	991.316110569332 + 0.00000000000000i
15	1750.61847279348 + 0.00000000000000i
16	1583.68513192035 + 0.00000000000000i
17	1328.89685038245 + 0.00000000000000i
18	1337.04706614546 + 0.00000000000000i
19	579.715553787838 + 0.00000000000000i
20	457.443982503887 + 0.00000000000000i
21	417.706689199242 + 0.00000000000000i
22	383.649020500590 + 0.00000000000000i
23	281.191326164380 + 0.00000000000000i
24	261.929205244626 + 0.00000000000000i
25	210.383174484552 + 0.00000000000000i
26	0.00000000000000 - 172.710226490670i
27	152.432541947752 + 0.00000000000000i
28	90.1412073615448 + 0.00000000000000i
29	83.6030986384768 + 0.00000000000000i
30	85.6093824937235 + 0.00000000000000i
31	72.5221789000212 + 0.00000000000000i
32	30.9612370031807 + 0.00000000000000i
33	32.9522462718415 + 0.00000000000000i
34	36.1573630281572 + 0.00000000000000i
35	14.0834174128278 + 0.00000000000000i
36	13.3851067806199 + 0.00000000000000i

Mode shapes	1	2	3	4	5	6	7	8	9	10	11	12	13	14	15	16	17	18
1	-1.79E-17	-4.01E-17	1.33E-11	1.13E-14	1.09E-01	-1.00E+00	1.99E-06	-1.87E-01	-8.88E-09	1.03E-06	2.24E-07	-6.26E-07	-3.71E-02	2.75E-02	1.65E-07	-8.64E-07	-5.67E-07	-2.53E-06
2	1.05E-28	-2.11E-26	-6.63E-24	-1.59E-14	-1.44E-14	-8.41E-13	-5.11E-09	-1.95E-09	4.40E-03	-8.35E-08	-2.05E-03	-1.24E-02	-1.78E-06	2.48E-07	-1.65E-01	-2.76E-04	1.11E-04	1.51E-05
3	-2.35E-26	1.79E-29	3.07E-25	-4.97E-16	-8.81E-16	-5.33E-14	2.36E-08	-1.35E-07	6.03E-02	3.70E-07	-6.41E-03	2.47E-03	1.83E-07	-2.92E-07	2.76E-02	4.48E-05	-1.75E-05	-2.95E-05
4	3.96E-31	-8.15E-30	-2.31E-28	-4.77E-18	-9.21E-17	-1.12E-14	-2.89E-09	2.00E-08	-8.60E-03	-3.22E-07	1.05E-03	-1.30E-03	-1.98E-07	1.11E-07	-1.95E-02	-3.56E-05	1.62E-05	8.68E-06
5	-6.32E-25	1.81E-27	8.64E-24	-1.25E-14	-2.32E-14	-1.41E-12	4.44E-07	-2.19E-06	1.00E+00	-5.88E-06	-8.70E-02	2.31E-02	3.72E-07	-1.21E-06	1.67E-01	1.97E-04	-3.61E-05	-2.04E-04
6	-1.24E-27	1.86E-25	5.85E-23	1.40E-13	1.25E-13	7.06E-12	2.76E-08	1.06E-07	-7.30E-02	-1.49E-06	1.91E-02	8.17E-02	1.04E-05	-5.89E-07	1.00E+00	1.55E-03	-5.29E-04	-4.90E-05
7	-5.69E-17	1.54E-17	-5.65E-08	4.27E-13	-1.00E+00	-2.02E-02	7.95E-06	-9.51E-01	-4.44E-08	7.81E-06	1.30E-06	-3.66E-06	-2.34E-01	1.88E-01	1.02E-06	-5.51E-06	-3.75E-06	-1.67E-05
8	1.90E-21	1.78E-17	4.66E-18	1.02E-09	3.57E-11	8.18E-10	1.91E-06	-1.41E-06	-7.12E-04	1.68E-05	7.95E-03	5.96E-01	-2.62E-05	1.09E-05	-2.03E-02	-5.91E-03	5.00E-03	2.27E-04
9	1.79E-17	7.19E-20	-1.74E-19	3.33E-11	1.87E-12	3.49E-11	-2.67E-06	-9.74E-07	-1.11E-02	-5.40E-05	-4.56E-01	1.06E-02	-1.01E-05	-2.63E-05	3.55E-03	-7.97E-05	1.08E-04	-2.47E-03
10	1.17E-21	-1.27E-22	-8.03E-24	2.80E-15	2.31E-17	-4.92E-15	-3.36E-10	-5.85E-11	1.34E-06	-1.21E-08	-6.50E-06	-4.45E-07	5.13E-10	6.01E-09	7.63E-06	2.31E-08	-3.53E-08	1.58E-07
11	1.33E-17	-1.44E-19	-1.75E-19	1.45E-11	1.04E-12	1.82E-11	-1.93E-06	-6.04E-07	-3.39E-02	-5.83E-05	-2.91E-01	4.48E-03	-5.92E-06	-2.42E-06	-9.13E-03	-8.82E-05	1.15E-04	-1.18E-03
12	1.86E-19	-9.28E-18	-2.49E-18	-5.42E-10	-1.89E-11	-4.30E-10	-1.01E-06	7.15E-07	1.55E-03	-1.25E-05	-5.53E-03	-2.99E-01	1.20E-05	-2.84E-06	-3.37E-02	2.71E-03	-2.17E-03	-6.83E-05
13	4.73E-17	2.87E-17	2.99E-05	-1.99E-11	6.05E-01	3.76E-01	7.12E-06	-1.00E+00	-4.62E-08	1.08E-05	1.50E-06	-4.24E-06	-2.86E-01	2.43E-01	1.23E-06	-6.77E-06	-4.72E-06	-2.10E-05
14	1.34E-16	-5.98E-11	-1.10E-14	-2.22E-07	-3.23E-10	-3.22E-09	-3.37E-06	1.60E-06	2.64E-04	5.48E-06	-5.56E-03	-4.26E-01	1.23E-05	-1.90E-06	2.34E-02	2.41E-03	-1.51E-03	-7.31E-05
15	-5.15E-11	-1.37E-16	6.99E-16	-1.68E-09	-8.75E-12	-6.96E-11	4.14E-06	1.02E-06	4.56E-03	-9.39E-06	3.25E-01	-7.70E-03	5.05E-06	7.68E-06	-4.04E-03	5.17E-05	-6.98E-05	7.34E-04
16	-7.44E-15	-4.46E-13	-5.82E-16	-1.16E-08	-1.04E-11	6.13E-12	1.79E-06	1.65E-07	2.68E-06	3.16E-06	1.25E-04	-6.74E-05	-6.55E-07	-4.18E-07	7.88E-06	-5.87E-05	1.04E-04	5.69E-07
17	-9.26E-10	-6.04E-12	4.31E-15	-1.96E-07	-3.81E-10	-2.91E-09	5.95E-05	1.04E-05	1.45E-02	-9.46E-04	1.00E+00	-2.01E-02	-3.78E-05	-2.57E-04	-1.19E-02	-6.04E-04	1.18E-03	-1.51E-02
18	1.61E-13	8.23E-10	2.03E-13	4.09E-06	5.55E-09	5.01E-08	3.87E-05	-1.34E-05	-5.00E-04	-2.59E-04	1.48E-02	9.21E-01	8.30E-05	-9.40E-05	-5.12E-02	2.12E-02	-3.11E-02	-1.40E-03
19	-8.72E-16	-4.76E-16	-1.41E-01	8.50E-09	-3.60E-02	-5.64E-02	-2.31E-05	9.89E-01	5.30E-08	3.52E-05	4.99E-07	-1.76E-06	-3.46E-01	5.13E-01	1.26E-06	-8.94E-06	-8.05E-06	-3.56E-05
20	-3.61E-07	1.41E-01	-3.61E-11	-6.64E-05	-2.93E-09	-5.31E-09	4.20E-05	2.82E-06	-7.69E-07	-2.37E-05	2.01E-05	2.88E-03	-1.09E-05	-2.68E-06	-4.29E-04	2.83E-01	-5.08E-04	-2.46E-05
21	1.41E-01	3.61E-07	-1.77E-09	-1.91E-06	1.61E-08	5.64E-08	1.14E-05	-1.77E-06	-1.21E-05	1.64E-04	-1.44E-03	3.25E-05	-1.13E-05	2.62E-05	2.82E-05	3.91E-06	-6.03E-05	2.83E-01
22	6.41E-11	-9.10E-11	2.83E-11	-2.03E-06	-9.09E-08	-1.10E-06	-6.21E-03	-2.78E-04	6.39E-07	1.42E-03	3.72E-05	6.15E-05	2.41E-04	1.18E-04	-6.14E-06	1.08E-03	-3.08E-05	-1.58E-04
23	1.53E-03	2.76E-08	2.85E-10	6.16E-04	8.52E-08	1.98E-07	-6.58E-03	-6.04E-04	-1.94E-04	-2.09E-02	-2.16E-02	9.51E-04	1.67E-03	2.72E-03	3.12E-04	7.68E-04	-8.78E-04	1.58E-02
24	1.49E-08	-4.12E-02	-4.42E-08	-8.19E-02	-4.56E-06	-1.77E-05	-5.81E-03	1.15E-03	4.05E-04	-7.38E-03	3.98E-03	-1.00E+00	-5.02E-03	1.51E-03	1.02E-01	-7.90E-01	1.00E+00	4.40E-02
25	1.19E-11	3.62E-15	1.00E+00	2.17E-09	-3.61E-02	-5.65E-02	-2.31E-05	9.89E-01	5.29E-08	3.53E-05	4.95E-07	-1.75E-06	-3.46E-01	5.13E-01	1.26E-06	-8.93E-06	-8.05E-06	-3.56E-05
26	2.56E-06	-1.00E+00	2.56E-10	4.75E-04	2.62E-08	1.03E-07	7.41E-05	-2.78E-06	-7.56E-07	7.99E-05	2.15E-05	2.88E-03	9.42E-07	5.02E-06	-4.30E-04	2.83E-01	-5.09E-04	-3.36E-05
27	-1.00E+00	-2.56E-06	1.25E-08	1.36E-05	-1.22E-07	-4.69E-07	-1.55E-04	2.53E-05	-1.21E-05	-3.47E-04	-1.45E-03	2.27E-05	-6.95E-05	-1.16E-05	2.93E-05	7.32E-06	-5.25E-05	2.83E-01
28	-1.03E-08	-8.17E-10	-4.53E-09	3.25E-04	1.46E-05	1.76E-04	1.00E+00	4.50E-02	-1.06E-04	-2.16E-01	-6.30E-03	-8.54E-03	-3.95E-02	-2.04E-02	7.86E-04	-4.37E-02	4.36E-03	2.62E-02
29	-7.58E-02	-1.37E-06	-2.86E-05	-3.04E-02	2.76E-04	1.05E-03	3.27E-01	-5.47E-02	-7.97E-05	1.00E+00	-7.64E-03	2.06E-02	1.18E-01	7.83E-02	-1.80E-03	-6.04E-03	-1.64E-02	-7.22E-02
30	-1.82E-07	5.04E-01	5.40E-07	1.00E+00	5.38E-05	1.98E-04	5.83E-02	-1.00E-02	4.31E-04	2.00E-01	6.86E-03	-1.00E+00	1.87E-02	1.69E-02	1.02E-01	-7.95E-01	9.98E-01	2.61E-02
31	-5.22E-12	-8.39E-17	-1.48E-04	-2.73E-08	1.45E-03	5.47E-03	5.13E-05	-4.32E-01	-4.03E-08	-3.14E-04	-4.14E-06	1.23E-05	1.00E+00	1.00E+00	-4.38E-06	2.28E-05	9.16E-06	4.24E-05
32	-3.06E-13	1.20E-07	-3.64E-14	-7.39E-07	-1.35E-09	-1.91E-08	-1.56E-04	-9.67E-06	3.23E-07	-2.61E-05	-1.46E-05	-2.51E-03	5.62E-05	-1.37E-05	7.55E-04	-1.00E+00	-5.26E-03	-2.16E-04
33	8.53E-08	2.18E-13	-1.28E-12	-1.51E-08	3.35E-09	3.05E-08	2.49E-05	-6.72E-06	3.07E-06	-1.78E-04	6.86E-04	-1.13E-05	7.32E-05	-3.94E-05	-2.44E-05	-9.15E-06	1.97E-04	-1.00E+00
34	1.26E-14	1.51E-09	9.76E-15	-1.07E-08	-1.95E-09	-5.34E-08	-6.81E-04	-4.66E-05	1.10E-07	-1.11E-03	9.80E-06	-1.78E-05	1.01E-04	1.43E-04	7.82E-06	-1.26E-02	-8.35E-05	-1.04E-04
35	3.19E-11	1.52E-14	1.81E-06	1.67E-07	-1.78E-05	-6.73E-05	-2.23E-04	5.35E-03	7.99E-08	5.17E-03	1.21E-05	-3.41E-05	-1.26E-02	-1.29E-02	4.12E-06	1.62E-05	6.41E-05	2.78E-04
36	-3.20E-15	-6.13E-12	-9.44E-15	-1.58E-07	-2.01E-10	-1.69E-09	-1.06E-06	2.99E-07	-1.24E-08	2.97E-05	-3.17E-07	4.74E-05	-1.35E-06	-3.38E-06	-6.60E-06	6.31E-05	-1.13E-04	-2.93E-06

19	20	21	22	23	24	25	26	27	28	29	30	31	32	33	34	35	36
-4.45E-07	5.18E-07	-5.77E-07	1.20E-07	-6.93E-08	-5.01E-08	2.00E-07	-1.70E-08	5.91E-11	3.47E-08	-2.56E-08	1.01E-08	-1.24E-09	-4.77E-10	-3.76E-10	-1.85E-11	1.85E-13	-9.17E-14
2.28E-03	1.28E-01	2.19E-01	-8.56E-02	-3.22E-02	-6.94E-02	3.97E-03	-2.33E-01	-2.94E-04	-1.25E-02	-8.13E-04	5.29E-04	-4.13E-03	4.03E-03	2.17E-03	5.92E-03	6.29E-06	7.55E-04
1.52E-02	1.73E-01	1.00E-01	-1.04E-01	4.81E-02	6.75E-02	7.64E-04	3.05E-01	3.70E-04	8.81E-03	4.33E-04	-3.25E-04	2.42E-02	-4.53E-03	3.11E-03	-7.78E-03	-1.82E-05	-9.75E-04
2.86E-03	4.30E-02	-4.36E-02	-4.03E-02	2.87E-01	7.58E-01	8.02E-02	-1.00E+00	1.14E-03	-7.90E-02	-4.99E-03	3.15E-03	-1.07E-01	3.29E-02	-1.00E-02	-6.32E-03	8.18E-05	-8.93E-04
-1.62E-02	-2.88E-01	-2.19E-01	2.15E-01	-1.05E-01	-1.50E-01	-5.33E-03	-7.60E-01	-8.72E-04	-2.47E-02	-1.58E-03	1.05E-03	-5.75E-02	1.20E-02	-6.58E-03	1.87E-02	4.38E-05	2.34E-03
3.77E-03	2.27E-01	3.98E-01	-1.93E-01	-6.17E-02	-1.63E-01	9.40E-03	-5.78E-01	-6.91E-04	-3.01E-02	-1.95E-03	1.27E-03	-1.61E-02	1.03E-02	3.34E-03	1.43E-02	1.58E-05	1.81E-03
-3.14E-06	3.67E-06	-4.10E-06	8.54E-07	-4.95E-07	-3.58E-07	1.43E-06	-1.22E-07	4.23E-10	2.48E-07	-1.83E-07	7.24E-08	-8.85E-09	-3.41E-09	-2.71E-09	-1.33E-10	5.38E-13	-5.09E-13
4.34E-03	-3.80E-03	-1.07E-02	-3.08E-02	-8.65E-02	9.90E-02	-7.83E-03	-8.75E-03	2.14E-04	1.63E-02	3.22E-04	-3.24E-04	7.36E-01	-6.35E-02	1.91E-01	-2.17E-03	-3.19E-04	7.67E-04
-7.73E-02	7.74E-02	-9.20E-02	2.15E-02	-8.76E-03	-8.38E-03	-2.28E-02	3.89E-02	-7.34E-05	-2.48E-01	-2.78E-02	1.48E-02	3.87E-02	7.24E-02	6.10E-02	-6.66E-03	-1.61E-05	-1.05E-03
8.06E-05	-2.81E-04	2.91E-04	3.22E-04	-4.54E-03	-1.37E-02	-2.14E-03	-3.76E-02	5.31E-02	1.29E-02	8.71E-05	-2.87E-03	2.67E-02	1.02E-01	-9.21E-02	-1.00E+00	1.02E-04	-1.28E-01
3.51E-01	7.60E-01	-9.46E-01	3.87E-01	-4.50E-02	-8.83E-02	-1.05E-01	-4.17E-01	-5.09E-04	2.35E-01	2.13E-02	-1.20E-02	-7.55E-02	-6.30E-02	-6.34E-02	1.77E-02	4.23E-05	2.41E-03
2.48E-02	-1.59E-01	-7.36E-01	-1.00E+00	1.76E-01	-2.88E-01	5.29E-03	-2.43E-01	-1.16E-04	3.55E-03	-6.79E-04	3.05E-04	9.00E-01	-6.91E-02	2.27E-01	4.88E-03	-4.63E-04	1.83E-03
-4.14E-06	4.86E-06	-5.43E-06	1.13E-06	-6.57E-07	-4.75E-07	1.90E-06	-1.62E-07	5.63E-10	3.31E-07	-2.44E-07	9.64E-08	-1.18E-08	-4.54E-09	-3.62E-09	-1.77E-10	5.30E-13	-3.84E-13
-3.96E-03	2.03E-02	1.03E-01	1.52E-01	-2.09E-02	4.58E-02	-2.29E-03	-3.92E-03	2.30E-04	1.63E-02	4.52E-04	-3.75E-04	7.46E-01	-6.46E-02	1.95E-01	-2.33E-03	-3.57E-04	7.68E-04
5.81E-02	6.05E-02	-9.35E-02	4.60E-02	-1.15E-02	-1.96E-02	5.13E-04	3.11E-02	-1.65E-04	-2.53E-01	-2.71E-02	1.46E-02	3.96E-02	7.45E-02	6.28E-02	-6.62E-03	-1.86E-05	-1.06E-03
-1.85E-03	1.13E-03	-6.68E-04	1.48E-04	2.41E-03	5.28E-03	-5.04E-04	-1.43E-02	-1.00E+00	1.68E-02	5.16E-03	9.50E-03	4.35E-02	8.87E-02	-9.01E-02	-8.91E-01	1.06E-04	-2.44E-01
-1.00E+00	1.00E+00	-1.00E+00	1.51E-01	-1.45E-02	3.17E-02	-3.81E-01	-3.34E-01	4.73E-04	2.73E-01	1.11E-02	-8.52E-03	-8.51E-02	-8.02E-02	-7.85E-02	1.73E-02	7.01E-05	2.52E-03
-5.81E-02	7.98E-02	4.15E-01	8.90E-01	9.24E-01	-9.08E-01	6.77E-02	-1.90E-01	5.15E-05	2.29E-03	7.21E-04	-2.31E-04	1.00E+00	-7.82E-02	2.60E-01	3.58E-03	-8.89E-04	1.84E-03
-1.01E-05	1.21E-05	-1.37E-05	2.86E-06	-1.68E-06	-1.22E-06	4.91E-06	-4.25E-07	1.46E-09	8.58E-07	-6.34E-07	2.50E-07	-3.06E-08	-1.18E-08	-9.41E-09	-4.59E-10	1.64E-12	2.38E-12
-2.05E-04	3.61E-04	-2.07E-03	-2.41E-03	-1.37E-03	4.81E-04	9.47E-04	4.42E-04	-1.51E-04	7.39E-04	5.77E-04	-4.70E-04	-2.65E-01	-3.51E-01	8.07E-01	-3.71E-02	-1.86E-03	-8.16E-04
8.42E-03	-2.01E-02	2.81E-02	-7.33E-03	8.06E-03	6.62E-03	-3.76E-02	-6.93E-03	-5.97E-05	5.41E-02	-1.23E-02	3.65E-03	-3.83E-02	6.64E-01	4.18E-01	1.89E-02	1.70E-04	-2.05E-03
-9.39E-06	-1.69E-05	4.90E-05	1.62E-06	-2.61E-06	1.24E-05	-1.49E-05	-2.14E-04	1.14E-02	9.07E-03	2.59E-02	6.52E-02	9.20E-04	-2.86E-02	9.96E-03	1.97E-01	-2.18E-05	-9.74E-01
2.23E-01	-4.96E-01	6.89E-01	-1.72E-01	1.94E-01	1.58E-01	-9.44E-01	-1.90E-01	-2.32E-04	-9.78E-02	-4.71E-02	2.07E-02	-2.48E-02	-8.71E-01	-5.29E-01	-1.79E-02	-2.47E-04	4.13E-03
-2.46E-02	1.59E-02	3.70E-01	7.56E-01	9.99E-01	-1.00E+00	5.75E-02	-1.77E-01	6.87E-04	-2.72E-02	-7.16E-04	5.27E-04	-2.42E-01	-4.52E-01	9.98E-01	-3.90E-02	-3.37E-03	-8.72E-04
-1.01E-05	1.22E-05	-1.37E-05	2.86E-06	-1.69E-06	-1.22E-06	4.91E-06	-4.25E-07	1.46E-09	8.59E-07	-6.35E-07	2.51E-07	-3.07E-08	-1.18E-08	-9.42E-09	-4.60E-10	1.64E-12	2.38E-12
-2.08E-04	3.64E-04	-2.07E-03	-2.41E-03	-1.37E-03	4.82E-04	9.42E-04	4.41E-04	-1.51E-04	7.30E-04	5.83E-04	-4.74E-04	-2.65E-01	-3.51E-01	8.07E-01	-3.71E-02	-1.86E-03	-8.16E-04
8.43E-03	-2.01E-02	2.82E-02	-7.33E-03	8.06E-03	6.61E-03	-3.76E-02	-6.93E-03	-5.96E-05	5.42E-02	-1.23E-02	3.67E-03	-3.83E-02	6.64E-01	4.18E-01	1.89E-02	1.70E-04	-2.05E-03
6.98E-03	-7.17E-03	6.73E-03	-3.89E-04	-9.65E-04	-1.64E-03	1.35E-02	3.71E-03	1.14E-02	2.88E-02	6.89E-03	6.83E-02	-2.03E-04	-3.12E-02	8.08E-03	1.97E-01	-9.12E-05	-9.74E-01
1.95E-01	-4.67E-01	6.62E-01	-1.70E-01	1.98E-01	1.65E-01	-1.00E+00	-2.06E-01	-4.88E-04	-1.84E-01	1.83E-02	-2.49E-02	-2.00E-02	-8.60E-01	-5.21E-01	-1.68E-02	4.03E-05	3.62E-03
-3.02E-02	2.18E-02	3.64E-01	7.57E-01	1.00E+00	-9.99E-01	4.62E-02	-1.80E-01	6.35E-04	-4.48E-02	1.26E-02	-8.71E-03	-2.41E-01	-4.50E-01	1.00E+00	-3.88E-02	-3.32E-03	-9.74E-04
-1.46E-04	3.15E-04	-4.36E-04	1.11E-04	-1.27E-04	-1.07E-04	6.81E-04	9.19E-05	3.91E-07	6.65E-04	-5.71E-04	2.15E-04	-3.67E-05	-7.80E-05	-5.48E-05	-2.22E-06	-3.88E-08	6.08E-08
-2.46E-04	4.03E-04	-2.27E-03	-2.60E-03	-1.43E-03	4.98E-04	9.73E-04	4.36E-04	-1.43E-04	8.38E-04	8.19E-04	1.42E-04	-2.66E-01	-3.51E-01	8.07E-01	-3.72E-02	-1.86E-03	-8.01E-04
1.11E-02	-2.36E-02	3.22E-02	-8.20E-03	8.54E-03	6.95E-03	-3.89E-02	-6.78E-03	-6.06E-05	5.45E-02	-1.24E-02	3.69E-03	-3.84E-02	6.65E-01	4.19E-01	1.89E-02	1.70E-04	-2.05E-03
-1.51E-04	2.57E-04	-3.19E-04	-8.62E-06	6.72E-05	1.72E-04	-2.35E-03	6.84E-04	-4.76E-03	-1.53E-01	-3.97E-01	-1.00E+00	1.04E-02	-3.54E-02	7.64E-03	2.43E-01	-1.50E-04	-1.00E+00
-4.07E-03	1.58E-02	-2.71E-02	8.32E-03	-1.88E-02	-1.83E-02	1.83E-01	-3.86E-02	2.01E-04	1.00E+00	-1.00E+00	3.58E-01	-8.56E-02	-1.00E+00	-6.19E-01	-2.07E-02	-2.92E-05	3.73E-03
1.83E-05	-2.24E-05	-4.13E-04	-1.03E-03	-2.52E-03	2.91E-03	-2.27E-04	-1.19E-03	-5.07E-06	1.04E-03	-2.28E-04	3.00E-04	9.48E-03	1.18E-01	-2.24E-01	6.92E-03	-1.00E+00	-1.06E-02

FRF Output - X Direction

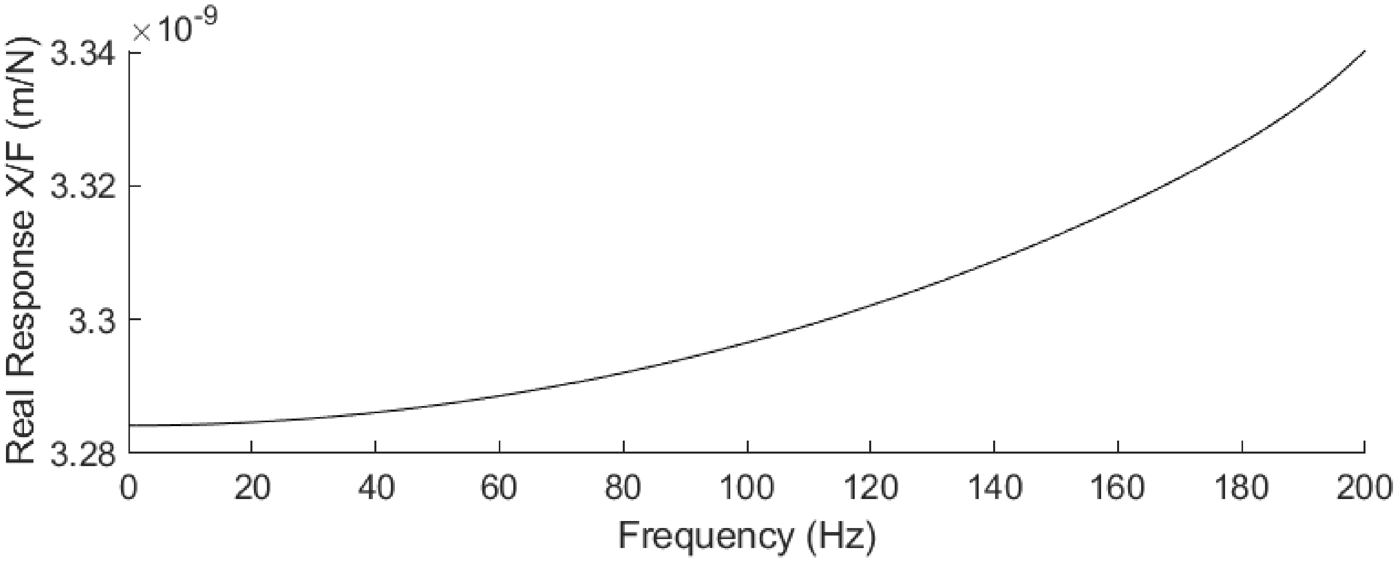

Modes: [none]

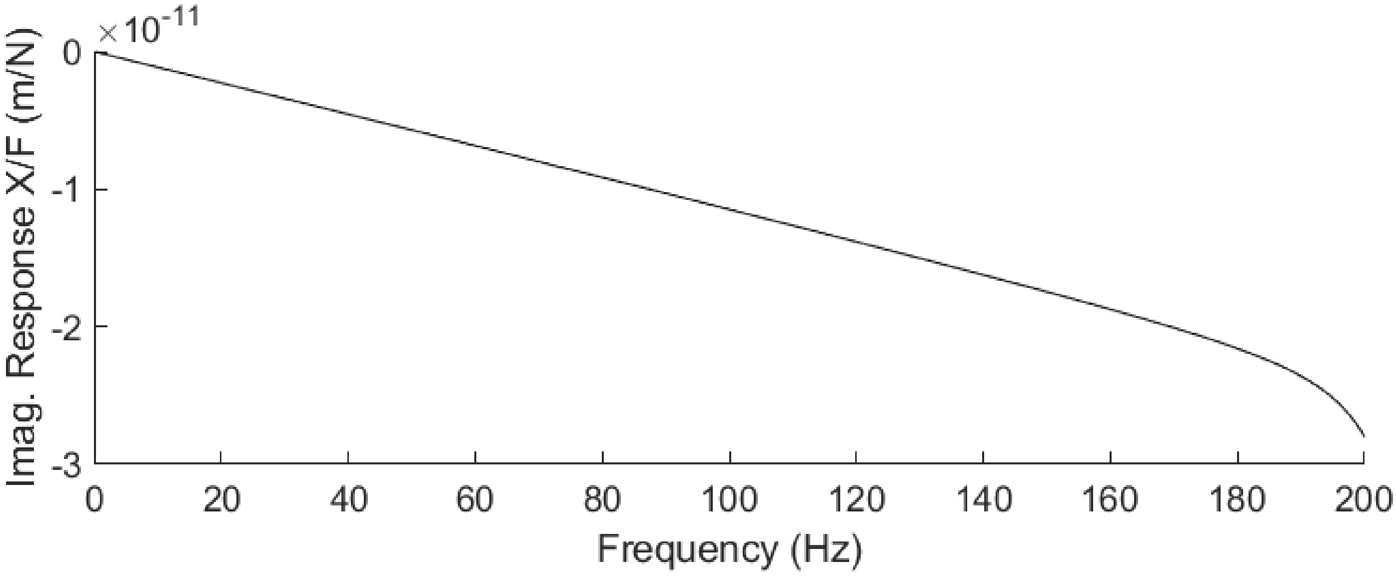

FRF Output - Y Direction

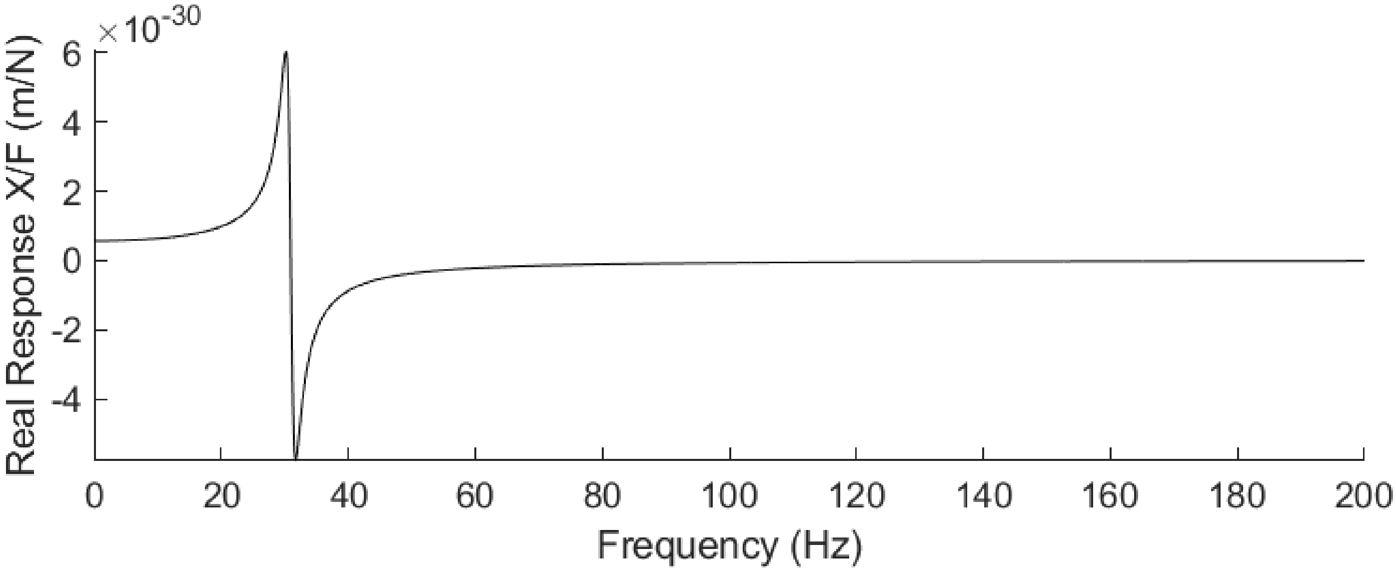

Modes: [30.2Hz, 6.03693e-30m]

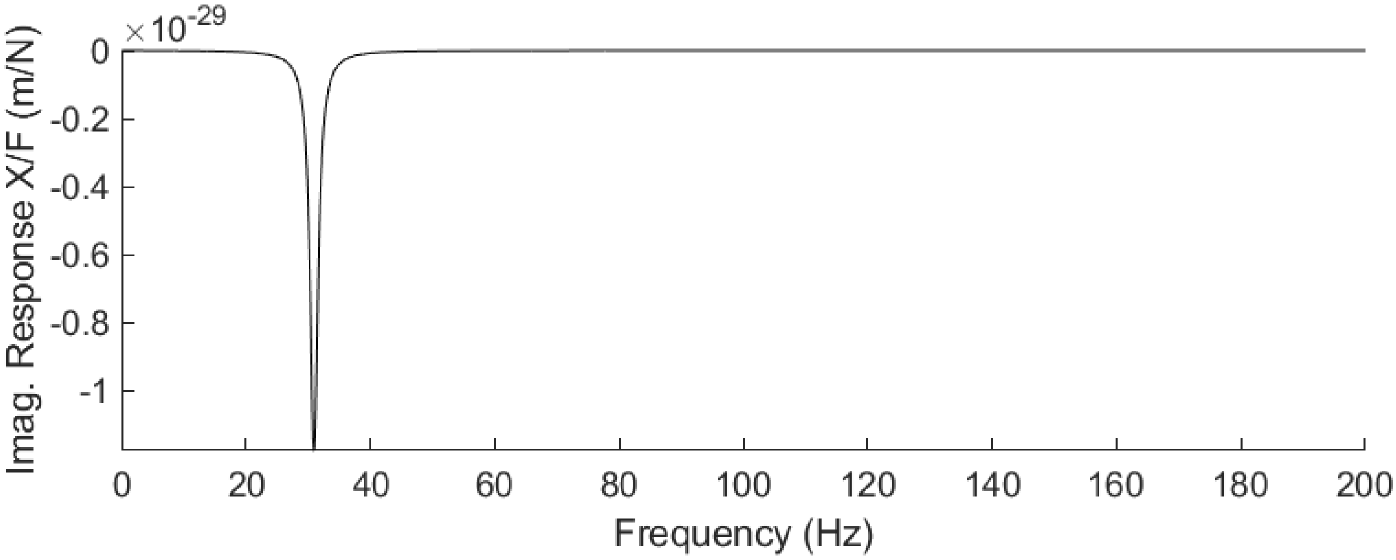

J.4 FRF Generator Program Evaluation – Configuration 4

K_C	1	2	3	4	5	6	7	8	9	10	11	12	13	14	15	16	17	18
1	1.09E+10	-5.03E-06	-3.69E-06	-1.10E-07	-1.28E-06	5.43E-07	-1.53E+09	2.57E-07	1.37E-06	-4.30E-09	2.90E-07	-3.52E-08	0.00E+00	0.00E+00	0.00E+00	0.00E+00	0.00E+00	0.00E+00
2	-2.58E-06	4.13E+08	-3.09E-06	2.07E-08	-4.58E-07	-1.74E+08	1.21E-08	-6.95E+06	-6.87E-09	-2.43E-10	-2.33E-10	4.46E+06	0.00E+00	0.00E+00	0.00E+00	0.00E+00	0.00E+00	0.00E+00
3	9.91E-07	3.26E-06	4.13E+08	-1.53E-08	1.74E+08	-5.39E-07	-6.11E-07	-3.49E-09	-6.95E+06	3.64E-10	-4.46E+06	-8.15E-10	0.00E+00	0.00E+00	0.00E+00	0.00E+00	0.00E+00	0.00E+00
4	5.78E-08	-1.72E-08	-4.22E-08	1.46E+06	-2.22E+06	-2.57E+06	7.25E-10	-2.45E-10	-1.32E-11	-7.58E+04	-1.23E+03	1.30E+02	0.00E+00	0.00E+00	0.00E+00	0.00E+00	0.00E+00	0.00E+00
5	-1.36E-07	6.24E-07	1.74E+08	-2.22E+06	8.87E+07	-1.19E+07	-2.21E-08	-1.57E-09	-4.46E+06	-1.23E+03	-4.72E+06	9.54E+04	0.00E+00	0.00E+00	0.00E+00	0.00E+00	0.00E+00	0.00E+00
6	3.35E-07	-1.74E+08	5.02E-07	-2.57E+06	-1.19E+07	8.43E+07	6.40E-10	4.46E+06	1.40E-09	1.30E+02	9.54E+04	-3.83E+06	0.00E+00	0.00E+00	0.00E+00	0.00E+00	0.00E+00	0.00E+00
7	-1.53E+09	2.57E-07	1.37E-06	-4.30E-09	2.90E-07	-3.52E-08	5.49E+09	-8.53E-07	1.94E-06	-3.93E-09	-1.76E-07	5.38E-08	-3.96E+09	5.96E-07	-3.31E-06	8.23E-09	-1.14E-07	-1.87E-08
8	1.21E-08	-6.95E+06	-6.87E-09	-2.43E-10	-2.33E-10	4.46E+06	6.62E-08	3.43E+08	3.64E-07	-2.62E-08	1.61E-08	-3.44E+07	-7.82E-08	-3.36E+08	-3.58E-07	2.64E-08	-1.58E-08	3.00E+07
9	-6.11E-07	-3.49E-09	-6.95E+06	3.64E-10	-4.46E+06	-8.15E-10	2.09E-06	1.28E-06	3.43E+08	-9.68E-09	3.44E+07	-4.67E-08	-1.48E-06	-1.28E-06	-3.36E+08	9.31E-09	-3.00E+07	4.75E-08
10	7.25E-10	-2.45E-10	-1.32E-11	-7.58E+04	-1.23E+03	1.30E+02	-2.21E-09	8.56E-09	8.19E-09	1.47E+05	6.14E+03	1.06E+03	1.49E-09	-8.31E-09	-8.18E-09	-7.07E+04	-4.91E+03	-1.19E+03
11	-2.21E-08	-1.57E-09	-4.46E+06	-1.23E+03	-4.72E+06	9.54E+04	2.88E-08	2.95E-08	3.44E+07	6.14E+03	8.91E+06	5.43E+04	-6.75E-09	-2.79E-08	-3.00E+07	-4.91E+03	-4.19E+06	-1.50E+05
12	6.40E-10	4.46E+06	1.40E-09	1.30E+02	9.54E+04	-3.83E+06	-1.09E-08	-3.44E+07	5.12E-09	1.06E+03	5.43E+04	7.43E+06	1.02E-08	3.00E+07	-6.52E-09	-1.19E+03	-1.50E+05	-3.60E+06
13	0.00E+00	0.00E+00	0.00E+00	0.00E+00	0.00E+00	0.00E+00	-3.96E+09	5.96E-07	-3.31E-06	8.23E-09	-1.14E-07	-1.87E-08	4.58E+09	-7.45E-07	3.34E-06	-7.32E-09	1.30E-07	4.81E-08
14	0.00E+00	0.00E+00	0.00E+00	0.00E+00	0.00E+00	0.00E+00	-7.82E-08	-3.36E+08	-3.58E-07	2.64E-08	-1.58E-08	3.00E+07	6.61E-08	3.37E+08	3.52E-07	-2.64E-08	1.56E-08	-3.07E+07
15	0.00E+00	0.00E+00	0.00E+00	0.00E+00	0.00E+00	0.00E+00	-1.48E-06	-1.28E-06	-3.36E+08	9.31E-09	-3.00E+07	4.75E-08	1.51E-06	1.27E-06	3.37E+08	-9.28E-09	3.07E+07	-4.71E-08
16	0.00E+00	0.00E+00	0.00E+00	0.00E+00	0.00E+00	0.00E+00	1.49E-09	-8.31E-09	-8.18E-09	-7.07E+04	-4.91E+03	-1.19E+03	-3.00E-09	8.19E-09	7.96E-09	8.17E+04	5.02E+03	8.33E+02
17	0.00E+00	0.00E+00	0.00E+00	0.00E+00	0.00E+00	0.00E+00	-6.75E-09	-2.79E-08	-3.00E+07	-4.91E+03	-4.19E+06	-1.50E+05	1.31E-08	2.83E-08	3.07E+07	5.02E+03	4.75E+06	1.37E+05
18	0.00E+00	0.00E+00	0.00E+00	0.00E+00	0.00E+00	0.00E+00	1.02E-08	3.00E+07	-6.52E-09	-1.19E+03	-1.50E+05	-3.60E+06	-8.64E-09	-3.07E+07	6.90E-09	8.33E+02	1.37E+05	4.20E+06
19	0.00E+00	0.00E+00	0.00E+00	0.00E+00	0.00E+00	0.00E+00	0.00E+00	0.00E+00	0.00E+00	0.00E+00	0.00E+00	0.00E+00	-6.17E+08	1.49E-07	-2.98E-08	-9.11E-10	-1.66E-08	-2.95E-08
20	0.00E+00	0.00E+00	0.00E+00	0.00E+00	0.00E+00	0.00E+00	0.00E+00	0.00E+00	0.00E+00	0.00E+00	0.00E+00	0.00E+00	1.22E-08	-1.27E+06	6.05E-09	1.46E-11	2.04E-10	7.27E+05
21	0.00E+00	0.00E+00	0.00E+00	0.00E+00	0.00E+00	0.00E+00	0.00E+00	0.00E+00	0.00E+00	0.00E+00	0.00E+00	0.00E+00	-3.59E-08	1.26E-08	-1.27E+06	-2.91E-11	-7.27E+05	-3.49E-10
22	0.00E+00	0.00E+00	0.00E+00	0.00E+00	0.00E+00	0.00E+00	0.00E+00	0.00E+00	0.00E+00	0.00E+00	0.00E+00	0.00E+00	1.51E-09	1.27E-10	2.16E-10	-1.10E+04	-1.12E+02	3.52E+02
23	0.00E+00	0.00E+00	0.00E+00	0.00E+00	0.00E+00	0.00E+00	0.00E+00	0.00E+00	0.00E+00	0.00E+00	0.00E+00	0.00E+00	-6.34E-09	-3.49E-10	-7.27E+05	-1.12E+02	-5.60E+05	1.32E+04
24	0.00E+00	0.00E+00	0.00E+00	0.00E+00	0.00E+00	0.00E+00	0.00E+00	0.00E+00	0.00E+00	0.00E+00	0.00E+00	0.00E+00	-1.60E-09	7.27E+05	-3.78E-10	3.52E+02	1.32E+04	-5.97E+05
25	0.00E+00	0.00E+00	0.00E+00	0.00E+00	0.00E+00	0.00E+00	0.00E+00	0.00E+00	0.00E+00	0.00E+00	0.00E+00	0.00E+00	0.00E+00	0.00E+00	0.00E+00	0.00E+00	0.00E+00	0.00E+00
26	0.00E+00	0.00E+00	0.00E+00	0.00E+00	0.00E+00	0.00E+00	0.00E+00	0.00E+00	0.00E+00	0.00E+00	0.00E+00	0.00E+00	0.00E+00	0.00E+00	0.00E+00	0.00E+00	0.00E+00	0.00E+00
27	0.00E+00	0.00E+00	0.00E+00	0.00E+00	0.00E+00	0.00E+00	0.00E+00	0.00E+00	0.00E+00	0.00E+00	0.00E+00	0.00E+00	0.00E+00	0.00E+00	0.00E+00	0.00E+00	0.00E+00	0.00E+00
28	0.00E+00	0.00E+00	0.00E+00	0.00E+00	0.00E+00	0.00E+00	0.00E+00	0.00E+00	0.00E+00	0.00E+00	0.00E+00	0.00E+00	0.00E+00	0.00E+00	0.00E+00	0.00E+00	0.00E+00	0.00E+00
29	0.00E+00	0.00E+00	0.00E+00	0.00E+00	0.00E+00	0.00E+00	0.00E+00	0.00E+00	0.00E+00	0.00E+00	0.00E+00	0.00E+00	0.00E+00	0.00E+00	0.00E+00	0.00E+00	0.00E+00	0.00E+00
30	0.00E+00	0.00E+00	0.00E+00	0.00E+00	0.00E+00	0.00E+00	0.00E+00	0.00E+00	0.00E+00	0.00E+00	0.00E+00	0.00E+00	0.00E+00	0.00E+00	0.00E+00	0.00E+00	0.00E+00	0.00E+00
31	0.00E+00	0.00E+00	0.00E+00	0.00E+00	0.00E+00	0.00E+00	0.00E+00	0.00E+00	0.00E+00	0.00E+00	0.00E+00	0.00E+00	0.00E+00	0.00E+00	0.00E+00	0.00E+00	0.00E+00	0.00E+00
32	0.00E+00	0.00E+00	0.00E+00	0.00E+00	0.00E+00	0.00E+00	0.00E+00	0.00E+00	0.00E+00	0.00E+00	0.00E+00	0.00E+00	0.00E+00	0.00E+00	0.00E+00	0.00E+00	0.00E+00	0.00E+00
33	0.00E+00	0.00E+00	0.00E+00	0.00E+00	0.00E+00	0.00E+00	0.00E+00	0.00E+00	0.00E+00	0.00E+00	0.00E+00	0.00E+00	0.00E+00	0.00E+00	0.00E+00	0.00E+00	0.00E+00	0.00E+00
34	0.00E+00	0.00E+00	0.00E+00	0.00E+00	0.00E+00	0.00E+00	0.00E+00	0.00E+00	0.00E+00	0.00E+00	0.00E+00	0.00E+00	0.00E+00	0.00E+00	0.00E+00	0.00E+00	0.00E+00	0.00E+00
35	0.00E+00	0.00E+00	0.00E+00	0.00E+00	0.00E+00	0.00E+00	0.00E+00	0.00E+00	0.00E+00	0.00E+00	0.00E+00	0.00E+00	0.00E+00	0.00E+00	0.00E+00	0.00E+00	0.00E+00	0.00E+00
36	0.00E+00	0.00E+00	0.00E+00	0.00E+00	0.00E+00	0.00E+00	0.00E+00	0.00E+00	0.00E+00	0.00E+00	0.00E+00	0.00E+00	0.00E+00	0.00E+00	0.00E+00	0.00E+00	0.00E+00	0.00E+00

19	20	21	22	23	24	25	26	27	28	29	30	31	32	33	34	35	36
0.00E+00	0.00E+00	0.00E+00	0.00E+00	0.00E+00	0.00E+00	0.00E+00	0.00E+00	0.00E+00	0.00E+00	0.00E+00	0.00E+00	0.00E+00	0.00E+00	0.00E+00	0.00E+00	0.00E+00	0.00E+00
0.00E+00	0.00E+00	0.00E+00	0.00E+00	0.00E+00	0.00E+00	0.00E+00	0.00E+00	0.00E+00	0.00E+00	0.00E+00	0.00E+00	0.00E+00	0.00E+00	0.00E+00	0.00E+00	0.00E+00	0.00E+00
0.00E+00	0.00E+00	0.00E+00	0.00E+00	0.00E+00	0.00E+00	0.00E+00	0.00E+00	0.00E+00	0.00E+00	0.00E+00	0.00E+00	0.00E+00	0.00E+00	0.00E+00	0.00E+00	0.00E+00	0.00E+00
0.00E+00	0.00E+00	0.00E+00	0.00E+00	0.00E+00	0.00E+00	0.00E+00	0.00E+00	0.00E+00	0.00E+00	0.00E+00	0.00E+00	0.00E+00	0.00E+00	0.00E+00	0.00E+00	0.00E+00	0.00E+00
0.00E+00	0.00E+00	0.00E+00	0.00E+00	0.00E+00	0.00E+00	0.00E+00	0.00E+00	0.00E+00	0.00E+00	0.00E+00	0.00E+00	0.00E+00	0.00E+00	0.00E+00	0.00E+00	0.00E+00	0.00E+00
0.00E+00	0.00E+00	0.00E+00	0.00E+00	0.00E+00	0.00E+00	0.00E+00	0.00E+00	0.00E+00	0.00E+00	0.00E+00	0.00E+00	0.00E+00	0.00E+00	0.00E+00	0.00E+00	0.00E+00	0.00E+00
0.00E+00	0.00E+00	0.00E+00	0.00E+00	0.00E+00	0.00E+00	0.00E+00	0.00E+00	0.00E+00	0.00E+00	0.00E+00	0.00E+00	0.00E+00	0.00E+00	0.00E+00	0.00E+00	0.00E+00	0.00E+00
0.00E+00	0.00E+00	0.00E+00	0.00E+00	0.00E+00	0.00E+00	0.00E+00	0.00E+00	0.00E+00	0.00E+00	0.00E+00	0.00E+00	0.00E+00	0.00E+00	0.00E+00	0.00E+00	0.00E+00	0.00E+00
0.00E+00	0.00E+00	0.00E+00	0.00E+00	0.00E+00	0.00E+00	0.00E+00	0.00E+00	0.00E+00	0.00E+00	0.00E+00	0.00E+00	0.00E+00	0.00E+00	0.00E+00	0.00E+00	0.00E+00	0.00E+00
0.00E+00	0.00E+00	0.00E+00	0.00E+00	0.00E+00	0.00E+00	0.00E+00	0.00E+00	0.00E+00	0.00E+00	0.00E+00	0.00E+00	0.00E+00	0.00E+00	0.00E+00	0.00E+00	0.00E+00	0.00E+00
0.00E+00	0.00E+00	0.00E+00	0.00E+00	0.00E+00	0.00E+00	0.00E+00	0.00E+00	0.00E+00	0.00E+00	0.00E+00	0.00E+00	0.00E+00	0.00E+00	0.00E+00	0.00E+00	0.00E+00	0.00E+00
0.00E+00	0.00E+00	0.00E+00	0.00E+00	0.00E+00	0.00E+00	0.00E+00	0.00E+00	0.00E+00	0.00E+00	0.00E+00	0.00E+00	0.00E+00	0.00E+00	0.00E+00	0.00E+00	0.00E+00	0.00E+00
-6.17E+08	1.49E-07	-2.98E-08	-9.11E-10	-1.66E-08	-2.95E-08	0.00E+00	0.00E+00	0.00E+00	0.00E+00	0.00E+00	0.00E+00	0.00E+00	0.00E+00	0.00E+00	0.00E+00	0.00E+00	0.00E+00
1.22E-08	-1.27E+06	6.05E-09	1.46E-11	2.04E-10	7.27E+05	0.00E+00	0.00E+00	0.00E+00	0.00E+00	0.00E+00	0.00E+00	0.00E+00	0.00E+00	0.00E+00	0.00E+00	0.00E+00	0.00E+00
-3.59E-08	1.26E-08	-1.27E+06	-2.91E-11	-7.27E+05	-3.49E-10	0.00E+00	0.00E+00	0.00E+00	0.00E+00	0.00E+00	0.00E+00	0.00E+00	0.00E+00	0.00E+00	0.00E+00	0.00E+00	0.00E+00
1.51E-09	1.27E-10	2.16E-10	-1.10E+04	-1.12E+02	3.52E+02	0.00E+00	0.00E+00	0.00E+00	0.00E+00	0.00E+00	0.00E+00	0.00E+00	0.00E+00	0.00E+00	0.00E+00	0.00E+00	0.00E+00
-6.34E-09	-3.49E-10	-7.27E+05	-1.12E+02	-5.60E+05	1.32E+04	0.00E+00	0.00E+00	0.00E+00	0.00E+00	0.00E+00	0.00E+00	0.00E+00	0.00E+00	0.00E+00	0.00E+00	0.00E+00	0.00E+00
-1.60E-09	7.27E+05	-3.78E-10	3.52E+02	1.32E+04	-5.97E+05	0.00E+00	0.00E+00	0.00E+00	0.00E+00	0.00E+00	0.00E+00	0.00E+00	0.00E+00	0.00E+00	0.00E+00	0.00E+00	0.00E+00
3.15E+11	-1.77E+01	-6.56E+00	5.45E-06	-1.63E-03	4.40E-03	-3.14E+11	1.77E+01	6.56E+00	-5.45E-06	1.63E-03	-4.40E-03	0.00E+00	0.00E+00	0.00E+00	0.00E+00	0.00E+00	0.00E+00
-2.81E-01	3.77E+14	5.04E+01	-1.98E-04	1.25E-02	-1.88E+11	2.81E-01	-3.77E+14	-5.04E+01	1.98E-04	-1.25E-02	1.88E+11	0.00E+00	0.00E+00	0.00E+00	0.00E+00	0.00E+00	0.00E+00
-2.66E-01	8.80E+01	3.77E+14	-1.14E-04	1.88E+11	-2.23E-02	2.66E-01	-8.80E+01	-3.77E+14	1.14E-04	-1.88E+11	2.23E-02	0.00E+00	0.00E+00	0.00E+00	0.00E+00	0.00E+00	0.00E+00
-3.86E-06	7.83E-04	7.73E-04	2.21E+06	1.91E+06	2.17E+06	3.85E-06	-7.83E-04	-7.73E-04	-2.19E+06	-1.91E+06	-2.17E+06	0.00E+00	0.00E+00	0.00E+00	0.00E+00	0.00E+00	0.00E+00
-2.29E-05	1.61E-02	1.88E+11	1.91E+06	1.14E+08	-1.40E+07	2.29E-05	-1.61E-02	-1.88E+11	-1.91E+06	-1.13E+08	1.40E+07	0.00E+00	0.00E+00	0.00E+00	0.00E+00	0.00E+00	0.00E+00
2.29E-05	-1.88E+11	-9.91E-03	2.17E+06	-1.40E+07	1.10E+08	-2.29E-05	1.88E+11	9.91E-03	-2.17E+06	1.40E+07	-1.10E+08	0.00E+00	0.00E+00	0.00E+00	0.00E+00	0.00E+00	0.00E+00
-3.14E+11	1.77E+01	6.56E+00	-5.45E-06	1.63E-03	-4.40E-03	3.14E+11	-1.77E+01	-6.56E+00	5.45E-06	-6.47E+04	4.40E-03	-1.11E+08	0.00E+00	6.57E-09	-4.00E-11	6.47E+04	2.55E-11
2.81E-01	-3.77E+14	-5.04E+01	1.98E-04	-1.25E-02	1.88E+11	-2.81E-01	3.77E+14	5.04E+01	6.47E+04	1.25E-02	-1.88E+11	0.00E+00	-1.47E+08	0.00E+00	-6.47E+04	1.60E-10	-5.06E-11
2.66E-01	-8.80E+01	-3.77E+14	1.14E-04	-1.88E+11	2.23E-02	-2.66E-01	8.80E+01	3.77E+14	-1.14E-04	1.88E+11	-2.23E-02	6.57E-09	0.00E+00	-3.53E+06	-8.85E-09	4.86E-10	3.20E-09
3.85E-06	-7.83E-04	-7.73E-04	-2.19E+06	-1.91E+06	-2.17E+06	-3.85E-06	6.47E+04	7.73E-04	2.21E+06	1.91E+06	2.17E+06	-4.26E-10	-6.47E+04	3.27E-10	-1.84E+04	-2.53E+00	-1.60E+00
2.29E-05	-1.61E-02	-1.88E+11	-1.91E+06	-1.13E+08	1.40E+07	-6.47E+04	1.61E-02	1.88E+11	1.91E+06	1.13E+08	-1.40E+07	6.47E+04	2.91E-11	1.26E-09	-2.53E+00	-1.84E+04	-2.68E-01
-2.29E-05	1.88E+11	9.91E-03	-2.17E+06	1.40E+07	-1.10E+08	2.29E-05	-1.88E+11	-9.91E-03	2.17E+06	-1.40E+07	1.10E+08	1.94E-10	8.21E-11	-3.68E-10	-1.60E+00	-2.68E-01	-3.65E+02
0.00E+00	0.00E+00	0.00E+00	0.00E+00	0.00E+00	0.00E+00	-1.11E+08	0.00E+00	6.57E-09	-4.00E-11	6.47E+04	2.55E-11	1.11E+08	0.00E+00	-6.57E-09	4.00E-11	-6.47E+04	-2.55E-11
0.00E+00	0.00E+00	0.00E+00	0.00E+00	0.00E+00	0.00E+00	0.00E+00	-1.47E+08	0.00E+00	-6.47E+04	1.60E-10	-5.06E-11	0.00E+00	1.47E+08	0.00E+00	6.47E+04	-1.60E-10	5.06E-11
0.00E+00	0.00E+00	0.00E+00	0.00E+00	0.00E+00	0.00E+00	6.57E-09	0.00E+00	-3.53E+06	-8.85E-09	4.86E-10	3.20E-09	-6.57E-09	0.00E+00	3.53E+06	8.85E-09	-4.86E-10	-3.20E-09
0.00E+00	0.00E+00	0.00E+00	0.00E+00	0.00E+00	0.00E+00	-4.26E-10	-6.47E+04	3.27E-10	-1.84E+04	-2.53E+00	-1.60E+00	4.26E-10	6.47E+04	-3.27E-10	1.84E+04	2.53E+00	1.60E+00
0.00E+00	0.00E+00	0.00E+00	0.00E+00	0.00E+00	0.00E+00	6.47E+04	2.91E-11	1.26E-09	-2.53E+00	-1.84E+04	-2.68E-01	-6.47E+04	-2.91E-11	-1.26E-09	2.53E+00	1.84E+04	2.68E-01
0.00E+00	0.00E+00	0.00E+00	0.00E+00	0.00E+00	0.00E+00	1.94E-10	8.21E-11	-3.68E-10	-1.60E+00	-2.68E-01	-3.65E+02	-1.94E-10	-8.21E-11	3.68E-10	1.60E+00	2.68E-01	3.65E+02

M_C (convert to diagonal)	
1	478.1478155
2	478.1478155
3	478.1478155
4	37.02574151
5	8.696964853
6	37.76596901
7	154.2855258
8	154.2855258
9	154.2855258
10	46.53450509
11	38.12340971
12	44.97469488
13	213.9519076
14	213.9519076
15	213.9519076
16	1.65570336
17	7.629083828
18	9.397191395
19	186.6735005
20	186.6735005
21	186.6735005
22	35.3669832
23	19.39194778
24	17.18611581
25	26.32104143
26	26.32104143
27	26.32104143
28	0.034193328
29	0.318311204
30	0.023454029
31	60
32	60
33	60
34	2.7375
35	2.7375
36	1.875

Natural Frequencies	
1	4042601.44534215 + 0.00000000000000i
2	4043062.49288864 + 0.00000000000000i
3	116716.335239325 + 0.00000000000000i
4	26663.4063402176 + 0.00000000000000i
5	7224.95575782495 + 0.00000000000000i
6	8918.89154198438 + 0.00000000000000i
7	4778.31161073871 + 0.00000000000000i
8	2570.69645247171 + 0.00000000000000i
9	3313.03607822799 + 0.00000000000000i
10	0.00000000000000 - 1729.22957238622i
11	1596.98846433335 + 0.00000000000000i
12	981.104721312888 + 0.00000000000000i
13	1771.73364889085 + 0.00000000000000i
14	2060.86761847349 + 0.00000000000000i
15	2038.36468583451 + 0.00000000000000i
16	1727.62300192963 + 0.00000000000000i
17	528.818587281458 + 0.00000000000000i
18	452.890827456238 + 0.00000000000000i
19	410.655142977179 + 0.00000000000000i
20	358.490946055471 + 0.00000000000000i
21	321.153847366859 + 0.00000000000000i
22	0.00000000000000 - 190.094677324342i
23	276.648535335087 + 0.00000000000000i
24	268.428065429263 + 0.00000000000000i
25	225.314472369318 + 0.00000000000000i
26	148.962734431002 + 0.00000000000000i
27	140.802406026320 + 0.00000000000000i
28	80.3239781896575 + 0.00000000000000i
29	87.2961506463536 + 0.00000000000000i
30	86.5570537134033 + 0.00000000000000i
31	71.2163069699312 + 0.00000000000000i
32	42.5594530730057 + 0.00000000000000i
33	29.7205574403019 + 0.00000000000000i
34	31.7755328226926 + 0.00000000000000i
35	13.9317853176720 + 0.00000000000000i
36	14.7322295037590 + 0.00000000000000i

Mode shapes	**1**	**2**	**3**	**4**	**5**	**6**	**7**	**8**	**9**	**10**	**11**	**12**	**13**	**14**	**15**	**16**	**17**	**18**
1	9.69E-18	4.92E-18	1.33E-11	-2.73E-14	1.09E-01	1.70E-09	1.00E+00	-1.86E-01	-2.19E-11	3.67E-07	-3.76E-02	2.55E-02	1.37E-06	1.64E-07	1.62E-08	-1.73E-10	1.85E-07	1.92E-07
2	1.17E-28	-1.64E-26	-2.15E-25	-1.29E-15	-1.81E-15	4.00E-14	3.25E-12	-2.36E-10	1.33E-03	-1.70E-09	2.85E-08	2.77E-08	3.93E-04	-1.38E-03	1.23E-02	-1.72E-01	-4.47E-03	3.26E-01
3	-1.94E-26	-5.05E-29	-5.14E-26	-1.32E-15	-4.66E-14	5.49E-12	8.81E-11	-4.08E-09	3.60E-02	7.70E-09	-4.48E-08	-1.05E-07	-4.98E-05	-2.77E-03	-1.58E-03	2.20E-02	-1.56E-02	5.27E-01
4	-1.69E-29	-4.88E-31	1.05E-28	2.22E-18	5.84E-15	-3.86E-13	-1.28E-11	7.92E-10	-5.26E-03	-1.15E-08	1.63E-08	3.93E-08	5.83E-05	5.41E-04	1.56E-03	-2.62E-02	-3.45E-03	9.46E-02
5	-7.89E-25	-4.34E-27	-2.33E-24	-5.35E-14	-1.39E-12	1.90E-10	2.45E-09	-9.35E-08	1.00E+00	-5.16E-07	-5.54E-07	-6.23E-07	-3.11E-04	-5.18E-02	-1.52E-02	1.28E-01	2.25E-02	-9.39E-01
6	1.80E-29	1.42E-25	1.86E-24	1.12E-14	4.42E-14	-2.42E-12	-9.01E-11	5.53E-09	-3.68E-02	-5.18E-08	-1.09E-07	1.62E-08	-2.33E-03	1.21E-02	-7.93E-02	1.00E+00	-7.43E-03	5.86E-01
7	1.30E-17	-1.58E-17	-5.65E-08	4.86E-12	-1.00E+00	-3.01E-08	2.02E-02	-9.50E-01	-8.37E-11	2.97E-06	-2.40E-01	1.75E-01	8.45E-06	9.59E-07	9.51E-08	-1.08E-09	1.31E-06	1.37E-06
8	6.49E-22	1.48E-17	9.89E-20	5.08E-11	1.18E-12	8.54E-11	-2.50E-11	-3.77E-08	-1.51E-04	5.78E-07	-4.46E-07	-2.35E-07	-2.56E-03	1.41E-02	-6.56E-01	-1.72E-02	-9.96E-03	-1.56E-02
9	1.67E-17	1.02E-21	-2.19E-20	4.80E-11	1.86E-11	-1.20E-08	-2.51E-10	-5.54E-07	-4.09E-03	-7.86E-06	-7.04E-06	-1.41E-05	-5.62E-06	-5.15E-01	-1.82E-02	2.08E-03	7.21E-02	8.10E-02
10	5.33E-21	-1.04E-21	-4.50E-24	1.24E-14	8.16E-15	-5.68E-12	-9.38E-14	-1.02E-10	-1.80E-06	-4.81E-09	1.10E-09	1.55E-08	-5.13E-08	-3.19E-05	5.90E-06	1.44E-05	-5.69E-04	-9.56E-04
11	8.02E-18	-1.61E-19	-9.79E-21	2.32E-11	9.09E-12	-5.88E-09	-1.46E-10	-2.45E-07	-1.24E-02	-4.70E-06	-2.52E-06	-1.18E-06	4.77E-06	-2.14E-01	-6.11E-03	-4.02E-03	-2.11E-01	5.34E-01
12	1.68E-19	-5.38E-18	-3.70E-20	-1.84E-11	-2.50E-13	-1.55E-10	8.08E-12	1.05E-08	5.10E-04	-4.16E-07	1.82E-07	5.57E-07	9.26E-04	-5.97E-03	2.26E-01	-2.51E-02	-2.47E-02	-2.32E-01
13	5.31E-18	-3.05E-17	2.99E-05	-1.27E-10	6.05E-01	5.09E-08	-3.76E-01	-1.00E+00	-7.17E-11	4.32E-06	-2.94E-01	2.26E-01	1.02E-05	1.11E-06	1.10E-07	-1.30E-09	1.73E-06	1.81E-06
14	1.51E-16	-5.14E-11	-2.17E-16	-6.05E-09	-8.49E-12	-3.14E-09	8.59E-11	4.01E-08	3.37E-05	4.62E-07	2.07E-07	2.60E-08	1.26E-03	-9.98E-03	4.68E-01	2.14E-02	6.06E-03	3.58E-02
15	-5.14E-11	-1.57E-16	1.25E-16	-5.25E-09	-1.53E-10	1.50E-07	8.75E-10	5.99E-07	9.07E-04	-3.58E-06	3.23E-06	3.64E-06	6.19E-06	3.68E-01	1.31E-02	-2.66E-03	-4.64E-02	4.21E-02
16	-2.81E-15	-9.96E-15	-4.79E-17	3.24E-10	-7.07E-11	8.31E-08	2.72E-10	4.49E-08	4.04E-06	2.54E-06	-2.11E-07	-6.76E-07	-1.48E-06	8.78E-04	-1.35E-04	-5.18E-06	1.64E-02	1.16E-02
17	-8.26E-10	-8.36E-14	3.53E-16	-1.16E-07	-3.05E-09	3.07E-06	1.57E-08	5.53E-06	2.56E-03	-1.76E-04	-2.71E-05	-1.34E-04	2.05E-05	1.00E+00	2.99E-02	-7.19E-03	1.00E+00	1.00E+00
18	5.64E-14	6.71E-10	4.27E-15	1.18E-07	2.07E-10	-1.35E-09	-1.64E-09	-3.90E-07	-5.26E-05	-1.08E-05	1.81E-06	2.46E-06	3.51E-03	2.57E-02	-1.00E+00	-4.54E-02	1.39E-01	2.85E-01
19	-3.08E-15	-6.68E-15	-1.41E-01	3.04E-08	-3.59E-02	-8.32E-07	5.62E-02	9.69E-01	2.82E-10	1.75E-05	-3.81E-01	4.79E-01	1.00E-05	4.27E-07	4.81E-08	-1.39E-09	4.26E-06	4.51E-06
20	-4.17E-07	1.41E-01	-4.27E-11	-6.14E-05	-8.81E-09	9.99E-07	3.13E-08	3.05E-06	-3.85E-08	-1.89E-05	1.34E-05	9.77E-07	2.82E-01	5.53E-05	-2.53E-03	3.33E-04	1.36E-03	3.49E-03
21	1.41E-01	4.17E-07	-9.27E-10	-4.20E-06	9.71E-10	1.25E-05	-1.66E-08	-1.29E-06	-1.29E-06	4.28E-05	3.69E-06	7.14E-06	-1.14E-06	-1.34E-03	-4.40E-05	1.37E-05	-1.39E-02	-2.42E-02
22	1.39E-10	-2.11E-09	5.67E-11	-8.95E-05	5.27E-07	-9.60E-04	-8.60E-07	-3.68E-05	9.98E-09	1.14E-03	5.32E-05	1.54E-05	7.34E-04	6.22E-06	-5.47E-06	8.84E-07	-3.60E-05	-4.11E-05
23	6.79E-04	2.68E-08	1.12E-09	1.10E-03	2.13E-06	-3.32E-03	-4.65E-06	-3.84E-04	-9.77E-06	-8.49E-03	1.28E-03	1.58E-03	4.24E-04	-1.00E-02	-4.86E-04	9.34E-05	-1.08E-01	-1.74E-01
24	1.67E-10	-7.66E-04	-9.42E-10	-1.36E-03	-1.32E-07	-7.02E-05	5.10E-07	3.04E-05	4.69E-07	-8.26E-04	-5.49E-05	-3.07E-05	-3.82E-03	-1.35E-04	1.32E-02	8.34E-04	-1.54E-02	-4.48E-02
25	6.24E-12	4.76E-14	1.00E+00	1.76E-08	-3.61E-02	-7.94E-07	5.63E-02	9.69E-01	2.81E-10	1.75E-05	-3.81E-01	4.79E-01	1.00E-05	4.25E-07	4.79E-08	-1.39E-09	4.26E-06	4.52E-06
26	2.96E-06	-1.00E+00	3.03E-10	4.39E-04	3.98E-08	2.68E-05	-1.56E-07	-8.04E-06	-3.55E-08	2.85E-04	3.31E-05	1.15E-05	2.82E-01	5.75E-05	-2.53E-03	3.33E-04	1.36E-03	3.49E-03
27	-1.00E+00	-2.95E-06	6.57E-09	2.98E-05	-5.77E-09	-9.02E-05	1.12E-07	7.65E-06	-1.30E-06	-2.18E-04	-1.27E-05	-1.64E-06	1.21E-05	-1.34E-03	-4.40E-05	1.38E-05	-1.39E-02	-2.42E-02
28	-1.44E-07	2.07E-06	-5.86E-08	9.26E-02	-5.51E-04	1.00E+00	9.11E-04	4.14E-02	-1.18E-05	-1.00E+00	-6.98E-02	-3.63E-02	1.81E-02	-8.20E-03	3.69E-04	1.35E-04	-1.01E-02	-1.11E-02
29	-4.13E-02	-1.63E-06	-1.50E-05	-6.69E-02	1.56E-05	2.02E-01	-2.63E-04	-1.83E-02	-5.15E-06	5.12E-01	3.40E-02	1.91E-02	-2.60E-02	-6.31E-03	-6.11E-04	2.50E-06	-1.03E-01	-1.69E-01
30	-1.22E-07	5.61E-01	6.90E-07	1.00E+00	9.70E-05	5.14E-02	-3.73E-04	-2.22E-02	6.42E-06	6.07E-01	3.94E-02	2.10E-02	-3.56E-02	4.40E-03	1.32E-02	7.28E-04	-9.59E-03	-3.83E-02
31	-2.73E-12	-1.18E-16	-1.36E-04	-1.02E-07	1.32E-03	2.82E-06	-4.95E-03	-3.76E-01	-6.68E-10	-1.07E-04	1.00E+00	1.00E+00	-3.60E-05	-3.16E-06	-3.24E-07	4.62E-09	7.79E-05	1.20E-04
32	-4.43E-13	1.50E-07	-4.99E-14	-1.66E-06	9.98E-09	-1.48E-05	-2.95E-08	-6.01E-06	1.17E-08	-6.94E-05	-5.58E-05	-7.63E-06	-1.00E+00	-7.34E-05	3.63E-03	-1.52E-03	1.53E-03	3.80E-03
33	3.60E-09	1.06E-14	-2.84E-14	-2.47E-09	6.52E-12	6.68E-08	-2.91E-10	-6.88E-08	6.99E-09	-4.20E-06	2.99E-07	1.07E-07	-2.31E-07	1.88E-05	6.32E-07	-2.78E-07	3.70E-03	9.76E-03
34	-1.87E-15	1.45E-09	2.95E-14	-8.92E-07	7.10E-08	-8.46E-05	-2.68E-07	-4.22E-05	7.37E-09	-2.24E-03	1.84E-04	2.55E-04	-9.71E-03	1.23E-05	3.45E-05	-1.50E-05	2.63E-04	4.14E-04
35	1.70E-11	-2.70E-15	1.73E-06	6.33E-07	-1.69E-05	-1.71E-05	6.35E-05	4.83E-03	3.16E-09	1.15E-03	-1.29E-02	-1.30E-02	5.61E-05	1.00E-05	9.93E-07	-5.76E-09	2.54E-03	5.71E-03
36	3.64E-16	-6.68E-12	-9.70E-15	-2.74E-07	-3.53E-10	-1.37E-07	3.15E-09	6.48E-07	-1.13E-10	3.93E-05	-2.99E-06	-4.21E-06	2.20E-06	-2.00E-07	-6.18E-07	-4.75E-08	6.77E-06	3.66E-05

19	20	21	22	23	24	25	26	27	28	29	30	31	32	33	34	35	36
3.99E-08	1.98E-07	4.37E-08	7.83E-09	3.45E-08	-3.18E-08	4.54E-10	-1.23E-07	3.76E-08	2.33E-08	9.60E-09	1.29E-08	3.94E-09	-1.11E-11	-4.30E-10	-3.29E-10	1.61E-13	6.00E-12
2.01E-03	-1.18E-01	3.89E-02	2.46E-01	3.97E-02	-1.27E-01	-3.20E-04	-7.35E-03	-1.04E-03	4.95E-04	-1.51E-03	-5.80E-03	1.05E-02	6.54E-03	3.61E-03	1.74E-04	-8.12E-06	8.25E-04
9.21E-03	-2.36E-02	-9.04E-02	-2.18E-01	-2.15E-02	9.34E-02	2.79E-04	2.23E-03	4.17E-03	2.20E-04	6.42E-06	-4.15E-05	-2.07E-02	-5.68E-03	-1.93E-03	4.14E-03	1.38E-05	-7.14E-04
5.66E-03	1.28E-01	-2.42E-01	1.00E+00	-2.39E-01	1.00E+00	2.25E-03	-6.89E-02	-2.78E-02	2.34E-03	-8.80E-03	-3.28E-02	1.47E-01	-3.70E-03	2.79E-02	-1.90E-02	-9.20E-05	-3.50E-04
-1.70E-02	7.83E-02	1.98E-01	5.46E-01	4.45E-02	-2.10E-01	-6.51E-04	-1.89E-03	-1.09E-02	-5.48E-06	-5.23E-04	-2.10E-03	5.00E-02	1.36E-02	5.70E-03	-9.20E-03	-3.31E-05	1.71E-03
4.20E-03	-2.33E-01	5.08E-02	6.14E-01	8.90E-02	-2.87E-01	-7.42E-04	-1.57E-02	1.51E-03	1.14E-03	-3.57E-03	-1.37E-02	3.13E-02	1.57E-02	9.21E-03	-1.23E-03	-2.02E-05	1.98E-03
2.84E-07	1.41E-06	3.12E-07	5.62E-08	2.47E-07	-2.27E-07	3.24E-09	-8.78E-07	2.69E-07	1.67E-07	6.87E-08	9.22E-08	2.82E-08	-7.81E-11	-3.09E-09	-2.36E-09	3.05E-13	4.27E-11
7.57E-02	-3.35E-02	1.27E-01	7.61E-05	-1.48E-02	4.57E-02	1.42E-04	-1.39E-02	-5.40E-02	4.08E-03	-1.68E-03	-8.39E-03	-7.60E-01	5.01E-03	-6.25E-02	1.77E-01	3.15E-04	8.88E-04
1.51E-02	1.20E-01	2.92E-02	-1.51E-02	-1.21E-02	-3.41E-02	7.93E-05	1.35E-02	-1.17E-02	2.60E-02	-3.82E-02	-1.55E-01	5.96E-02	-6.65E-03	7.40E-02	4.66E-02	-5.36E-06	-8.38E-04
-5.52E-06	-1.34E-03	4.02E-03	4.23E-02	6.14E-03	-2.51E-02	3.18E-02	6.21E-03	2.62E-03	-3.60E-04	-6.36E-04	1.32E-02	-6.78E-02	-1.00E+00	4.73E-02	-4.28E-02	-1.07E-04	-1.24E-01
3.23E-05	1.00E+00	2.83E-01	2.51E-01	-6.12E-02	-1.89E-01	-1.18E-03	1.07E-01	-2.88E-02	-2.04E-02	3.96E-02	1.55E-01	-4.51E-02	1.50E-02	-7.21E-02	-4.80E-02	-5.21E-06	1.87E-03
1.32E-01	1.85E-01	-1.00E+00	2.09E-01	9.23E-02	-3.05E-01	-7.66E-04	3.06E-02	6.93E-02	5.19E-03	-3.30E-03	-1.49E-02	-9.30E-01	1.42E-02	-7.23E-02	2.11E-01	4.56E-04	2.06E-03
3.76E-07	1.87E-06	4.14E-07	7.49E-08	3.28E-07	-3.01E-07	4.31E-09	-1.17E-06	3.58E-07	2.22E-07	9.15E-08	1.23E-07	3.76E-08	-1.02E-10	-4.12E-09	-3.14E-09	5.48E-14	5.31E-11
-3.13E-02	-3.22E-02	1.87E-01	-6.21E-03	-1.99E-02	6.82E-02	2.10E-04	-4.19E-03	-1.61E-02	3.94E-03	-1.88E-03	-8.95E-03	-7.68E-01	4.93E-03	-6.39E-02	1.82E-01	3.53E-04	8.97E-04
-2.76E-03	1.40E-01	4.49E-02	-9.48E-03	1.68E-03	-3.84E-02	-1.87E-04	-8.89E-03	-8.42E-04	2.51E-02	-3.90E-02	-1.57E-01	5.91E-02	-6.61E-03	7.64E-02	4.87E-02	-1.73E-06	-8.72E-04
3.29E-04	-3.68E-03	-5.26E-04	2.40E-02	-3.00E-02	6.03E-02	-1.00E+00	-2.28E-02	2.01E-03	-2.88E-03	1.15E-02	-9.29E-04	-7.07E-02	-8.76E-01	4.10E-02	-4.05E-02	-1.13E-04	-2.39E-01
1.91E-01	8.69E-01	1.33E-01	1.88E-01	-2.25E-01	-1.56E-01	1.66E-03	3.75E-01	-1.56E-01	-8.62E-03	4.72E-02	1.73E-01	-3.71E-02	1.46E-02	-9.30E-02	-6.75E-02	-4.61E-05	2.25E-03
-1.00E+00	2.20E-01	-4.31E-01	1.35E-01	4.17E-02	-7.84E-02	-8.49E-05	1.46E-01	5.11E-01	3.51E-03	-5.55E-03	-2.11E-02	-1.00E+00	1.35E-02	-8.47E-02	2.59E-01	8.79E-04	2.16E-03
9.46E-07	4.74E-06	1.05E-06	1.96E-07	8.39E-07	-7.73E-07	1.11E-08	-3.03E-06	9.28E-07	5.77E-07	2.38E-07	3.19E-07	9.76E-08	-2.42E-10	-1.07E-08	-8.17E-09	-5.71E-13	8.76E-11
-1.92E-02	7.76E-03	-2.98E-02	-5.28E-03	5.10E-03	-1.41E-02	-5.51E-06	-3.04E-02	-8.07E-02	-1.49E-03	1.16E-03	5.62E-03	2.61E-01	-1.46E-02	-3.12E-01	7.73E-01	1.80E-03	1.52E-04
-5.77E-03	-5.32E-02	-1.75E-02	7.06E-03	-3.00E-01	-4.39E-02	-7.08E-05	8.15E-02	-2.51E-02	1.51E-02	1.04E-02	2.73E-02	1.57E-02	7.59E-03	6.44E-01	3.76E-01	-1.57E-04	-1.46E-03
-6.50E-05	-3.59E-05	-5.91E-05	2.34E-04	1.15E-04	-2.73E-04	6.24E-03	-5.70E-04	1.97E-04	-1.19E-02	8.00E-02	-8.07E-02	7.58E-04	1.61E-01	-1.80E-02	5.38E-03	-5.06E-05	-9.69E-01
-4.57E-02	-3.19E-01	-8.95E-02	7.18E-02	-9.90E-02	9.53E-02	-1.74E-03	9.86E-01	-3.21E-01	4.63E-02	-8.24E-03	-6.97E-02	6.92E-02	-5.05E-03	-8.70E-01	-4.96E-01	2.14E-04	3.15E-03
2.56E-01	-8.95E-02	3.55E-01	6.55E-02	-6.22E-02	1.61E-01	-3.69E-04	3.54E-01	1.00E+00	-2.33E-03	-3.87E-03	-1.12E-02	3.00E-01	-1.07E-02	-4.15E-01	9.98E-01	3.28E-03	8.42E-04
9.47E-07	4.74E-06	1.06E-06	1.96E-07	8.40E-07	-7.74E-07	1.11E-08	-3.03E-06	9.29E-07	5.78E-07	2.38E-07	3.19E-07	9.77E-08	-2.42E-10	-1.07E-08	-8.18E-09	-5.96E-13	8.76E-11
-1.92E-02	7.76E-03	-2.98E-02	-5.28E-03	5.10E-03	-1.41E-02	-5.61E-06	-3.04E-02	-8.07E-02	-1.50E-03	1.15E-03	5.63E-03	2.61E-01	-1.46E-02	-3.12E-01	7.73E-01	1.80E-03	1.51E-04
-5.77E-03	-5.32E-02	-1.75E-02	7.06E-03	-3.00E-01	-4.39E-02	-7.07E-05	8.15E-02	-2.51E-02	1.51E-02	1.04E-02	2.72E-02	1.57E-02	7.59E-03	6.44E-01	3.76E-01	-1.57E-04	-1.46E-03
-8.04E-04	-9.89E-03	-6.20E-04	-2.63E-03	-3.38E-03	-1.23E-04	6.54E-03	-2.81E-02	1.05E-02	6.01E-03	1.35E-01	-1.15E-01	5.52E-03	1.59E-01	-2.12E-02	2.36E-03	5.04E-04	-9.68E-01
-4.54E-02	-3.14E-01	-8.93E-02	7.33E-02	-9.72E-02	9.52E-02	-1.92E-03	1.00E+00	-3.27E-01	3.83E-02	-4.02E-02	-4.76E-02	6.69E-02	-3.57E-03	-8.68E-01	-4.95E-01	-6.93E-05	2.34E-03
2.57E-01	-8.37E-02	3.55E-01	6.72E-02	-6.02E-02	1.61E-01	-5.71E-04	3.70E-01	9.94E-01	-1.21E-02	-4.04E-02	1.36E-02	2.97E-01	-9.02E-03	-4.13E-01	1.00E+00	2.97E-03	-7.70E-05
3.14E-05	2.13E-04	6.01E-05	-3.52E-05	6.58E-05	-6.46E-05	1.34E-06	-8.50E-04	2.92E-04	5.64E-04	1.96E-04	2.68E-04	1.21E-04	-7.78E-07	-7.69E-05	-5.12E-05	-9.95E-09	4.81E-08
-2.06E-02	8.19E-03	-3.11E-02	-5.20E-03	5.27E-03	-1.45E-02	-2.34E-06	-3.07E-02	-8.13E-02	-1.56E-03	1.65E-03	5.15E-03	2.61E-01	-1.46E-02	-3.12E-01	7.73E-01	1.80E-03	1.65E-04
3.09E-03	4.50E-02	2.34E-02	4.38E-03	1.00E+00	1.97E-01	-5.13E-04	1.31E-01	-3.78E-02	1.69E-02	1.19E-02	3.12E-02	1.71E-02	7.83E-03	6.54E-01	3.83E-01	-1.58E-04	-1.46E-03
-1.75E-04	6.32E-04	-2.79E-04	-4.52E-04	3.83E-04	-1.44E-04	-9.97E-04	1.17E-02	-6.56E-03	1.49E-01	-1.00E+00	1.00E+00	1.48E-02	2.18E-01	-2.40E-02	1.60E-03	4.29E-04	-1.00E+00
1.88E-03	1.73E-02	6.21E-03	1.15E-02	9.34E-03	-9.77E-03	2.92E-04	-4.33E-01	1.67E-01	1.00E+00	2.94E-01	4.09E-01	2.74E-01	-4.90E-03	-1.00E+00	-5.83E-01	-8.63E-05	2.43E-03
-2.97E-04	1.27E-04	-6.72E-04	3.60E-04	1.54E-04	-4.35E-04	2.07E-06	-3.28E-03	-9.85E-03	4.19E-04	9.34E-04	-2.23E-04	-1.19E-02	1.14E-03	1.17E-01	-2.39E-01	1.00E+00	-6.19E-04

FRF Output – X Direction

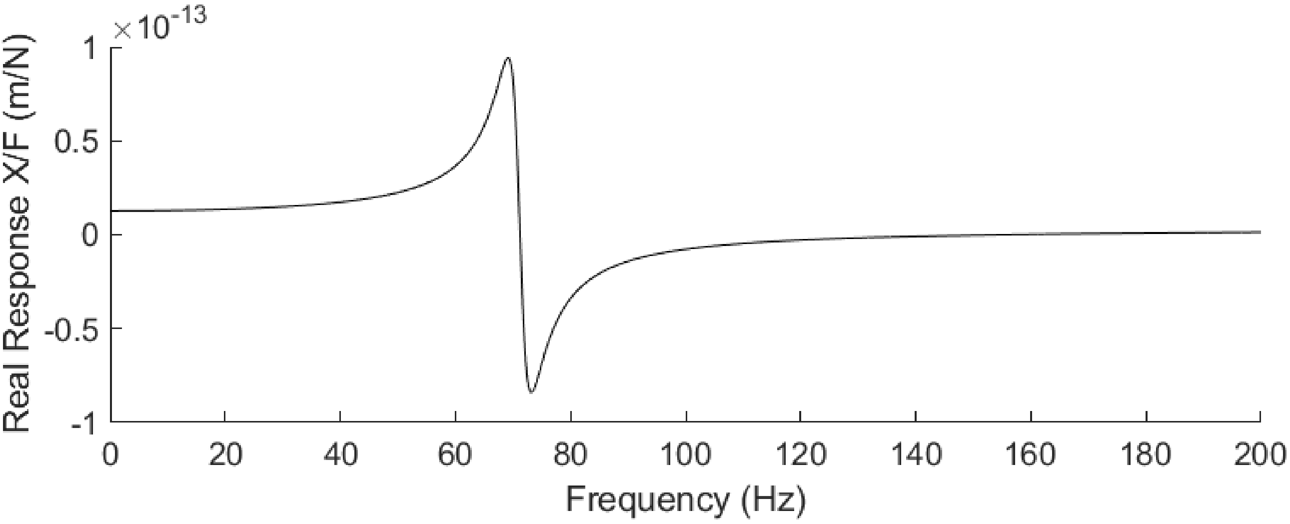

Modes: [69.2Hz, 9.41982e-14m]

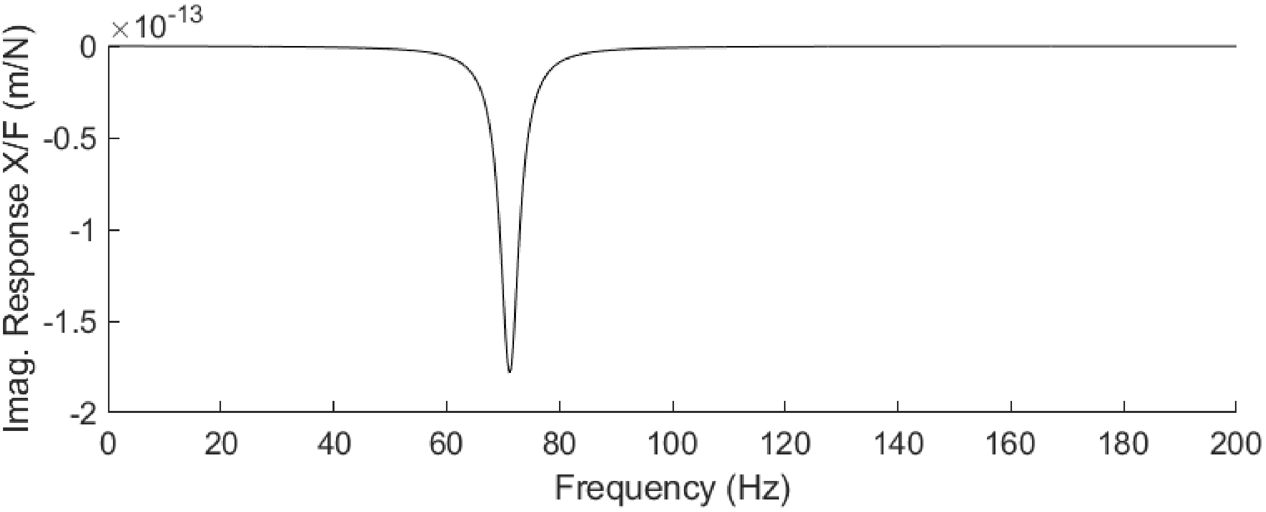

FRF Output – Y Direction

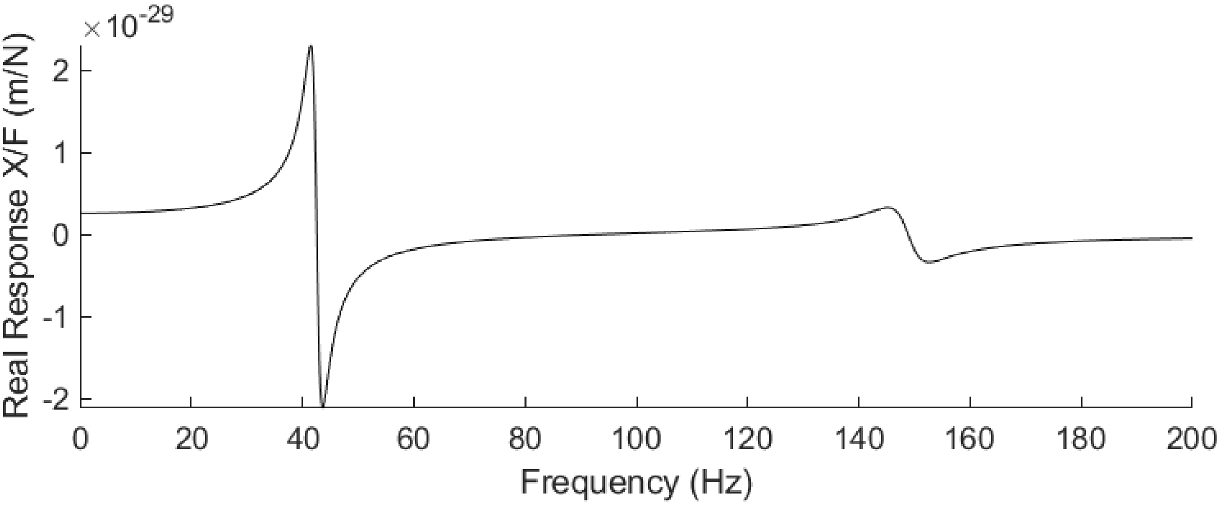

Modes: [41.5 Hz, 2.33839e-29m ;145.4 Hz, 3.22126e-30m]

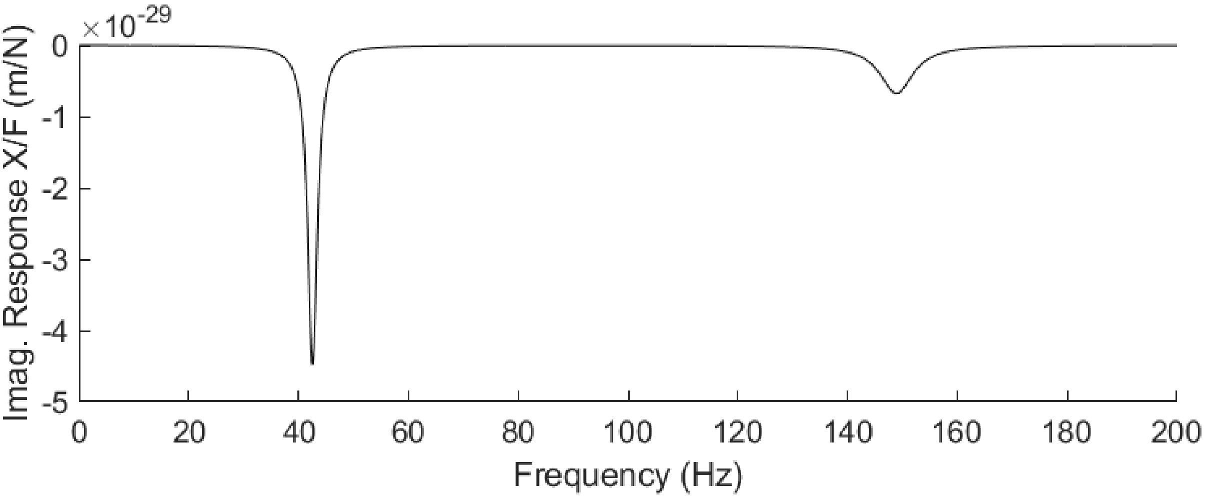

19 Appendix K

K.1 Stability Lobe Inputs and Outputs Graphs - Configuration 1

FRF Inputs

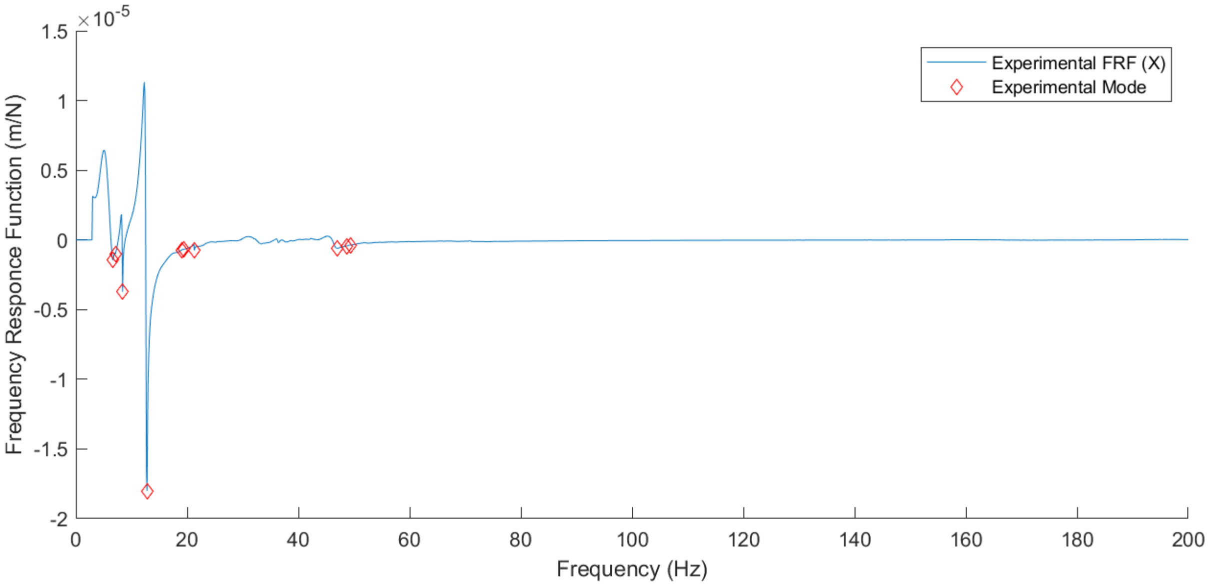

Modes (Descending order of negative response)										
Frequency (Hz)	12.8	8.4	6.7	7.1	19	21.3	19.4	47	48.7	49.4
Response (m/N)	-1.80 x10^-5	-3.72 x10^-6	-1.44 x10^-6	-1.03 x10^-6	-7.60 x10^-7	-7.50 x10^-7	-7.07 x10^-7	-6.01 x10^-7	-4.35 x10^-7	-3.66 x10^-7
Lower bound (Hz)	10.24	6.72	5.36	5.68	15.2	17.04	15.52	37.6	38.96	39.52
Upper Bound (Hz)	15.36	10.08	8.04	8.52	22.8	25.56	23.28	56.4	58.44	59.28

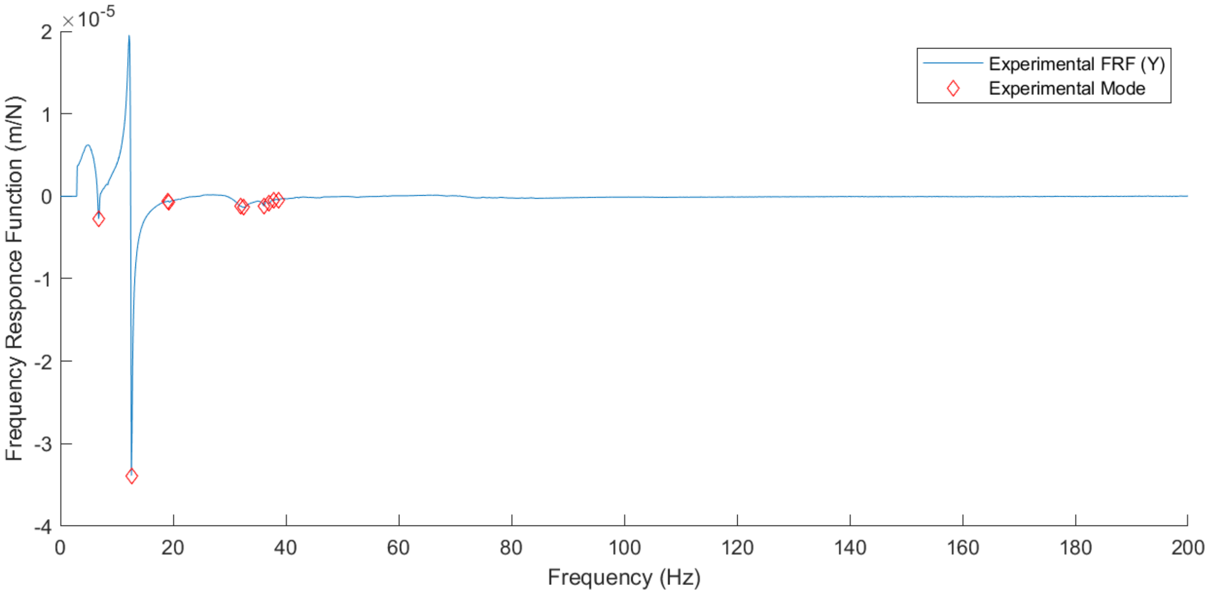

Frequency (Hz)	12.6	6.8	32.5	32	36.1	37	19.3	19	37.8	38.7
Response (m/N)	-3.39 x10^-5	-2.74 x10^-6	-1.34 x10^-6	-1.23 x10^-6	-1.16 x10^-6	-8.90 x10^-7	-7.29 x10^-7	-6.61 x10^-7	-5.32 x10^-7	-4.98 x10^-7
Lower bound (Hz)	10.08	5.44	26	25.6	28.88	29.6	15.44	15.2	30.24	30.96
Upper Bound (Hz)	15.12	8.16	39	38.4	43.32	44.4	23.16	22.8	45.36	46.44

Cutpro Stability Lobes Output

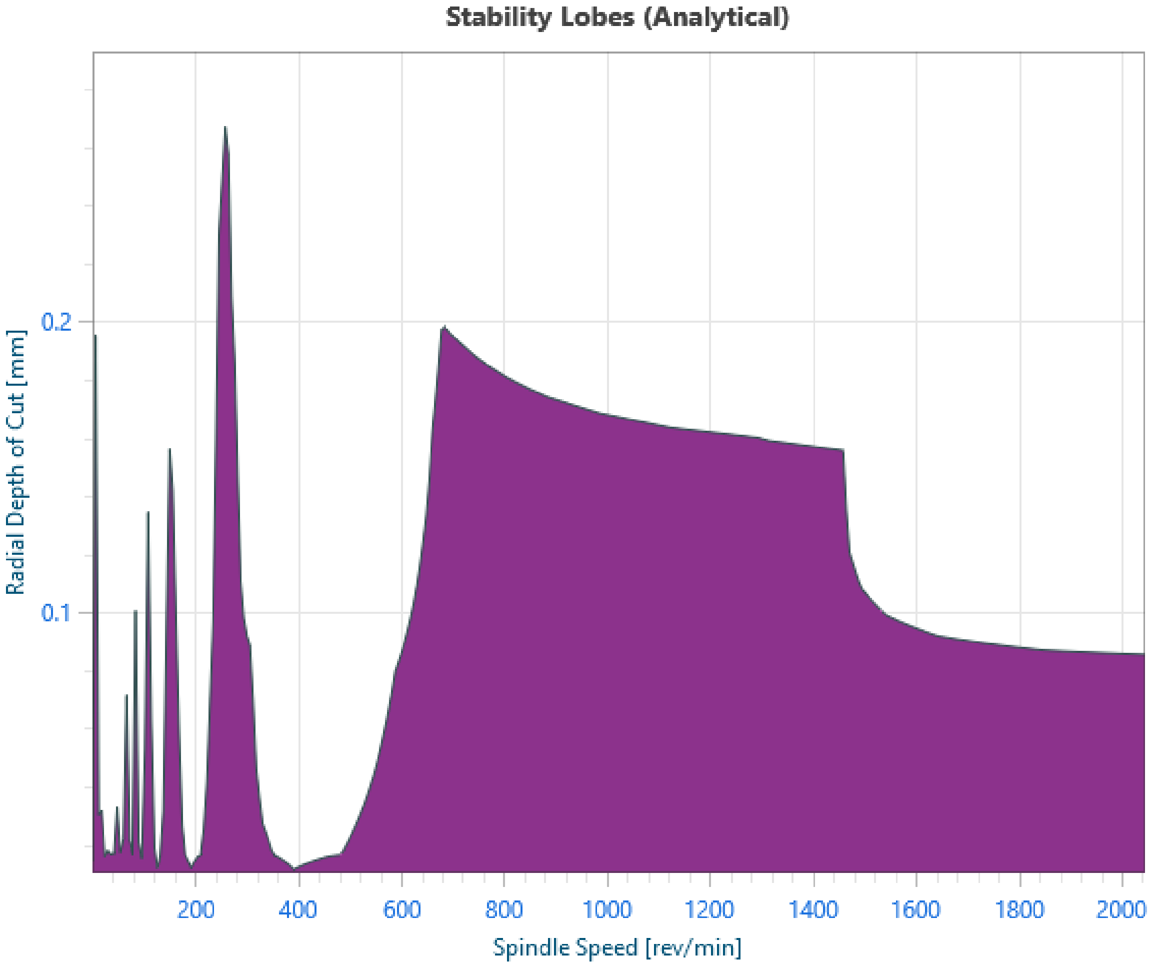

RPM	mm
259.108	0.2668
679.283	0.197113

Matlab Stability Lobes Output

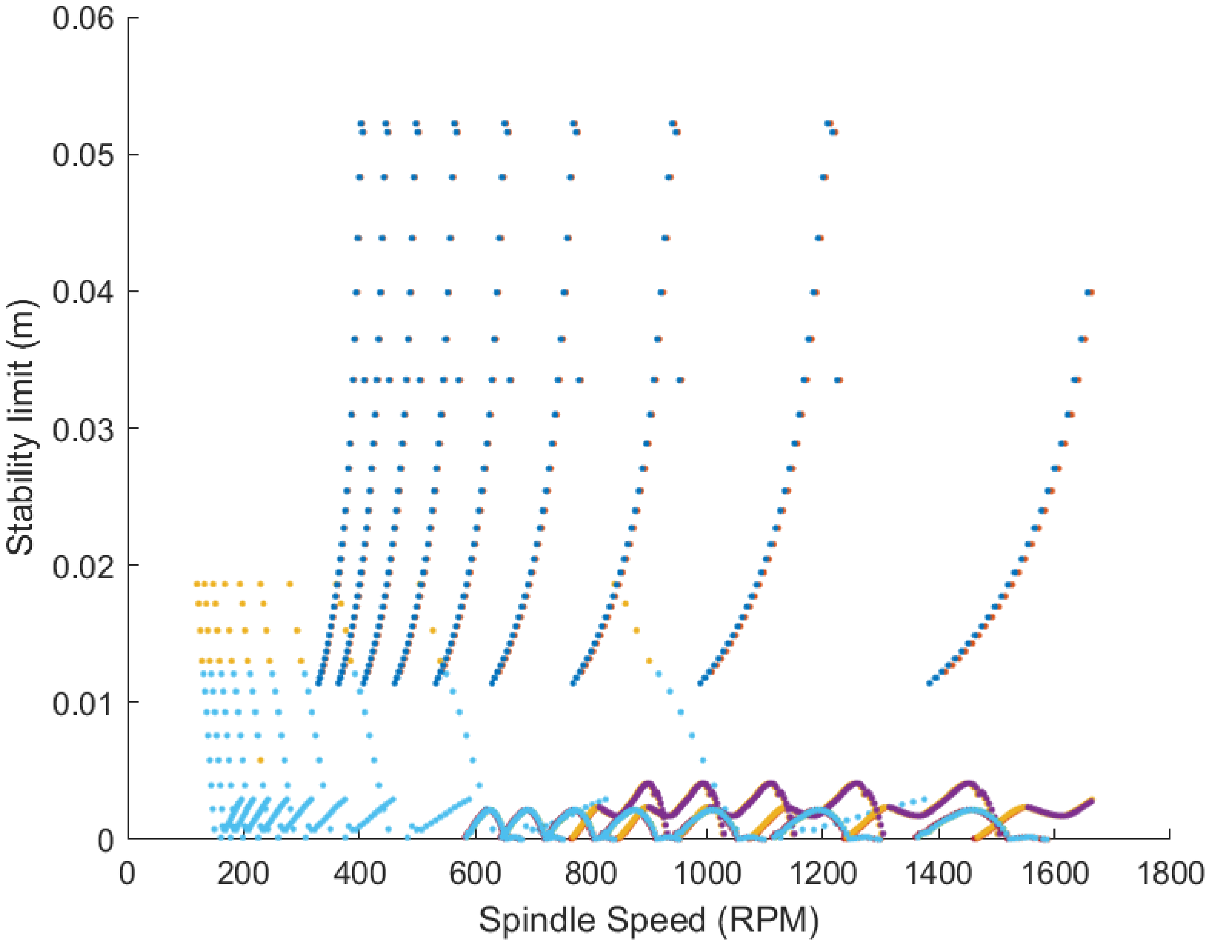

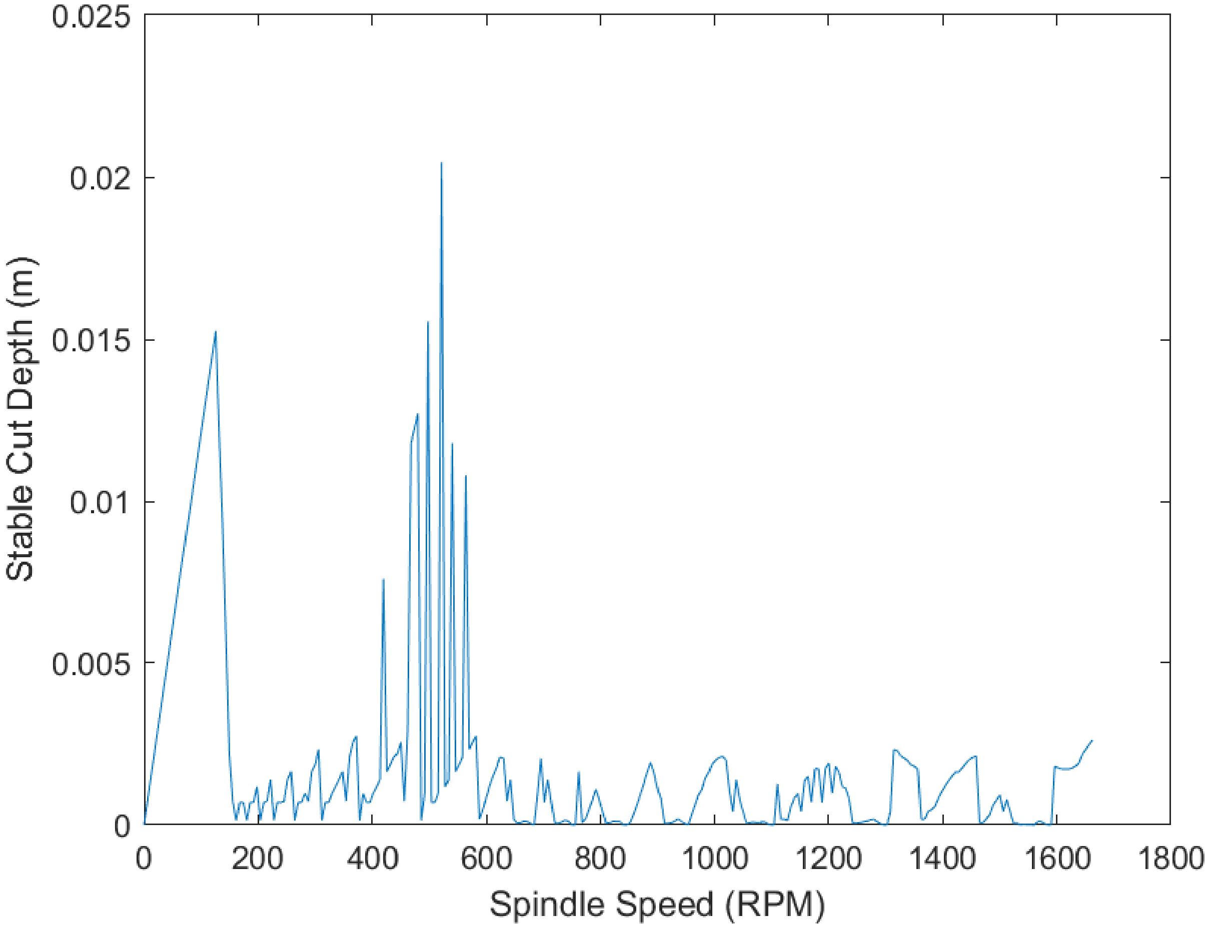

RPM	m
150	0.0171264
582	0.00715799

K.2 Stability Lobe Inputs and Outputs Graphs - Configuration 2

FRF Inputs

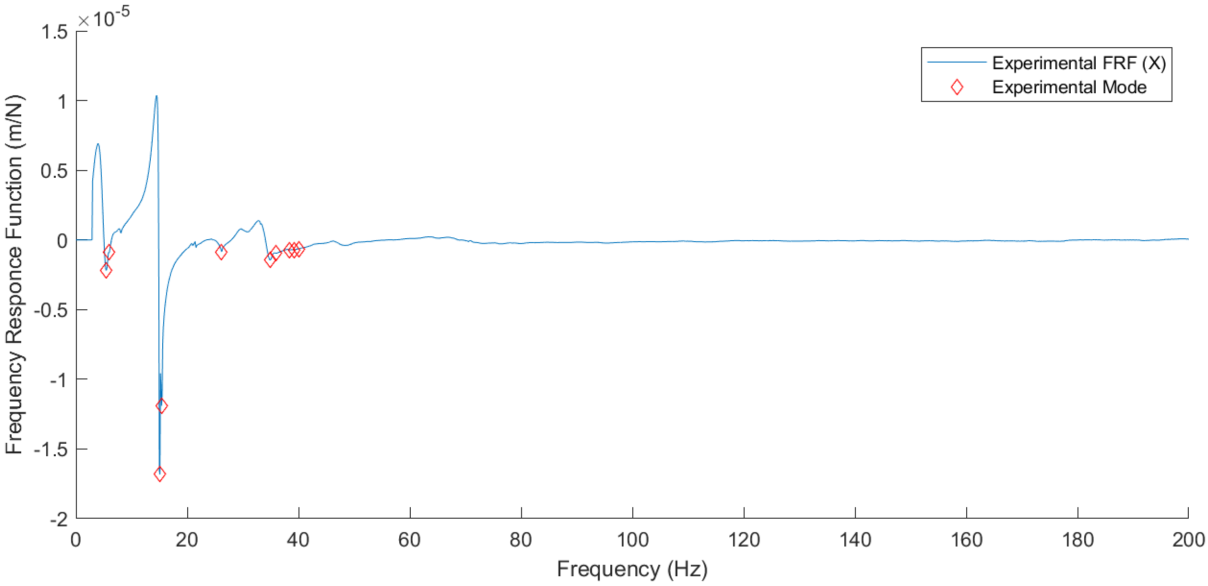

Frequency (Hz)	15.1	15.4	5.5	34.9	36	6	26.2	38.4	39.2	40
Response (m/N)	-1.68 x10^-5	-1.19 x10^-5	-2.17 x10^-6	-1.45 x10^-6	-9.54 x10^-7	-9.15 x10^-7	-8.51 x10^-7	-7.34 x10^-7	-7.14 x10^-7	-6.49 x10^-7
Upper bound (Hz)	12.08	12.32	4.4	27.92	28.8	4.8	20.96	30.72	31.36	32
Lower bound (Hz)	18.12	18.48	6.6	41.88	43.2	7.2	31.44	46.08	47.04	48

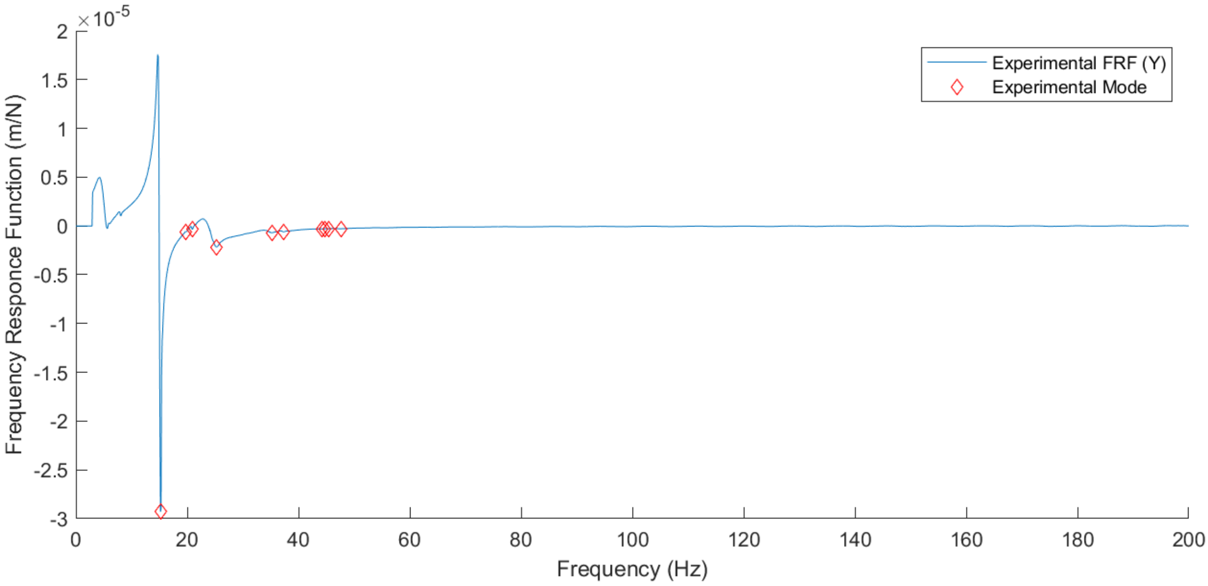

Frequency (Hz)	15.2	25.3	35.2	37.3	19.8	20.9	44.2	45.5	44.8	47.6
Response (m/N)	-2.93 x10^-5	-2.16 x10^-6	-6.94 x10^-7	-6.05 x10^-7	-5.94 x10^-7	-3.68 x10^-7	-3.01 x10^-7	-2.93 x10^-7	-2.91 x10^-7	-2.83 x10^-7
Upper bound (Hz)	12.16	20.24	28.16	29.84	15.84	16.72	35.36	36.4	35.84	38.08
Lower bound (Hz)	18.24	30.36	42.24	44.76	23.76	25.08	53.04	54.6	53.76	57.12

Cutpro Stability Lobes Output

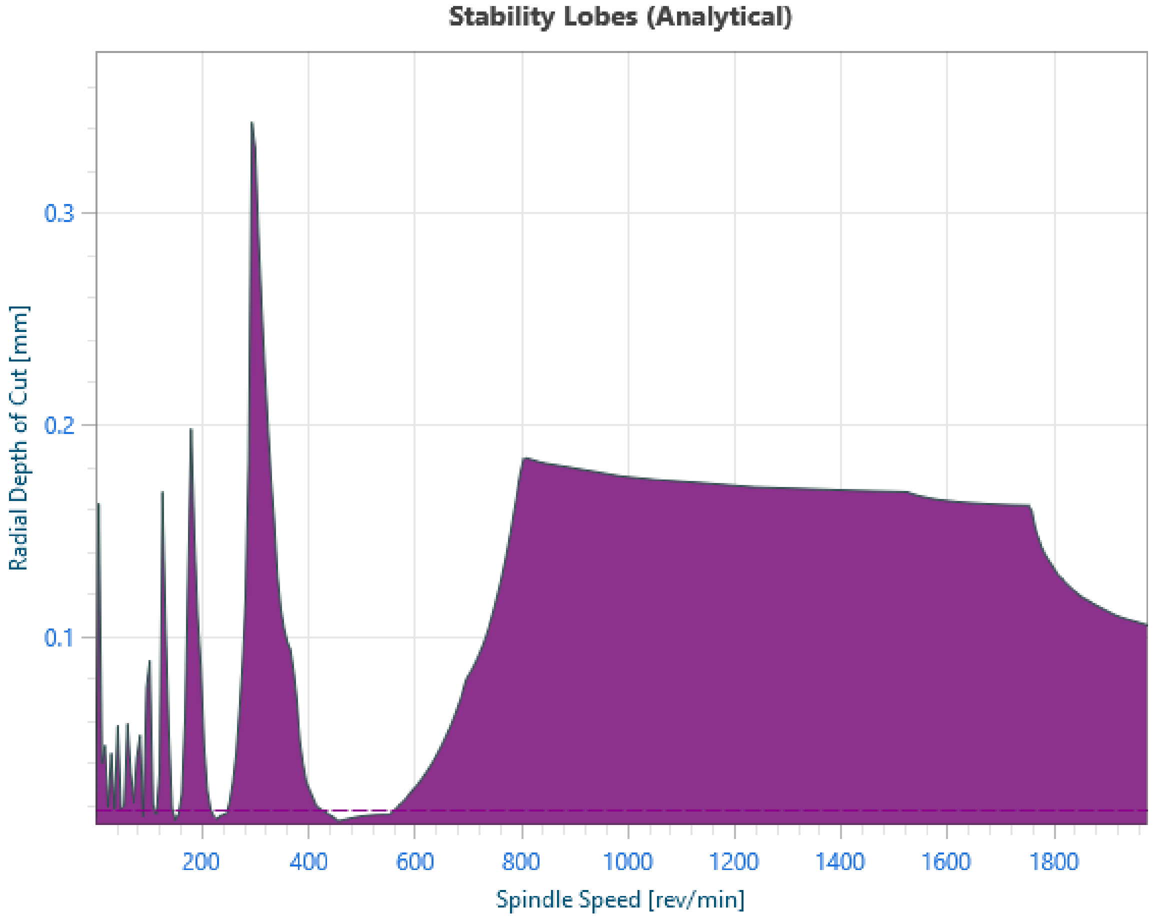

RPM	mm
295.123	0.342378
811.338	0.183911

Matlab Stability Lobes Output

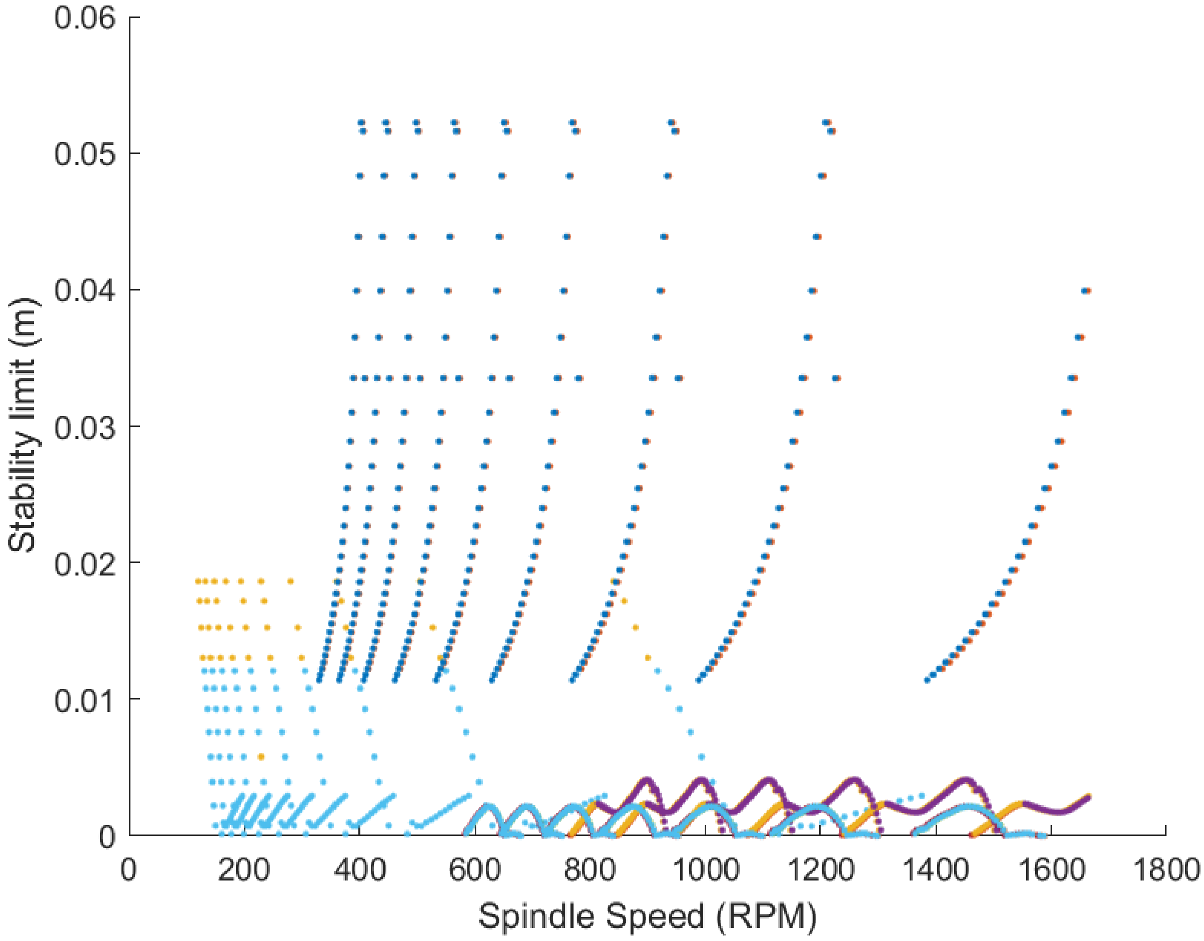

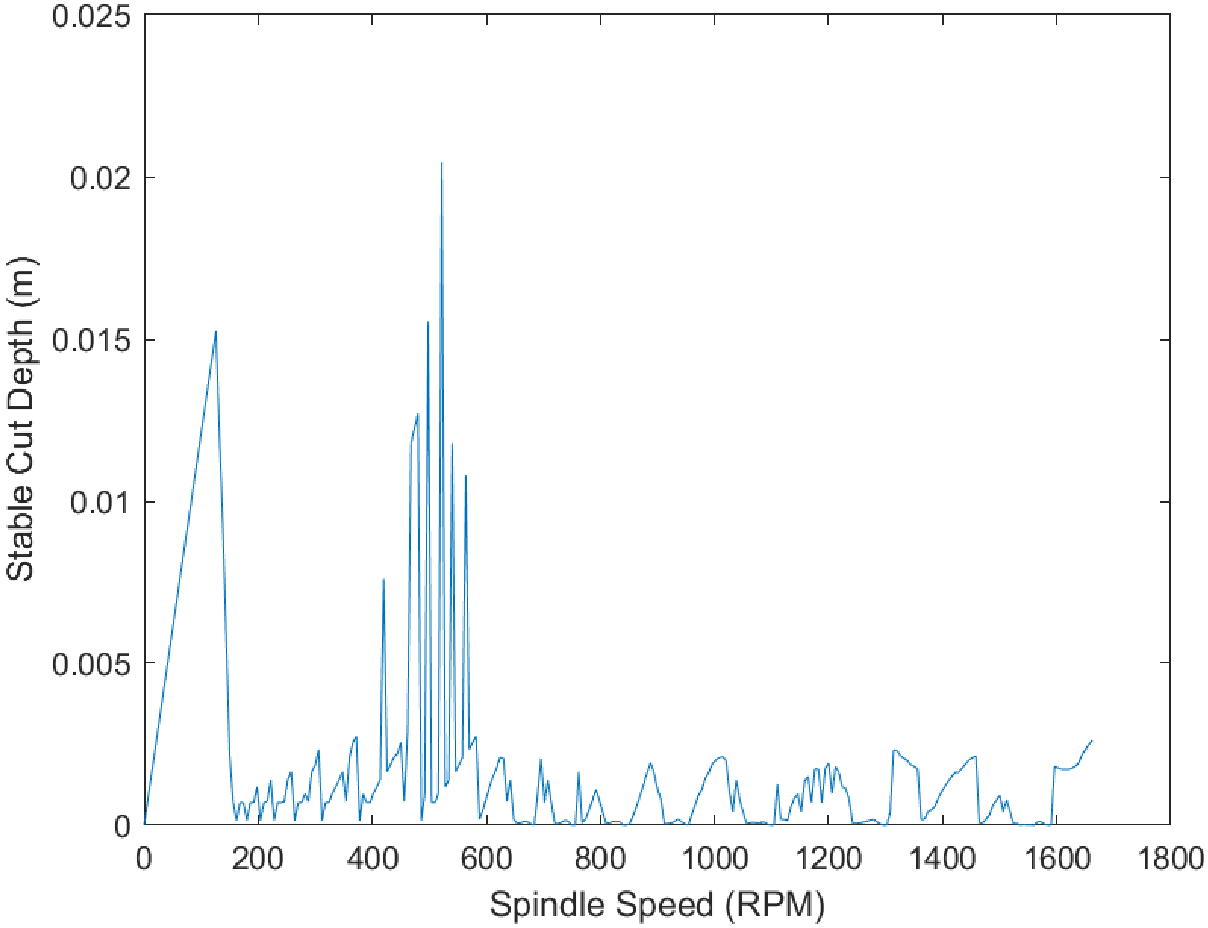

RPM	m
126	0.0152467
522	0.0204559

K.3 Stability Lobe Inputs and Outputs Graphs - Configuration 3

FRF Inputs

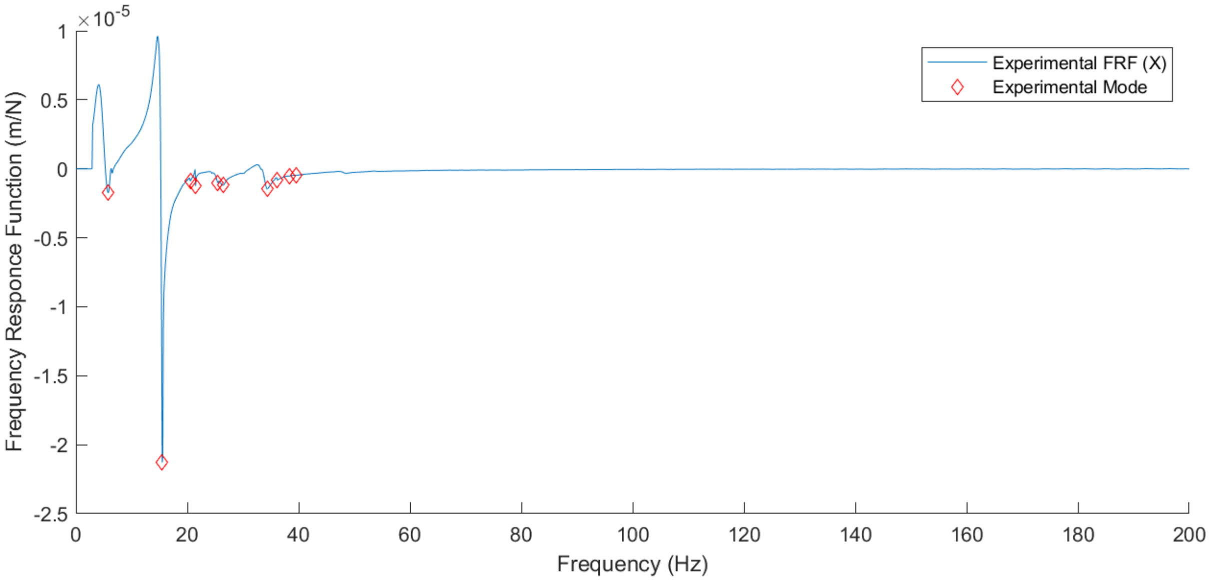

Frequency (Hz)	15.5	5.8	34.4	21.5	26.4	25.5	20.6	36.2	38.3	39.6
Response (m/N)	-2.13 x10^-5	-1.74 x10^-6	-1.46 x10^-6	-1.25 x10^-6	-1.20 x10^-6	-1.02 x10^-6	-8.94 x10^-7	-8.34 x10^-7	-5.31 x10^-7	-4.77 x10^-7
Upper bound (Hz)	12.16	20.24	28.16	29.84	15.84	16.72	35.36	36.4	35.84	38.08
Lower bound (Hz)	18.24	30.36	42.24	44.76	23.76	25.08	53.04	54.6	53.76	57.12

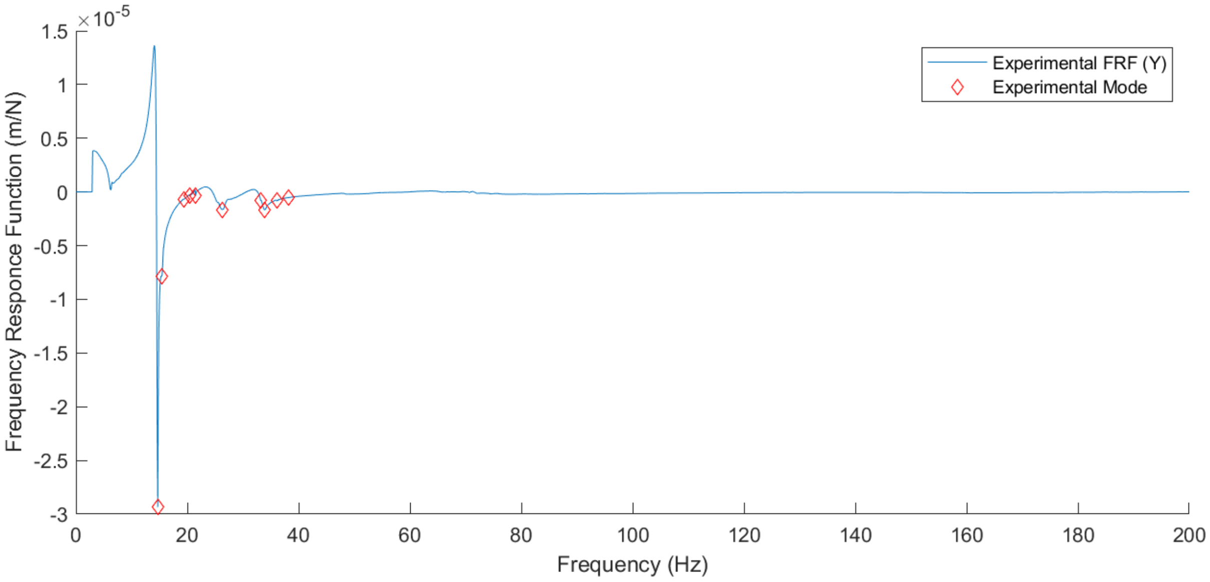

Frequency (Hz)	14.7	15.4	33.9	26.3	36.1	33.2	19.4	38.2	21.5	20.5
Response (m/N)	-2.93 x10^-5	-7.86 x10^-6	-1.66 x10^-6	-1.65 x10^-6	-8.26 x10^-7	-8.10 x10^-7	-6.93 x10^-7	-5.36 x10^-7	-3.57 x10^-7	-3.20 x10^-7
Upper bound (Hz)	11.76	12.32	27.12	21.04	28.88	26.56	15.52	30.56	17.2	16.4
Lower bound (Hz)	17.64	18.48	40.68	31.56	43.32	39.84	23.28	45.84	25.8	24.6

Cutpro Stability Lobes Output

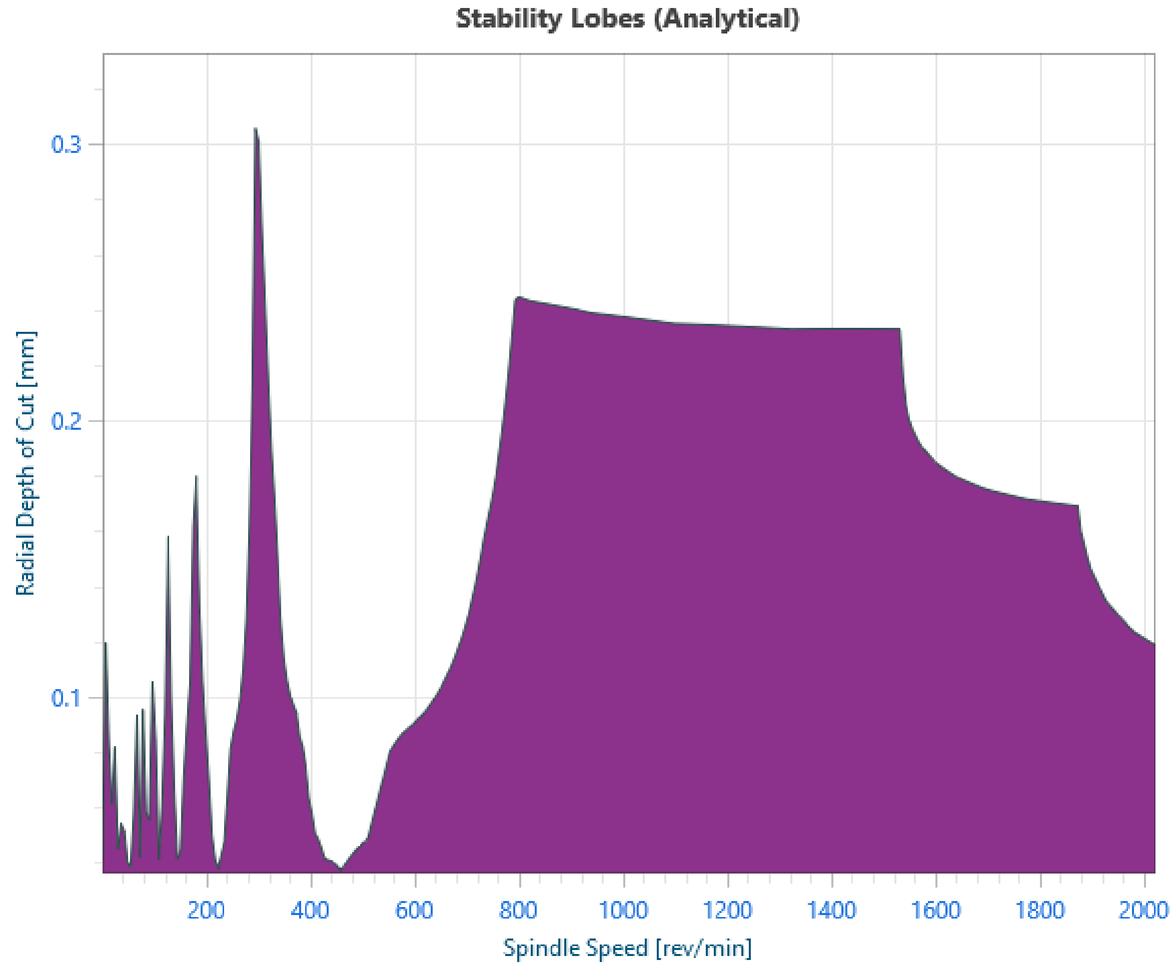

RPM	mm
295.123	0.305383
799.333	0.24464

Matlab Stability Lobes Output

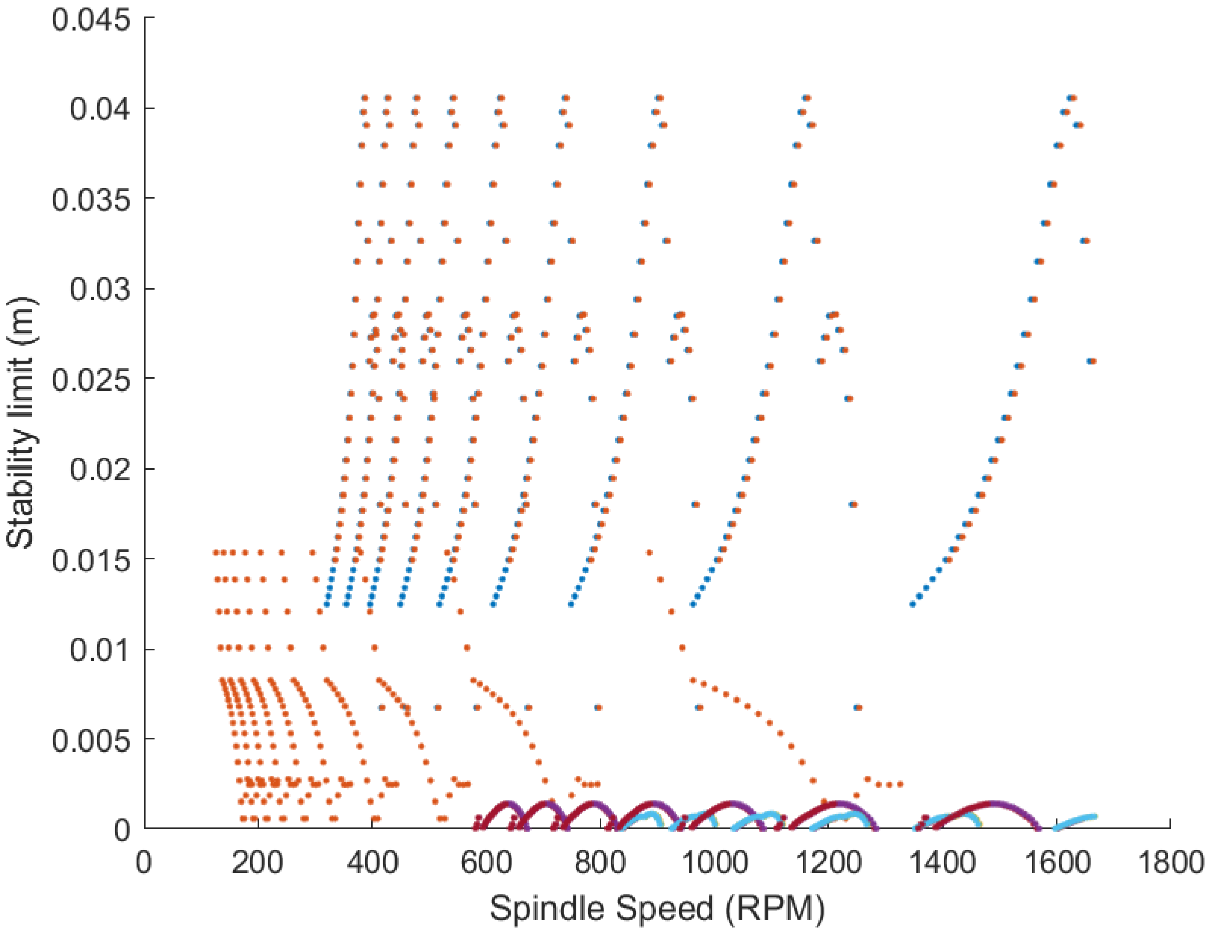

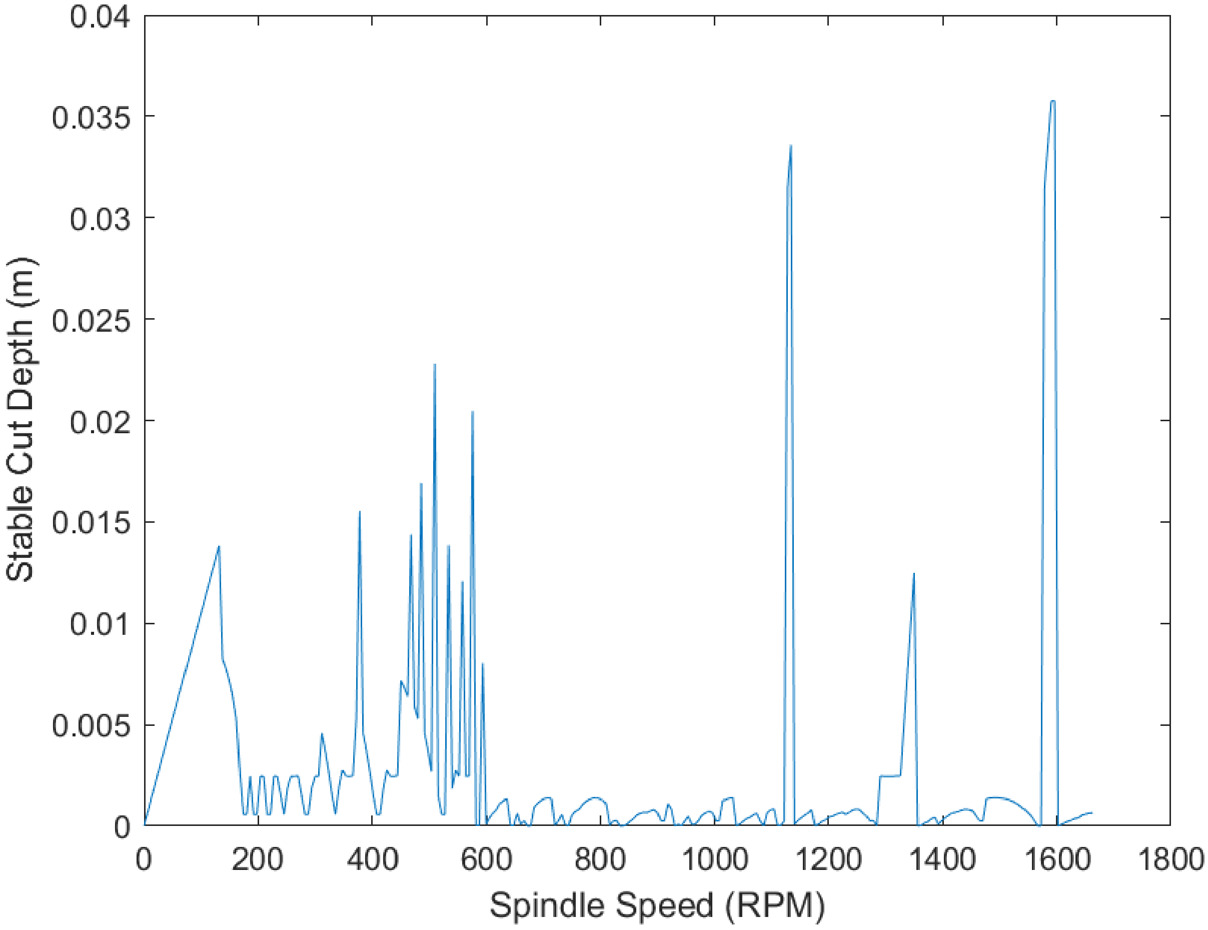

RPM	m
132	0.0138395
510	0.022806
1134	0.0336097
1590	0.0357678

K.4 Stability Lobe Inputs and Outputs Graphs - Configuration 4

FRF Inputs

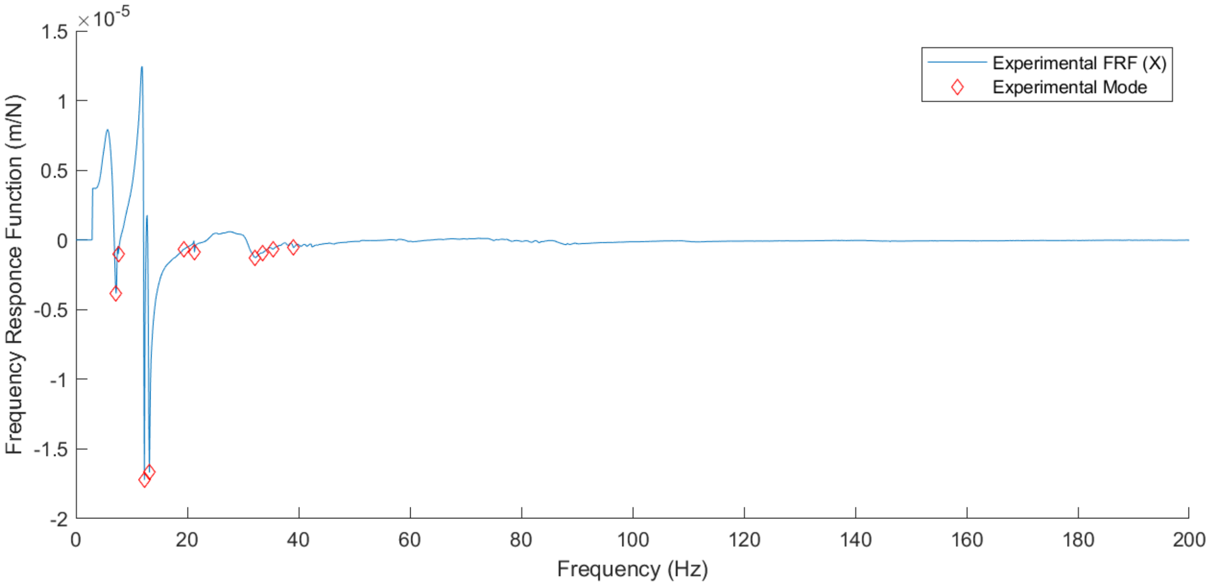

Frequency (Hz)	12.3	13.2	7.2	32.2	7.6	33.5	21.3	19.4	35.4	39.1
Response (m/N)	-1.72 x10^-5	-1.67 x10^-5	-3.84 x10^-6	-1.26 x10^-6	-1.00 x10^-6	-9.33 x10^-7	-8.81 x10^-7	-6.91 x10^-7	-6.69 x10^-7	-5.49 x10^-7
Upper bound (Hz)	9.84	10.56	5.76	25.76	6.08	26.8	17.04	15.52	28.32	31.28
Lower bound (Hz)	14.76	15.84	8.64	38.64	9.12	40.2	25.56	23.28	42.48	46.92

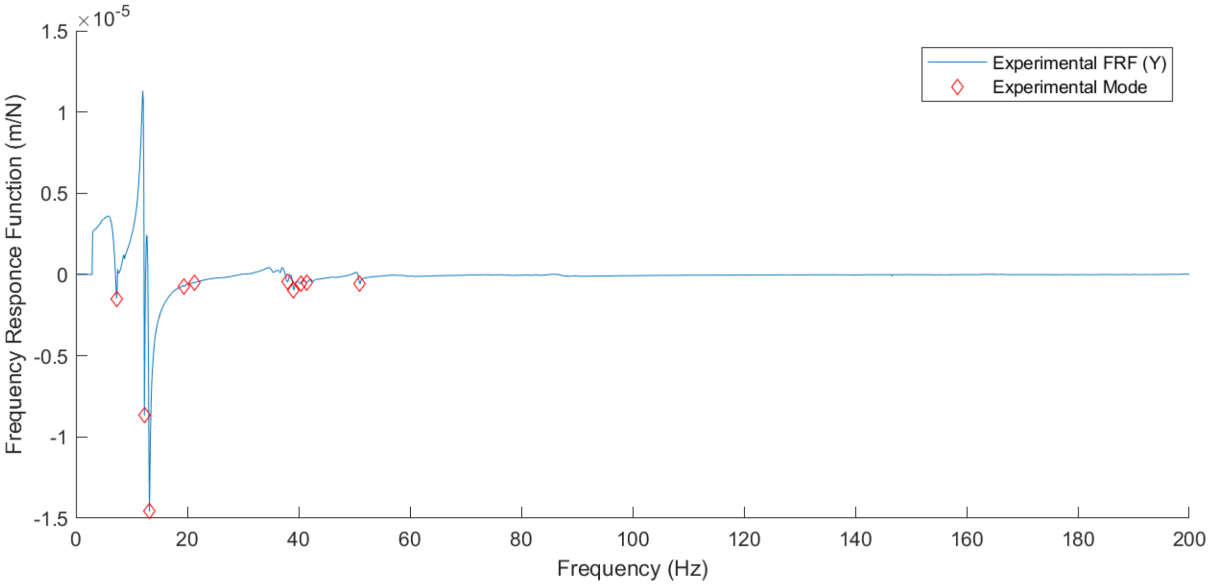

Frequency (Hz)	13.2	12.3	7.3	39.1	19.4	51	40.4	21.3	41.4	38
Response (m/N)	-1.46 x10^-5	-8.68 x10^-6	-1.48 x10^-6	-9.53 x10^-7	-7.52 x10^-7	-5.85 x10^-7	-5.66 x10^-7	-5.21 x10^-7	-5.01 x10^-7	-4.62 x10^-7
Upper bound (Hz)	10.56	9.84	5.84	31.28	15.52	40.8	32.32	17.04	33.12	30.4
Lower bound (Hz)	15.84	14.76	8.76	46.92	23.28	61.2	48.48	25.56	49.68	45.6

Cutpro Stability Lobes Output

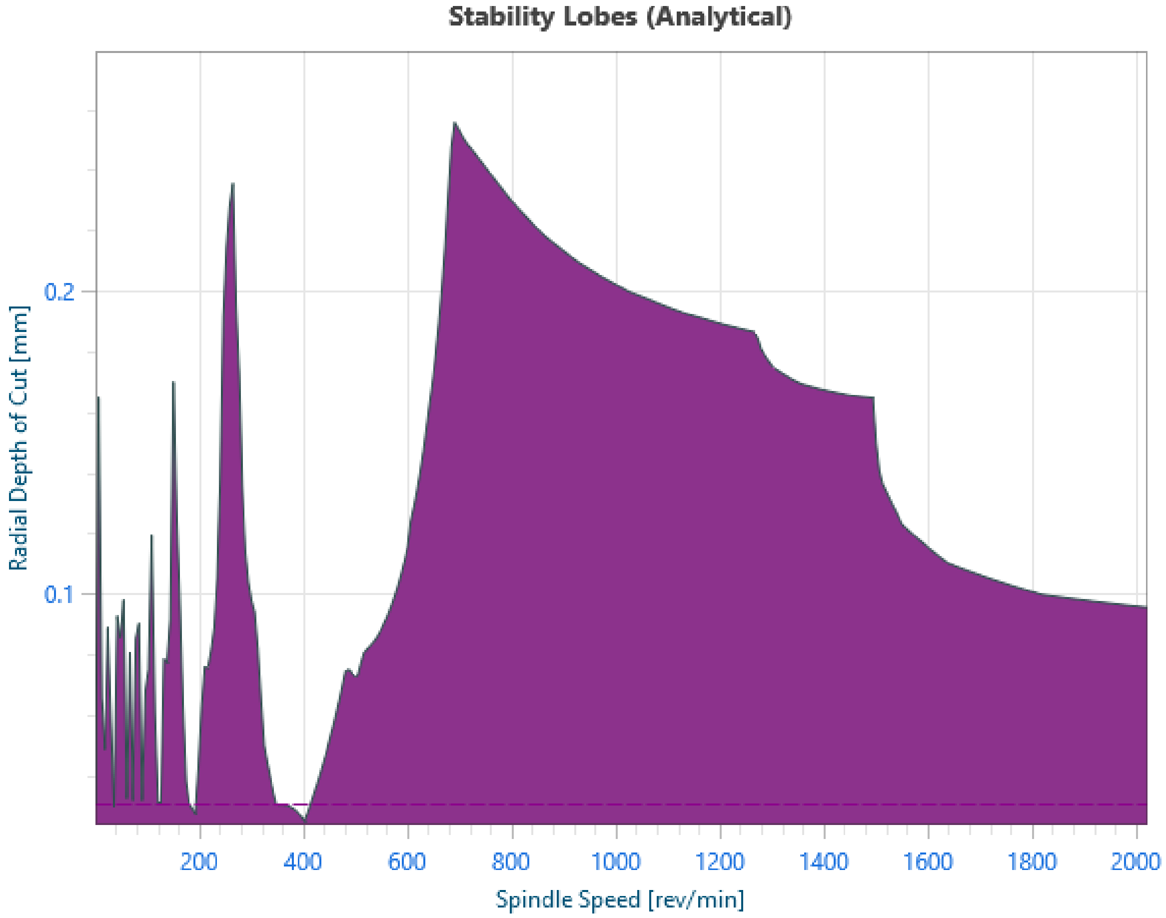

RPM	mm
265.11	0.235321
691.288	0.255449

Matlab Stability Lobes Output

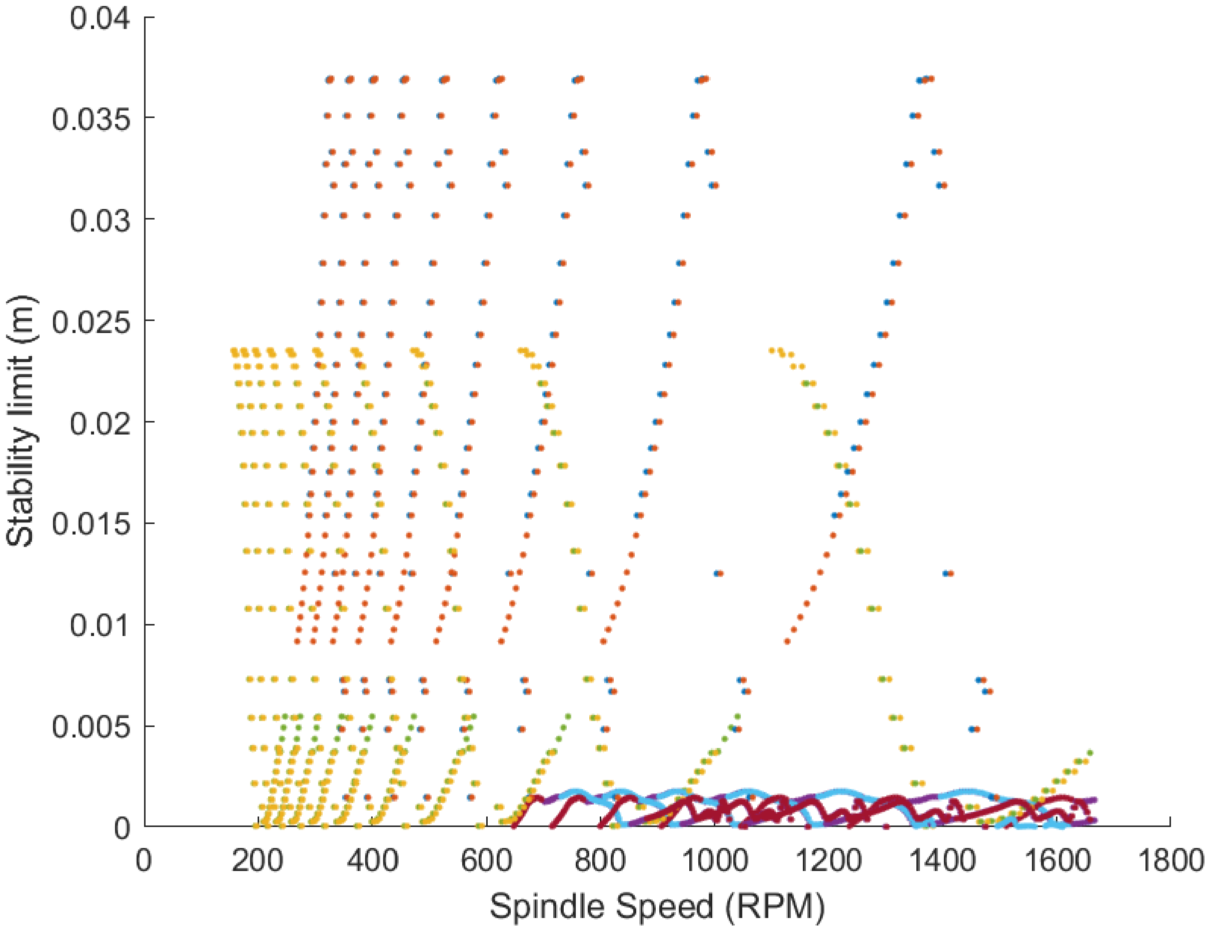

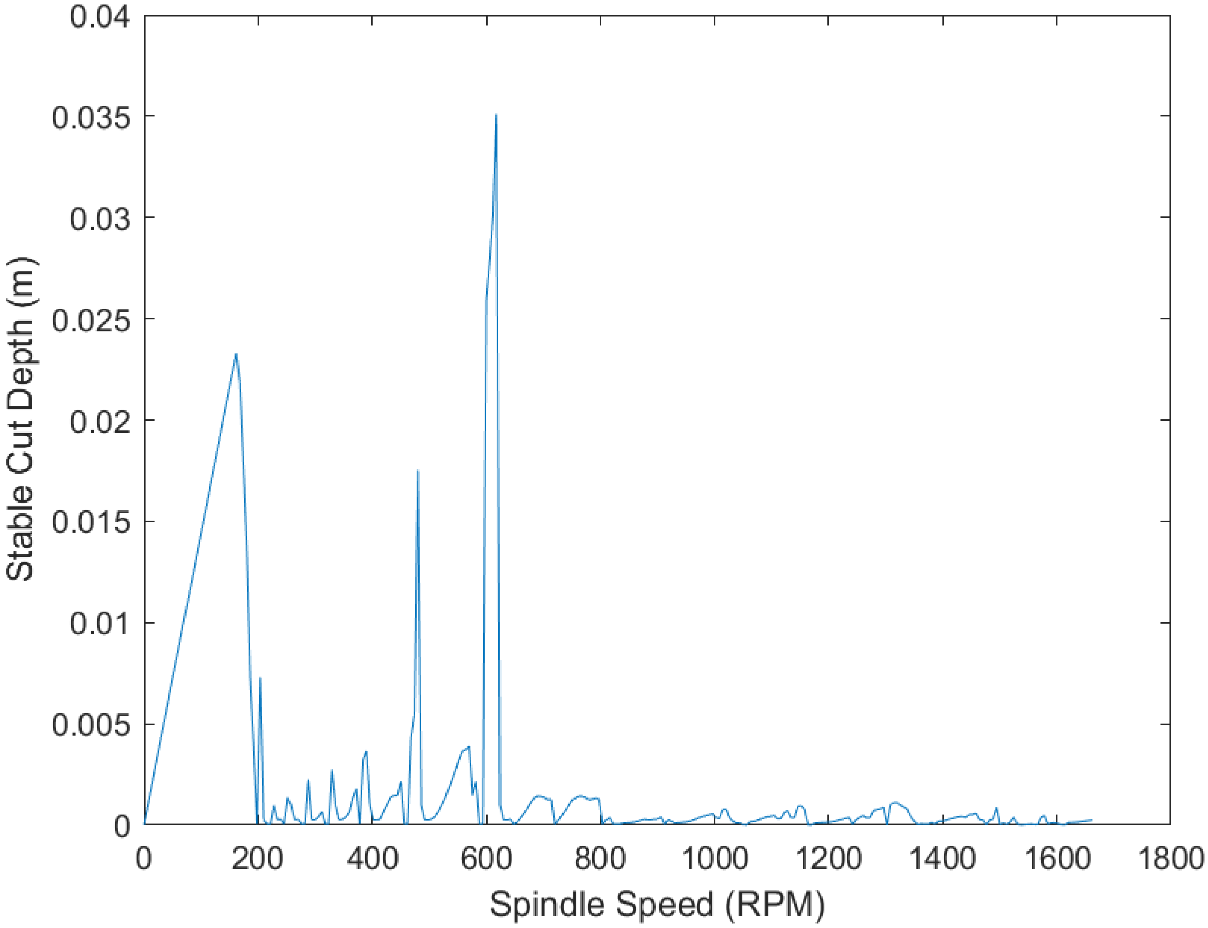

RPM	m
162	0.0233168
618	0.0351